

INTERNATIONAL LINEAR COLLIDER REFERENCE DESIGN REPORT

**ILC Global Design Effort and
World Wide Study**

AUGUST, 2007

Volume 1: EXECUTIVE SUMMARY

Editors:

James Brau, Yasuhiro Okada, Nicholas Walker

Volume 2: PHYSICS AT THE ILC

Editors:

**Abdelhak Djouadi, Joseph Lykken, Klaus Mönig
Yasuhiro Okada, Mark Oreglia, Satoru Yamashita**

Volume 3: ACCELERATOR

Editors:

Nan Phinney, Nobukazu Toge, Nicholas Walker

Volume 4: DETECTORS

Editors:

Ties Behnke, Chris Damerell, John Jaros, Akiya Miyamoto

Volume 2: PHYSICS AT THE ILC

Editors:

Abdelhak Djouadi, Joseph Lykken, Klaus Mönig

Yasuhiro Okada, Mark Oreglia, Satoru Yamashita

List of Contributors

Gerald Aarons²⁰³, Toshinori Abe²⁹⁰, Jason Abernathy²⁹³, Medina Ablikim⁸⁷,
Halina Abramowicz²¹⁶, David Adey²³⁶, Catherine Adloff¹²⁸, Chris Adolphsen²⁰³,
Konstantin Afanaciev^{11,47}, Ilya Agapov^{192,35}, Jung-Keun Ahn¹⁸⁷, Hiroaki Aihara²⁹⁰,
Mitsuo Akemoto⁶⁷, Maria del Carmen Alabau¹³⁰, Justin Albert²⁹³, Hartwig Albrecht⁴⁷,
Michael Albrecht²⁷³, David Alesini¹³⁴, Gideon Alexander²¹⁶, Jim Alexander⁴³,
Wade Allison²⁷⁶, John Amann²⁰³, Ramila Amirikas⁴⁷, Qi An²⁸³, Shozo Anami⁶⁷,
B. Ananthanarayan⁷⁴, Terry Anderson⁵⁴, Ladislav Andricek¹⁴⁷, Marc Anduze⁵⁰,
Michael Anerella¹⁹, Nikolai Anfimov¹¹⁵, Deepa Angal-Kalinin^{38,26}, Sergei Antipov⁸,
Claire Antoine^{28,54}, Mayumi Aoki⁸⁶, Atsushi Aoza¹⁹³, Steve Aplin⁴⁷, Rob Appleby^{38,265},
Yasuo Arai⁶⁷, Sakae Araki⁶⁷, Tug Arkan⁵⁴, Ned Arnold⁸, Ray Arnold²⁰³,
Richard Arnowitt²¹⁷, Xavier Artru⁸¹, Kunal Arya^{245,244}, Alexander Aryshev⁶⁷,
Eri Asakawa^{149,67}, Fred Asiri²⁰³, David Asner²⁴, Muzaffer Atac⁵⁴, Grigor Atoian³²³,
David Attié²⁸, Jean-Eudes Augustin³⁰², David B. Augustine⁵⁴, Bradley Ayres⁷⁸,
Tariq Aziz²¹¹, Derek Baars¹⁵⁰, Frederique Badaud¹³¹, Nigel Baddams³⁵,
Jonathan Bagger¹¹⁴, Sha Bai⁸⁷, David Bailey²⁶⁵, Ian R. Bailey^{38,263}, David Baker^{25,203},
Nikolai I. Balalykin¹¹⁵, Juan Pablo Balbuena³⁴, Jean-Luc Baldy³⁵, Markus Ball^{255,47},
Maurice Ball⁵⁴, Alessandro Ballestrero¹⁰³, Jamie Ballin⁷², Charles Baltay³²³,
Philip Bambade¹³⁰, Syuichi Ban⁶⁷, Henry Band²⁹⁷, Karl Bane²⁰³, Bakul Banerjee⁵⁴,
Serena Barbanotti⁹⁶, Daniele Barbareschi^{313,54,99}, Angela Barbaro-Galtieri¹³⁷,
Desmond P. Barber^{47,38,263}, Mauricio Barbi²⁸¹, Dmitri Y. Bardin¹¹⁵, Barry Barish^{23,59},
Timothy L. Barklow²⁰³, Roger Barlow^{38,265}, Virgil E. Barnes¹⁸⁶, Maura Barone^{54,59},
Christoph Bartels⁴⁷, Valeria Bartsch²³⁰, Rahul Basu⁸⁸, Marco Battaglia^{137,239},
Yuri Batygin²⁰³, Jerome Baudot^{84,301}, Ulrich Baur²⁰⁵, D. Elwyn Baynham²⁷,
Carl Beard^{38,26}, Chris Bebek¹³⁷, Philip Bechtel⁴⁷, Ulrich J. Becker¹⁴⁶, Franco Bedeschi¹⁰²,
Marc Bedjidian²⁹⁹, Prafulla Behera²⁶¹, Ties Behnke⁴⁷, Leo Bellantoni⁵⁴, Alain Bellerive²⁴,
Paul Bellomo²⁰³, Lynn D. Bentson²⁰³, Mustapha Benyamna¹³¹, Thomas Bergauer¹⁷⁷,
Edmond Berger⁸, Matthias Bergholz^{48,17}, Suman Beri¹⁷⁸, Martin Berndt²⁰³,
Werner Bernreuther¹⁹⁰, Alessandro Bertolini⁴⁷, Marc Besancon²⁸, Auguste Besson^{84,301},
Andre Beteille¹³², Simona Bettoni¹³⁴, Michael Beyer³⁰⁵, R.K. Bhandari³¹⁵,
Vinod Bharadwaj²⁰³, Vipin Bhatnagar¹⁷⁸, Satyaki Bhattacharya²⁴⁸,
Gautam Bhattacharyya¹⁹⁴, Biplob Bhattacharjee²², Ruchika Bhuyan⁷⁶, Xiao-Jun Bi⁸⁷,
Marica Biagini¹³⁴, Wilhelm Bialowons⁴⁷, Otmar Biebel¹⁴⁴, Thomas Bieler¹⁵⁰,
John Bierwagen¹⁵⁰, Alison Birch^{38,26}, Mike Bisset³¹, S.S. Biswal⁷⁴, Victoria Blackmore²⁷⁶,
Grahame Blair¹⁹², Guillaume Blanchard¹³¹, Gerald Blazey¹⁷¹, Andrew Blue²⁵⁴,
Johannes Blümlein⁴⁸, Christian Boffo⁵⁴, Courtlandt Bohn^{171,*}, V. I. Boiko¹¹⁵,
Veronique Boisvert¹⁹², Eduard N. Bondarchuk⁴⁵, Roberto Boni¹³⁴, Giovanni Bonvicini³²¹,

Stewart Boogert¹⁹², Maarten Boonekamp²⁸, Gary Boorman¹⁹², Kerstin Borrás⁴⁷,
 Daniela Bortoletto¹⁸⁶, Alessio Bosco¹⁹², Carlo Bosio³⁰⁸, Pierre Bosland²⁸, Angelo Bosotti⁹⁶,
 Vincent Boudry⁵⁰, Djamel-Eddine Boumediene¹³¹, Bernard Bouquet¹³⁰, Serguei Bourov⁴⁷,
 Gordon Bowden²⁰³, Gary Bower²⁰³, Adam Boyarski²⁰³, Ivanka Bozovic-Jelisavcic³¹⁶,
 Concezio Bozzi⁹⁷, Axel Brachmann²⁰³, Tom W. Bradshaw²⁷, Andrew Brandt²⁸⁸,
 Hans Peter Brasser⁶, Benjamin Brau²⁴³, James E. Brau²⁷⁵, Martin Breidenbach²⁰³,
 Steve Bricker¹⁵⁰, Jean-Claude Brient⁵⁰, Ian Brock³⁰³, Stanley Brodsky²⁰³,
 Craig Brooksby¹³⁸, Timothy A. Broome²⁷, David Brown¹³⁷, David Brown²⁶⁴,
 James H. Brownell⁴⁶, Mélanie Bruchon²⁸, Heiner Brueck⁴⁷, Amanda J. Brummitt²⁷,
 Nicole Brun¹³¹, Peter Buchholz³⁰⁶, Yulian A. Budagov¹¹⁵, Antonio Bulgheroni³¹⁰,
 Eugene Bulyak¹¹⁸, Adriana Bungau^{38,265}, Jochen Bürger⁴⁷, Dan Burke^{28,24},
 Craig Burkhart²⁰³, Philip Burrows²⁷⁶, Graeme Burt³⁸, David Burton^{38,136},
 Karsten Büsser⁴⁷, John Butler¹⁶, Jonathan Butterworth²³⁰, Alexei Buzulutskov²¹,
 Enric Cabruja³⁴, Massimo Caccia^{311,96}, Yunhai Cai²⁰³, Alessandro Calcaterra¹³⁴,
 Stephane Calier¹³⁰, Tiziano Camporesi³⁵, Jun-Jie Cao⁶⁶, J.S. Cao⁸⁷, Ofelia Capatina³⁵,
 Chiara Cappellini^{96,311}, Ruben Carcagno⁵⁴, Marcela Carena⁵⁴, Cristina Carloganu¹³¹,
 Roberto Carosi¹⁰², F. Stephen Carr²⁷, Francisco Carrion⁵⁴, Harry F. Carter⁵⁴,
 John Carter¹⁹², John Carwardine⁸, Richard Cassel²⁰³, Ronald Cassell²⁰³,
 Giorgio Cavallari²⁸, Emanuela Cavallo¹⁰⁷, Jose A. R. Cembranos^{241,269},
 Dhiman Chakraborty¹⁷¹, Frederic Chandez¹³¹, Matthew Charles²⁶¹, Brian Chase⁵⁴,
 Subhasis Chattopadhyay³¹⁵, Jacques Chauveau³⁰², Maximilien Chefdeville^{160,28},
 Robert Chehab¹³⁰, Stéphane Chel²⁸, Georgy Chelkov¹¹⁵, Chiping Chen¹⁴⁶,
 He Sheng Chen⁸⁷, Huai Bi Chen³¹, Jia Er Chen¹⁰, Sen Yu Chen⁸⁷, Shaomin Chen³¹,
 Shenjian Chen¹⁵⁷, Xun Chen¹⁴⁷, Yuan Bo Chen⁸⁷, Jian Cheng⁸⁷, M. Chevallier⁸¹,
 Yun Long Chi⁸⁷, William Chickering²³⁹, Gi-Chol Cho¹⁷⁵, Moo-Hyun Cho¹⁸²,
 Jin-Hyuk Choi¹⁸², Jong Bum Choi³⁷, Seong Youl Choi³⁷, Young-Il Choi²⁰⁸,
 Brajesh Choudhary²⁴⁸, Debajyoti Choudhury²⁴⁸, S. Rai Choudhury¹⁰⁹, David Christian⁵⁴,
 Glenn Christian²⁷⁶, Grojean Christophe^{35,29}, Jin-Hyuk Chung³⁰, Mike Church⁵⁴,
 Jacek Ciborowski²⁹⁴, Selcuk Cihangir⁵⁴, Gianluigi Ciovati²²⁰, Christine Clarke²⁷⁶,
 Don G. Clarke²⁶, James A. Clarke^{38,26}, Elizabeth Clements^{54,59}, Cornelia Coca²,
 Paul Coe²⁷⁶, John Cogan²⁰³, Paul Colas²⁸, Caroline Collard¹³⁰, Claude Colledani⁸⁴,
 Christophe Combaret²⁹⁹, Albert Comerma²³², Chris Compton¹⁵⁰, Ben Constance²⁷⁶,
 John Conway²⁴⁰, Ed Cook¹³⁸, Peter Cooke^{38,263}, William Cooper⁵⁴, Sean Corcoran³¹⁸,
 Rémi Cornat¹³¹, Laura Corner²⁷⁶, Eduardo Cortina Gil³³, W. Clay Corvin²⁰³,
 Angelo Cotta Ramusino⁹⁷, Ray Cowan¹⁴⁶, Curtis Crawford⁴³, Lucien M Cremaldi²⁷⁰,
 James A. Crittenden⁴³, David Cussans²³⁷, Jaroslav Cvach⁹⁰, Wilfrid Da Silva³⁰²,
 Hamid Dabiri Khah²⁷⁶, Anne Dabrowski¹⁷², Wladyslaw Dabrowski³, Olivier Dadoun¹³⁰,
 Jian Ping Dai⁸⁷, John Dainton^{38,263}, Colin Daly²⁹⁶, Chris Damerell²⁷, Mikhail Danilov⁹²,
 Witold Daniluk²¹⁹, Sarojini Daram²⁶⁹, Anindya Datta²², Paul Dauncey⁷², Jacques David³⁰²,
 Michel Davier¹³⁰, Ken P. Davies²⁶, Sally Dawson¹⁹, Wim De Boer³⁰⁴, Stefania De Curtis⁹⁸,
 Nicolo De Groot¹⁶⁰, Christophe De La Taille¹³⁰, Antonio de Lira²⁰³, Albert De Roeck³⁵,
 Riccardo De Sangro¹³⁴, Stefano De Santis¹³⁷, Laurence Deacon¹⁹², Aldo Deandrea²⁹⁹,
 Klaus Dehmelt⁴⁷, Eric Delagnes²⁸, Jean-Pierre Delahaye³⁵, Pierre Delebecque¹²⁸,
 Nicholas Delerue²⁷⁶, Olivier Delferriere²⁸, Marcel Demarteau⁵⁴, Zhi Deng³¹,
 Yu. N. Denisov¹¹⁵, Christopher J. Densham²⁷, Klaus Desch³⁰³, Nilendra Deshpande²⁷⁵,
 Guillaume Devanz²⁸, Erik Devetak²⁷⁶, Amos Dexter³⁸, Vito Di Benedetto¹⁰⁷,
 Ángel Diéguez²³², Ralf Diener²⁵⁵, Nguyen Dinh Dinh^{89,135}, Madhu Dixit^{24,226},

Sudhir Dixit²⁷⁶, Abdelhak Djouadi¹³³, Zdenek Dolezal³⁶, Ralph Dollan⁶⁹, Dong Dong⁸⁷,
 Hai Yi Dong⁸⁷, Jonathan Dorfan²⁰³, Andrei Dorokhov⁸⁴, George Doucas²⁷⁶,
 Robert Downing¹⁸⁸, Eric Doyle²⁰³, Guy Doziere⁸⁴, Alessandro Drago¹³⁴, Alex Dragt²⁶⁶,
 Gary Drake⁸, Zbynek Drásal³⁶, Herbert Dreiner³⁰³, Persis Drell²⁰³, Chafik Driouichi¹⁶⁵,
 Alexandr Drozhdin⁵⁴, Vladimir Drugakov^{47,11}, Shuxian Du⁸⁷, Gerald Dugan⁴³,
 Viktor Duginov¹¹⁵, Wojciech Dulinski⁸⁴, Frederic Dulucq¹³⁰, Sukanta Dutta²⁴⁹,
 Jishnu Dwivedi¹⁸⁹, Alexandre Dychkant¹⁷¹, Daniel Dzahini¹³², Guenter Eckerlin⁴⁷,
 Helen Edwards⁵⁴, Wolfgang Ehrenfeld^{255,47}, Michael Ehrlichman²⁶⁹, Heiko Ehrlichmann⁴⁷,
 Gerald Eigen²³⁵, Andrey Elagin^{115,217}, Luciano Elementi⁵⁴, Peder Eliasson³⁵, John Ellis³⁵,
 George Ellwood^{38,26}, Eckhard Elsen⁴⁷, Louis Emery⁸, Kazuhiro Enami⁶⁷, Kuninori Endo⁶⁷,
 Atsushi Enomoto⁶⁷, Fabien Eozénou²⁸, Robin Erbacher²⁴⁰, Roger Erickson²⁰³,
 K. Oleg Eyser⁴⁷, Vitaliy Fadeyev²⁴⁵, Shou Xian Fang⁸⁷, Karen Fant²⁰³, Alberto Fasso²⁰³,
 Michele Faucci Giannelli¹⁹², John Fehlberg¹⁸⁴, Lutz Feld¹⁹⁰, Jonathan L. Feng²⁴¹,
 John Ferguson³⁵, Marcos Fernandez-Garcia⁹⁵, J. Luis Fernandez-Hernando^{38,26},
 Pavel Fiala¹⁸, Ted Fieguth²⁰³, Alexander Finch¹³⁶, Giuseppe Finocchiaro¹³⁴,
 Peter Fischer²⁵⁷, Peter Fisher¹⁴⁶, H. Eugene Fisk⁵⁴, Mike D. Fitton²⁷, Ivor Fleck³⁰⁶,
 Manfred Fleischer⁴⁷, Julien Fleury¹³⁰, Kevin Flood²⁹⁷, Mike Foley⁵⁴, Richard Ford⁵⁴,
 Dominique Fortin²⁴², Brian Foster²⁷⁶, Nicolas Fourches²⁸, Kurt Francis¹⁷¹, Ariane Frey¹⁴⁷,
 Raymond Frey²⁷⁵, Horst Friedsam⁸, Josef Frisch²⁰³, Anatoli Frishman¹⁰⁷, Joel Fuerst⁸,
 Keisuke Fujii⁶⁷, Junpei Fujimoto⁶⁷, Masafumi Fukuda⁶⁷, Shigeki Fukuda⁶⁷,
 Yoshisato Funahashi⁶⁷, Warren Funk²²⁰, Julia Furletova⁴⁷, Kazuro Furukawa⁶⁷,
 Fumio Furuta⁶⁷, Takahiro Fusayasu¹⁵⁴, Juan Fuster⁹⁴, Karsten Gadow⁴⁷, Frank Gaede⁴⁷,
 Renaud Gaglione²⁹⁹, Wei Gai⁸, Jan Gajewski³, Richard Galik⁴³, Alexei Galkin¹⁷⁴,
 Valery Galkin¹⁷⁴, Laurent Gallin-Martel¹³², Fred Gannaway²⁷⁶, Jian She Gao⁸⁷, Jie Gao⁸⁷,
 Yuanning Gao³¹, Peter Garbincius⁵⁴, Luis Garcia-Tabares³³, Lynn Garren⁵⁴,
 Luís Garrido²³², Erika Garutti⁴⁷, Terry Garvey¹³⁰, Edward Garwin²⁰³, David Gascón²³²,
 Martin Gastal³⁵, Corrado Gatto¹⁰⁰, Raoul Gatto^{300,35}, Pascal Gay¹³¹, Lixin Ge²⁰³,
 Ming Qi Ge⁸⁷, Rui Ge⁸⁷, Achim Geiser⁴⁷, Andreas Gellrich⁴⁷, Jean-Francois Genat³⁰²,
 Zhe Qiao Geng⁸⁷, Simonetta Gentile³⁰⁸, Scot Gerbick⁸, Rod Gerig⁸, Dilip Kumar Ghosh²⁴⁸,
 Kirtiman Ghosh²², Lawrence Gibbons⁴³, Arnaud Giganon²⁸, Allan Gillespie²⁵⁰,
 Tony Gillman²⁷, Ilya Ginzburg^{173,201}, Ioannis Giomataris²⁸, Michele Giunta^{102,312},
 Peter Gladkikh¹¹⁸, Janusz Gluza²⁸⁴, Rohini Godbole⁷⁴, Stephen Godfrey²⁴,
 Gerson Goldhaber^{137,239}, Joel Goldstein²³⁷, George D. Gollin²⁶⁰,
 Francisco Javier Gonzalez-Sanchez⁹⁵, Maurice Goodrick²⁴⁶, Yuri Gornushkin¹¹⁵,
 Mikhail Gostkin¹¹⁵, Erik Gottschalk⁵⁴, Philippe Goudket^{38,26}, Ivo Gough Eschrich²⁴¹,
 Filimon Gournaris²³⁰, Ricardo Graciani²³², Norman Graf²⁰³, Christian Grah⁴⁸,
 Francesco Grancagnolo⁹⁹, Damien Grandjean⁸⁴, Paul Grannis²⁰⁶, Anna Grassellino²⁷⁹,
 Eugeni Graugés²³², Stephen Gray⁴³, Michael Green¹⁹², Justin Greenhalgh^{38,26},
 Timothy Greenshaw²⁶³, Christian Grefe²⁵⁵, Ingrid-Maria Gregor⁴⁷, Gerald Grenier²⁹⁹,
 Mark Grimes²³⁷, Terry Grimm¹⁵⁰, Philippe Gris¹³¹, Jean-Francois Grivaz¹³⁰,
 Marius Groll²⁵⁵, Jeffrey Gronberg¹³⁸, Denis Grondin¹³², Donald Groom¹³⁷, Eilam Gross³²²,
 Martin Grunewald²³¹, Claus Grupen³⁰⁶, Grzegorz Grzelak²⁹⁴, Jun Gu⁸⁷, Yun-Ting Gu⁶¹,
 Monoranjan Guchait²¹¹, Susanna Guiducci¹³⁴, Ali Murat Guler¹⁵¹, Hayg Guler⁵⁰,
 Erhan Gulmez^{261,15}, John Gunion²⁴⁰, Zhi Yu Guo¹⁰, Atul Gurtu²¹¹, Huy Bang Ha¹³⁵,
 Tobias Haas⁴⁷, Andy Haase²⁰³, Naoyuki Haba¹⁷⁶, Howard Haber²⁴⁵, Stephan Haensel¹⁷⁷,
 Lars Hage⁴⁷, Hiroyuki Hagura^{67,117}, Csaba Hajdu⁷⁰, Gunther Haller²⁰³,
 Johannes Haller²⁵⁵, Lea Hallermann^{47,255}, Valerie Halyo¹⁸⁵, Koichi Hamaguchi²⁹⁰,

Larry Hammond⁵⁴, Liang Han²⁸³, Tao Han²⁹⁷, Louis Hand⁴³, Virender K. Handu¹³,
 Hitoshi Hano²⁹⁰, Christian Hansen²⁹³, Jørn Dines Hansen¹⁶⁵, Jorgen Beck Hansen¹⁶⁵,
 Kazufumi Hara⁶⁷, Kristian Harder²⁷, Anthony Hartin²⁷⁶, Walter Hartung¹⁵⁰,
 Carsten Hast²⁰³, John Hauptman¹⁰⁷, Michael Hauschild³⁵, Claude Hauviller³⁵,
 Miroslav Havranek⁹⁰, Chris Hawkes²³⁶, Richard Hawkings³⁵, Hitoshi Hayano⁶⁷,
 Masashi Hazumi⁶⁷, An He⁸⁷, Hong Jian He³¹, Christopher Hearty²³⁸, Helen Heath²³⁷,
 Thomas Hebbeker¹⁹⁰, Vincent Hedberg¹⁴⁵, David Hedin¹⁷¹, Samuel Heifets²⁰³,
 Sven Heinemeyer⁹⁵, Sebastien Heini⁸⁴, Christian Helebrant^{47,255}, Richard Helms⁴³,
 Brian Heltsley⁴³, Sophie Henrot-Versille¹³⁰, Hans Henschel⁴⁸, Carsten Hensel²⁶²,
 Richard Hermel¹²⁸, Atila Herms²³², Gregor Herten⁴, Stefan Hesselbach²⁸⁵,
 Rolf-Dieter Heuer^{47,255}, Clemens A. Heusch²⁴⁵, Joanne Hewett²⁰³, Norio Higashi⁶⁷,
 Takatoshi Higashi¹⁹³, Yasuo Higashi⁶⁷, Toshiyasu Higo⁶⁷, Michael D. Hildreth²⁷³,
 Karlheinz Hiller⁴⁸, Sonja Hillert²⁷⁶, Stephen James Hillier²³⁶, Thomas Himel²⁰³,
 Abdelkader Himmi⁸⁴, Ian Hinchliffe¹³⁷, Zenro Hioki²⁸⁹, Koichiro Hirano¹¹²,
 Tachishige Hirose³²⁰, Hiromi Hisamatsu⁶⁷, Junji Hisano⁸⁶, Chit Thu Hlaing²³⁹,
 Kai Meng Hock^{38,263}, Martin Hoefkamp²⁷², Mark Hohlfeld³⁰³, Yousuke Honda⁶⁷,
 Juho Hong¹⁸², Tae Min Hong²⁴³, Hiroyuki Honma⁶⁷, Yasuyuki Horii²²², Dezso Horvath⁷⁰,
 Kenji Hosoyama⁶⁷, Jean-Yves Hostachy¹³², Mi Hou⁸⁷, Wei-Shu Hou¹⁶⁴, David Howell²⁷⁶,
 Maxine Hronek^{54,59}, Yee B. Hsiung¹⁶⁴, Bo Hu¹⁵⁶, Tao Hu⁸⁷, Jung-Yun Huang¹⁸²,
 Tong Ming Huang⁸⁷, Wen Hui Huang³¹, Emil Huedem⁵⁴, Peter Huggard²⁷,
 Cyril Hugonie¹²⁷, Christine Hu-Guo⁸⁴, Katri Huitu^{258,65}, Youngseok Hwang³⁰,
 Marek Idzik³, Alexandr Ignatenko¹¹, Fedor Ignatov²¹, Hirokazu Ikeda¹¹¹,
 Katsumasa Ikematsu⁴⁷, Tatiana Ilicheva^{115,60}, Didier Imbault³⁰², Andreas Imhof²⁵⁵,
 Marco Incagli¹⁰², Ronen Ingbir²¹⁶, Hitoshi Inoue⁶⁷, Youichi Inoue²²¹, Gianluca Introzzi²⁷⁸,
 Katerina Ioakeimidi²⁰³, Satoshi Ishihara²⁵⁹, Akimasa Ishikawa¹⁹³, Tadashi Ishikawa⁶⁷,
 Vladimir Issakov³²³, Kazutoshi Ito²²², V. V. Ivanov¹¹⁵, Valentin Ivanov⁵⁴,
 Yury Ivanyushenkov²⁷, Masako Iwasaki²⁹⁰, Yoshihisa Iwashita⁸⁵, David Jackson²⁷⁶,
 Frank Jackson^{38,26}, Bob Jacobsen^{137,239}, Ramaswamy Jaganathan⁸⁸, Steven Jamison^{38,26},
 Matthias Enno Janssen^{47,255}, Richard Jaramillo-Echeverria⁹⁵, John Jaros²⁰³,
 Clement Jauffret⁵⁰, Suresh B. Jawale¹³, Daniel Jeans¹²⁰, Ron Jedziniak⁵⁴, Ben Jeffery²⁷⁶,
 Didier Jehanno¹³⁰, Leo J. Jenner^{38,263}, Chris Jensen⁵⁴, David R. Jensen²⁰³,
 Hairong Jiang¹⁵⁰, Xiao Ming Jiang⁸⁷, Masato Jimbo²²³, Shan Jin⁸⁷, R. Keith Jobe²⁰³,
 Anthony Johnson²⁰³, Erik Johnson²⁷, Matt Johnson¹⁵⁰, Michael Johnston²⁷⁶,
 Paul Joireman⁵⁴, Stevan Jokic³¹⁶, James Jones^{38,26}, Roger M. Jones^{38,265},
 Erik Jongewaard²⁰³, Leif Jönsson¹⁴⁵, Gopal Joshi¹³, Satish C. Joshi¹⁸⁹, Jin-Young Jung¹³⁷,
 Thomas Junk²⁶⁰, Aurelio Juste⁵⁴, Marumi Kado¹³⁰, John Kadyk¹³⁷, Daniela Käfer⁴⁷,
 Eiji Kako⁶⁷, Puneeth Kalavase²⁴³, Alexander Kalinin^{38,26}, Jan Kalinowski²⁹⁵,
 Takuya Kamitani⁶⁷, Yoshio Kamiya¹⁰⁶, Yukihide Kamiya⁶⁷, Jun-ichi Kamoshita⁵⁵,
 Sergey Kananov²¹⁶, Kazuyuki Kanaya²⁹², Ken-ichi Kanazawa⁶⁷, Shinya Kanemura²²⁵,
 Heung-Sik Kang¹⁸², Wen Kang⁸⁷, D. Kanjial¹⁰⁵, Frédéric Kapusta³⁰², Pavel Karataev¹⁹²,
 Paul E. Karchin³²¹, Dean Karlen^{293,226}, Yannis Karyotakis¹²⁸, Vladimir Kashikhin⁵⁴,
 Shigeru Kashiwagi¹⁷⁶, Paul Kasley⁵⁴, Hiroaki Katagiri⁶⁷, Takashi Kato¹⁶⁷, Yukihiro Kato¹¹⁹,
 Judith Katzy⁴⁷, Alexander Kaukher³⁰⁵, Manjit Kaur¹⁷⁸, Kiyotomo Kawagoe¹²⁰,
 Hiroyuki Kawamura¹⁹¹, Sergei Kazakov⁶⁷, V. D. Kekelidze¹¹⁵, Lewis Keller²⁰³,
 Michael Kelley³⁹, Marc Kelly²⁶⁵, Michael Kelly⁸, Kurt Kennedy¹³⁷, Robert Kephart⁵⁴,
 Justin Keung^{279,54}, Oleg Khainovski²³⁹, Sameen Ahmed Khan¹⁹⁵, Prashant Khare¹⁸⁹,
 Nikolai Khovansky¹¹⁵, Christian Kiesling¹⁴⁷, Mitsuo Kikuchi⁶⁷, Wolfgang Kilian³⁰⁶,

Martin Killenberg³⁰³, Donghee Kim³⁰, Eun San Kim³⁰, Eun-Joo Kim³⁷, Guinyun Kim³⁰,
 Hongjoo Kim³⁰, Hyoungsuk Kim³⁰, Hyun-Chui Kim¹⁸⁷, Jonghoon Kim²⁰³, Kwang-Je Kim⁸,
 Kyung Sook Kim³⁰, Peter Kim²⁰³, Seunghwan Kim¹⁸², Shin-Hong Kim²⁹², Sun Kee Kim¹⁹⁷,
 Tae Jeong Kim¹²⁵, Youngim Kim³⁰, Young-Kee Kim^{54,52}, Maurice Kimmitt²⁵²,
 Robert Kirby²⁰³, François Kircher²⁸, Danuta Kisielewska³, Olaf Kittel³⁰³,
 Robert Klanner²⁵⁵, Arkadiy L. Klebaner⁵⁴, Claus Kleinwort⁴⁷, Tatsiana Klimkovich⁴⁷,
 Esben Klinkby¹⁶⁵, Stefan Kluth¹⁴⁷, Marc Knecht³², Peter Kneisel²²⁰, In Soo Ko¹⁸²,
 Kwok Ko²⁰³, Makoto Kobayashi⁶⁷, Nobuko Kobayashi⁶⁷, Michael Kobel²¹⁴,
 Manuel Koch³⁰³, Peter Kodys³⁶, Uli Koetz⁴⁷, Robert Kohrs³⁰³, Yuuji Kojima⁶⁷,
 Hermann Kolanoski⁶⁹, Karol Kolodziej²⁸⁴, Yury G. Kolomensky²³⁹, Sachio Komamiya¹⁰⁶,
 Xiang Cheng Kong⁸⁷, Jacobo Konigsberg²⁵³, Volker Korb⁴⁷, Shane Koscielniak²²⁶,
 Sergey Kostromin¹¹⁵, Robert Kowalewski²⁹³, Sabine Kraml³⁵, Manfred Krammer¹⁷⁷,
 Anatoly Krasnykh²⁰³, Thorsten Krautscheid³⁰³, Maria Krawczyk²⁹⁵, H. James Krebs²⁰³,
 Kurt Krempetz⁵⁴, Graham Kribs²⁷⁵, Srinivas Krishnagopal¹⁸⁹, Richard Kriske²⁶⁹,
 Andreas Kronfeld⁵⁴, Jürgen Kroseberg²⁴⁵, Uladzimir Kruchonak¹¹⁵, Dirk Kruecker⁴⁷,
 Hans Krüger³⁰³, Nicholas A. Krumpa²⁶, Zinovii Krumshstein¹¹⁵, Yu Ping Kuang³¹,
 Kiyoshi Kubo⁶⁷, Vic Kuchler⁵⁴, Noboru Kudoh⁶⁷, Szymon Kulis³, Masayuki Kumada¹⁶¹,
 Abhay Kumar¹⁸⁹, Tatsuya Kume⁶⁷, Anirban Kundu²², German Kurevlev^{38,265},
 Yoshimasa Kurihara⁶⁷, Masao Kuriki⁶⁷, Shigeru Kuroda⁶⁷, Hirotoshi Kuroiwa⁶⁷,
 Shin-ichi Kurokawa⁶⁷, Tomonori Kusano²²², Pradeep K. Kush¹⁸⁹, Robert Kutschke⁵⁴,
 Ekaterina Kuznetsova³⁰⁸, Peter Kvasnicka³⁶, Youngjoon Kwon³²⁴, Luis Labarga²²⁸,
 Carlos Lacasta⁹⁴, Sharon Lackey⁵⁴, Thomas W. Lackowski⁵⁴, Remi Lafaye¹²⁸,
 George Lafferty²⁶⁵, Eric Lagorio¹³², Imad Laktineh²⁹⁹, Shankar Lal¹⁸⁹, Maurice Laloum⁸³,
 Briant Lam²⁰³, Mark Lancaster²³⁰, Richard Lander²⁴⁰, Wolfgang Lange⁴⁸,
 Ulrich Langenfeld³⁰³, Willem Langeveld²⁰³, David Larbalestier²⁹⁷, Ray Larsen²⁰³,
 Tomas Lastovicka²⁷⁶, Gordana Lastovicka-Medin²⁷¹, Andrea Latina³⁵, Emmanuel Latour⁵⁰,
 Lisa Laurent²⁰³, Ba Nam Le⁶², Duc Ninh Le^{89,129}, Francois Le Diberder¹³⁰,
 Patrick Le Du²⁸, Hervé Lebbolo⁸³, Paul Lebrun⁵⁴, Jacques Lecoq¹³¹, Sung-Won Lee²¹⁸,
 Frank Lehner⁴⁷, Jerry Leibfritz⁵⁴, Frank Lenkszus⁸, Tadeusz Lesiak²¹⁹, Aharon Levy²¹⁶,
 Jim Lewandowski²⁰³, Greg Leyh²⁰³, Cheng Li²⁸³, Chong Sheng Li¹⁰, Chun Hua Li⁸⁷,
 Da Zhang Li⁸⁷, Gang Li⁸⁷, Jin Li³¹, Shao Peng Li⁸⁷, Wei Ming Li¹⁶², Weiguo Li⁸⁷,
 Xiao Ping Li⁸⁷, Xue-Qian Li¹⁵⁸, Yuanjing Li³¹, Yulan Li³¹, Zenghai Li²⁰³, Zhong Quan Li⁸⁷,
 Jian Tao Liang²¹², Yi Liao¹⁵⁸, Lutz Lilje⁴⁷, J. Guilherme Lima¹⁷¹, Andrew J. Lintern²⁷,
 Ronald Lipton⁵⁴, Benno List²⁵⁵, Jenny List⁴⁷, Chun Liu⁹³, Jian Fei Liu¹⁹⁹, Ke Xin Liu¹⁰,
 Li Qiang Liu²¹², Shao Zhen Liu⁸⁷, Sheng Guang Liu⁶⁷, Shubin Liu²⁸³, Wanming Liu⁸,
 Wei Bin Liu⁸⁷, Ya Ping Liu⁸⁷, Yu Dong Liu⁸⁷, Nigel Lockyer^{226,238}, Heather E. Logan²⁴,
 Pavel V. Logatchev²¹, Wolfgang Lohmann⁴⁸, Thomas Lohse⁶⁹, Smaragda Lola²⁷⁷,
 Amparo Lopez-Virto⁹⁵, Peter Loveridge²⁷, Manuel Lozano³⁴, Cai-Dian Lu⁸⁷,
 Changguo Lu¹⁸⁵, Gong-Lu Lu⁶⁶, Wen Hui Lu²¹², Henry Lubatti²⁹⁶, Arnaud Lucotte¹³²,
 Björn Lundberg¹⁴⁵, Tracy Lundin⁶³, Mingxing Luo³²⁵, Michel Luong²⁸, Vera Luth²⁰³,
 Benjamin Lutz^{47,255}, Pierre Lutz²⁸, Thorsten Lux²²⁹, Pawel Luzniak⁹¹, Alexey Lyapin²³⁰,
 Joseph Lykken⁵⁴, Clare Lynch²³⁷, Li Ma⁸⁷, Lili Ma^{38,26}, Qiang Ma⁸⁷, Wen-Gan Ma^{283,87},
 David Macfarlane²⁰³, Arthur Maciel¹⁷¹, Allan MacLeod²³³, David MacNair²⁰³,
 Wolfgang Mader²¹⁴, Stephen Magill⁸, Anne-Marie Magnan⁷², Bino Maiheu²³⁰,
 Manas Maity³¹⁹, Millicent Majchrzak²⁶⁹, Gobinda Majumder²¹¹, Roman Makarov¹¹⁵,
 Dariusz Makowski^{213,47}, Bogdan Malaescu¹³⁰, C. Mallik³¹⁵, Usha Mallik²⁶¹,
 Stephen Malton^{230,192}, Oleg B. Malyshev^{38,26}, Larisa I. Malysheva^{38,263},

John Mammosser²²⁰, Mamta²⁴⁹, Judita Mamuzic^{48,316}, Samuel Manen¹³¹,
 Massimo Manghisoni^{307,101}, Steven Manly²⁸², Fabio Marcellini¹³⁴, Michal Marcisovsky⁹⁰,
 Thomas W. Markiewicz²⁰³, Steve Marks¹³⁷, Andrew Marone¹⁹, Felix Marti¹⁵⁰,
 Jean-Pierre Martin⁴², Victoria Martin²⁵¹, Gisèle Martin-Chassard¹³⁰, Manel Martinez²²⁹,
 Celso Martinez-Rivero⁹⁵, Dennis Martsch²⁵⁵, Hans-Ulrich Martyn^{190,47},
 Takashi Maruyama²⁰³, Mika Masuzawa⁶⁷, Hervé Mathez²⁹⁹, Takeshi Matsuda⁶⁷,
 Hiroshi Matsumoto⁶⁷, Shuji Matsumoto⁶⁷, Toshihiro Matsumoto⁶⁷, Hiroyuki Matsunaga¹⁰⁶,
 Peter Mättig²⁹⁸, Thomas Mattison²³⁸, Georgios Mavromanolakis^{246,54},
 Kentarou Mawatari¹²⁴, Anna Mazzacane³¹³, Patricia McBride⁵⁴, Douglas McCormick²⁰³,
 Jeremy McCormick²⁰³, Kirk T. McDonald¹⁸⁵, Mike McGee⁵⁴, Peter McIntosh^{38,26},
 Bobby McKee²⁰³, Robert A. McPherson²⁹³, Mandi Meidlinger¹⁵⁰, Karlheinz Meier²⁵⁷,
 Barbara Mele³⁰⁸, Bob Meller⁴³, Isabell-Alissandra Melzer-Pellmann⁴⁷, Hector Mendez²⁸⁰,
 Adam Mercer^{38,265}, Mikhail Merkin¹⁴¹, I. N. Meshkov¹¹⁵, Robert Messner²⁰³,
 Jessica Metcalfe²⁷², Chris Meyer²⁴⁴, Hendrik Meyer⁴⁷, Joachim Meyer⁴⁷, Niels Meyer⁴⁷,
 Norbert Meyners⁴⁷, Paolo Michelato⁹⁶, Shinichiro Michizono⁶⁷, Daniel Mihalcea¹⁷¹,
 Satoshi Mihara¹⁰⁶, Takanori Mihara¹²⁶, Yoshinari Mikami²³⁶,
 Alexander A. Mikhailichenko⁴³, Catia Milardi¹³⁴, David J. Miller²³⁰, Owen Miller²³⁶,
 Roger J. Miller²⁰³, Caroline Milstene⁵⁴, Toshihiro Mimashi⁶⁷, Irakli Minashvili¹¹⁵,
 Ramon Miquel^{229,80}, Shekhar Mishra⁵⁴, Winfried Mitaroff¹⁷⁷, Chad Mitchell²⁶⁶,
 Takako Miura⁶⁷, Akiya Miyamoto⁶⁷, Hitoshi Miyata¹⁶⁶, Ulf Mjörnmark¹⁴⁵,
 Joachim Mnich⁴⁷, Klaus Moenig⁴⁸, Kenneth Moffeit²⁰³, Nikolai Mokhov⁵⁴,
 Stephen Molloy²⁰³, Laura Monaco⁹⁶, Paul R. Monasterio²³⁹, Alessandro Montanari⁴⁷,
 Sung Ik Moon¹⁸², Gudrid A. Moortgat-Pick^{38,49}, Paulo Mora De Freitas⁵⁰, Federic Morel⁸⁴,
 Stefano Moretti²⁸⁵, Vasily Morgunov^{47,92}, Toshinori Mori¹⁰⁶, Laurent Morin¹³²,
 François Morisseau¹³¹, Yoshiyuki Morita⁶⁷, Youhei Morita⁶⁷, Yuichi Morita¹⁰⁶,
 Nikolai Morozov¹¹⁵, Yuichi Morozumi⁶⁷, William Morse¹⁹, Hans-Guenther Moser¹⁴⁷,
 Gilbert Moulta¹²⁷, Sekazi Mtingwa¹⁴⁶, Mihajlo Mudrinic³¹⁶, Alex Mueller⁸¹,
 Wolfgang Mueller⁸², Astrid Muennich¹⁹⁰, Milada Margarete Muhlleitner^{129,35},
 Bhaskar Mukherjee⁴⁷, Biswarup Mukhopadhyaya⁶⁴, Thomas Müller³⁰⁴, Morrison Munro²⁰³,
 Hitoshi Murayama^{239,137}, Toshiya Muto²²², Ganapati Rao Myneni²²⁰, P.Y. Nabhiraj³¹⁵,
 Sergei Nagaitsev⁵⁴, Tadashi Nagamine²²², Ai Nagano²⁹², Takashi Naito⁶⁷, Hirotaka Nakai⁶⁷,
 Hiromitsu Nakajima⁶⁷, Isamu Nakamura⁶⁷, Tomoya Nakamura²⁹⁰, Tsutomu Nakanishi¹⁵⁵,
 Katsumi Nakao⁶⁷, Noriaki Nakao⁵⁴, Kazuo Nakayoshi⁶⁷, Sang Nam¹⁸², Yoshihito Namito⁶⁷,
 Won Namkung¹⁸², Chris Nantista²⁰³, Olivier Napoly²⁸, Meenakshi Narain²⁰,
 Beate Naroska²⁵⁵, Uriel Nauenberg²⁴⁷, Ruchika Nayyar²⁴⁸, Homer Neal²⁰³,
 Charles Nelson²⁰⁴, Janice Nelson²⁰³, Timothy Nelson²⁰³, Stanislav Nemecek⁹⁰,
 Michael Neubauer²⁰³, David Neuffer⁵⁴, Myriam Q. Newman²⁷⁶, Oleg Nezhevenko⁵⁴,
 Cho-Kuen Ng²⁰³, Anh Ky Nguyen^{89,135}, Minh Nguyen²⁰³, Hong Van Nguyen Thi^{1,89},
 Carsten Niebuhr⁴⁷, Jim Niehoff⁵⁴, Piotr Niezurawski²⁹⁴, Tomohiro Nishitani¹¹²,
 Osamu Nitoh²²⁴, Shuichi Noguchi⁶⁷, Andrei Nomerotski²⁷⁶, John Noonan⁸,
 Edward Norbeck²⁶¹, Yuri Nosochkov²⁰³, Dieter Notz⁴⁷, Grazyna Nowak²¹⁹,
 Hannelies Nowak⁴⁸, Matthew Noy⁷², Mitsuaki Nozaki⁶⁷, Andreas Nyffeler⁶⁴,
 David Nygren¹³⁷, Piermaria Oddone⁵⁴, Joseph O'Dell^{38,26}, Jong-Seok Oh¹⁸²,
 Sun Kun Oh¹²², Kazumasa Ohkuma⁵⁶, Martin Ohlerich^{48,17}, Kazuhito Ohmi⁶⁷,
 Yuki Yoshi Ohnishi⁶⁷, Satoshi Ohsawa⁶⁷, Norihito Ohuchi⁶⁷, Katsunobu Oide⁶⁷,
 Nobuchika Okada⁶⁷, Yasuhiro Okada^{67,202}, Takahiro Okamura⁶⁷, Toshiyuki Okugi⁶⁷,
 Shoji Okumi¹⁵⁵, Ken-ichi Okumura²²², Alexander Olchevski¹¹⁵, William Oliver²²⁷,

Bob Olivier¹⁴⁷, James Olsen¹⁸⁵, Jeff Olsen²⁰³, Stephen Olsen²⁵⁶, A. G. Olshevsky¹¹⁵,
 Jan Olsson⁴⁷, Tsunehiko Omori⁶⁷, Yasar Onel²⁶¹, Gulsen Onengut⁴⁴, Hiroaki Ono¹⁶⁸,
 Dmitry Onoprienko¹¹⁶, Mark Oreglia⁵², Will Oren²²⁰, Toyoko J. Orimoto²³⁹,
 Marco Oriunno²⁰³, Marius Ciprian Orlandea², Masahiro Oroku²⁹⁰, Lynne H. Orr²⁸²,
 Robert S. Orr²⁹¹, Val Oshea²⁵⁴, Anders Oskarsson¹⁴⁵, Per Osland²³⁵, Dmitri Ossetski¹⁷⁴,
 Lennart Österman¹⁴⁵, Francois Ostiguy⁵⁴, Hidetoshi Otono²⁹⁰, Brian Ottewell²⁷⁶,
 Qun Ouyang⁸⁷, Hasan Padamsee⁴³, Cristobal Padilla²²⁹, Carlo Pagani⁹⁶, Mark A. Palmer⁴³,
 Wei Min Pam⁸⁷, Manjiri Pande¹³, Rajni Pande¹³, V.S. Pandit³¹⁵, P.N. Pandita¹⁷⁰,
 Mila Pandurovic³¹⁶, Alexander Pankov^{180,179}, Nicola Panzeri⁹⁶, Zisis Papandreou²⁸¹,
 Rocco Paparella⁹⁶, Adam Para⁵⁴, Hwanbae Park³⁰, Brett Parker¹⁹, Chris Parkes²⁵⁴,
 Vittorio Parma³⁵, Zohreh Parsa¹⁹, Justin Parsons²⁶¹, Richard Partridge^{20,203},
 Ralph Pasquinelli⁵⁴, Gabriella Pásztor^{242,70}, Ewan Paterson²⁰³, Jim Patrick⁵⁴,
 Piero Patteri¹³⁴, J. Ritchie Patterson⁴³, Giovanni Pauletta³¹⁴, Nello Paver³⁰⁹,
 Vince Pavlicek⁵⁴, Bogdan Pawlik²¹⁹, Jacques Payet²⁸, Norbert Pchalek⁴⁷, John Pedersen³⁵,
 Guo Xi Pei⁸⁷, Shi Lun Pei⁸⁷, Jerzy Pelka¹⁸³, Giulio Pellegrini³⁴, David Pellett²⁴⁰,
 G.X. Peng⁸⁷, Gregory Penn¹³⁷, Aldo Penzo¹⁰⁴, Colin Perry²⁷⁶, Michael Peskin²⁰³,
 Franz Peters²⁰³, Troels Christian Petersen^{165,35}, Daniel Peterson⁴³, Thomas Peterson⁵⁴,
 Maureen Petterson^{245,244}, Howard Pfeffer⁵⁴, Phil Pfund⁵⁴, Alan Phelps²⁸⁶,
 Quang Van Phi⁸⁹, Jonathan Phillips²⁵⁰, Nan Phinney²⁰³, Marcello Piccolo¹³⁴,
 Livio Piemontese⁹⁷, Paolo Pierini⁹⁶, W. Thomas Piggott¹³⁸, Gary Pike⁵⁴, Nicolas Pillet⁸⁴,
 Talini Pinto Jayawardena²⁷, Phillippe Piot¹⁷¹, Kevin Pitts²⁶⁰, Mauro Pivi²⁰³,
 Dave Plate¹³⁷, Marc-Andre Pleier³⁰³, Andrei Poblaguev³²³, Michael Poehler³²³,
 Matthew Poelker²²⁰, Paul Poffenberger²⁹³, Igor Pogorelsky¹⁹, Freddy Poirier⁴⁷,
 Ronald Poling²⁶⁹, Mike Poole^{38,26}, Sorina Popescu², John Popielarski¹⁵⁰, Roman Pöschl¹³⁰,
 Martin Postranecky²³⁰, Prakash N. Potukochi¹⁰⁵, Julie Prast¹²⁸, Serge Prat¹³⁰,
 Miro Preger¹³⁴, Richard Prepost²⁹⁷, Michael Price¹⁹², Dieter Proch⁴⁷,
 Avinash Puntambekar¹⁸⁹, Qing Qin⁸⁷, Hua Min Qu⁸⁷, Arnulf Quadt⁵⁸,
 Jean-Pierre Quesnel³⁵, Veljko Radeka¹⁹, Rahmat Rahmat²⁷⁵, Santosh Kumar Rai²⁵⁸,
 Pantaleo Raimondi¹³⁴, Erik Ramberg⁵⁴, Kirti Ranjan²⁴⁸, Sista V.L.S. Rao¹³,
 Alexei Raspereza¹⁴⁷, Alessandro Ratti¹³⁷, Lodovico Ratti^{278,101}, Tor Raubenheimer²⁰³,
 Ludovic Raux¹³⁰, V. Ravindran⁶⁴, Sreerup Raychaudhuri^{77,211}, Valerio Re^{307,101},
 Bill Rease¹⁴², Charles E. Reece²²⁰, Meinhard Regler¹⁷⁷, Kay Rehlich⁴⁷, Ina Reichel¹³⁷,
 Armin Reichold²⁷⁶, John Reid⁵⁴, Ron Reid^{38,26}, James Reidy²⁷⁰, Marcel Reinhard⁵⁰,
 Uwe Renz⁴, Jose Repond⁸, Javier Resta-Lopez²⁷⁶, Lars Reuen³⁰³, Jacob Ribnik²⁴³,
 Tyler Rice²⁴⁴, François Richard¹³⁰, Sabine Riemann⁴⁸, Tord Riemann⁴⁸, Keith Riles²⁶⁸,
 Daniel Riley⁴³, Cécile Rimbault¹³⁰, Saurabh Rindani¹⁸¹, Louis Rinolfi³⁵, Fabio Risigo⁹⁶,
 Imma Riu²²⁹, Dmitri Rizhikov¹⁷⁴, Thomas Rizzo²⁰³, James H. Rochford²⁷,
 Ponciano Rodriguez²⁰³, Martin Roeben¹³⁸, Gigi Rolandi³⁵, Aaron Roodman²⁰³,
 Eli Rosenberg¹⁰⁷, Robert Roser⁵⁴, Marc Ross⁵⁴, François Rossel³⁰², Robert Rossmanith⁷,
 Stefan Roth¹⁹⁰, André Rouge⁵⁰, Allan Rowe⁵⁴, Amit Roy¹⁰⁵, Sendhunil B. Roy¹⁸⁹,
 Sourov Roy⁷³, Laurent Royer¹³¹, Perrine Royole-Degieux^{130,59}, Christophe Royon²⁸,
 Manqi Ruan³¹, David Rubin⁴³, Ingo Ruehl³⁵, Alberto Ruiz Jimeno⁹⁵, Robert Ruland²⁰³,
 Brian Rusnak¹³⁸, Sun-Young Ryu¹⁸⁷, Gian Luca Sabbi¹³⁷, Iftach Sadeh²¹⁶,
 Ziraddin Y Sadygov¹¹⁵, Takayuki Saeki⁶⁷, David Sagan⁴³, Vinod C. Sahni^{189,13},
 Arun Saini²⁴⁸, Kenji Saito⁶⁷, Kiwamu Saito⁶⁷, Gerard Sajot¹³², Shogo Sakanaka⁶⁷,
 Kazuyuki Sakaue³²⁰, Zen Salata²⁰³, Sabah Salih²⁶⁵, Fabrizio Salvatore¹⁹²,
 Joergen Samson⁴⁷, Toshiya Sanami⁶⁷, Allister Levi Sanchez⁵⁰, William Sands¹⁸⁵,

John Santic^{54,*}, Tomoyuki Sanuki²²², Andrey Sapronov^{115,48}, Utpal Sarkar¹⁸¹,
 Noboru Sasao¹²⁶, Kotaro Satoh⁶⁷, Fabio Sauli³⁵, Claude Saunders⁸, Valeri Saveliev¹⁷⁴,
 Aurore Savoy-Navarro³⁰², Lee Sawyer¹⁴³, Laura Saxton¹⁵⁰, Oliver Schäfer³⁰⁵,
 Andreas Schällicke⁴⁸, Peter Schade^{47,255}, Sebastien Schaetzel⁴⁷, Glenn Scheitrum²⁰³,
 Émilie Schibler²⁹⁹, Rafe Schindler²⁰³, Markus Schlösser⁴⁷, Ross D. Schlueter¹³⁷,
 Peter Schmid⁴⁸, Ringo Sebastian Schmidt^{48,17}, Uwe Schneekloth⁴⁷,
 Heinz Juergen Schreiber⁴⁸, Siegfried Schreiber⁴⁷, Henning Schroeder³⁰⁵, K. Peter Schüler⁴⁷,
 Daniel Schulte³⁵, Hans-Christian Schultz-Coulon²⁵⁷, Markus Schumacher³⁰⁶,
 Steffen Schumann²¹⁵, Bruce A. Schumm^{244,245}, Reinhard Schwienhorst¹⁵⁰,
 Rainer Schwierz²¹⁴, Duncan J. Scott^{38,26}, Fabrizio Scuri¹⁰², Felix Sefkow⁴⁷, Rachid Sefri⁸³,
 Nathalie Seguin-Moreau¹³⁰, Sally Seidel²⁷², David Seidman¹⁷², Sezen Sekmen¹⁵¹,
 Sergei Seletskiy²⁰³, Eibun Senaha¹⁵⁹, Rohan Senanayake²⁷⁶, Hiroshi Sendai⁶⁷,
 Daniele Sertore⁹⁶, Andrei Seryi²⁰³, Ronald Settles^{147,47}, Ramazan Sever¹⁵¹,
 Nicholas Shales^{38,136}, Ming Shao²⁸³, G. A. Shelkov¹¹⁵, Ken Shepard⁸,
 Claire Shepherd-Themistocleous²⁷, John C. Sheppard²⁰³, Cai Tu Shi⁸⁷, Tetsuo Shidara⁶⁷,
 Yeo-Jeong Shim¹⁸⁷, Hirotaka Shimizu⁶⁸, Yasuhiro Shimizu¹²³, Yuuki Shimizu¹⁹³,
 Tetsushi Shimogawa¹⁹³, Seunghwan Shin³⁰, Masaomi Shioden⁷¹, Ian Shipsey¹⁸⁶,
 Grigori Shirkov¹¹⁵, Toshio Shishido⁶⁷, Ram K. Shivpuri²⁴⁸, Purushottam Shrivastava¹⁸⁹,
 Sergey Shulga^{115,60}, Nikolai Shumeiko¹¹, Sergey Shuvalov⁴⁷, Zongguo Si¹⁹⁸,
 Azher Majid Siddiqui¹¹⁰, James Siegrist^{137,239}, Claire Simon²⁸, Stefan Simrock⁴⁷,
 Nikolai Sinev²⁷⁵, Bhartendu K. Singh¹², Jasbir Singh¹⁷⁸, Pitamber Singh¹³, R.K. Singh¹²⁹,
 S.K. Singh⁵, Monito Singini²⁷⁸, Anil K. Sinha¹³, Nita Sinha⁸⁸, Rahul Sinha⁸⁸,
 Klaus Sinram⁴⁷, A. N. Sissakian¹¹⁵, N. B. Skachkov¹¹⁵, Alexander Skrinsky²¹,
 Mark Slater²⁴⁶, Wojciech Slominski¹⁰⁸, Ivan Smiljanic³¹⁶, A J Stewart Smith¹⁸⁵,
 Alex Smith²⁶⁹, Brian J. Smith²⁷, Jeff Smith^{43,203}, Jonathan Smith^{38,136}, Steve Smith²⁰³,
 Susan Smith^{38,26}, Tonee Smith²⁰³, W. Neville Snodgrass²⁶, Blanka Sobloher⁴⁷,
 Young-Uk Sohn¹⁸², Ruelson Solidum^{153,152}, Nikolai Solyak⁵⁴, Dongchul Son³⁰,
 Nasuf Sonmez⁵¹, Andre Sopczak^{38,136}, V. Soskov¹³⁹, Cherrill M. Spencer²⁰³,
 Panagiotis Spentzouris⁵⁴, Valeria Speziali²⁷⁸, Michael Spira²⁰⁹, Daryl Sprehn²⁰³,
 K. Sridhar²¹¹, Asutosh Srivastava^{248,14}, Steve St. Lorant²⁰³, Achim Stahl¹⁹⁰,
 Richard P. Stanek⁵⁴, Marcel Stanitzki²⁷, Jacob Stanley^{245,244}, Konstantin Stefanov²⁷,
 Werner Stein¹³⁸, Herbert Steiner¹³⁷, Evert Stenlund¹⁴⁵, Amir Stern²¹⁶, Matt Sternberg²⁷⁵,
 Dominik Stockinger²⁵⁴, Mark Stockton²³⁶, Holger Stoeck²⁸⁷, John Strachan²⁶,
 V. Strakhovenko²¹, Michael Strauss²⁷⁴, Sergei I. Striganov⁵⁴, John Strologas²⁷²,
 David Strom²⁷⁵, Jan Strube²⁷⁵, Gennady Stupakov²⁰³, Dong Su²⁰³, Yuji Sudo²⁹²,
 Taikan Suehara²⁹⁰, Toru Suehiro²⁹⁰, Yusuke Suetsugu⁶⁷, Ryuhei Sugahara⁶⁷,
 Yasuhiro Sugimoto⁶⁷, Akira Sugiyama¹⁹³, Jun Suhk Suh³⁰, Goran Sukovic²⁷¹, Hong Sun⁸⁷,
 Stephen Sun²⁰³, Werner Sun⁴³, Yi Sun⁸⁷, Yipeng Sun^{87,10}, Leszek Suszycki³,
 Peter Sutcliffe^{38,263}, Rameshwar L. Suthar¹³, Tsuyoshi Suwada⁶⁷, Atsuto Suzuki⁶⁷,
 Chihiro Suzuki¹⁵⁵, Shiro Suzuki¹⁹³, Takashi Suzuki²⁹², Richard Swent²⁰³,
 Krzysztof Swientek³, Christina Swinson²⁷⁶, Evgeny Syresin¹¹⁵, Michal Szeleper¹⁷²,
 Alexander Tadday²⁵⁷, Rika Takahashi^{67,59}, Tohru Takahashi⁶⁸, Mikio Takano¹⁹⁶,
 Fumihiko Takasaki⁶⁷, Seishi Takeda⁶⁷, Tateru Takenaka⁶⁷, Tohru Takeshita²⁰⁰,
 Yosuke Takubo²²², Masami Tanaka⁶⁷, Chuan Xiang Tang³¹, Takashi Taniguchi⁶⁷,
 Sami Tantawi²⁰³, Stefan Tapprogge¹¹³, Michael A. Tartaglia⁵⁴,
 Giovanni Francesco Tassielli³¹³, Toshiaki Tauchi⁶⁷, Laurent Taviani³⁵, Hiroko Tawara⁶⁷,
 Geoffrey Taylor²⁶⁷, Alexandre V. Telnov¹⁸⁵, Valery Telnov²¹, Peter Tenenbaum²⁰³,

Eliza Teodorescu², Akio Terashima⁶⁷, Giuseppina Terracciano⁹⁹, Nobuhiro Terunuma⁶⁷,
 Thomas Teubner²⁶³, Richard Teuscher^{293,291}, Jay Theilacker⁵⁴, Mark Thomson²⁴⁶,
 Jeff Tice²⁰³, Maury Tigner⁴³, Jan Timmermans¹⁶⁰, Maxim Titov²⁸, Nobukazu Toge⁶⁷,
 N. A. Tokareva¹¹⁵, Kirsten Tollefson¹⁵⁰, Lukas Tomasek⁹⁰, Savo Tomovic²⁷¹,
 John Tompkins⁵⁴, Manfred Tonutti¹⁹⁰, Anita Topkar¹³, Dragan Toplek^{38,265},
 Fernando Toral³³, Eric Torrence²⁷⁵, Gianluca Traversi^{307,101}, Marcel Trimpl⁵⁴,
 S. Mani Tripathi²⁴⁰, William Trischuk²⁹¹, Mark Trodden²¹⁰, G. V. Trubnikov¹¹⁵,
 Robert Tschirhart⁵⁴, Edisher Tskhadadze¹¹⁵, Kiyosumi Tsuchiya⁶⁷,
 Toshifumi Tsukamoto⁶⁷, Akira Tsunemi²⁰⁷, Robin Tucker^{38,136}, Renato Turchetta²⁷,
 Mike Tyndel²⁷, Nobuhiro Uekusa^{258,65}, Kenji Ueno⁶⁷, Kensei Umemori⁶⁷,
 Martin Ummenhofer³⁰³, David Underwood⁸, Satoru Uozumi²⁰⁰, Junji Urakawa⁶⁷,
 Jeremy Urban⁴³, Didier Uriot²⁸, David Urner²⁷⁶, Andrei Ushakov⁴⁸, Tracy Usher²⁰³,
 Sergey Uzunyan¹⁷¹, Brigitte Vachon¹⁴⁸, Linda Valerio⁵⁴, Isabelle Valin⁸⁴, Alex Valishev⁵⁴,
 Raghava Vamra⁷⁵, Harry Van Der Graaf^{160,35}, Rick Van Kooten⁷⁹, Gary Van Zandbergen⁵⁴,
 Jean-Charles Vanel⁵⁰, Alessandro Variola¹³⁰, Gary Varner²⁵⁶, Mayda Velasco¹⁷²,
 Ulrich Velte⁴⁷, Jaap Velthuis²³⁷, Sundir K. Vempati⁷⁴, Marco Venturini¹³⁷,
 Christophe Vescovi¹³², Henri Videau⁵⁰, Ivan Vila⁹⁵, Pascal Vincent³⁰², Jean-Marc Virey³²,
 Bernard Visentin²⁸, Michele Viti⁴⁸, Thanh Cuong Vo³¹⁷, Adrian Vogel⁴⁷, Harald Vogt⁴⁸,
 Eckhard Von Toerne^{303,116}, S. B. Vorozhtsov¹¹⁵, Marcel Vos⁹⁴, Margaret Votava⁵⁴,
 Vaclav Vrba⁹⁰, Doreen Wackerroth²⁰⁵, Albrecht Wagner⁴⁷, Carlos E. M. Wagner^{8,52},
 Stephen Wagner²⁴⁷, Masayoshi Wake⁶⁷, Roman Walczak²⁷⁶, Nicholas J. Walker⁴⁷,
 Wolfgang Walkowiak³⁰⁶, Samuel Wallon¹³³, Roberval Walsh²⁵¹, Sean Walston¹³⁸,
 Wolfgang Waltenberger¹⁷⁷, Dieter Walz²⁰³, Chao En Wang¹⁶³, Chun Hong Wang⁸⁷,
 Dou Wang⁸⁷, Faya Wang²⁰³, Guang Wei Wang⁸⁷, Haitao Wang⁸, Jiang Wang⁸⁷,
 Jiu Qing Wang⁸⁷, Juwen Wang²⁰³, Lanfa Wang²⁰³, Lei Wang²⁴⁴, Min-Zu Wang¹⁶⁴,
 Qing Wang³¹, Shu Hong Wang⁸⁷, Xiaolian Wang²⁸³, Xue-Lei Wang⁶⁶, Yi Fang Wang⁸⁷,
 Zheng Wang⁸⁷, Rainer Wanzenberg⁴⁷, Bennie Ward⁹, David Ward²⁴⁶,
 Barbara Warmbein^{47,59}, David W. Warner⁴⁰, Matthew Warren²³⁰, Masakazu Washio³²⁰,
 Isamu Watanabe¹⁶⁹, Ken Watanabe⁶⁷, Takashi Watanabe¹²¹, Yuichi Watanabe⁶⁷,
 Nigel Watson²³⁶, Nanda Wattimena^{47,255}, Mitchell Wayne²⁷³, Marc Weber²⁷,
 Harry Weerts⁸, Georg Weiglein⁴⁹, Thomas Weiland⁸², Stefan Weinzierl¹¹³, Hans Weise⁴⁷,
 John Weisend²⁰³, Manfred Wendt⁵⁴, Oliver Wendt^{47,255}, Hans Wenzel⁵⁴,
 William A. Wenzel¹³⁷, Norbert Wermes³⁰³, Ulrich Werthenbach³⁰⁶, Steve Wesseln⁵⁴,
 William Wester⁵⁴, Andy White²⁸⁸, Glen R. White²⁰³, Katarzyna Wichmann⁴⁷,
 Peter Wienemann³⁰³, Wojciech Wierba²¹⁹, Tim Wilksen⁴³, William Willis⁴¹,
 Graham W. Wilson²⁶², John A. Wilson²³⁶, Robert Wilson⁴⁰, Matthew Wing²³⁰,
 Marc Winter⁸⁴, Brian D. Wirth²³⁹, Stephen A. Wolbers⁵⁴, Dan Wolff⁵⁴,
 Andrzej Wolski^{38,263}, Mark D. Woodley²⁰³, Michael Woods²⁰³, Michael L. Woodward²⁷,
 Timothy Woolliscroft^{263,27}, Steven Worm²⁷, Guy Wormser¹³⁰, Dennis Wright²⁰³,
 Douglas Wright¹³⁸, Andy Wu²²⁰, Tao Wu¹⁹², Yue Liang Wu⁹³, Stefania Xella¹⁶⁵,
 Guoxing Xia⁴⁷, Lei Xia⁸, Aimin Xiao⁸, Liling Xiao²⁰³, Jia Lin Xie⁸⁷, Zhi-Zhong Xing⁸⁷,
 Lian You Xiong²¹², Gang Xu⁸⁷, Qing Jing Xu⁸⁷, Urjit A. Yajnik⁷⁵, Vitaly Yakimenko¹⁹,
 Ryuji Yamada⁵⁴, Hiroshi Yamaguchi¹⁹³, Akira Yamamoto⁶⁷, Hitoshi Yamamoto²²²,
 Masahiro Yamamoto¹⁵⁵, Naoto Yamamoto¹⁵⁵, Richard Yamamoto¹⁴⁶,
 Yasuchika Yamamoto⁶⁷, Takashi Yamanaka²⁹⁰, Hiroshi Yamaoka⁶⁷, Satoru Yamashita¹⁰⁶,
 Hideki Yamazaki²⁹², Wenbiao Yan²⁴⁶, Hai-Jun Yang²⁶⁸, Jin Min Yang⁹³, Jongmann Yang⁵³,
 Zhenwei Yang³¹, Yoshiharu Yano⁶⁷, Efe Yazgan^{218,35}, G. P. Yeh⁵⁴, Hakan Yilmaz⁷²,

Philip Yock²³⁴, Hakutaro Yoda²⁹⁰, John Yoh⁵⁴, Kaoru Yokoya⁶⁷, Hirokazu Yokoyama¹²⁶,
 Richard C. York¹⁵⁰, Mitsuhiro Yoshida⁶⁷, Takuo Yoshida⁵⁷, Tamaki Yoshioka¹⁰⁶,
 Andrew Young²⁰³, Cheng Hui Yu⁸⁷, Jaehoon Yu²⁸⁸, Xian Ming Yu⁸⁷, Changzheng Yuan⁸⁷,
 Chong-Xing Yue¹⁴⁰, Jun Hui Yue⁸⁷, Josef Zacek³⁶, Igor Zagorodnov⁴⁷, Jaroslav Zalesak⁹⁰,
 Boris Zalikhanov¹¹⁵, Aleksander Filip Zarnecki²⁹⁴, Leszek Zawiejski²¹⁹,
 Christian Zeitnitz²⁹⁸, Michael Zeller³²³, Dirk Zerwas¹³⁰, Peter Zerwas^{47,190},
 Mehmet Zeyrek¹⁵¹, Ji Yuan Zhai⁸⁷, Bao Cheng Zhang¹⁰, Bin Zhang³¹, Chuang Zhang⁸⁷,
 He Zhang⁸⁷, Jiawen Zhang⁸⁷, Jing Zhang⁸⁷, Jing Ru Zhang⁸⁷, Jinlong Zhang⁸,
 Liang Zhang²¹², X. Zhang⁸⁷, Yuan Zhang⁸⁷, Zhige Zhang²⁷, Zhiqing Zhang¹³⁰,
 Ziping Zhang²⁸³, Haiwen Zhao²⁷⁰, Ji Jiu Zhao⁸⁷, Jing Xia Zhao⁸⁷, Ming Hua Zhao¹⁹⁹,
 Sheng Chu Zhao⁸⁷, Tianchi Zhao²⁹⁶, Tong Xian Zhao²¹², Zhen Tang Zhao¹⁹⁹,
 Zhengguo Zhao^{268,283}, De Min Zhou⁸⁷, Feng Zhou²⁰³, Shun Zhou⁸⁷, Shou Hua Zhu¹⁰,
 Xiong Wei Zhu⁸⁷, Valery Zhukov³⁰⁴, Frank Zimmermann³⁵, Michael Ziolkowski³⁰⁶,
 Michael S. Zisman¹³⁷, Fabian Zomer¹³⁰, Zhang Guo Zong⁸⁷, Osman Zorba⁷²,
 Vishnu Zutshi¹⁷¹

List of Institutions

- ¹ *Abdus Salam International Centre for Theoretical Physics, Strada Costiera 11, 34014 Trieste, Italy*
- ² *Academy, RPR, National Institute of Physics and Nuclear Engineering ‘Horia Hulubei’ (IFIN-HH), Str. Atomistilor no. 407, P.O. Box MG-6, R-76900 Bucharest - Magurele, Romania*
- ³ *AGH University of Science and Technology Akademia Gorniczo-Hutnicza im. Stanislaw Staszica w Krakowie al. Mickiewicza 30 PL-30-059 Cracow, Poland*
- ⁴ *Albert-Ludwigs Universität Freiburg, Physikalisches Institut, Hermann-Herder Str. 3, D-79104 Freiburg, Germany*
- ⁵ *Aligarh Muslim University, Aligarh, Uttar Pradesh 202002, India*
- ⁶ *Amberg Engineering AG, Trockenloostr. 21, P.O.Box 27, 8105 Regensdorf-Watt, Switzerland*
- ⁷ *Angstromquelle Karlsruhe (ANKA), Forschungszentrum Karlsruhe, Hermann-von-Helmholtz-Platz 1, D-76344 Eggenstein-Leopoldshafen, Germany*
- ⁸ *Argonne National Laboratory (ANL), 9700 S. Cass Avenue, Argonne, IL 60439, USA*
- ⁹ *Baylor University, Department of Physics, 101 Bagby Avenue, Waco, TX 76706, USA*
- ¹⁰ *Beijing University, Department of Physics, Beijing, China 100871*
- ¹¹ *Belarusian State University, National Scientific & Educational Center, Particle & HEP Physics, M. Bogdanovich St., 153, 240040 Minsk, Belarus*
- ¹² *Benares Hindu University, Benares, Varanasi 221005, India*
- ¹³ *Bhabha Atomic Research Centre, Trombay, Mumbai 400085, India*
- ¹⁴ *Birla Institute of Technology and Science, EEE Dept., Pilani, Rajasthan, India*
- ¹⁵ *Bogazici University, Physics Department, 34342 Bebek / Istanbul, 80820 Istanbul, Turkey*
- ¹⁶ *Boston University, Department of Physics, 590 Commonwealth Avenue, Boston, MA 02215, USA*
- ¹⁷ *Brandenburg University of Technology, Postfach 101344, D-03013 Cottbus, Germany*
- ¹⁸ *Brno University of Technology, Antonínská; 548/1, CZ 601 90 Brno, Czech Republic*
- ¹⁹ *Brookhaven National Laboratory (BNL), P.O.Box 5000, Upton, NY 11973-5000, USA*
- ²⁰ *Brown University, Department of Physics, Box 1843, Providence, RI 02912, USA*
- ²¹ *Budkar Institute for Nuclear Physics (BINP), 630090 Novosibirsk, Russia*
- ²² *Calcutta University, Department of Physics, 92 A.P.C. Road, Kolkata 700009, India*
- ²³ *California Institute of Technology, Physics, Mathematics and Astronomy (PMA), 1200 East California Blvd, Pasadena, CA 91125, USA*
- ²⁴ *Carleton University, Department of Physics, 1125 Colonel By Drive, Ottawa, Ontario, Canada K1S 5B6*

- ²⁵ Carnegie Mellon University, Department of Physics, Wean Hall 7235, Pittsburgh, PA 15213, USA
- ²⁶ CCLRC Daresbury Laboratory, Daresbury, Warrington, Cheshire WA4 4AD, UK
- ²⁷ CCLRC Rutherford Appleton Laboratory, Chilton, Didcot, Oxton OX11 0QX, UK
- ²⁸ CEA Saclay, DAPNIA, F-91191 Gif-sur-Yvette, France
- ²⁹ CEA Saclay, Service de Physique Théorique, CEA/DSM/SPhT, F-91191 Gif-sur-Yvette Cedex, France
- ³⁰ Center for High Energy Physics (CHEP) / Kyungpook National University, 1370 Sankyuk-dong, Buk-gu, Daegu 702-701, Korea
- ³¹ Center for High Energy Physics (TUHEP), Tsinghua University, Beijing, China 100084
- ³² Centre de Physique Theorique, CNRS - Luminy, Universiti d'Aix - Marseille II, Campus of Luminy, Case 907, 13288 Marseille Cedex 9, France
- ³³ Centro de Investigaciones Energéticas, Medioambientales y Tecnológicas, CIEMAT, Avenia Complutense 22, E-28040 Madrid, Spain
- ³⁴ Centro Nacional de Microelectrónica (CNM), Instituto de Microelectrónica de Barcelona (IMB), Campus UAB, 08193 Cerdanyola del Vallès (Bellaterra), Barcelona, Spain
- ³⁵ CERN, CH-1211 Genève 23, Switzerland
- ³⁶ Charles University, Institute of Particle & Nuclear Physics, Faculty of Mathematics and Physics, V Holesovickach 2, CZ-18000 Praque 8, Czech Republic
- ³⁷ Chonbuk National University, Physics Department, Chonju 561-756, Korea
- ³⁸ Cockcroft Institute, Daresbury, Warrington WA4 4AD, UK
- ³⁹ College of William and Mary, Department of Physics, Williamsburg, VA, 23187, USA
- ⁴⁰ Colorado State University, Department of Physics, Fort Collins, CO 80523, USA
- ⁴¹ Columbia University, Department of Physics, New York, NY 10027-6902, USA
- ⁴² Concordia University, Department of Physics, 1455 De Maisonneuve Blvd. West, Montreal, Quebec, Canada H3G 1M8
- ⁴³ Cornell University, Laboratory for Elementary-Particle Physics (LEPP), Ithaca, NY 14853, USA
- ⁴⁴ Cukurova University, Department of Physics, Fen-Ed. Fakultesi 01330, Balcali, Turkey
- ⁴⁵ D. V. Efremov Research Institute, SINTEZ, 196641 St. Petersburg, Russia
- ⁴⁶ Dartmouth College, Department of Physics and Astronomy, 6127 Wilder Laboratory, Hanover, NH 03755, USA
- ⁴⁷ DESY-Hamburg site, Deutsches Elektronen-Synchrotron in der Helmholtz-Gemeinschaft, Notkestrasse 85, 22607 Hamburg, Germany
- ⁴⁸ DESY-Zeuthen site, Deutsches Elektronen-Synchrotron in der Helmholtz-Gemeinschaft, Platanenallee 6, D-15738 Zeuthen, Germany
- ⁴⁹ Durham University, Department of Physics, Ogen Center for Fundamental Physics, South Rd., Durham DH1 3LE, UK
- ⁵⁰ Ecole Polytechnique, Laboratoire Leprince-Ringuet (LLR), Route de Saclay, F-91128 Palaiseau Cedex, France
- ⁵¹ Ege University, Department of Physics, Faculty of Science, 35100 Izmir, Turkey
- ⁵² Enrico Fermi Institute, University of Chicago, 5640 S. Ellis Avenue, RI-183, Chicago, IL 60637, USA
- ⁵³ Ewha Womans University, 11-1 Daehyun-Dong, Seodaemun-Gu, Seoul, 120-750, Korea
- ⁵⁴ Fermi National Accelerator Laboratory (FNAL), P.O.Box 500, Batavia, IL 60510-0500, USA
- ⁵⁵ Fujita Gakuen Health University, Department of Physics, Toyoake, Aichi 470-1192, Japan

- ⁵⁶ Fukui University of Technology, 3-6-1 Gakuen, Fukui-shi, Fukui 910-8505, Japan
- ⁵⁷ Fukui University, Department of Physics, 3-9-1 Bunkyo, Fukui-shi, Fukui 910-8507, Japan
- ⁵⁸ Georg-August-Universität Göttingen, II. Physikalisches Institut, Friedrich-Hund-Platz 1, 37077 Göttingen, Germany
- ⁵⁹ Global Design Effort
- ⁶⁰ Gomel State University, Department of Physics, Ul. Sovetskaya 104, 246699 Gomel, Belarus
- ⁶¹ Guangxi University, College of Physics science and Engineering Technology, Nanning, China 530004
- ⁶² Hanoi University of Technology, 1 Dai Co Viet road, Hanoi, Vietnam
- ⁶³ Hanson Professional Services, Inc., 1525 S. Sixth St., Springfield, IL 62703, USA
- ⁶⁴ Harish-Chandra Research Institute, Chhatnag Road, Jhusi, Allahabad 211019, India
- ⁶⁵ Helsinki Institute of Physics (HIP), P.O. Box 64, FIN-00014 University of Helsinki, Finland
- ⁶⁶ Henan Normal University, College of Physics and Information Engineering, Xinxiang, China 453007
- ⁶⁷ High Energy Accelerator Research Organization, KEK, 1-1 Oho, Tsukuba, Ibaraki 305-0801, Japan
- ⁶⁸ Hiroshima University, Department of Physics, 1-3-1 Kagamiyama, Higashi-Hiroshima, Hiroshima 739-8526, Japan
- ⁶⁹ Humboldt Universität zu Berlin, Fachbereich Physik, Institut für Elementarteilchenphysik, Newtonstr. 15, D-12489 Berlin, Germany
- ⁷⁰ Hungarian Academy of Sciences, KFKI Research Institute for Particle and Nuclear Physics, P.O. Box 49, H-1525 Budapest, Hungary
- ⁷¹ Ibaraki University, College of Technology, Department of Physics, Nakanarusawa 4-12-1, Hitachi, Ibaraki 316-8511, Japan
- ⁷² Imperial College, Blackett Laboratory, Department of Physics, Prince Consort Road, London, SW7 2BW, UK
- ⁷³ Indian Association for the Cultivation of Science, Department of Theoretical Physics and Centre for Theoretical Sciences, Kolkata 700032, India
- ⁷⁴ Indian Institute of Science, Centre for High Energy Physics, Bangalore 560012, Karnataka, India
- ⁷⁵ Indian Institute of Technology, Bombay, Powai, Mumbai 400076, India
- ⁷⁶ Indian Institute of Technology, Guwahati, Guwahati, Assam 781039, India
- ⁷⁷ Indian Institute of Technology, Kanpur, Department of Physics, IIT Post Office, Kanpur 208016, India
- ⁷⁸ Indiana University - Purdue University, Indianapolis, Department of Physics, 402 N. Blackford St., LD 154, Indianapolis, IN 46202, USA
- ⁷⁹ Indiana University, Department of Physics, Swain Hall West 117, 727 E. 3rd St., Bloomington, IN 47405-7105, USA
- ⁸⁰ Institutio Catalana de Recerca i Estudis, ICREA, Passeig Lluís Companys, 23, Barcelona 08010, Spain
- ⁸¹ Institut de Physique Nucléaire, F-91406 Orsay, France
- ⁸² Institut für Theorie Elektromagnetischer Felder (TEMF), Technische Universität Darmstadt, Schloßgartenstr. 8, D-64289 Darmstadt, Germany
- ⁸³ Institut National de Physique Nucleaire et de Physique des Particules, 3, Rue Michel-Ange, 75794 Paris Cedex 16, France

- ⁸⁴ *Institut Pluridisciplinaire Hubert Curien, 23 Rue du Loess - BP28, 67037 Strasbourg Cedex 2, France*
- ⁸⁵ *Institute for Chemical Research, Kyoto University, Gokasho, Uji, Kyoto 611-0011, Japan*
- ⁸⁶ *Institute for Cosmic Ray Research, University of Tokyo, 5-1-5 Kashiwa-no-Ha, Kashiwa, Chiba 277-8582, Japan*
- ⁸⁷ *Institute of High Energy Physics - IHEP, Chinese Academy of Sciences, P.O. Box 918, Beijing, China 100049*
- ⁸⁸ *Institute of Mathematical Sciences, Taramani, C.I.T. Campus, Chennai 600113, India*
- ⁸⁹ *Institute of Physics and Electronics, Vietnamese Academy of Science and Technology (VAST), 10 Dao-Tan, Ba-Dinh, Hanoi 10000, Vietnam*
- ⁹⁰ *Institute of Physics, ASCR, Academy of Science of the Czech Republic, Division of Elementary Particle Physics, Na Slovance 2, CS-18221 Prague 8, Czech Republic*
- ⁹¹ *Institute of Physics, Pomorska 149/153, PL-90-236 Lodz, Poland*
- ⁹² *Institute of Theoretical and Experimental Physics, B. Cheremushkinskaya, 25, RU-117259, Moscow, Russia*
- ⁹³ *Institute of Theoretical Physics, Chinese Academy of Sciences, P.O.Box 2735, Beijing, China 100080*
- ⁹⁴ *Instituto de Fisica Corpuscular (IFIC), Centro Mixto CSIC-UVEG, Edificio Investigacion Paterna, Apartado 22085, 46071 Valencia, Spain*
- ⁹⁵ *Instituto de Fisica de Cantabria, (IFCA, CSIC-UC), Facultad de Ciencias, Avda. Los Castros s/n, 39005 Santander, Spain*
- ⁹⁶ *Instituto Nazionale di Fisica Nucleare (INFN), Laboratorio LASA, Via Fratelli Cervi 201, 20090 Segrate, Italy*
- ⁹⁷ *Instituto Nazionale di Fisica Nucleare (INFN), Sezione di Ferrara, via Paradiso 12, I-44100 Ferrara, Italy*
- ⁹⁸ *Instituto Nazionale di Fisica Nucleare (INFN), Sezione di Firenze, Via G. Sansone 1, I-50019 Sesto Fiorentino (Firenze), Italy*
- ⁹⁹ *Instituto Nazionale di Fisica Nucleare (INFN), Sezione di Lecce, via Arnesano, I-73100 Lecce, Italy*
- ¹⁰⁰ *Instituto Nazionale di Fisica Nucleare (INFN), Sezione di Napoli, Complesso Università di Monte Sant'Angelo, via, I-80126 Naples, Italy*
- ¹⁰¹ *Instituto Nazionale di Fisica Nucleare (INFN), Sezione di Pavia, Via Bassi 6, I-27100 Pavia, Italy*
- ¹⁰² *Instituto Nazionale di Fisica Nucleare (INFN), Sezione di Pisa, Edificio C - Polo Fibonacci Largo B. Pontecorvo, 3, I-56127 Pisa, Italy*
- ¹⁰³ *Instituto Nazionale di Fisica Nucleare (INFN), Sezione di Torino, c/o Università' di Torino facoltà' di Fisica, via P Giuria 1, 10125 Torino, Italy*
- ¹⁰⁴ *Instituto Nazionale di Fisica Nucleare (INFN), Sezione di Trieste, Padriciano 99, I-34012 Trieste (Padriciano), Italy*
- ¹⁰⁵ *Inter-University Accelerator Centre, Aruna Asaf Ali Marg, Post Box 10502, New Delhi 110067, India*
- ¹⁰⁶ *International Center for Elementary Particle Physics, University of Tokyo, Hongo 7-3-1, Bunkyo District, Tokyo 113-0033, Japan*
- ¹⁰⁷ *Iowa State University, Department of Physics, High Energy Physics Group, Ames, IA 50011, USA*
- ¹⁰⁸ *Jagiellonian University, Institute of Physics, Ul. Reymonta 4, PL-30-059 Cracow, Poland*

- ¹⁰⁹ *Jamia Millia Islamia, Centre for Theoretical Physics, Jamia Nagar, New Delhi 110025, India*
- ¹¹⁰ *Jamia Millia Islamia, Department of Physics, Jamia Nagar, New Delhi 110025, India*
- ¹¹¹ *Japan Aerospace Exploration Agency, Sagamihara Campus, 3-1-1 Yoshinodai, Sagamihara, Kanagawa 220-8510, Japan*
- ¹¹² *Japan Atomic Energy Agency, 4-49 Muramatsu, Tokai-mura, Naka-gun, Ibaraki 319-1184, Japan*
- ¹¹³ *Johannes Gutenberg Universität Mainz, Institut für Physik, 55099 Mainz, Germany*
- ¹¹⁴ *Johns Hopkins University, Applied Physics Laboratory, 11100 Johns Hopkins RD., Laurel, MD 20723-6099, USA*
- ¹¹⁵ *Joint Institute for Nuclear Research (JINR), Joliot-Curie 6, 141980, Dubna, Moscow Region, Russia*
- ¹¹⁶ *Kansas State University, Department of Physics, 116 Cardwell Hall, Manhattan, KS 66506, USA*
- ¹¹⁷ *KCS Corp., 2-7-25 Muramatsukita, Tokai, Ibaraki 319-1108, Japan*
- ¹¹⁸ *Kharkov Institute of Physics and Technology, National Science Center, 1, Akademicheskaya St., Kharkov, 61108, Ukraine*
- ¹¹⁹ *Kinki University, Department of Physics, 3-4-1 Kowakae, Higashi-Osaka, Osaka 577-8502, Japan*
- ¹²⁰ *Kobe University, Faculty of Science, 1-1 Rokkodai-cho, Nada-ku, Kobe, Hyogo 657-8501, Japan*
- ¹²¹ *Kogakuin University, Department of Physics, Shinjuku Campus, 1-24-2 Nishi-Shinjuku, Shinjuku-ku, Tokyo 163-8677, Japan*
- ¹²² *Konkuk University, 93-1 Mojin-dong, Kwanglin-gu, Seoul 143-701, Korea*
- ¹²³ *Korea Advanced Institute of Science & Technology, Department of Physics, 373-1 Kusong-dong, Yusong-gu, Taejeon 305-701, Korea*
- ¹²⁴ *Korea Institute for Advanced Study (KIAS), School of Physics, 207-43 Cheongryangri-dong, Dongdaemun-gu, Seoul 130-012, Korea*
- ¹²⁵ *Korea University, Department of Physics, Seoul 136-701, Korea*
- ¹²⁶ *Kyoto University, Department of Physics, Kitashirakawa-Oiwakecho, Sakyo-ku, Kyoto 606-8502, Japan*
- ¹²⁷ *L.P.T.A., UMR 5207 CNRS-UM2, Université Montpellier II, Case Courrier 070, Bât. 13, place Eugène Bataillon, 34095 Montpellier Cedex 5, France*
- ¹²⁸ *Laboratoire d'Annecy-le-Vieux de Physique des Particules (LAPP), Chemin du Bellevue, BP 110, F-74941 Annecy-le-Vieux Cedex, France*
- ¹²⁹ *Laboratoire d'Annecy-le-Vieux de Physique Theorique (LAPTH), Chemin de Bellevue, BP 110, F-74941 Annecy-le-Vieux Cedex, France*
- ¹³⁰ *Laboratoire de l'Accélérateur Linéaire (LAL), Université Paris-Sud 11, Bâtiment 200, 91898 Orsay, France*
- ¹³¹ *Laboratoire de Physique Corpusculaire de Clermont-Ferrand (LPC), Université Blaise Pascal, I.N.2.P.3./C.N.R.S., 24 avenue des Landais, 63177 Aubière Cedex, France*
- ¹³² *Laboratoire de Physique Subatomique et de Cosmologie (LPSC), Université Joseph Fourier (Grenoble 1), 53, ave. des Marthyrs, F-38026 Grenoble Cedex, France*
- ¹³³ *Laboratoire de Physique Theorique, Université de Paris-Sud XI, Batiment 210, F-91405 Orsay Cedex, France*
- ¹³⁴ *Laboratori Nazionali di Frascati, via E. Fermi, 40, C.P. 13, I-00044 Frascati, Italy*

- ¹³⁵ *Laboratory of High Energy Physics and Cosmology, Department of Physics, Hanoi National University, 334 Nguyen Trai, Hanoi, Vietnam*
- ¹³⁶ *Lancaster University, Physics Department, Lancaster LA1 4YB, UK*
- ¹³⁷ *Lawrence Berkeley National Laboratory (LBNL), 1 Cyclotron Rd, Berkeley, CA 94720, USA*
- ¹³⁸ *Lawrence Livermore National Laboratory (LLNL), Livermore, CA 94551, USA*
- ¹³⁹ *Lebedev Physical Institute, Leninsky Prospect 53, RU-117924 Moscow, Russia*
- ¹⁴⁰ *Liaoning Normal University, Department of Physics, Dalian, China 116029*
- ¹⁴¹ *Lomonosov Moscow State University, Skobeltsyn Institute of Nuclear Physics (MSU SINP), 1(2), Leninskie gory, GSP-1, Moscow 119991, Russia*
- ¹⁴² *Los Alamos National Laboratory (LANL), P.O.Box 1663, Los Alamos, NM 87545, USA*
- ¹⁴³ *Louisiana Technical University, Department of Physics, Ruston, LA 71272, USA*
- ¹⁴⁴ *Ludwig-Maximilians-Universität München, Department für Physik, Schellingstr. 4, D-80799 Munich, Germany*
- ¹⁴⁵ *Lunds Universitet, Fysiska Institutionen, Avdelningen för Experimentell Högenergifysik, Box 118, 221 00 Lund, Sweden*
- ¹⁴⁶ *Massachusetts Institute of Technology, Laboratory for Nuclear Science & Center for Theoretical Physics, 77 Massachusetts Ave., NW16, Cambridge, MA 02139, USA*
- ¹⁴⁷ *Max-Planck-Institut für Physik (Werner-Heisenberg-Institut), Föhringer Ring 6, 80805 München, Germany*
- ¹⁴⁸ *McGill University, Department of Physics, Ernest Rutherford Physics Bldg., 3600 University Ave., Montreal, Quebec, H3A 2T8 Canada*
- ¹⁴⁹ *Meiji Gakuin University, Department of Physics, 2-37 Shirokanedai 1-chome, Minato-ku, Tokyo 244-8539, Japan*
- ¹⁵⁰ *Michigan State University, Department of Physics and Astronomy, East Lansing, MI 48824, USA*
- ¹⁵¹ *Middle East Technical University, Department of Physics, TR-06531 Ankara, Turkey*
- ¹⁵² *Mindanao Polytechnic State College, Lapasan, Cagayan de Oro City 9000, Phillipines*
- ¹⁵³ *MSU-Iligan Institute of Technology, Department of Physics, Andres Bonifacio Avenue, 9200 Iligan City, Phillipines*
- ¹⁵⁴ *Nagasaki Institute of Applied Science, 536 Abamachi, Nagasaki-Shi, Nagasaki 851-0193, Japan*
- ¹⁵⁵ *Nagoya University, Fundamental Particle Physics Laboratory, Division of Particle and Astrophysical Sciences, Furo-cho, Chikusa-ku, Nagoya, Aichi 464-8602, Japan*
- ¹⁵⁶ *Nanchang University, Department of Physics, Nanchang, China 330031*
- ¹⁵⁷ *Nanjing University, Department of Physics, Nanjing, China 210093*
- ¹⁵⁸ *Nankai University, Department of Physics, Tianjin, China 300071*
- ¹⁵⁹ *National Central University, High Energy Group, Department of Physics, Chung-li, Taiwan 32001*
- ¹⁶⁰ *National Institute for Nuclear & High Energy Physics, PO Box 41882, 1009 DB Amsterdam, Netherlands*
- ¹⁶¹ *National Institute of Radiological Sciences, 4-9-1 Anagawa, Inaga, Chiba 263-8555, Japan*
- ¹⁶² *National Synchrotron Radiation Laboratory, University of Science and Technology of china, Hefei, Anhui, China 230029*
- ¹⁶³ *National Synchrotron Research Center, 101 Hsin-Ann Rd., Hsinchu Science Part, Hsinchu, Taiwan 30076*

- ¹⁶⁴ National Taiwan University, Physics Department, Taipei, Taiwan 106
- ¹⁶⁵ Niels Bohr Institute (NBI), University of Copenhagen, Blegdamsvej 17, DK-2100 Copenhagen, Denmark
- ¹⁶⁶ Niigata University, Department of Physics, Ikarashi, Niigata 950-218, Japan
- ¹⁶⁷ Nikken Sekkai Ltd., 2-18-3 Iidabashi, Chiyoda-Ku, Tokyo 102-8117, Japan
- ¹⁶⁸ Nippon Dental University, 1-9-20 Fujimi, Chiyoda-Ku, Tokyo 102-8159, Japan
- ¹⁶⁹ North Asia University, Akita 010-8515, Japan
- ¹⁷⁰ North Eastern Hill University, Department of Physics, Shillong 793022, India
- ¹⁷¹ Northern Illinois University, Department of Physics, DeKalb, Illinois 60115-2825, USA
- ¹⁷² Northwestern University, Department of Physics and Astronomy, 2145 Sheridan Road., Evanston, IL 60208, USA
- ¹⁷³ Novosibirsk State University (NGU), Department of Physics, Pirogov st. 2, 630090 Novosibirsk, Russia
- ¹⁷⁴ Obninsk State Technical University for Nuclear Engineering (IATE), Obninsk, Russia
- ¹⁷⁵ Ochanomizu University, Department of Physics, Faculty of Science, 1-1 Otsuka 2, Bunkyo-ku, Tokyo 112-8610, Japan
- ¹⁷⁶ Osaka University, Laboratory of Nuclear Studies, 1-1 Machikaneyama, Toyonaka, Osaka 560-0043, Japan
- ¹⁷⁷ Österreichische Akademie der Wissenschaften, Institut für Hochenergiephysik, Nikolsdorfergasse 18, A-1050 Vienna, Austria
- ¹⁷⁸ Panjab University, Chandigarh 160014, India
- ¹⁷⁹ Pavel Sukhoi Gomel State Technical University, ICTP Affiliated Centre & Laboratory for Physical Studies, October Avenue, 48, 246746, Gomel, Belarus
- ¹⁸⁰ Pavel Sukhoi Gomel State Technical University, Physics Department, October Ave. 48, 246746 Gomel, Belarus
- ¹⁸¹ Physical Research Laboratory, Navrangpura, Ahmedabad 380 009, Gujarat, India
- ¹⁸² Pohang Accelerator Laboratory (PAL), San-31 Hyoja-dong, Nam-gu, Pohang, Gyeongbuk 790-784, Korea
- ¹⁸³ Polish Academy of Sciences (PAS), Institute of Physics, Al. Lotnikow 32/46, PL-02-668 Warsaw, Poland
- ¹⁸⁴ Primera Engineers Ltd., 100 S Wacker Drive, Suite 700, Chicago, IL 60606, USA
- ¹⁸⁵ Princeton University, Department of Physics, P.O. Box 708, Princeton, NJ 08542-0708, USA
- ¹⁸⁶ Purdue University, Department of Physics, West Lafayette, IN 47907, USA
- ¹⁸⁷ Pusan National University, Department of Physics, Busan 609-735, Korea
- ¹⁸⁸ R. W. Downing Inc., 6590 W. Box Canyon Dr., Tucson, AZ 85745, USA
- ¹⁸⁹ Raja Ramanna Center for Advanced Technology, Indore 452013, India
- ¹⁹⁰ Rheinisch-Westfälische Technische Hochschule (RWTH), Physikalisches Institut, Physikzentrum, Sommerfeldstrasse 14, D-52056 Aachen, Germany
- ¹⁹¹ RIKEN, 2-1 Hirosawa, Wako, Saitama 351-0198, Japan
- ¹⁹² Royal Holloway, University of London (RHUL), Department of Physics, Egham, Surrey TW20 0EX, UK
- ¹⁹³ Saga University, Department of Physics, 1 Honjo-machi, Saga-shi, Saga 840-8502, Japan
- ¹⁹⁴ Saha Institute of Nuclear Physics, 1/AF Bidhan Nagar, Kolkata 700064, India
- ¹⁹⁵ Salalah College of Technology (SCOT), Engineering Department, Post Box No. 608, Postal Code 211, Salalah, Sultanate of Oman
- ¹⁹⁶ Saube Co., Hanabatake, Tsukuba, Ibaraki 300-3261, Japan

- ¹⁹⁷ *Seoul National University, San 56-1, Shinrim-dong, Kwanak-gu, Seoul 151-742, Korea*
- ¹⁹⁸ *Shandong University, 27 Shanda Nanlu, Jinan, China 250100*
- ¹⁹⁹ *Shanghai Institute of Applied Physics, Chinese Academy of Sciences, 2019 Jiaruo Rd.,
Jiading, Shanghai, China 201800*
- ²⁰⁰ *Shinshu University, 3-1-1, Asahi, Matsumoto, Nagano 390-8621, Japan*
- ²⁰¹ *Sobolev Institute of Mathematics, Siberian Branch of the Russian Academy of Sciences,
4 Acad. Koptug Avenue, 630090 Novosibirsk, Russia*
- ²⁰² *Sokendai, The Graduate University for Advanced Studies, Shonan Village, Hayama,
Kanagawa 240-0193, Japan*
- ²⁰³ *Stanford Linear Accelerator Center (SLAC), 2575 Sand Hill Road, Menlo Park, CA
94025, USA*
- ²⁰⁴ *State University of New York at Binghamton, Department of Physics, PO Box 6016,
Binghamton, NY 13902, USA*
- ²⁰⁵ *State University of New York at Buffalo, Department of Physics & Astronomy, 239
Franczak Hall, Buffalo, NY 14260, USA*
- ²⁰⁶ *State University of New York at Stony Brook, Department of Physics and Astronomy,
Stony Brook, NY 11794-3800, USA*
- ²⁰⁷ *Sumitomo Heavy Industries, Ltd., Natsushima-cho, Yokosuka, Kanagawa 237-8555,
Japan*
- ²⁰⁸ *Sungkyunkwan University (SKKU), Natural Science Campus 300, Physics Research
Division, Chunchun-dong, Jangan-gu, Suwon, Kyunggi-do 440-746, Korea*
- ²⁰⁹ *Swiss Light Source (SLS), Paul Scherrer Institut (PSI), PSI West, CH-5232 Villigen
PSI, Switzerland*
- ²¹⁰ *Syracuse University, Department of Physics, 201 Physics Building, Syracuse, NY
13244-1130, USA*
- ²¹¹ *Tata Institute of Fundamental Research, School of Natural Sciences, Homi Bhabha Rd.,
Mumbai 400005, India*
- ²¹² *Technical Institute of Physics and Chemistry, Chinese Academy of Sciences, 2 North 1st
St., Zhongguancun, Beijing, China 100080*
- ²¹³ *Technical University of Lodz, Department of Microelectronics and Computer Science, al.
Politechniki 11, 90-924 Lodz, Poland*
- ²¹⁴ *Technische Universität Dresden, Institut für Kern- und Teilchenphysik, D-01069
Dresden, Germany*
- ²¹⁵ *Technische Universität Dresden, Institut für Theoretische Physik, D-01062 Dresden,
Germany*
- ²¹⁶ *Tel-Aviv University, School of Physics and Astronomy, Ramat Aviv, Tel Aviv 69978,
Israel*
- ²¹⁷ *Texas A&M University, Physics Department, College Station, 77843-4242 TX, USA*
- ²¹⁸ *Texas Tech University, Department of Physics, Campus Box 41051, Lubbock, TX
79409-1051, USA*
- ²¹⁹ *The Henryk Niewodniczanski Institute of Nuclear Physics (NINP), High Energy Physics
Lab, ul. Radzikowskiego 152, PL-31342 Cracow, Poland*
- ²²⁰ *Thomas Jefferson National Accelerator Facility (TJNAF), 12000 Jefferson Avenue,
Newport News, VA 23606, USA*
- ²²¹ *Tohoku Gakuin University, Faculty of Technology, 1-13-1 Chuo, Tagajo, Miyagi
985-8537, Japan*

- ²²² Tohoku University, Department of Physics, Aoba District, Sendai, Miyagi 980-8578, Japan
- ²²³ Tokyo Management College, Computer Science Lab, Ichikawa, Chiba 272-0001, Japan
- ²²⁴ Tokyo University of Agriculture Technology, Department of Applied Physics, Naka-machi, Koganei, Tokyo 183-8488, Japan
- ²²⁵ Toyama University, Department of Physics, 3190 Gofuku, Toyama-shi 930-8588, Japan
- ²²⁶ TRIUMF, 4004 Wesbrook Mall, Vancouver, BC V6T 2A3, Canada
- ²²⁷ Tufts University, Department of Physics and Astronomy, Robinson Hall, Medford, MA 02155, USA
- ²²⁸ Universidad Autònoma de Madrid (UAM), Facultad de Ciencias C-XI, Departamento de Física Teórica, Cantoblanco, Madrid 28049, Spain
- ²²⁹ Universitat Autònoma de Barcelona, Institut de Física d'Altes Energies (IFAE), Campus UAB, Edifici Cn, E-08193 Bellaterra, Barcelona, Spain
- ²³⁰ University College of London (UCL), High Energy Physics Group, Physics and Astronomy Department, Gower Street, London WC1E 6BT, UK
- ²³¹ University College, National University of Ireland (Dublin), Department of Experimental Physics, Science Buildings, Belfield, Dublin 4, Ireland
- ²³² University de Barcelona, Facultat de Física, Av. Diagonal, 647, Barcelona 08028, Spain
- ²³³ University of Abertay Dundee, Department of Physics, Bell St, Dundee, DD1 1HG, UK
- ²³⁴ University of Auckland, Department of Physics, Private Bag, Auckland 1, New Zealand
- ²³⁵ University of Bergen, Institute of Physics, Allegaten 55, N-5007 Bergen, Norway
- ²³⁶ University of Birmingham, School of Physics and Astronomy, Particle Physics Group, Edgbaston, Birmingham B15 2TT, UK
- ²³⁷ University of Bristol, H. H. Wills Physics Lab, Tyndall Ave., Bristol BS8 1TL, UK
- ²³⁸ University of British Columbia, Department of Physics and Astronomy, 6224 Agricultural Rd., Vancouver, BC V6T 1Z1, Canada
- ²³⁹ University of California Berkeley, Department of Physics, 366 Le Conte Hall, #7300, Berkeley, CA 94720, USA
- ²⁴⁰ University of California Davis, Department of Physics, One Shields Avenue, Davis, CA 95616-8677, USA
- ²⁴¹ University of California Irvine, Department of Physics and Astronomy, High Energy Group, 4129 Frederick Reines Hall, Irvine, CA 92697-4575 USA
- ²⁴² University of California Riverside, Department of Physics, Riverside, CA 92521, USA
- ²⁴³ University of California Santa Barbara, Department of Physics, Broida Hall, Mail Code 9530, Santa Barbara, CA 93106-9530, USA
- ²⁴⁴ University of California Santa Cruz, Department of Astronomy and Astrophysics, 1156 High Street, Santa Cruz, CA 05060, USA
- ²⁴⁵ University of California Santa Cruz, Institute for Particle Physics, 1156 High Street, Santa Cruz, CA 95064, USA
- ²⁴⁶ University of Cambridge, Cavendish Laboratory, J J Thomson Avenue, Cambridge CB3 0HE, UK
- ²⁴⁷ University of Colorado at Boulder, Department of Physics, 390 UCB, University of Colorado, Boulder, CO 80309-0390, USA
- ²⁴⁸ University of Delhi, Department of Physics and Astrophysics, Delhi 110007, India
- ²⁴⁹ University of Delhi, S.G.T.B. Khalsa College, Delhi 110007, India
- ²⁵⁰ University of Dundee, Department of Physics, Nethergate, Dundee, DD1 4HN, Scotland, UK

- ²⁵¹ University of Edinburgh, School of Physics, James Clerk Maxwell Building, The King's Buildings, Mayfield Road, Edinburgh EH9 3JZ, UK
- ²⁵² University of Essex, Department of Physics, Wivenhoe Park, Colchester CO4 3SQ, UK
- ²⁵³ University of Florida, Department of Physics, Gainesville, FL 32611, USA
- ²⁵⁴ University of Glasgow, Department of Physics & Astronomy, University Avenue, Glasgow G12 8QQ, Scotland, UK
- ²⁵⁵ University of Hamburg, Physics Department, Institut für Experimentalphysik, Luruper Chaussee 149, 22761 Hamburg, Germany
- ²⁵⁶ University of Hawaii, Department of Physics and Astronomy, HEP, 2505 Correa Rd., WAT 232, Honolulu, HI 96822-2219, USA
- ²⁵⁷ University of Heidelberg, Kirchhoff Institute of Physics, Albert Überle Strasse 3-5, DE-69120 Heidelberg, Germany
- ²⁵⁸ University of Helsinki, Department of Physical Sciences, P.O. Box 64 (Vaino Auerin katu 11), FIN-00014, Helsinki, Finland
- ²⁵⁹ University of Hyogo, School of Science, Kouto 3-2-1, Kamigori, Ako, Hyogo 678-1297, Japan
- ²⁶⁰ University of Illinois at Urbana-Champaign, Department of Phys., High Energy Physics, 441 Loomis Lab. of Physics 1110 W. Green St., Urbana, IL 61801-3080, USA
- ²⁶¹ University of Iowa, Department of Physics and Astronomy, 203 Van Allen Hall, Iowa City, IA 52242-1479, USA
- ²⁶² University of Kansas, Department of Physics and Astronomy, Malott Hall, 1251 Wescoe Hall Drive, Room 1082, Lawrence, KS 66045-7582, USA
- ²⁶³ University of Liverpool, Department of Physics, Oliver Lodge Lab, Oxford St., Liverpool L69 7ZE, UK
- ²⁶⁴ University of Louisville, Department of Physics, Louisville, KY 40292, USA
- ²⁶⁵ University of Manchester, School of Physics and Astronomy, Schuster Lab, Manchester M13 9PL, UK
- ²⁶⁶ University of Maryland, Department of Physics and Astronomy, Physics Building (Bldg. 082), College Park, MD 20742, USA
- ²⁶⁷ University of Melbourne, School of Physics, Victoria 3010, Australia
- ²⁶⁸ University of Michigan, Department of Physics, 500 E. University Ave., Ann Arbor, MI 48109-1120, USA
- ²⁶⁹ University of Minnesota, 148 Tate Laboratory Of Physics, 116 Church St. S.E., Minneapolis, MN 55455, USA
- ²⁷⁰ University of Mississippi, Department of Physics and Astronomy, 108 Lewis Hall, PO Box 1848, Oxford, Mississippi 38677-1848, USA
- ²⁷¹ University of Montenegro, Faculty of Sciences and Math., Department of Phys., P.O. Box 211, 81001 Podgorica, Serbia and Montenegro
- ²⁷² University of New Mexico, New Mexico Center for Particle Physics, Department of Physics and Astronomy, 800 Yale Boulevard N.E., Albuquerque, NM 87131, USA
- ²⁷³ University of Notre Dame, Department of Physics, 225 Nieuwland Science Hall, Notre Dame, IN 46556, USA
- ²⁷⁴ University of Oklahoma, Department of Physics and Astronomy, Norman, OK 73071, USA
- ²⁷⁵ University of Oregon, Department of Physics, 1371 E. 13th Ave., Eugene, OR 97403, USA

- ²⁷⁶ University of Oxford, Particle Physics Department, Denys Wilkinson Bldg., Keble Road, Oxford OX1 3RH England, UK
- ²⁷⁷ University of Patras, Department of Physics, GR-26100 Patras, Greece
- ²⁷⁸ University of Pavia, Department of Nuclear and Theoretical Physics, via Bassi 6, I-27100 Pavia, Italy
- ²⁷⁹ University of Pennsylvania, Department of Physics and Astronomy, 209 South 33rd Street, Philadelphia, PA 19104-6396, USA
- ²⁸⁰ University of Puerto Rico at Mayaguez, Department of Physics, P.O. Box 9016, Mayaguez, 00681-9016 Puerto Rico
- ²⁸¹ University of Regina, Department of Physics, Regina, Saskatchewan, S4S 0A2 Canada
- ²⁸² University of Rochester, Department of Physics and Astronomy, Bausch & Lomb Hall, P.O. Box 270171, 600 Wilson Boulevard, Rochester, NY 14627-0171 USA
- ²⁸³ University of Science and Technology of China, Department of Modern Physics (DMP), Jin Zhai Road 96, Hefei, China 230026
- ²⁸⁴ University of Silesia, Institute of Physics, Ul. Uniwersytecka 4, PL-40007 Katowice, Poland
- ²⁸⁵ University of Southampton, School of Physics and Astronomy, Highfield, Southampton S017 1BJ, England, UK
- ²⁸⁶ University of Strathclyde, Physics Department, John Anderson Building, 107 Rottenrow, Glasgow, G4 0NG, Scotland, UK
- ²⁸⁷ University of Sydney, Falkiner High Energy Physics Group, School of Physics, A28, Sydney, NSW 2006, Australia
- ²⁸⁸ University of Texas, Center for Accelerator Science and Technology, Arlington, TX 76019, USA
- ²⁸⁹ University of Tokushima, Institute of Theoretical Physics, Tokushima-shi 770-8502, Japan
- ²⁹⁰ University of Tokyo, Department of Physics, 7-3-1 Hongo, Bunkyo District, Tokyo 113-0033, Japan
- ²⁹¹ University of Toronto, Department of Physics, 60 St. George St., Toronto M5S 1A7, Ontario, Canada
- ²⁹² University of Tsukuba, Institute of Physics, 1-1-1 Ten'nodai, Tsukuba, Ibaraki 305-8571, Japan
- ²⁹³ University of Victoria, Department of Physics and Astronomy, P.O.Box 3055 Stn Csc, Victoria, BC V8W 3P6, Canada
- ²⁹⁴ University of Warsaw, Institute of Physics, Ul. Hoza 69, PL-00 681 Warsaw, Poland
- ²⁹⁵ University of Warsaw, Institute of Theoretical Physics, Ul. Hoza 69, PL-00 681 Warsaw, Poland
- ²⁹⁶ University of Washington, Department of Physics, PO Box 351560, Seattle, WA 98195-1560, USA
- ²⁹⁷ University of Wisconsin, Physics Department, Madison, WI 53706-1390, USA
- ²⁹⁸ University of Wuppertal, Gaußstraße 20, D-42119 Wuppertal, Germany
- ²⁹⁹ Université Claude Bernard Lyon-I, Institut de Physique Nucléaire de Lyon (IPNL), 4, rue Enrico Fermi, F-69622 Villeurbanne Cedex, France
- ³⁰⁰ Université de Genève, Section de Physique, 24, quai E. Ansermet, 1211 Genève 4, Switzerland
- ³⁰¹ Université Louis Pasteur (Strasbourg I), UFR de Sciences Physiques, 3-5 Rue de l'Université, F-67084 Strasbourg Cedex, France

- ³⁰² *Université Pierre et Marie Curie (Paris VI-VII) (6-7) (UPMC), Laboratoire de Physique Nucléaire et de Hautes Energies (LPNHE), 4 place Jussieu, Tour 33, Rez de chaussée, 75252 Paris Cedex 05, France*
- ³⁰³ *Universität Bonn, Physikalisches Institut, Nußallee 12, 53115 Bonn, Germany*
- ³⁰⁴ *Universität Karlsruhe, Institut für Physik, Postfach 6980, Kaiserstrasse 12, D-76128 Karlsruhe, Germany*
- ³⁰⁵ *Universität Rostock, Fachbereich Physik, Universitätsplatz 3, D-18051 Rostock, Germany*
- ³⁰⁶ *Universität Siegen, Fachbereich für Physik, Emmy Noether Campus, Walter-Flex-Str.3, D-57068 Siegen, Germany*
- ³⁰⁷ *Università de Bergamo, Dipartimento di Fisica, via Salvecchio, 19, I-24100 Bergamo, Italy*
- ³⁰⁸ *Università degli Studi di Roma La Sapienza, Dipartimento di Fisica, Istituto Nazionale di Fisica Nucleare, Piazzale Aldo Moro 2, I-00185 Rome, Italy*
- ³⁰⁹ *Università degli Studi di Trieste, Dipartimento di Fisica, via A. Valerio 2, I-34127 Trieste, Italy*
- ³¹⁰ *Università degli Studi di “Roma Tre”, Dipartimento di Fisica “Edoardo Amaldi”, Istituto Nazionale di Fisica Nucleare, Via della Vasca Navale 84, 00146 Roma, Italy*
- ³¹¹ *Università dell’Insubria in Como, Dipartimento di Scienze CC.FF.MM., via Valleggio 11, I-22100 Como, Italy*
- ³¹² *Università di Pisa, Dipartimento di Fisica ‘Enrico Fermi’, Largo Bruno Pontecorvo 3, I-56127 Pisa, Italy*
- ³¹³ *Università di Salento, Dipartimento di Fisica, via Arnesano, C.P. 193, I-73100 Lecce, Italy*
- ³¹⁴ *Università di Udine, Dipartimento di Fisica, via delle Scienze, 208, I-33100 Udine, Italy*
- ³¹⁵ *Variable Energy Cyclotron Centre, 1/AF, Bidhan Nagar, Kolkata 700064, India*
- ³¹⁶ *VINCA Institute of Nuclear Sciences, Laboratory of Physics, PO Box 522, YU-11001 Belgrade, Serbia and Montenegro*
- ³¹⁷ *Vinh University, 182 Le Duan, Vinh City, Nghe An Province, Vietnam*
- ³¹⁸ *Virginia Polytechnic Institute and State University, Physics Department, Blacksburg, VA 2406, USA*
- ³¹⁹ *Visva-Bharati University, Department of Physics, Santiniketan 731235, India*
- ³²⁰ *Waseda University, Advanced Research Institute for Science and Engineering, Shinjuku, Tokyo 169-8555, Japan*
- ³²¹ *Wayne State University, Department of Physics, Detroit, MI 48202, USA*
- ³²² *Weizmann Institute of Science, Department of Particle Physics, P.O. Box 26, Rehovot 76100, Israel*
- ³²³ *Yale University, Department of Physics, New Haven, CT 06520, USA*
- ³²⁴ *Yonsei University, Department of Physics, 134 Sinchon-dong, Sudaemoon-gu, Seoul 120-749, Korea*
- ³²⁵ *Zhejiang University, College of Science, Department of Physics, Hangzhou, China 310027*
- * deceased

Acknowledgements

We would like to acknowledge the support and guidance of the International Committee on Future Accelerators (ICFA), chaired by A. Wagner of DESY, and the International Linear Collider Steering Committee (ILCSC), chaired by S. Kurokawa of KEK, who established the ILC Global Design Effort, as well as the World Wide Study of the Physics and Detectors.

We are grateful to the ILC Machine Advisory Committee (MAC), chaired by F. Willeke of DESY and the International ILC Cost Review Committee, chaired by L. Evans of CERN, for their advice on the ILC Reference Design. We also thank the consultants who participated in the Conventional Facilities Review at CalTech and in the RDR Cost Review at SLAC.

We would like to thank the directors of the institutions who have hosted ILC meetings: KEK, ANL/FNAL/SLAC/U. Colorado (Snowmass), INFN/Frascati, IIT/Bangalore, TRIUMF/U. British Columbia, U. Valencia, IHEP/Beijing and DESY.

We are grateful for the support of the Funding Agencies for Large Colliders (FALC), chaired by R. Petronzio of INFN, and we thank all of the international, regional and national funding agencies whose generous support has made the ILC Reference Design possible.

Each of the GDE regional teams in the Americas, Asia and Europe are grateful for the support of their local scientific societies, industrial forums, advisory committees and reviewers.

CONTENTS

| | | |
|----------|--|-----------|
| 1 | Introduction | 1 |
| 1.1 | Questions about the universe | 1 |
| 1.2 | The new landscape of particle physics | 3 |
| 1.3 | Running scenarios | 5 |
| 1.4 | Physics and the detectors | 6 |
| 2 | Higgs physics | 9 |
| 2.1 | The Higgs sector of the SM and beyond | 10 |
| 2.1.1 | The Higgs boson in the SM | 10 |
| 2.1.2 | The Higgs particles in the MSSM | 11 |
| 2.1.3 | Higgs bosons in non-minimal SUSY models | 13 |
| 2.1.4 | Higgs bosons in alternative models | 14 |
| 2.1.5 | The expectations at the LHC | 15 |
| 2.2 | The Higgs boson in the Standard Model | 17 |
| 2.2.1 | Higgs decays and production | 17 |
| 2.2.2 | Higgs detection at the ILC | 20 |
| 2.2.3 | Determination of the SM Higgs properties | 21 |
| 2.3 | The Higgs bosons in SUSY theories | 29 |
| 2.3.1 | Decays and production of the MSSM Higgs bosons | 29 |
| 2.3.2 | Measurements in the MSSM Higgs sector | 33 |
| 2.3.3 | The Higgs sector beyond the MSSM | 35 |
| 2.4 | The Higgs sector in alternative scenarios | 37 |
| 3 | Couplings of gauge bosons | 39 |
| 3.1 | Couplings of gauge bosons to fermions | 40 |
| 3.2 | Couplings among gauge bosons | 43 |
| 3.2.1 | Measurements of the triple couplings | 43 |
| 3.2.2 | Measurements of the quartic couplings | 45 |
| 3.3 | The strong interaction coupling | 46 |
| 4 | Top quark physics | 49 |
| 4.1 | The top quark mass and width | 50 |
| 4.2 | Top quark interactions | 52 |
| 4.2.1 | The coupling to the Higgs boson | 52 |
| 4.2.2 | Couplings to electroweak gauge bosons | 52 |
| 4.2.3 | Couplings to gluons | 55 |

CONTENTS

| | | |
|----------|---|------------|
| 4.3 | New decay modes | 55 |
| 5 | Supersymmetry | 57 |
| 5.1 | Introduction | 57 |
| 5.1.1 | Motivations for supersymmetry | 57 |
| 5.1.2 | Summary of SUSY models | 58 |
| 5.1.3 | Probing SUSY and the role of the ILC | 59 |
| 5.2 | Precision SUSY measurements at the ILC | 61 |
| 5.2.1 | The chargino/neutralino sector | 61 |
| 5.2.2 | The slepton sector | 63 |
| 5.2.3 | The squark sector | 66 |
| 5.2.4 | Measurements in other scenarios/extensions | 67 |
| 5.3 | Determining the SUSY Lagrangian | 69 |
| 5.3.1 | A summary of measurements and tests at the ILC | 69 |
| 5.3.2 | Determination of the low energy SUSY parameters | 70 |
| 5.3.3 | Reconstructing the fundamental SUSY parameters | 71 |
| 5.3.4 | Analyses in other GUT scenarios | 73 |
| 6 | Alternative scenarios | 75 |
| 6.1 | General motivation and scenarios | 75 |
| 6.2 | Extra dimensional models | 76 |
| 6.2.1 | Large extra dimensions | 76 |
| 6.2.2 | Warped extra dimensions | 78 |
| 6.2.3 | Universal extra dimensions | 80 |
| 6.3 | Strong interaction models | 81 |
| 6.3.1 | Little Higgs models | 81 |
| 6.3.2 | Strong electroweak symmetry breaking | 83 |
| 6.3.3 | Higgsless scenarios in extra dimensions | 85 |
| 6.4 | New particles and interactions | 86 |
| 6.4.1 | New gauge bosons | 86 |
| 6.4.2 | Exotic fermions | 88 |
| 6.4.3 | Difermions | 89 |
| 6.4.4 | Compositeness | 90 |
| 7 | Connections to cosmology | 91 |
| 7.1 | Dark matter | 92 |
| 7.1.1 | DM and new physics | 92 |
| 7.1.2 | SUSY dark matter | 93 |
| 7.1.3 | DM in extra dimensional scenarios | 98 |
| 7.2 | The baryon asymmetry | 101 |
| 7.2.1 | Electroweak baryogenesis in the MSSM | 101 |
| 7.2.2 | Leptogenesis and right-handed neutrinos | 103 |
| | Bibliography | 105 |
| | List of figures | 117 |
| | List of tables | 119 |

CHAPTER 1

Introduction

1.1 QUESTIONS ABOUT THE UNIVERSE

- *What is the universe? How did it begin?*
- *What are matter and energy? What are space and time?*

Throughout human history, scientific theories and experiments of increasing power and sophistication have addressed these basic questions about the universe. The resulting knowledge has revolutionized our view of the world around us, transforming our society and advancing our civilization.

Everyday phenomena are governed by universal laws and principles whose natural realm is at scales of time and distance far removed from our direct experience. Particle physics is a primary avenue of inquiry into these most basic workings of the universe. Experiments using particle accelerators convert matter into energy and back to matter again, exploiting the insights summarized by the equation $E = mc^2$. Other experiments exploit naturally occurring particles, such as neutrinos from the Sun or cosmic rays striking Earth’s atmosphere. Many experiments use exquisitely sensitive detectors to search for rare phenomena or exotic particles. Physicists combine astrophysical observations with results from laboratory experiments, pushing towards a great intellectual synthesis of the laws of the large with laws of the small.

The triumph of 20th century particle physics was the development of the Standard Model and the confirmation of many of its aspects. Experiments determined the particle constituents of ordinary matter, and identified four forces that hold matter together and transform it from one form to another. Particle interactions were found to obey precise laws of relativity and quantum theory. Remarkable features of quantum physics were observed, including the real effects of “virtual” particles on the visible world.

Building on this success, particle physicists are now able to address questions that are even more fundamental, and explore some of the deepest mysteries in science. The scope of these questions is illustrated by this summary from the report *Quantum Universe* [1]:

1. *Are there undiscovered principles of nature?*
2. *How can we solve the mystery of dark energy?*
3. *Are there extra dimensions of space?*
4. *Do all the forces become one?*

INTRODUCTION

5. *Why are there so many particles?*
6. *What is dark matter? How can we make it in the laboratory?*
7. *What are neutrinos telling us?*
8. *How did the universe begin?*
9. *What happened to the antimatter?*

A worldwide program of particle physics investigations, using multiple approaches, is already underway to explore this compelling scientific landscape. As emphasized in many scientific studies [2, 3, 4, 5, 6, 7, 8, 9, 10], the International Linear Collider is expected to play a central role in what is likely to be an era of revolutionary advances. As already documented in [11], discoveries from the ILC could have breakthrough impact on many of these fundamental questions.

Many of the scientific opportunities for the ILC involve the Higgs particle and related new phenomena at Terascale energies. The Standard Model boldly hypothesizes a new form of Terascale energy, called the Higgs field, that permeates the entire universe. Elementary particles acquire mass by interacting with this field. The Higgs field also breaks a fundamental electroweak force into two forces, the electromagnetic and weak forces, which are observed by experiments in very different forms.

So far, there is no direct experimental evidence for a Higgs field or the Higgs particle that should accompany it. Furthermore, quantum effects of the type already observed in experiments should destabilize the Higgs boson of the Standard Model, preventing its operation at Terascale energies. The proposed antidotes for this quantum instability mostly involve dramatic phenomena at the Terascale: new forces, a new principle of nature called supersymmetry, or even extra dimensions of space.

Thus for particle physicists the Higgs boson is at the center of a much broader program of discovery, taking off from a long list of questions. Is there really a Higgs boson? If not, what are the mechanisms that give mass to particles and break the electroweak force? If there is a Higgs boson, does it differ from the hypothetical Higgs of the Standard Model? Is there more than one Higgs particle? What are the new phenomena that stabilize the Higgs boson at the Terascale? What properties of Higgs boson inform us about these new phenomena?

Another major opportunity for the ILC is to shed light on the dark side of the universe. Astrophysical data shows that dark matter dominates over visible matter, and that almost all of this dark matter cannot be composed of known particles. This data, combined with the concordance model of Big Bang cosmology, suggests that dark matter is comprised of new particles that interact weakly with ordinary matter and have Terascale masses. It is truly remarkable that astrophysics and cosmology, completely independently of the particle physics considerations reviewed above, point to new phenomena at the Terascale.

If Terascale dark matter exists, experiments at the ILC should be able to produce such particles in the laboratory and study their properties. Another list of questions will then beckon. Do these new particles really have the correct properties to be the dark matter? Do they account for all of the dark matter, or only part of it? What do their properties tell us about the evolution of the universe? How is dark matter connected to new principles or forces of nature?

A third cluster of scientific opportunities for the ILC focus on Einstein's vision of an ultimate unified theory. Particle physics data already suggests that three of the fundamental forces originated from a single "grand" unified force in the first instant of the Big Bang. Experiments at the ILC could test this idea and look for evidence of a related unified origin

of matter involving supersymmetry. A theoretical framework called string theory goes beyond grand unification to include gravity, extra spatial dimensions, and new fundamental entities called superstrings. Theoretical models to explain the properties of neutrinos, and account for the mysterious dominance of matter over antimatter, also posit unification at high energies. While the realm of unification is almost certainly beyond the direct reach of experiments, different unification models predict different patterns of new phenomena at Terascale energies. ILC experiments could distinguish among these patterns, effectively providing a telescopic view of ultimate unification. Combined with future data from astrophysics, this view should also give insights about our cosmic origins.

1.2 THE NEW LANDSCAPE OF PARTICLE PHYSICS

During the next few years, experiments at CERN's Large Hadron Collider will have the first direct look at Terascale physics. Like the discovery of an uncharted continent, this exploration of the Terascale will transform forever the geography of our universe. Equally compelling will be the interplay of LHC discoveries with other experiments and observations, including those that can probe the fundamental nature of dark matter, neutrinos and sources of matter–antimatter asymmetry. Some aspects of the new phenomena may fit well with existing speculative theoretical frameworks, suggesting a radical rewriting of the laws of nature. Other aspects may be initially ambiguous or mystifying, with data raising more questions than it answers. Particle physics should be entering a new era of intellectual ferment and revolutionary advance, unparalleled in the past half-century.

No one knows what will be found at the LHC, but the discovery potential of the LHC experiments is well studied [12, 13]. If there is a Higgs boson, it is almost certain to be found by the ATLAS and CMS experiments. Its mass should be measured with an accuracy between 0.1 and 1%, and at least one of its decay modes should be observed. If the Higgs particle decays into more than one type of particle, the LHC experiments should measure the ratio of the Higgs couplings to those different particles, with an accuracy between about 7 and 30%. If there is more than one type of Higgs boson, ATLAS and CMS will have a reasonably good chance of seeing both the lighter and heavier Higgs bosons. In favorable cases, these experiments will have some ability to discriminate the spin and CP properties of the Higgs particle.

Thus for LHC there are three possible outcomes with respect to the Higgs particle. The first is that a Higgs boson has been found, and at first look its properties seem consistent with the Standard Model. Then the compelling issue will be whether a more complete and precise experimental analysis reveals nonstandard properties. This will be especially compelling if other new phenomena, possibly related to the Higgs sector, have also been discovered. The second possible outcome is that a Higgs boson is found with gross features at variance with the Standard Model. This variation could be something as simple as a Higgs mass of 200 GeV or more, which would conflict with existing precision data without other new phenomena to compensate for it. The variation could also come from a large deviation in the predicted pattern of Higgs decay or the discovery of multiple Higgs particles. The third possible outcome is that no Higgs boson is discovered. In this case particle physicists will need either a radical rethink of the origin of mass, or new experimental tools to uncover a “hidden” or “invisible” Higgs boson.

For all of these possible outcomes, the ILC will be essential to move forward on our under-

INTRODUCTION

standing of the Higgs mechanism and of its relation to other new fundamental phenomena. This claim is documented in many detailed studies which are reviewed in this report.

LHC experiments have impressive capabilities to discover new heavy particles, especially particles which are strongly produced in proton-proton collisions, or particles seen as resonances in the production of pairs of fermions or gauge bosons. ATLAS and CMS could detect a new Z' gauge boson as heavy as 5 TeV [14], and the squarks and gluinos of supersymmetry even if they are as heavy as 2.5 TeV [12]. New particles associated with the existence of extra spatial dimensions could be seen, if their masses are less than a few TeV [12, 13].

The discovery of a Z' particle would indicate a new fundamental force of nature. LHC measurements may discriminate somewhat between possible origins of the new force, but this potential is limited to Z' particles lighter than 2.5 TeV in the most optimistic scenarios, and 1 TeV in others [14]. Through precision measurements of how the Z' interacts with other particles, the ILC could determine the properties of this new force, its origins, its relation to the other forces in a unified framework, and its role in the earliest moments of the Big Bang.

If supersymmetry is responsible for the existence of the Terascale and a light Higgs boson, then signals of superpartner particles should be seen at LHC. Since supersymmetry is an organizing principle of nature (like relativity), it can be realized in an infinite variety of ways. Thus a supersymmetry signal will raise two urgent issues. The first is whether the new heavy particles seen at LHC are actually superpartners, with the spins and couplings to other particles predicted by supersymmetry. Some results bearing on this may be available from LHC, but only ILC can provide an unequivocal answer. The second issue involves a set of fundamental questions: How does supersymmetry manifest itself in nature? What mechanism makes it appear as a “broken” symmetry? Is supersymmetry related to unification at a higher energy scale? How is supersymmetry related to the Higgs mechanism? What role did supersymmetry play in our cosmic origins? Definitive answers to these questions will require precise measurements of the entire roster of superpartner particles as well as the Higgs particles. To achieve this, physicists will need to extract the best possible results from the LHC and the ILC in a combined analysis [15], supplemented by signals or constraints from future B physics experiments and other precision measurements.

Supersymmetry is a good example to illustrate the possibility of an exciting interplay between different experiments and observations. Missing energy signatures at the LHC may indicate a weakly interacting massive particle consistent with the lightest neutralino of supersymmetry. At the same time, next generation direct or indirect dark matter searches may see a signal for weakly interacting exotic particles in our galactic halo. Are these particles neutralinos? If so, are neutralinos responsible for all of the dark matter, or only part of it? Does the model for supersymmetry preferred by collider data predict the observed abundance of dark matter, or do cosmologists need to change their assumptions about the early history of the universe? For all of these questions, detailed studies show the central importance of ILC measurements.

Other new physics models which might be observed at the next generation colliders could involve extra spatial dimensions or new strong forces. These are exciting possibilities that can also lead to confusion, calling for ILC to reveal their true nature. In some scenarios the new phenomena are effectively hidden from the LHC detectors, but are revealed as small deviations in couplings measured at the ILC. In favorable cases the LHC experiments could uncover strong evidence for the existence of extra dimensions. In this event the ILC will be essential to explore the size, shape, origins and impact of this expanded universe.

1.3 RUNNING SCENARIOS

The basic parameters needed for the planned physics program are detailed in Ref. [16] and confirmed by the machine design. The maximal center of mass energy is designed to be $\sqrt{s} = 500$ GeV, with a possible upgrade to 1 TeV, where physics runs must be possible for every energy above $\sqrt{s} = 200$ GeV and some luminosity for calibration runs is needed at $\sqrt{s} = 91$ GeV. For mass measurements threshold scans are required so that it must be possible to change the beam energy fast in small steps.

The total luminosity is required to be around 500 fb^{-1} within the first four years and about 1000 fb^{-1} during the first phase of operation. For the electron beam, polarization with a degree of larger than $\pm 80\%$ is mandatory. For the positron beam, a polarization of more than $\pm 50\%$ is useful [17] which should be relatively easy to achieve with the undulator positron source in the present ILC design. To reduce systematic uncertainties, the polarization direction has to be switchable on the train by train basis. Beam energy and polarization have to be stable and measurable at a level of about 0.1%.

Contrary to a hadron machine, an e^+e^- collider produces at a given time events at one fixed center of mass energy \sqrt{s} and, if polarization should be exploited in the analyses, fixed polarization. A physics study has to assume a certain value for the integrated luminosity and polarization mix which may be in conflict with other studies. To check whether this feature does not prevent the ILC from doing the many precision measurements claimed in the individual analyses, in a toy study a scenario with many new particles has been performed [18]. This study assumes supersymmetry with all sleptons, the lightest chargino and the lightest two neutralinos in the ILC energy range. In addition, the top quark and a light Higgs boson are visible. A first run is done at $\sqrt{s} = 500$ GeV to get a first measurement of the particle masses to optimize the threshold scans. The rest of the time is spent with these scans for precision measurements. Those analyses that do not require a given beam energy apart from being above production thresholds are done during the scans. This applies especially to the precision Higgs measurements. It has been shown that in such a scenario, a precision close to the one claimed in the isolated studies can be reached for all relevant observables.

A representative set of physics scenarios has been studied and in all cases it has been found that a $\sqrt{s} = 500$ GeV collider adds enough to our physics knowledge to justify the project. However, in all cases, an upgrade to $\sqrt{s} \sim 1$ TeV increases significantly the value of the ILC. In the following chapters, also the case for an upgrade to $\sqrt{s} = 1$ TeV after the first phase of ILC running will be presented.

In addition to the standard e^+e^- running at $\sqrt{s} > 200$ GeV, the ILC offers some options that can be realized with reasonable modifications if required by physics.

In the GigaZ mode, the ILC can run with high luminosity and both beams polarized on the Z -boson resonance, producing 10^9 hadronic Z decays in less than a year or at the W -boson pair production threshold to measure the W boson mass with high precision [19]. This requires only minor modifications to the machine.

With relatively few modifications, both arms can accelerate electrons resulting in an e^-e^- collider [20]. This mode can especially be useful to measure the selectron mass if it exists in the ILC energy range.

If the electrons are collided with a very intense laser beam about 1 mm in front of the interaction point, a high energy photon beam can be produced with a similar beam quality as the undisturbed electron beam. Converting only one or both beams this results in an $e\gamma$ or $\gamma\gamma$ collider [21, 22]. This mode requires a larger crossing angle than e^+e^- and the installation

of a large laser system [23]. The feasibility of such a laser system has not yet been proven.

In the following, it will be assumed that all options are technically possible and they will be implemented when they are required by the ILC and LHC data.

To exploit fully the physics program of ILC will take a long time of possibly around 20 to 30 years. Possible options will certainly be realized only towards the end of the program.

1.4 PHYSICS AND THE DETECTORS

Detectors at the ILC face a very different set of challenges compared to the current state-of-the-art employed for LEP/SLD and hadron colliders [24]. While ILC detectors will enjoy lower rates, less background and lower radiation doses than those at the LHC, the ILC will be pursuing physics that places challenging demands on precision measurements and particle tracking and identification. The reasons for this can be illustrated by several important physics processes, namely measuring the properties of a Higgs boson, identifying strong electroweak symmetry breaking, identifying supersymmetric (SUSY) particles and their properties, and precision electroweak studies. These are just a few examples taken from benchmark studies for ILC detectors [25].

The Higgs boson(s) of the Standard Model (SM), minimal supersymmetric extension of the SM (MSSM), or extended models will require precision measurements of their mass and couplings in order to identify the theory [26]. The golden measurement channel of Higgs production is $e^+e^- \rightarrow ZH \rightarrow \ell^+\ell^-X$, with the Higgs mass measured by its recoil from the Z boson. The mass must be measured to a precision sufficient to cleanly separate the resonance from backgrounds – a precision of approximately 50 MeV is usually sufficient. This will require a resolution $\delta(1/p)$ better than $7 \times 10^{-5} \text{ GeV}^{-1}$ for a low mass Higgs boson, and that requires tracking performance an order of magnitude better than that achieved by LEP/SLD detectors. The need for this performance is illustrated in Figure 1.1, which shows the impact of tracker resolution on the significance of signal compared to expected backgrounds. The Higgs mass measurement also requires precise knowledge of the center of mass energy, and this requires precision measurement of the luminosity-weighted energy spectrum in order to measure the beamstrahlung energy loss (more information on this subject can be found in the top quark chapter).

Because of the important role played by heavy t, b, c quarks and the tau lepton in the SM and essentially all new physics models, the ILC detectors will require excellent vertex detection in a challenging high rate environment of low energy e^+e^- pairs. An even stronger requirement on the vertex detector is imposed by the desire to measure vertex charge with good efficiency. This is useful for reducing large combinatoric jet backgrounds and to distinguish b from \bar{b} for measurement of forward-backward asymmetries, which are very sensitive to new physics, or for establishing CP violation. To make the requisite improvements over the LEP/SLD detectors, the impact parameters will have to be measured to $(5 \oplus 10/p) \mu\text{m}$ (momentum p in GeV), and this will require putting finely-segmented ($20 \times 20 \mu\text{m}^2$) silicon arrays within 1.5 cm of the beamline. Figure 1.2 (left) shows the purity/efficiency obtained with a 5-layer vertex detector with inner radius 1.5cm, ladder thickness 0.1% X_0 and resolution $3.5 \mu\text{m}$; this study uses a “fast” version of the simulation program.

Excellent resolution on jet energy, which is essential for the unambiguous identification of many decay channels, enhances the impact of precision measurements, and lowers the integrated luminosity needed for many measurements. Figure 1.2 (right) demonstrates the

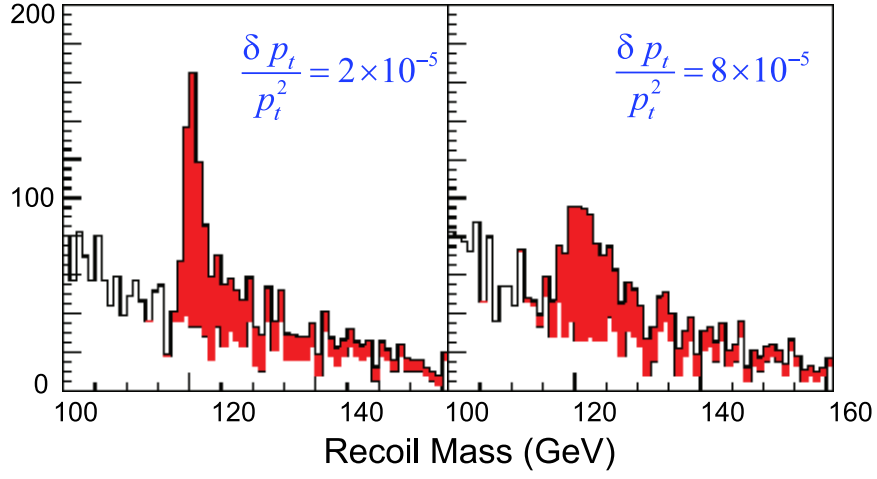


FIGURE 1.1. Histogram of mass recoiling from dimuons at $\sqrt{s} = 500$ GeV for a Higgs boson mass of 120 GeV, for two values of the tracking resolution; from Ref. [27].

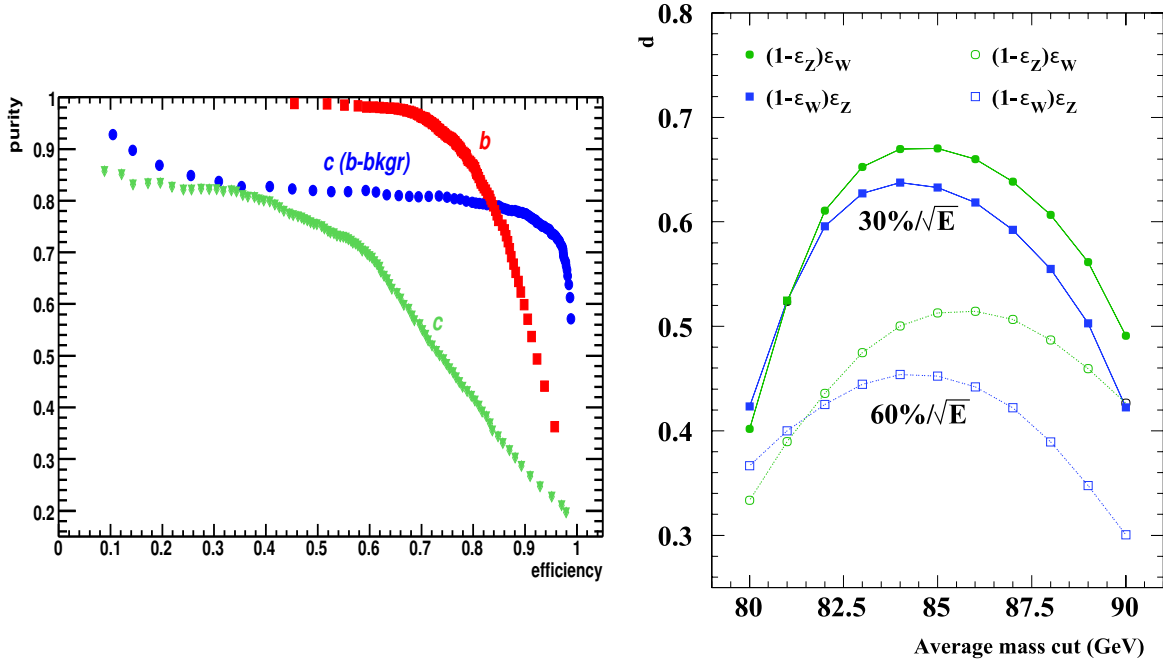


FIGURE 1.2. Left: purity v.s. efficiency for tagging of b and c jets in a simulated VTX detector described in the text; the points labeled “ c (b bkg)” indicate the case where only b -quark backgrounds are present in the c -study; from Ref. [28]. Right: purity factor d (for “dilution”) for the process $e^+e^- \rightarrow \nu\bar{\nu}WW/e^+e^-ZZ$ as a function of invariant mass cut for two values of the energy resolution; from Ref. [29].

luminosity dependence on jet energy resolution. Distinguishing WW from ZZ production at ILC energies is challenging, but essential for matching branching fractions to a model, such as identifying strong electroweak symmetry breaking or supersymmetric parameters. The low ILC backgrounds permit association of tracks and calorimeter clusters, making possible unprecedented jet energy measurement. However, to achieve WW/ZZ separation the

INTRODUCTION

detectors must measure jet energy about a factor of two better than the best achieved so far. The jet energy resolution must be roughly 5 GeV , corresponding to an energy resolution of $30\%/\sqrt{E_{\text{jet}}}$ for the $100\text{--}150 \text{ GeV}$ jets common at higher center of mass energies. Depending on the quark content, jets of these energies deposit roughly 65% of the visible energy in the form of charged particles, 25% in the form of photons, and 10% as neutral hadrons. In the relatively clean environment of ILC, the required energy resolution translates into a factor 2 improvement in hadron calorimeter performance over those currently operating. To meet such a goal, the method of "particle flow" association of tracks and calorimeter clusters must be validated. Figure 1.3 shows the "particle flow" for a jet in an ILC detector.

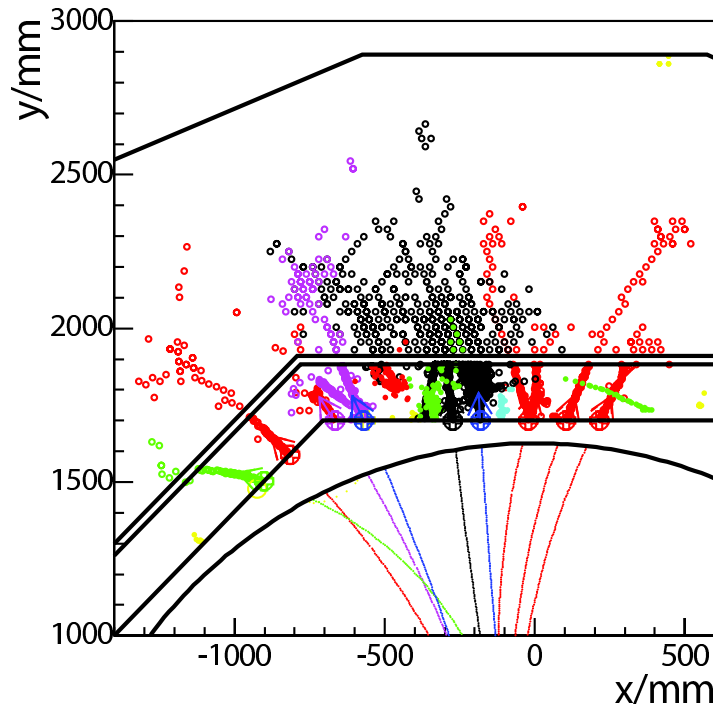


FIGURE 1.3. Simulation of a 100 GeV jet using the MOKKA simulation of the TESLA TDR detector; colors show tracks-cluster associations using PandoraPFA; from Ref. [30].

If low energy supersymmetry is indeed realized, one of the more important tasks for the ILC will be to identify SUSY particle spectra and decay chains, and to establish if SUSY particles could be some or all of the dark matter. Since the lightest SUSY particle will not be observable, the detectors must be extremely hermetic, particularly at extreme polar angles. To achieve these goals the effect of beam crossing angle, beamstrahlung and machine backgrounds must be well understood, and development of instrumentation is necessary to measure the luminosity spectrum and beam polarization.

CHAPTER 2

Higgs physics

The search and the study of Higgs bosons is one of the main missions of present and future high-energy colliders. The observation of these particles is of major importance for the present understanding of the interactions of the fundamental particles and the generation of their masses. In the Standard Model (SM), the existence of one isodoublet scalar field is required, the neutral component of which acquires a non-zero vacuum expectation value leading to the spontaneous breaking of the electroweak symmetry and the generation of the gauge boson and fermion masses. In this picture, one degree of freedom among the four degrees of freedom of the original isodoublet field is left over, corresponding to a physical scalar particle, the Higgs boson [31]. The discovery of this new type of matter particle is considered as being of profound importance. In fact, despite of its numerous successes in explaining the present data, the SM is not complete before this particle is experimentally observed and its fundamental properties studied in detail. Furthermore, even if we understand that the Higgs field is the source of particle masses, the origin of electroweak symmetry breaking itself needs to be explained and its dynamics to be clarified. Very little is known about this symmetry breaking and important questions include: does the dynamics involve new strong interactions and/or sizable CP violation, and, if elementary Higgs particles indeed exist in nature, how many fields are there and in which gauge representations do they appear. Theoretical realizations span a wide range of scenarios extending from weak to strong breaking mechanisms. Examples, on one side, are models involving light fundamental Higgs fields, such as the SM and its supersymmetric extensions which include two-Higgs doublets in the minimal version and additional singlet fields or higher representations in extended versions; on the other side, there are new strong interaction and extra-dimensional models without a fundamental Higgs field. Furthermore, the electroweak symmetry breaking mechanism might be related to other fundamental questions of particle physics and cosmology. For instance, the Higgs sector could play an important role in the annihilation of the new particles that are responsible of the cosmological dark matter and might shed light on how the baryon-antibaryon asymmetry proceeded in the early universe. It might also explain how and why the three generations of quarks and leptons are different.

Only detailed investigation of the properties of the Higgs particles will answer these questions. The ILC is a unique tool in this context and it could play an extremely important role: high-precision measurements would allow to determine with a high level of confidence the profile of the Higgs bosons and their fundamental properties and would provide a unique opportunity to establish experimentally the mechanism that generates the particle masses.

2.1 THE HIGGS SECTOR OF THE SM AND BEYOND

2.1.1 The Higgs boson in the SM

The Standard Model makes use of one isodoublet complex scalar field and, after spontaneous electroweak symmetry breaking (EWSB), three would-be Goldstone bosons among the four degrees of freedom are absorbed to build up the longitudinal components of the W^\pm, Z gauge bosons and generate their masses; the fermion masses are generated through a Yukawa interaction with the same scalar field. The remaining degree of freedom corresponds to the unique Higgs particle of the model with the $J^{PC} = 0^{++}$ assignment of spin, parity and charge conjugation quantum numbers [31, 32, 33]. Since the Higgs couplings to fermions and gauge bosons are related to the masses of these particles and the only free parameter of the model is the mass of the Higgs boson itself; there are, however, both experimental and theoretical constraints on this fundamental parameter, as will be summarized below.

The only available direct information on the Higgs mass is the lower limit $M_H \gtrsim 114.4$ GeV at 95% confidence level established at LEP2 [34]. The collaborations have also reported a small, $\lesssim 2\sigma$, excess of events beyond the expected SM backgrounds consistent with a SM-like Higgs boson with a mass $M_H \sim 115$ GeV [34]. This mass range can be tested soon at the Tevatron if high enough luminosity is collected. Furthermore, the high accuracy of the electroweak data measured at LEP, SLC and Tevatron [35] provides an indirect sensitivity to M_H : the Higgs boson contributes logarithmically, $\propto \log(M_H/M_W)$, to the radiative corrections to the W/Z boson propagators. A recent analysis, which uses the updated value of the top quark mass yields the value $M_H = 76^{+33}_{-24}$ GeV, corresponding to a 95% confidence level upper limit of $M_H \lesssim 144$ GeV [36]. The left-hand side of Fig. 2.1 shows the global fit to the electroweak data; the Higgs fit has a probability of 15.1%. If the Higgs boson turns out to be significantly heavier than 150 GeV, there should be an additional new ingredient that is relevant at the EWSB scale which should be observed at the next round of experiments.

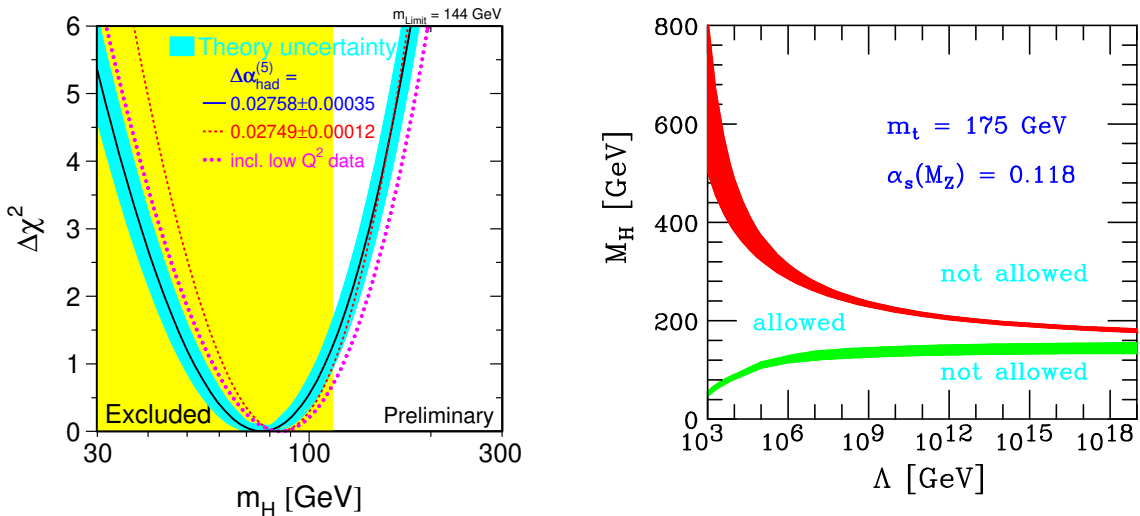


FIGURE 2.1. Left: Global fit to the electroweak precision data within the SM; the excluded region from direct Higgs searches is also shown [36]. Right: theoretical upper and lower bounds on M_H from the assumption that the SM is valid up to the cut-off scale Λ [37].

From the theoretical side, interesting constraints can be derived from assumptions on the energy range within which the SM is valid before perturbation theory breaks down and new phenomena would emerge. For instance, if the Higgs mass were larger than ~ 1 TeV, the W and Z bosons would interact very strongly with each other to ensure unitarity in their scattering at high energies. Imposing the unitarity requirement in the high-energy scattering of gauge bosons leads to the bound $M_H \lesssim 700$ GeV [38]. If the Higgs boson were too heavy, unitarity would be violated in these processes at energies above $\sqrt{s} \gtrsim 1.2$ TeV and new phenomena should appear to restore it.

Another important theoretical constraint comes from the fact that the quartic Higgs self-coupling, which at the scale M_H is fixed by M_H itself, grows logarithmically with the energy scale. If M_H is small, the energy cut-off Λ at which the coupling grows beyond any bound and new phenomena should occur, is large; if M_H is large, the cut-off Λ is small. The condition $M_H \lesssim \Lambda$ sets an upper limit on the Higgs mass in the SM, the triviality bound. A naive one-loop analysis assuming the validity of perturbation theory as well as lattice simulations lead to an estimate of $M_H \lesssim 630$ GeV for this limit [39]. Furthermore, loops involving top quarks tend to drive the coupling to negative values for which the vacuum is no longer stable.

Requiring the SM to be extended to, for instance, the GUT scale $\Lambda_{\text{GUT}} \sim 10^{16}$ GeV and including the effect of top quark loops on the running coupling, the Higgs boson mass should lie in the range $130 \text{ GeV} \lesssim M_H \lesssim 180 \text{ GeV}$ [37]; see the right-hand side of Fig. 2.1.

In fact in any model beyond the SM in which the theory is required to be weakly interacting up to the GUT or Planck scales the Higgs boson should be lighter than $M_H \lesssim 200$ GeV. Such a Higgs particle can be produced at the ILC already for center of mass energies of $\sqrt{s} \sim 300$ GeV. However, to cover the entire Higgs mass range in the SM, $M_H \lesssim 700$ GeV, c.m. energies close to $\sqrt{s} = 1$ TeV would be required.

2.1.2 The Higgs particles in the MSSM

It is well known that there are at least two severe problems in the SM, in particular when trying to extend its validity to the GUT scale Λ_{GUT} . The first one is the so-called naturalness problem: the Higgs boson tends to acquire a mass of the order of these large scales [the radiative corrections to M_H are quadratically divergent]; the second problem is that the running of the three gauge couplings of the SM is such that they do not meet at a single point and thus do not unify at the GUT scale. Low energy supersymmetry solves these two problems at once: supersymmetric particle loops cancel exactly the quadratic divergences and contribute to the running of the gauge couplings to allow their unification at Λ_{GUT} .

The minimal supersymmetric extension of the SM (MSSM), which will be discussed in chapter 5, requires the existence of two isodoublet Higgs fields to cancel anomalies and to give mass separately to up and down-type fermions. Two CP-even neutral Higgs bosons h, H , a pseudoscalar A boson and a pair of charged scalar particles, H^\pm , are introduced by this extension of the Higgs sector [32, 40]. Besides the four masses, two additional parameters define the properties of these particles: a mixing angle α in the neutral CP-even sector and the ratio of the two vacuum expectation values $\tan \beta$, which lies in the range $1 \lesssim \tan \beta \lesssim m_t/m_b$.

Supersymmetry leads to several relations among these parameters and only two of them, taken in general to be M_A and $\tan \beta$, are in fact independent. These relations impose a strong hierarchical structure on the mass spectrum, $M_h < M_Z, M_A < M_H$ and $M_W < M_{H^\pm}$, which however is broken by radiative corrections as the top quark mass is large; see Ref. [41] for a recent review. The leading part of this correction grows as the fourth power of m_t and

logarithmically with the SUSY scale or common squark mass M_S ; the mixing (or trilinear coupling) in the stop sector A_t plays an important role. For instance, the upper bound on the mass of the lightest Higgs boson h is shifted from the tree level value M_Z to $M_h \sim 130\text{--}140$ GeV in the maximal mixing scenario where $X_t = A_t - \mu/\tan\beta \sim 2M_S$ with $M_S = \mathcal{O}(1\text{ TeV})$ [41]; see the left-handed side of Fig. 2.2. The masses of the heavy neutral and charged Higgs particles are expected to range from M_Z to the SUSY breaking scale M_S .

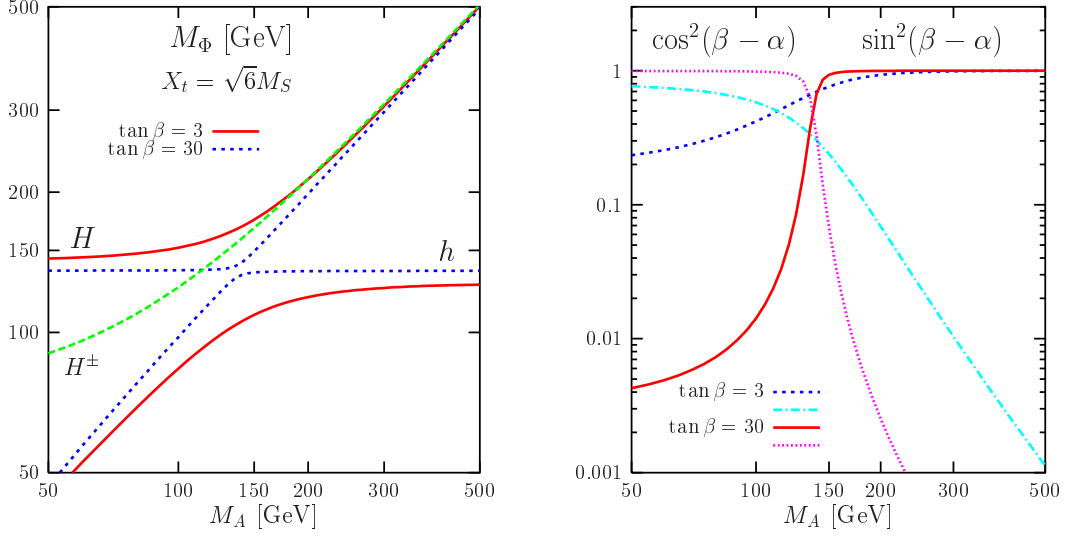


FIGURE 2.2. The masses (left) and the couplings to gauge bosons (right) of the MSSM Higgs bosons as a function of M_A for $\tan\beta = 3, 30$ with $M_S = 2\text{ TeV}$ and $X_t = \sqrt{6}M_S$.

The pseudoscalar Higgs boson A has no tree level couplings to gauge bosons, and its couplings to down (up) type fermions are (inversely) proportional to $\tan\beta$. This is also the case for the couplings of the charged Higgs boson to fermions, which are admixtures of scalar and pseudoscalar currents and depend only on $\tan\beta$. For the CP-even Higgs bosons h and H , the couplings to down (up) type fermions are enhanced (suppressed) compared to the SM Higgs couplings for $\tan\beta > 1$. They share the SM Higgs couplings to vector bosons as they are suppressed by \sin and $\cos(\beta - \alpha)$ factors, respectively for h and H ; see the right-hand side of Fig. 2.2 where the couplings to the W^\pm, Z bosons are displayed.

If the pseudoscalar mass is large, the h boson mass reaches its upper limit [which, depending on the value of $\tan\beta$ and stop mixing, is in the range 100–140 GeV] and its couplings to fermions and gauge bosons are SM-like; the heavier CP-even H and charged H^\pm bosons become degenerate with the pseudoscalar A boson and have couplings to fermions and gauge bosons of the same intensity. In this decoupling limit, which can be already reached for pseudoscalar masses $M_A \gtrsim 300$ GeV, it is very difficult to distinguish the Higgs sectors of the SM and MSSM if only the lighter h particle has been observed.

Finally, we note that there are experimental constraints on the MSSM Higgs masses, which mainly come from the negative LEP2 searches [42]. In the decoupling limit where the h boson is SM-like, the limit $M_h \gtrsim 114$ GeV from the Higgs-strahlung process holds; this constraint rules out $\tan\beta$ values smaller than $\tan\beta \sim 3$. Combining all processes, one obtains the absolute mass limits $M_h \sim M_A \gtrsim M_Z$ and $M_{H^\pm} \gtrsim M_W$ [42].

2.1.3 Higgs bosons in non-minimal SUSY models

The Higgs sector in SUSY models can be more complicated than previously discussed if some basic assumptions of the MSSM, such as the absence of new sources of CP violation, the presence of only two Higgs doublet fields, or R-parity conservation, are relaxed; see chapter 5 for a discussion. A few examples are listed below.

In the presence of CP-violation in the SUSY sector, which is required if baryogenesis is to be explained at the electroweak scale, the new phases will enter the MSSM Higgs sector [which is CP-conserving at tree-level] through the large radiative corrections. The masses and the couplings of the neutral and charged Higgs particles will be altered and, in particular, the three neutral Higgs bosons will not have definite CP quantum numbers and will mix with each other to produce the physical states H_1, H_2, H_3 . The properties of the various Higgs particles can be significantly affected; for reviews, see e.g. Refs. [43, 44]. Note, however, that there is a sum rule which forces the three H_i bosons to share the coupling of the SM Higgs to gauge bosons, $\sum_i g_{H_i VV}^2 = g_{H_{\text{SM}}}^2$, but only the CP-even component is projected out.

As examples of new features compared to the usual MSSM, we simply mention the possibility of a relatively light H_1 state with very weak couplings to the gauge bosons which could have escaped detection at LEP2 [45] and the possibility of resonant H/A mixing when the two Higgs particles are degenerate in mass [46]; an example of the Higgs mass spectrum is shown in Fig. 2.3 (left) as a function of the phase of the coupling A_t . These features have to be proven to be a result of CP-violation by, for instance, studying CP-odd observables.

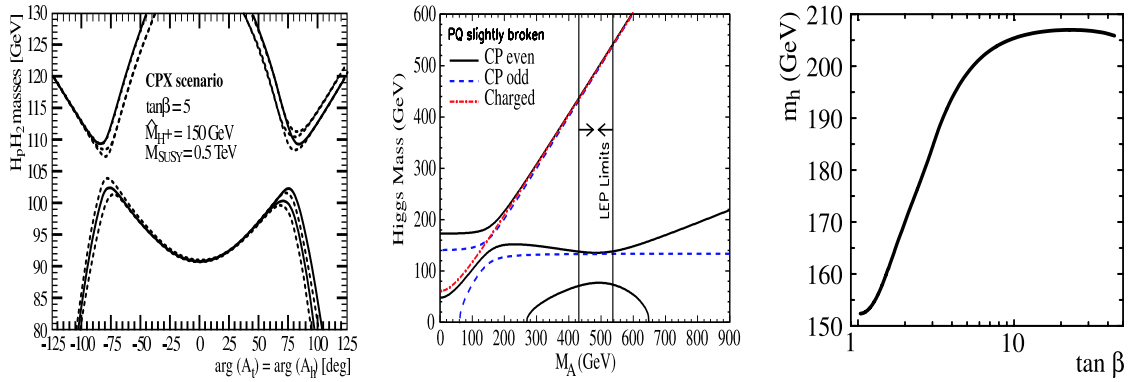


FIGURE 2.3. The spectrum of neutral Higgs particles in a CP-violating MSSM scenario (for $\tan\beta = 5$, $M_{H^\pm} = 150$ GeV and $M_S = 0.5$ TeV) [44] (left) typical Higgs mass spectrum in the NMSSM as a function of M_A [47] (center) and the upper bound on the lighter Higgs mass in a general SUSY model [48].

The next-to-minimal SUSY extension, the NMSSM, consists of simply introducing a complex iso-scalar field which naturally generates a weak scale Higgs-higgsino parameter μ (thus solving the μ problem); the model is more natural than the MSSM and has less fine-tuning [47, 49, 50]. The NMSSM Higgs sector is thus extended to include an additional CP-even and a CP-odd Higgs particle and an example of a Higgs mass spectrum is shown in Fig. 2.3 (center). The upper bound on the mass of the lighter CP-even particle slightly exceeds that of the MSSM h boson and the negative searches at LEP2 lead to looser constraints.

In a large area of the parameter space, the Higgs sector of the NMSSM reduces to the one of the MSSM but there is a possibility, which is not completely excluded, that one of the

neutral Higgs particles, in general the lightest pseudoscalar A_1 , is very light with a mass of a few ten's of GeV. The light CP-even Higgs boson, which is SM-like in general, could then decay into pairs of A_1 bosons, $H_1 \rightarrow A_1 A_1 \rightarrow 4b, 4\tau$, with a large branching fraction.

Higgs bosons in GUT theories. A large variety of theories, string theories, grand unified theories, left-right symmetric models, etc., suggest an additional gauge symmetry which may be broken only at the TeV scale; see chapter 6. This leads to an extended particle spectrum and, in particular, to additional Higgs fields beyond the minimal set of the MSSM. Especially common are new $U(1)'$ symmetries broken by the vev of a singlet field (as in the NMSSM) which leads to the presence of a Z' boson and one additional CP-even Higgs particle compared to the MSSM; this is the case, for instance, in the exceptional MSSM [51] based on the string inspired E_6 symmetry. The secluded $SU(2) \times U(1) \times U(1)'$ model [52], in turn, includes four additional singlets that are charged under $U(1)'$, leading to 6 CP-even and 4 CP-odd neutral Higgs states. Other exotic Higgs sectors in SUSY models [53] are, for instance, Higgs representations that transform as $SU(2)$ triplets or bi-doublets under the $SU(2)_L$ and $SU(2)_R$ groups in left-right symmetric models, that are motivated by the seesaw approach to explain the small neutrino masses and which lead e.g. to a doubly charged Higgs boson H^{--} . These extensions, which also predict extra matter fields, would lead to a very interesting phenomenology and new collider signatures in the Higgs sector.

In a general SUSY model, with an arbitrary number of singlet and doublet scalar fields [as well as a matter content which allows for the unification of the gauge couplings], a linear combination of Higgs fields has to generate the W/Z masses and thus, from the triviality argument discussed earlier, a Higgs particle should have a mass below 200 GeV and significant couplings to gauge bosons [48]. The upper bound on the mass of the lightest Higgs boson in this most general SUSY model is displayed in Fig. 2.3 (right) as a function of $\tan\beta$.

R-parity violating models. Models in which R-parity is spontaneously broken [and where one needs to either enlarge the SM symmetry or the spectrum to include additional gauge singlets], allow for an explanation of the light neutrino data [54]. Since R_p entails the breaking of the total lepton number L , one of the CP-odd scalars, the Majoron J , remains massless being the Goldstone boson associated to L . In these models, the neutral Higgs particles have also reduced couplings to the gauge bosons. More importantly, the CP-even Higgs particles can decay into pairs of invisible Majorons, $H_i \rightarrow JJ$, while the CP-odd particle can decay into a CP-even Higgs and a Majoron, $A_i \rightarrow H_i J$, and three Majorons, $A \rightarrow JJJ$ [54].

2.1.4 Higgs bosons in alternative models

There are also many non supersymmetric extensions of the SM which might lead to a different Higgs phenomenology. In some cases, the Higgs sector would consist of one scalar doublet leading to a Higgs boson which would mimic the SM Higgs, but the new particles that are present in the models might alter some of its properties. In other cases, the Higgs sector is extended to contain additional scalar fields leading to the presence of new Higgs particles. Another possibility is a scenario with a composite and strongly interacting Higgs, or where no Higgs particle is present at all, leading to strong interactions of the W/Z bosons. Many of these models, such as e.g. extra-dimensional, little Higgs and Higgsless models, will be discussed in chapter 6. Here will simply give a non exhaustive list of various possible scenarios.

Scenarios with Higgs mixing. In warped extra-dimensional models [55] the fluctuations of the size of the extra dimension about its stabilized value manifest themselves as a single scalar field, the radion. In the Randall Sundrum model with a bulk scalar field, it is expected

that the radion is the lightest state beyond the SM fields with a mass probably in the range between $\mathcal{O}(10 \text{ GeV})$ and $\Lambda = \mathcal{O}(\text{TeV})$ [56, 57]. The couplings of the radion are order of $1/\Lambda$ and are very similar to the couplings of the SM Higgs boson, except for one important difference: due to the trace anomaly, the radion directly couples to massless gauge bosons at one loop. Moreover, in the low energy four-dimensional effective theory, the radion can mix with the Higgs boson. This mixing can lead to important shifts in the Higgs couplings which become apparent in the Higgs decay widths and production cross sections. In large extra dimension models [58], mixing of the Higgs boson with graviscalars also occurs [59], leading to an invisible decay width. Mixing effects also occur if the SM is minimally extended in a renormalizable way to contain a singlet scalar field S that does not couple to the other SM particles; its main effect would be to alter the scalar potential and to mix with the SM Higgs field [60] and, in such a case, the Higgs could mainly decay into two invisible S particles.

Scenarios with an extended Higgs/gauge/matter sector. Non-supersymmetric extensions of the Higgs sector with additional singlet, doublet and higher representation fields have also been advocated [53]. Examples are the minimal SM extension with a singlet discussed above, two-Higgs doublet models which potentially include CP-violation, triplet Higgs fields in models for light neutrino mass generation, etc... These extensions lead to a rich spectrum of Higgs particles which could be produced at the ILC. In other extensions of the SM, new gauge bosons and new matter particles are predicted and they can affect the properties of the SM-like Higgs boson. For instance the new fermions present in little Higgs and extra-dimensional models might contribute to the loop induced Higgs couplings, while new heavy gauge bosons could alter the Higgs couplings to W and Z bosons for instance.

Scenarios with a composite Higgs boson. In little Higgs models [61], the dynamical scale is around $\Lambda = 10 \text{ TeV}$, unlike the traditional Technicolor model [62, 63]. A light Higgs boson can be generated as a pseudo Goldstone boson and its mass of order 100 GeV is protected against large radiative corrections individually in the boson and the fermion sectors. The models predict a rich spectrum of new particles not only at the scale Λ but also at lower scales. Axion-type pseudoscalar bosons may be associated with the spontaneous breaking of $U(1)$ factors in the extra global symmetries [64]. These particles have properties analogous to Higgs bosons and can be produced in e^+e^- collisions; deviations in the production and decay rates of the SM-like Higgs boson can also be induced by these particles. Note that, recently, a model-independent description of a strongly interacting light Higgs has been given [65].

Higgsless models and strong W/Z interactions. The problem of unitarity violation at high energies in the SM can also be solved, apart from introducing a relatively light Higgs boson, by assuming the W/Z bosons to become strongly interacting at TeV energies, thus damping the rise of the elastic W/Z scattering amplitudes. Naturally, the strong forces between the massive gauge bosons may be traced back to new fundamental interactions characterized by a scale of order 1 TeV [62]. Also in theories with extra space dimensions, the electroweak symmetries can be broken without introducing additional fundamental scalar fields, leading also to Higgsless theories [66]. Such scenarios can be studied in massive gauge boson scattering experiments, where the W/Z bosons are radiated, as quasi-real particles, off electrons and positrons in TeV linear colliders [7]. This aspect will be discussed in chapter 6.

2.1.5 The expectations at the LHC

The search for the Higgs boson(s) is the one of the primary tasks of the CMS and ATLAS experiments at the LHC. For the SM Higgs boson, detailed studies have been performed

[12, 13] with the conclusion that a 5σ discovery is possible with an integrated luminosity of 30 fb^{-1} for the entire Higgs mass range. Several production and decay channels can be used for this purpose; see Fig. 2.4 (left). The spin-zero nature of the Higgs boson can be determined and a preliminary probe of its CP nature can be performed. Furthermore, information on the Higgs couplings to gauge bosons and fermions can be obtained with a higher luminosity; the estimated precision for coupling ratios are typically $\mathcal{O}(10)\%$ with $\mathcal{L} = 100 \text{ fb}^{-1}$ [67]. Because of the small production rates and large backgrounds, the determination of the Higgs self-coupling is too difficult and will require a significantly higher luminosity.

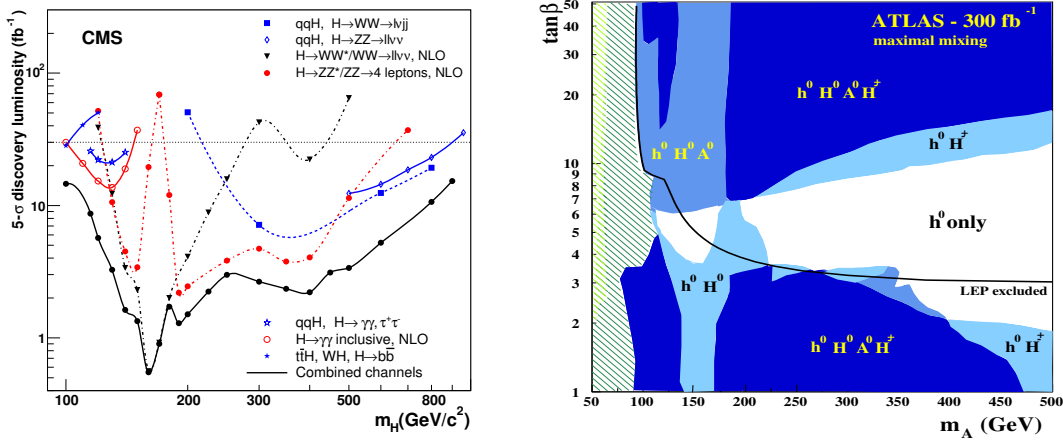


FIGURE 2.4. The required luminosity that is needed to achieve a 5σ discovery signal at LHC using various detection channels as a function of M_H [13] (left) and the number of Higgs particles that can be detected in the MSSM $[\tan\beta, M_A]$ parameter space [12] (right).

In the MSSM, all the Higgs bosons can be produced for masses below 1 TeV and large enough $\tan\beta$ values if a large integrated luminosity, $\sim 300 \text{ fb}^{-1}$, is collected; Fig. 2.4 (right). There is, however, a significant region of the parameter space where only the light SM-like h boson will be found. In such a case the mass of the h boson may be the only characteristic information of the MSSM Higgs sector at the LHC. Nevertheless, there are some situations in which MSSM Higgs searches at the LHC could be slightly more complicated. This is for instance the case when Higgs decays into SUSY particles such as charginos and (invisible) neutralinos are kinematically accessible and significant. Furthermore, in the so-called intense coupling regime where the three neutral Higgs particles are very close in mass and have strong couplings to b -quarks, not all three states can be resolved experimentally [68].

The search of the Higgs particles can be more complicated in some extensions of the MSSM. For instance, if CP-violation occurs, the lighter neutral H_1 boson can escape observation in a small region of the parameter space with low M_A and $\tan\beta$ values, while the heavier H, A and H^\pm bosons can be accessed in smaller areas than in the usual MSSM [43]. In the NMSSM with a relatively light pseudoscalar A_1 particle, the dominant decay of the lighter CP-even H_1 boson could be $H_1 \rightarrow A_1 A_1 \rightarrow 4b$, a signature which is extremely difficult to detect at the LHC [49]. A possibility that should not be overlooked is that in several extensions of the Higgs sector, such as non-minimal SUSY, extra-dimensional models and the extension with a singlet scalar field, the Higgs boson might decay invisibly making

its detection at the LHC very challenging if possible at all. In addition, in some other SM extensions, the rates for the dominant $gg \rightarrow H$ production can be strongly suppressed.

2.2 THE HIGGS BOSON IN THE STANDARD MODEL

2.2.1 Higgs decays and production

In the SM, the profile of the Higgs particle is uniquely determined once its mass M_H is fixed [32, 33]. The decay width, the branching ratios and the production cross sections are given by the strength of the Yukawa couplings to fermions and gauge bosons, the scale of which is set by the masses of these particles. The trilinear and quartic Higgs self couplings are also uniquely fixed in terms of the Higgs boson mass.

In the “low Higgs mass” range, $M_H \lesssim 140$ GeV, the Higgs boson decays into a large variety of channels. The main decay mode is by far the decay into $b\bar{b}$ pairs with a branching ratio of $\mathcal{O}(80\%)$ followed by the decays into $c\bar{c}$ and $\tau^+\tau^-$ pairs with fractions of $\mathcal{O}(5\%)$. Also of significance, the top-loop mediated Higgs decay into gluons which for M_H around 120 GeV occurs at the level of $\sim 5\%$. The top and W -loop mediated $\gamma\gamma$ and $Z\gamma$ decay modes are very rare the branching fractions being of $\mathcal{O}(10^{-3})$. However, these decays are, together with $H \rightarrow gg$, theoretically interesting being sensitive to new heavy states such as SUSY particles.

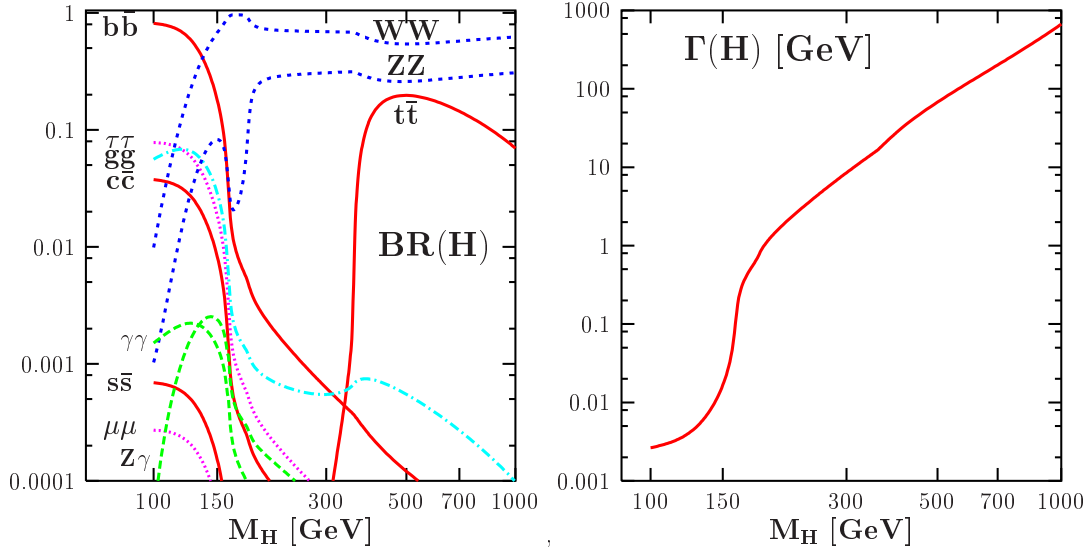


FIGURE 2.5. The decay branching ratios (left) and the total decay width (right) of the SM Higgs boson as a function of its mass M_H ; from Refs. [69, 70].

In the “high Higgs mass” range, $M_H \gtrsim 140$ GeV, the Higgs bosons decay mostly into $WW^{(*)}$ and $ZZ^{(*)}$ pairs, with one of the gauge bosons being virtual if below the WW threshold. Above the ZZ threshold, the Higgs boson decays almost exclusively into these channels with a branching ratio of $\frac{2}{3}$ for $H \rightarrow WW$ and $\frac{1}{3}$ for $H \rightarrow ZZ$ decays. The opening of the $t\bar{t}$ channel for $M_H \gtrsim 350$ GeV does not alter this pattern significantly as $\text{BR}(H \rightarrow t\bar{t})$ does not exceed the level of 10–15% when kinematically accessible.

In the low mass range, the Higgs boson is very narrow $\Gamma_H < 10$ MeV, but the width becomes rapidly wider for masses larger than 140 GeV, reaching $\Gamma_H \sim 1$ GeV at the ZZ

threshold. For large masses, $M_H \gtrsim 500$ GeV, the Higgs becomes obese since its total width is comparable to its mass, and it is hard to consider it as a resonance.

In e^+e^- collisions, the main production mechanisms for the SM Higgs particles are, Fig. 2.6a, the Higgs-strahlung [38, 71] and the WW fusion [72] processes

$$e^+e^- \rightarrow ZH \rightarrow f\bar{f}H \quad \text{and} \quad e^+e^- \rightarrow \bar{\nu}_e\nu_e H \quad (\text{i})$$

The final state $H\nu\bar{\nu}$ is generated in both the fusion and Higgs-strahlung processes. Besides the ZZ fusion mechanism [72] $e^+e^- \rightarrow e^+e^-H$ which is similar to WW fusion but with an order of magnitude smaller cross section, sub-leading Higgs production channels, Fig. 2.6b, are associated production with top quarks $e^+e^- \rightarrow t\bar{t}H$ [73] and double Higgs production [74, 75] in the Higgs-strahlung $e^+e^- \rightarrow ZHH$ and fusion $e^+e^- \rightarrow \bar{\nu}_e\nu_e HH$ processes. Despite the smaller production rates, the latter mechanisms are very useful when it comes to the study of the Higgs fundamental properties. The production rates for all these processes are shown in Fig. 2.7 at energies $\sqrt{s} = 500$ GeV and $\sqrt{s} = 1$ TeV as a function of M_H . Other sub-leading processes such as associated production with a photon $e^+e^- \rightarrow H\gamma$ and loop induced pair production $e^+e^- \rightarrow HH$ have even smaller rates and will not be discussed here.

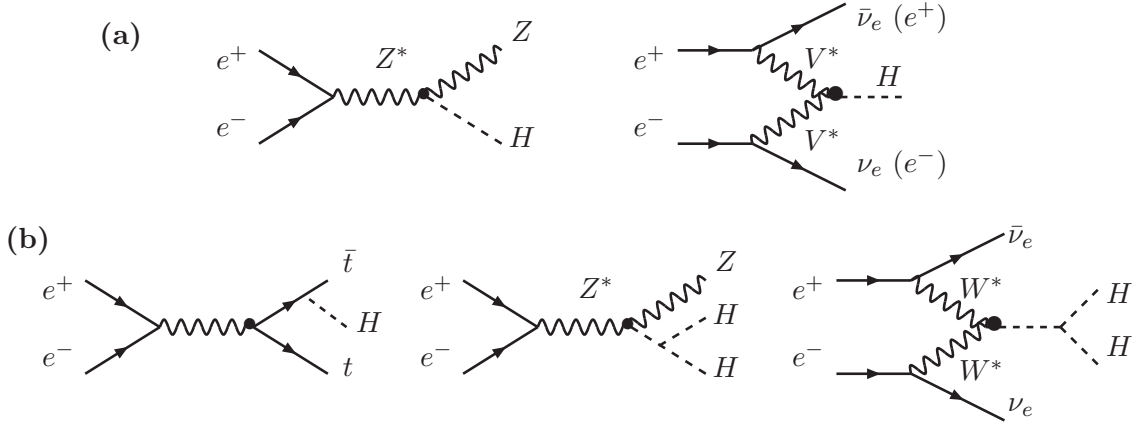


FIGURE 2.6. Diagrams for the dominant (a) and subleading (b) Higgs production mechanisms at ILC.

The cross section for Higgs-strahlung scales as $1/s$ and therefore dominates at low energies, while the one of the WW fusion mechanism rises like $\log(s/M_H^2)$ and becomes more important at high energies. At $\sqrt{s} \sim 500$ GeV, the two processes have approximately the same cross sections, $\mathcal{O}(50 \text{ fb})$ for the interesting Higgs mass range $115 \text{ GeV} \lesssim M_H \lesssim 200 \text{ GeV}$ favored by high-precision data. For the expected ILC integrated luminosity $\mathcal{L} \sim 500 \text{ fb}^{-1}$, approximately 30000 and 40000 events can be collected in, respectively, the $e^+e^- \rightarrow HZ$ and $e^+e^- \rightarrow \nu\bar{\nu}H$ channels for $M_H \sim 120$ GeV. This sample is more than enough to observe the Higgs particle at the ILC and to study its properties in great detail.

Turning to the sub-leading processes, the ZZ fusion mechanism $e^+e^- \rightarrow He^+e^-$ is similar to WW fusion but has a cross section that is one order of magnitude smaller as a result of the smaller neutral couplings compared to the charged current couplings. However, the full final state can be reconstructed in this case. Note that at $\sqrt{s} \gtrsim 1$ TeV, the cross section for this process is larger than that of Higgs-strahlung for $M_H \lesssim 300$ GeV.

The associated production with top quarks has a very small cross section at $\sqrt{s} = 500$ GeV due to phase space suppression but, at $\sqrt{s} = 800$ GeV, it can reach the level of a few

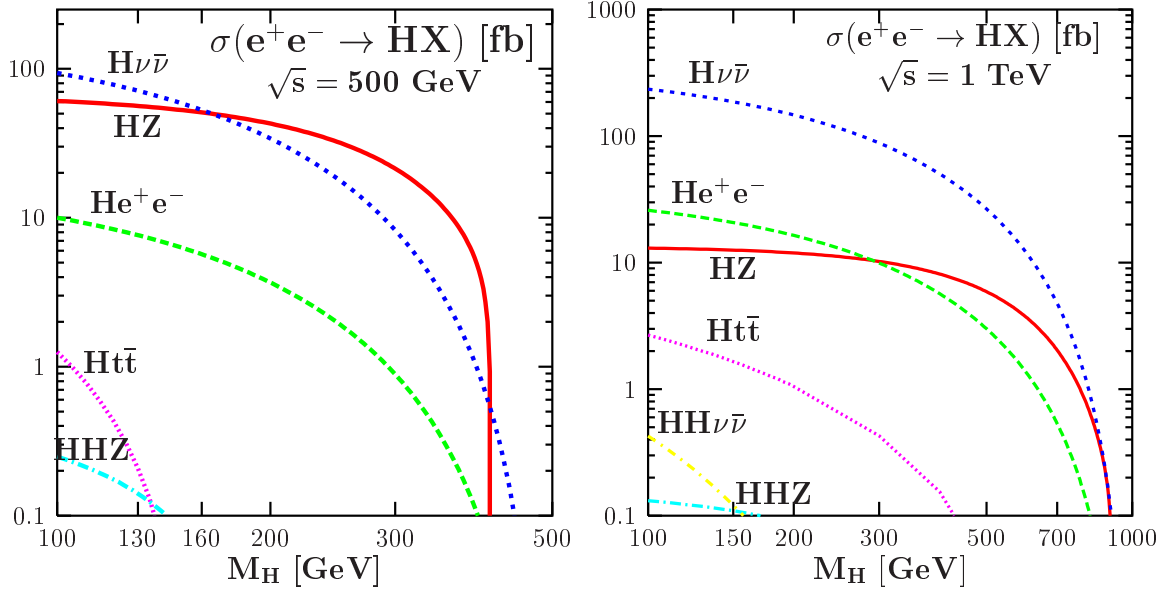


FIGURE 2.7. Production cross sections of the SM Higgs boson at the ILC as a function of M_H for $\sqrt{s} = 500$ GeV (left) and $\sqrt{s} = 1$ TeV (right); from Ref. [33].

femtobarns. The $t\bar{t}H$ final state is generated almost exclusively through Higgs-strahlung off top quarks and the process allows thus the determination of the important g_{Htt} Yukawa coupling in an almost unambiguous way. The electroweak and QCD corrections are known and are moderate [76], except near the production threshold where large coulombic corrections occur and double the production rate [77]. For $M_H \lesssim 140$ GeV, the main signal $t\bar{t}H \rightarrow W^+W^-b\bar{b}b\bar{b}$ is spectacular and b -quark tagging as well as the reconstruction of the Higgs mass peak are essential to suppress the large backgrounds. For larger Higgs masses, $M_H \gtrsim 140$ GeV, the process leads mainly to $Ht\bar{t} \rightarrow 4Wb\bar{b}$ final states which give rise to ten jets if all W bosons are allowed to decay hadronically to increase the statistics.

The cross section for double Higgs production in the strahlung process, $e^+e^- \rightarrow HHZ$, is at the level of $\sim \frac{1}{2}$ fb at $\sqrt{s} = 500$ GeV for a light Higgs boson, $M_H \sim 120$ GeV, and is smaller at higher energies [75]. It is rather sensitive to the trilinear Higgs-self coupling λ_{HHH} : for $\sqrt{s} = 500$ GeV and $M_H = 120$ GeV for instance, it varies by about 20% for a 50% variation of λ_{HHH} . The electroweak corrections to the process have been shown to be moderate [78]. The characteristic signal for $M_H \lesssim 140$ GeV consists of four b -quarks to be tagged and a Z boson which needs to be reconstructed in both leptonic and hadronic final states to increase the statistics. For higher Higgs masses, the dominant signature is $Z + 4W$ leading to multi-jet (up to 10) and/or multi-lepton final states. The rate for double Higgs production in WW fusion, $e^+e^- \rightarrow \nu_e\bar{\nu}_eHH$, is extremely small at $\sqrt{s} = 500$ GeV but reaches the level of $\frac{1}{2}$ fb at 1 TeV; in fact, at high energies, only the latter process can be used.

Finally, future linear colliders can be turned to $\gamma\gamma$ colliders, in which the photon beams are generated by Compton back-scattering of laser light with c.m. energies and integrated luminosities only slightly lower than that of the original e^+e^- collider. Tuning the maximum of the $\gamma\gamma$ spectrum to the value of M_H , the Higgs boson can be formed as s -channel resonances, $\gamma\gamma \rightarrow H$, decaying mostly into $b\bar{b}$ pairs and/or WW^*, ZZ^* final states. This allows precise measurement of the Higgs couplings to photons, which are mediated by loops possibly

involving new particles [22] as well as the CP nature of the Higgs particle [46, 79].

2.2.2 Higgs detection at the ILC

In Higgs-strahlung, the recoiling Z boson is mono-energetic and the Higgs mass can be derived from the Z energy since the initial e^\pm beam energies are sharp when beamstrahlung is ignored (the effects of beamstrahlung must be thus suppressed as strongly as possible). The Z boson can be tagged through its clean $\ell^+\ell^-$ decays ($\ell=e, \mu$) but also through decays into quarks which have a much larger statistics. Therefore, it will be easy to separate the signal from the backgrounds, Fig. 2.8 (left). In the low mass range, $M_H \lesssim 140$ GeV, the process leads to $b\bar{b}q\bar{q}$ and $b\bar{b}l\bar{l}$ final states, with the b quarks being efficiently tagged by micro-vertex detectors. For $M_H \gtrsim 140$ GeV where the decay $H \rightarrow WW^*$ dominates, the Higgs boson can be reconstructed by looking at the $\ell\ell + 4$ -jet or 6-jet final states, and using the kinematical constraints on the fermion invariant masses which peak at M_W and M_H , the backgrounds are efficiently suppressed. Also the $\ell\ell q\bar{q}\ell\nu$ and $q\bar{q}q\bar{q}\ell\nu$ channels are easily accessible.

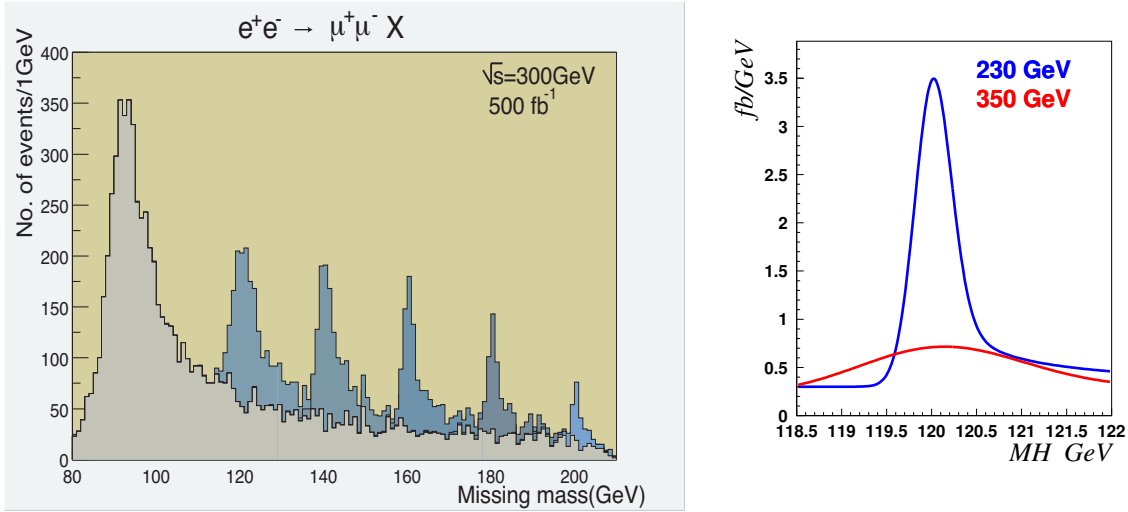


FIGURE 2.8. Left: distribution of the $\mu^+\mu^-$ recoil mass in $e^+e^- \rightarrow \mu^+\mu^- X$; the background from Z pair production and the SM Higgs signals with various masses are shown [8]. Right: differential cross section for $e^+e^- \rightarrow HZ \rightarrow H\mu^+\mu^-$ for two different c.m. energies with $M_H = 120$ GeV [80].

It has been shown in detailed simulations [7, 81] that only a few fb^{-1} data are needed to obtain a 5σ signal for a Higgs boson with a mass $M_H \lesssim 150$ GeV at a 500 GeV collider, even if it decays invisibly (as it could happen e.g. in the MSSM). In fact, for such small masses, it is better to move to lower energies where the Higgs-strahlung cross section is larger and the reconstruction of the Z boson is better [80]; for $M_H \sim 120$ GeV, the optimum energy is $\sqrt{s} = 230$ GeV as shown in Fig. 2.8 (right). Moving to higher energies, Higgs bosons with masses up to $M_H \sim 400$ GeV can be discovered in the Higgs-strahlung process at an energy of 500 GeV and with a luminosity of 500fb^{-1} . For even larger masses, one needs to increase the c.m. energy of the collider and, as a rule of thumb, Higgs masses up to $\sim 80\% \sqrt{s}$ can be probed. This means that a 1 TeV collider can probe the entire Higgs mass range that is theoretically allowed in the SM, $M_H \lesssim 700$ GeV.

The WW fusion mechanism offers a complementary production channel. For low M_H where the decay $H \rightarrow b\bar{b}$ is dominant, flavor tagging plays an important role to suppress the 2-jet plus missing energy background. The $e^+e^- \rightarrow H\nu\nu \rightarrow b\bar{b}\nu\nu$ final state can be separated [7] from the corresponding one in the Higgs-strahlung process, $e^+e^- \rightarrow HZ \rightarrow b\bar{b}\nu\nu$, by exploiting their different characteristics in the $\nu\bar{\nu}$ invariant mass which are measurable through the missing mass distribution; Fig. 2.9. The polarization of the electron and positron beams, which allows tuning of the WW fusion contribution, can be very useful to control the systematic uncertainties. For larger Higgs masses, when the decays $H \rightarrow WW^{(*)}, ZZ^{(*)}$ and even $t\bar{t}$ are dominant, the backgrounds can be suppressed using kinematical constraints from the reconstruction of the Higgs mass peak and exploiting the signal characteristics.

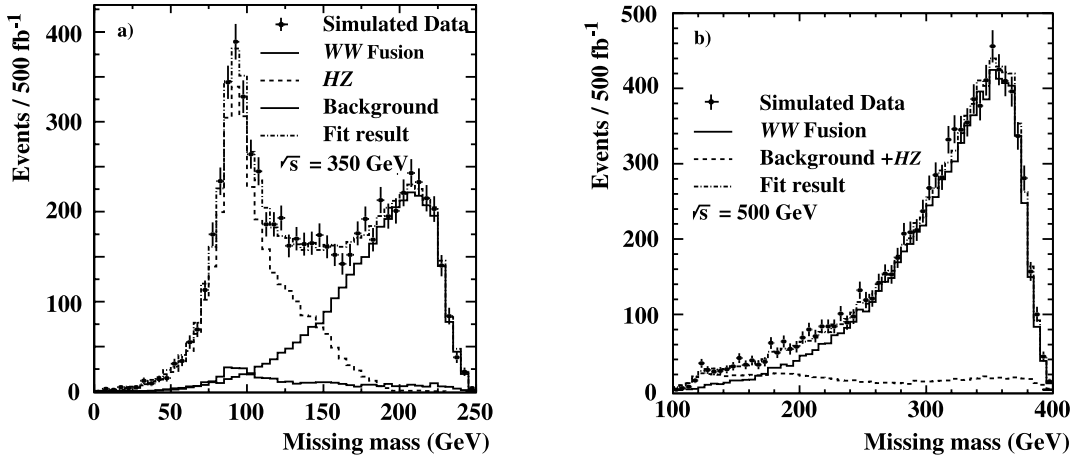


FIGURE 2.9. The missing mass distribution in the $\nu\bar{\nu}b\bar{b}$ final state at $\sqrt{s}=350\text{ GeV}$ (a) and 500 GeV (b) for $M_H=120\text{ GeV}$ in WW fusion, Higgs-strahlung, the interference, as well as for the background [7].

2.2.3 Determination of the SM Higgs properties

Once the Higgs boson is found it will be of great importance to explore all its fundamental properties. This can be done in great detail in the clean environment of e^+e^- linear colliders: the Higgs boson mass, its spin and parity quantum numbers and its couplings to fermions, massive and massless gauge bosons as well as its trilinear self-couplings can be measured with very high accuracies. The measurements would allow to probe in all its facets the electroweak symmetry breaking mechanism in the SM and probe small manifestations of new physics.

The Higgs mass

Many of the properties of the SM Higgs boson can be determined in a model independent way by exploiting the recoil mass technique in the Higgs-strahlung process, $e^+e^- \rightarrow HZ$. The measurement of the recoil $\ell^+\ell^-$ mass in $e^+e^- \rightarrow ZH \rightarrow H\ell\ell$ allows a very good determination of the Higgs mass [82]. At $\sqrt{s} = 350\text{ GeV}$ and with $\mathcal{L} = 500\text{ fb}^{-1}$, a precision of $\Delta M_H \sim 70\text{ MeV}$ can be reached for $M_H \sim 120\text{ GeV}$. The precision can be increased to $\Delta M_H \sim 40\text{ MeV}$ by using the hadronic decays of the Z boson in addition [83]. Note that here, running at energies $\sqrt{s} \sim M_H + 100\text{ GeV}$ is more adequate as the production cross section is largest and the resolution on the $Z \rightarrow \ell\ell$ decays is better [80]. For $M_H = 150\text{--}180\text{ GeV}$ when the Higgs

boson decays mostly into gauge bosons, accuracies of the same order can also be reached. The reconstructed Higgs mass peaks are shown in Fig. 2.2.3 at a c.m. energy of $\sqrt{s} = 350$ GeV in the channels $HZ \rightarrow b\bar{b}q\bar{q}$ and $HZ \rightarrow WW^*q\bar{q}$.

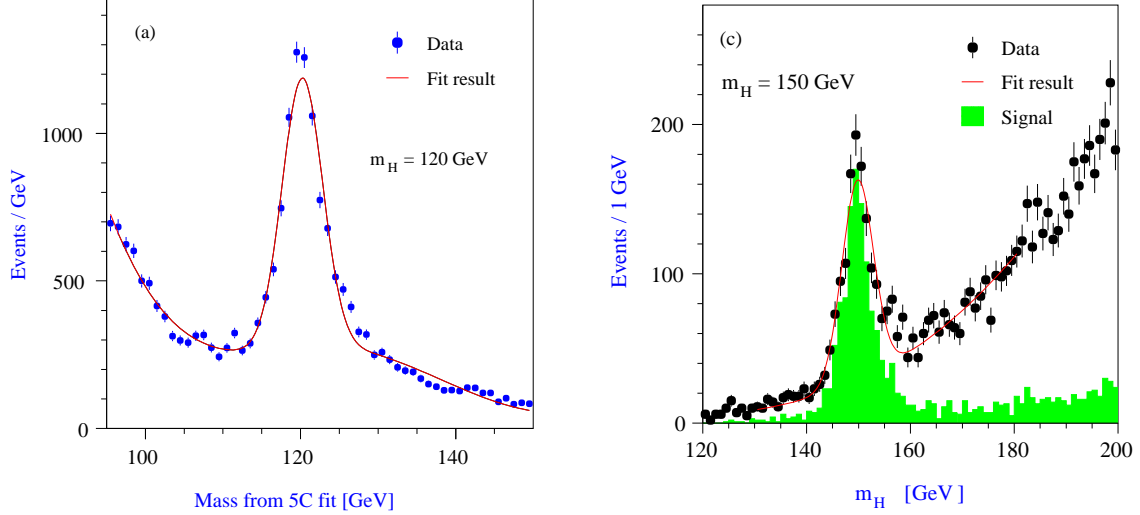


FIGURE 2.10. The Higgs mass peaks reconstructed in different channels with constrained fits for two values of M_H , a luminosity of 500 fb^{-1} and $\sqrt{s} = 350 \text{ GeV}$: $HZ \rightarrow b\bar{b}q\bar{q}$ at $M_H = 120 \text{ GeV}$ (left) and $HZ \rightarrow WW^*q\bar{q}$ at $M_H = 150 \text{ GeV}$ (right); from Ref. [7].

The Higgs spin and parity

The determination of the $J^P = 0^+$ quantum number of the SM Higgs boson can also be performed in the Higgs-strahlung process. The measurement of the rise of the cross section near threshold, $\sigma(e^+e^- \rightarrow HZ) \propto \lambda^{1/2}$, rules out $J^P = 0^-, 1^-, 2^-$ and higher spin $3^\pm, \dots$, which rise with higher powers of the velocity $\lambda^{1/2}$; the possibilities $1^+, 2^+$ can be ruled out by studying angular correlations [84]. A threshold scan with a luminosity of 20 fb^{-1} at three c.m. energies is sufficient to distinguish the various behaviors; Fig. 2.11 (left). The angular distribution of the Z/H bosons in Higgs-strahlung is also sensitive to the spin-zero of the Higgs particle: at high-energies, the Z is longitudinally polarized and the distribution follows the $\sim \sin^2 \theta$ law which unambiguously characterizes the production of a $J^P = 0^+$ particle. Assuming that the Higgs particle is a mixed CP-even and CP-odd state with η parameterizing the mixture, the angular distribution can be checked experimentally; Fig. 2.11 (right). The Higgs J^{PC} quantum numbers can also be checked by looking at correlations in the production $e^+e^- \rightarrow HZ \rightarrow 4f$ or in the decay $H \rightarrow WW^*, ZZ^* \rightarrow 4f$ processes [85].

The CP nature of the Higgs boson would be best tested in the couplings to fermions, where the scalar and pseudoscalar components might have comparable size. Such tests can be performed in the decay channel $H \rightarrow \tau^+\tau^-$ for $M_H \lesssim 140 \text{ GeV}$ by studying the spin correlations between the final decay products of the two τ leptons [88]. The acoplanarity angle between the decay planes of the two ρ mesons produced from τ^+ and τ^- , which can be reconstructed in the Higgs rest frame using the τ lifetime information, is a very sensitive probe, allowing a discrimination between a CP-even and CP-odd state at the 95% CL; additional information from the τ impact parameter is also useful. The CP quantum numbers

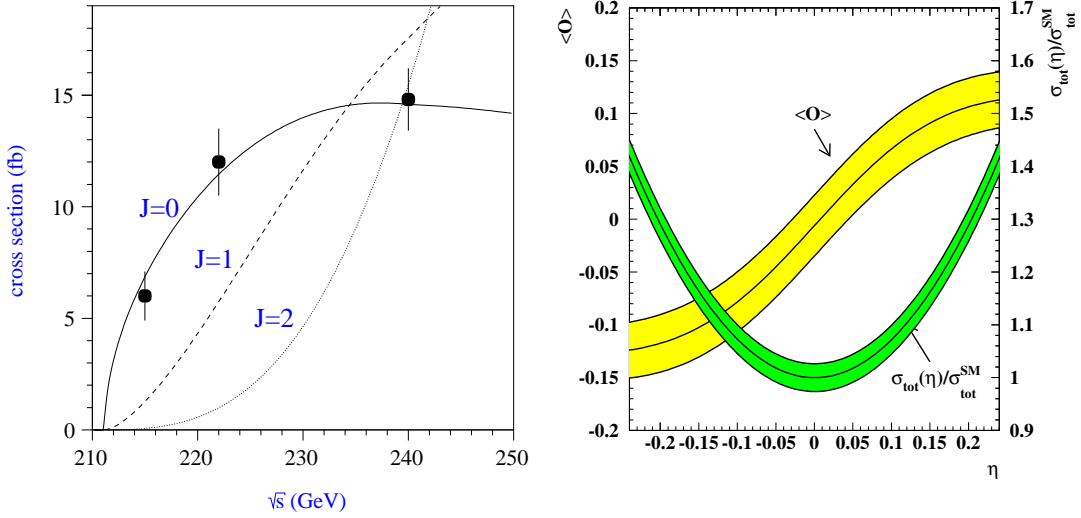


FIGURE 2.11. The $e^+e^- \rightarrow ZH$ cross section energy dependence near threshold for $M_H = 120$ GeV for spin 0^+ , 1^- and 2^+ bosons [86] (left); the determination of the CP mixture η with the bands showing the 1σ errors at $\sqrt{s} = 350$ GeV and 500 fb^{-1} [87] (right).

of the Higgs boson can be determined unambiguously in associated production with top quark pairs either by looking at regions of phase space which single out the different mass effects generated by scalar and pseudoscalar Higgs production or simply from the very different threshold behavior of the cross section as well as the polarization of the final top quarks [89].

The Higgs couplings to gauge bosons

The fundamental prediction that the Higgs couplings to W/Z bosons are proportional to the masses of these particles can be easily verified experimentally since these couplings can be directly determined by measuring the production cross sections in the Higgs-strahlung and fusion processes. $\sigma(e^+e^- \rightarrow HZ \rightarrow H\ell^+\ell^-)$ can be measured by analyzing the recoil mass against the Z boson and provides a determination of the couplings g_{HZZ} independently of the Higgs decay modes. Adding the two lepton channels, one obtains an accuracy of less than 3% at $\sqrt{s} \sim 350$ GeV with $\mathcal{L} = 500 \text{ fb}^{-1}$ [82]. The coupling g_{HWW} for $M_H \lesssim 2M_W$ can be determined, once the branching ratio of a visible channel is available, from the measurement of $\sigma(e^+e^- \rightarrow H\nu\bar{\nu})$ which, as mentioned previously, can be efficiently separated from the $e^+e^- \rightarrow HZ \rightarrow H\nu\bar{\nu}$ channel and from the backgrounds; a precision of less than 3% can also be achieved for $M_H = 120$ GeV, but at a slightly higher energy $\sqrt{s} \sim 500$ GeV, where the production rate is larger [90]. The precision on the Higgs couplings is half of these errors, since the cross sections scale as g_{HVV}^2 and, thus, a measurement of the HVV couplings can be performed at the statistical level of 1 to 2% and would allow probing the quantum corrections.

The Higgs decay branching ratios

The measurement of the branching ratios of the Higgs boson [8, 91, 92, 93, 94, 95, 96] is of utmost importance. For Higgs masses below $M_H \lesssim 140$ GeV, a large variety of branching ratios can be measured at the ILC, since the $b\bar{b}$, $c\bar{c}$ and gg final states have significant rates and can be very efficiently disentangled by means of micro-vertex detectors. The $b\bar{b}$, $c\bar{c}$ and $\tau^+\tau^-$ fractions allow to measure the relative couplings of the Higgs boson to these fermions

and to check the prediction of the Higgs mechanism that they are indeed proportional to fermion masses. In particular, $\text{BR}(H \rightarrow \tau^+\tau^-) \sim m_\tau^2/3\bar{m}_b^2$ allows such a test in a rather clean way. The gluonic branching ratio is indirectly sensitive to the $t\bar{t}H$ Yukawa coupling and would probe the existence of new strongly interacting particles that couple to the Higgs boson and which are too heavy to be produced directly. The branching ratio of the loop induced $\gamma\gamma$ and $Z\gamma$ Higgs decays are sensitive to new heavy particles and their measurement is thus very important. The branching ratio of the Higgs decays into W bosons starts to be significant for $M_H \gtrsim 120$ GeV and allows measurement of the HWW coupling in a model independent way. In the mass range $120 \text{ GeV} \lesssim M_H \lesssim 180 \text{ GeV}$, the $H \rightarrow ZZ^*$ fraction is too small to be precisely measured, but for higher masses it is accessible and allows an additional determination of the HZZ coupling.

TABLE 2.1

Expected precision of the Higgs branching ratio measurements at ILC for $M_H = 120$ GeV and a luminosity of 500 fb^{-1} . Ranges of results from various studies are shown with c.m. energies of 300 GeV [8], 350 GeV [93, 94, 95] and 350/500 GeV [96].

| Decay mode | Relative precision (%) | References |
|----------------|------------------------|-------------------|
| $b\bar{b}$ | 1.0–2.4 | [8][93] [94][97] |
| $c\bar{c}$ | 8.1–12.3 | [8][93] [94][97] |
| $\tau^+\tau^-$ | 4.6–7.1 | [8] [93] [94] |
| gg | 4.8–10 | [8] [93] [94][97] |
| WW | 3.6–5.3 | [8][93] [94] [95] |
| $\gamma\gamma$ | 23–35 | [94] [96] |

There are several studies on the sensitivity of the Higgs branching ratios for a light SM Higgs boson at ILC. Although each analysis is based on slightly different assumptions on detector performance, center-of-mass energy, and analysis method, overall consistent results are obtained. The accuracies of the branching ratio measurements for a SM Higgs boson with a mass of 120 GeV are listed in Tab. 2.1, while for $M_H = 120, 140$ and 160 GeV from the simulation study of Ref. [93], they are shown in Fig. 2.12. For $M_H \gtrsim 180$ GeV, the available decay modes are limited as the Higgs boson predominantly decays into two gauge bosons. In such cases, the measurement of at least one Higgs–fermion coupling is important for establishing the fermion mass generation mechanism. The $H \rightarrow b\bar{b}$ branching ratio can be determined with a 12%, 17% and 28% accuracy for, respectively, $M_H = 180, 200$ and 220 GeV, assuming an integrated luminosity of 1 ab^{-1} at $\sqrt{s} = 800$ GeV [98].

Note that invisible Higgs decays can also be probed with a very good accuracy, thanks to the missing mass technique. One can also look directly for the characteristic signature of missing energy and momentum. Recent studies show that in the range $120 \text{ GeV} \lesssim M_H \lesssim 160 \text{ GeV}$, an accuracy of $\sim 10\%$ can be obtained on a 5% invisible decay and a 5σ signal can be seen for a branching fraction as low as 2% [92].

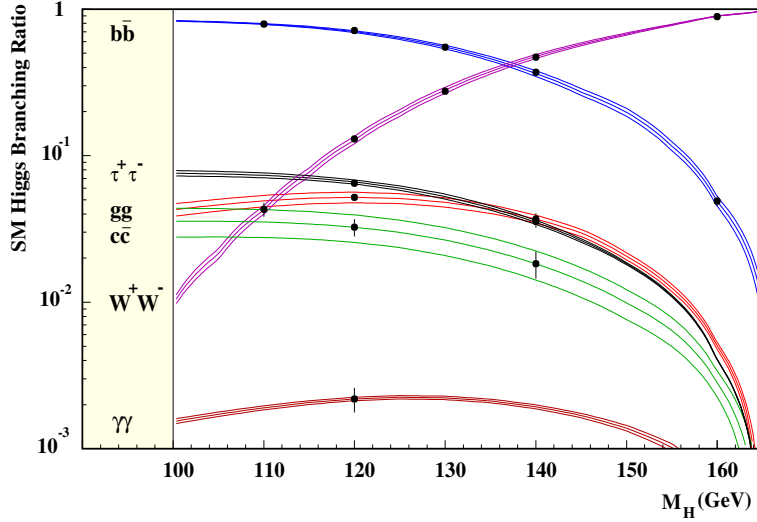


FIGURE 2.12. The branching ratio for the SM Higgs boson with the expected sensitivity at ILC. A luminosity of 500 fb^{-1} at a c.m. energy of 350 GeV are assumed; from Ref. [93].

The Higgs total decay width

The total decay width of the Higgs boson is large enough, for $M_H \gtrsim 2M_W$ GeV, to be accessible directly from the reconstruction of the Higgs boson lineshape. For this purpose, it is better to run the ILC at relatively low energies. It has been shown in Ref. [80] that, for $M_H = 175$ GeV, a measurement of the width $\Gamma_H \sim 0.5$ GeV to a precision of 10% requires 100 fb^{-1} data at $\sqrt{s} = 290$ GeV, while at $\sqrt{s} = 500$ GeV, one needs 5 times more luminosity.

For smaller Higgs masses, Γ_H can be determined indirectly by exploiting the relation between the total and partial decay widths for some given final states. For instance, in the decay $H \rightarrow WW^*$, the width is given by $\Gamma_H = \Gamma(H \rightarrow WW^*)/\text{BR}(H \rightarrow WW^*)$ and one can combine the direct measurement of $\text{BR}(H \rightarrow WW^*)$ and use the information on the HWW coupling from $\sigma(e^+e^- \rightarrow H\nu\nu)$ to determine the partial width $\Gamma(H \rightarrow WW^*)$. Alternatively, one can exploit the measurement of the HZZ coupling from $\sigma(e^+e^- \rightarrow HZ)$ for which the mass reach is higher than in WW fusion, and assume SU(2) invariance to relate the two couplings, $g_{HWW}/g_{HZZ} = 1/\cos\theta_W$. The accuracy on the total decay width measurement follows then from that of $\text{BR}(H \rightarrow WW^*)$ and g_{HWW} . In the range $120 \text{ GeV} \lesssim M_H \lesssim 160$ GeV, an accuracy ranging from 4% to 13% can be achieved on Γ_H if g_{HWW} is measured in the fusion process; Tab. 2.2. This accuracy greatly improves for higher M_H values by assuming SU(2) universality and if in addition one measures $\text{BR}(H \rightarrow WW)$ at higher energies.

TABLE 2.2

Relative precision in the determination of the SM Higgs decay width with $\int \mathcal{L} = 500 \text{ fb}^{-1}$ at $\sqrt{s} = 350$ GeV [7]; the last line shows the improvement which can be obtained when using in addition measurements at $\sqrt{s} \sim 1 \text{ TeV}$ with $\int \mathcal{L} = 1 \text{ ab}^{-1}$ [99].

| Channel | $M_H = 120 \text{ GeV}$ | $M_H = 140 \text{ GeV}$ | $M_H = 160 \text{ GeV}$ |
|---|-------------------------|-------------------------|-------------------------|
| g_{HWW} from $\sigma(e^+e^- \rightarrow H\nu\nu)$ | 6.1% | 4.5% | 13.4 % |
| g_{HWW} from $\sigma(e^+e^- \rightarrow HZ)$ | 5.6% | 3.7% | 3.6 % |
| $\text{BR}(WW)$ at $\sqrt{s} = 1 \text{ TeV}$ | 3.4% | 3.6% | 2.0 % |

Note that the same technique would allow extraction of the total Higgs decay width using

the $\gamma\gamma$ decays of the Higgs boson together with the cross section from $\gamma\gamma \rightarrow H \rightarrow b\bar{b}$ as measured at a photon collider. This is particularly true since the measurement of $\text{BR}(H \rightarrow \gamma\gamma)$ at $\sqrt{s} \sim 1$ TeV is rather precise, allowing the total width to be determined with an accuracy of $\sim 5\%$ with this method for $M_H = 120\text{--}140$ GeV.

The Higgs Yukawa coupling to top quarks

The Higgs Yukawa coupling to top quarks, which is the largest coupling in the electroweak SM, is directly accessible in the process where the Higgs is radiated off the top quarks, $e^+e^- \rightarrow t\bar{t}H$. Because of the limited phase space, this measurement can only be performed at high energies $\sqrt{s} \gtrsim 500$ GeV. For $M_H \lesssim 140$ GeV, the Yukawa coupling can be measured in the channel $WWb\bar{b}b\bar{b}$ with the W bosons decaying both leptonically and hadronically; b -tagging is essential in this mass range [100, 101, 102]. For higher Higgs masses, $M_H \gtrsim 140$ GeV, the complicated channels with $b\bar{b} + 4W$ have to be considered, with again, at least two W bosons decaying hadronically, leading to 2 leptons plus 6 jets and one lepton plus 8 jets, respectively [101]. The next-to-leading QCD corrections to $\sigma(e^+e^- \rightarrow t\bar{t}H)$ have been recently calculated and, at $\sqrt{s} = 500$ GeV, it has been shown that the total cross section is enhanced by a factor of two by threshold dynamics [77].

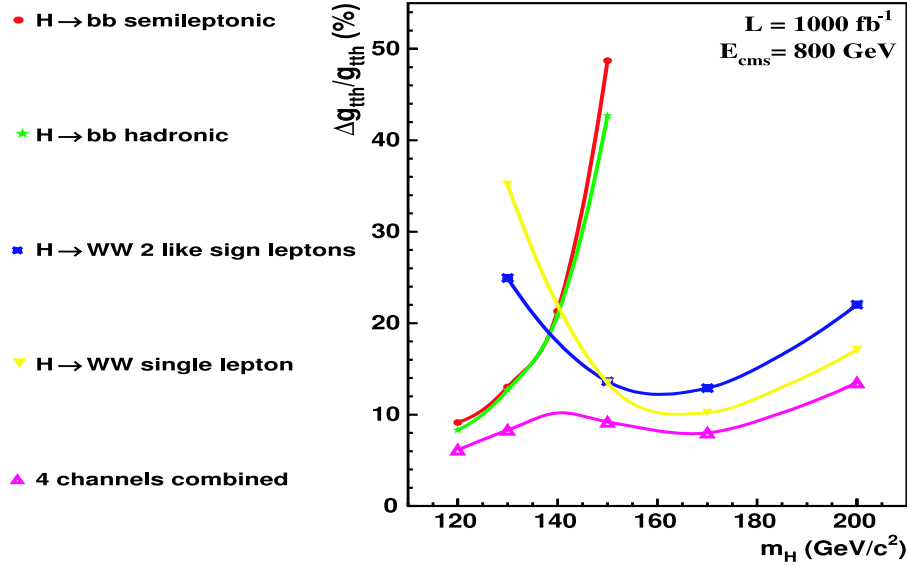


FIGURE 2.13. Expected accuracies for the measurement of the $Ht\bar{t}$ coupling as a function of M_H in $e^+e^- \rightarrow t\bar{t}H$ for $\sqrt{s} = 800$ GeV and 1 ab^{-1} in various decay channels [101].

The expected accuracies on the $Ht\bar{t}$ Yukawa coupling are shown in Fig. 2.13 as a function of the Higgs mass, for $\sqrt{s} = 800$ GeV and a luminosity of 1 ab^{-1} . Assuming a 5% systematical uncertainty on the normalization of the background, accuracies on the $Ht\bar{t}$ Yukawa coupling of the order of 5% can be achieved for Higgs masses in the low mass range, $M_H \lesssim 140$ GeV, when the $H \rightarrow b\bar{b}$ decays are dominant; in this case a 500 GeV ILC can reach an accuracy at the 10% level [102]. A 10% measurement of the Yukawa coupling is possible at $\sqrt{s} = 800$ GeV up to Higgs masses of the order of 200 GeV, when the $H \rightarrow WW$ channel takes over. Note that the measurement of this coupling is rather difficult at the LHC; see chapter 4.

For large masses, $M_H \gtrsim 350$ GeV, the $Ht\bar{t}$ coupling can be derived by measuring the ratio $\text{BR}(H \rightarrow t\bar{t})$ with the Higgs boson produced in the Higgs-strahlung and WW fusion processes [103]. A detailed simulation [7] shows that once the $t\bar{t}$ and $e^+e^-t\bar{t}$ backgrounds are removed, an accuracy of 5% (12%) for $M_H = 400$ (500) GeV can be achieved on $g_{Ht\bar{t}}$, again at a c.m. energy of $\sqrt{s} = 800$ GeV and with $\mathcal{L} \sim 1 \text{ ab}^{-1}$ data [104].

The trilinear Higgs coupling

The measurement of the trilinear Higgs self-coupling, which is the first non-trivial probe of the Higgs potential and, probably, the most decisive test of the EWSB mechanism, is possible in the double Higgs-strahlung process. For Higgs masses in the range $M_H \lesssim 140$ GeV, one has to rely on the $b\bar{b}$ decays and the cross section in the $e^+e^- \rightarrow HHZ \rightarrow b\bar{b}b\bar{b} + \ell^+\ell^-$ or $q\bar{q}$ channels is rather small, while the four and six fermion background are comparatively very large. The excellent b -tagging efficiencies and the energy flow which can be achieved at ILC makes it possible to overcome the formidable challenge of suppressing the backgrounds, while retaining a significant portion of the signal. Accuracies of about 20% can be obtained on the measurement of $\sigma(e^+e^- \rightarrow HHZ)$ in the mass range below 140 GeV; see Fig. 2.14. Neural network analyses allow to improve the accuracy from 17% to 13% at $M_H = 120$ GeV and to obtain a 6σ significance for the signal [105]; see also Ref. [106, 107].

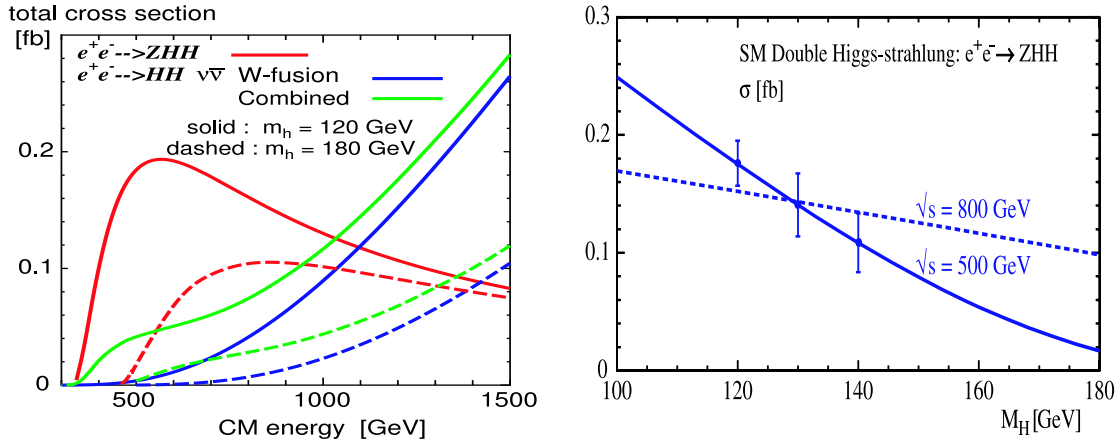


FIGURE 2.14. The separate and combined production cross sections for the ZHH and $\nu\bar{\nu}HH$ processes as a function of \sqrt{s} [108] (left) and the accuracy in the determination of $\sigma(e^+e^- \rightarrow HHZ)$ for several Higgs masses at $\sqrt{s} = 500$ GeV with $\mathcal{L} = 1 \text{ ab}^{-1}$ [105] (right).

Since the sensitivity of the process $e^+e^- \rightarrow HHZ$ to the trilinear Higgs coupling is diluted by the additional contributions originating from diagrams where the Higgs boson is emitted from the Z boson lines, only an accuracy of $\Delta\lambda_{HHH} \sim 22\%$ can be obtained for $M_H = 120$ GeV at $\sqrt{s} \sim 500$ GeV with a luminosity of $\mathcal{L} \sim 1 \text{ ab}^{-1}$. The accuracy becomes worse for higher Higgs masses, when the decays $H \rightarrow WW^*$ must be used. In this case, one can proceed to higher energy and take advantage of the fusion process $e^+e^- \rightarrow HH\nu\bar{\nu}$ [108] which has a larger cross section, in particular with longitudinally polarized e^\pm beams. The sensitivity of the triple coupling constant is dominated by Higgs-strahlung at low energy and WW fusion for $\sqrt{s} \gtrsim 700$ GeV. A recent simulation at $\sqrt{s} = 1$ TeV which combines both the $e^+e^- \rightarrow HHZ$ and $e^+e^- \rightarrow HH\nu\bar{\nu}$ processes with $HH \rightarrow 4b$ final states, assuming a 80% e_L^- polarization and a luminosity of 1 ab^{-1} , shows that an accuracy of $\Delta\lambda_{HHH}/\lambda_{HHH} \sim 12\%$

for $M_H = 120$ GeV could be achieved if λ_{HHH} is SM-like [109]. The relative phase of the coupling and its sign, may be also measured from the interference terms [108, 109].

Note that this coupling is not accessible at the LHC unless the integrated luminosity is significantly increased. The quartic Higgs self-coupling is not accessible at both the LHC and ILC as a result of the very small cross sections for tripe Higgs production.

The two-photon Higgs coupling

At the $\gamma\gamma$ option of the ILC, when the energy is tuned to M_H , the Higgs boson can be formed as an s -channel resonance, $\gamma\gamma \rightarrow \text{Higgs}$. This allows a very precise measurement of the loop induced two-photon Higgs coupling. For a low mass Higgs boson, when the decays $H \rightarrow b\bar{b}$ are dominant, the main background $\gamma\gamma \rightarrow b\bar{b}$ can be suppressed by choosing proper helicities for the initial e^\pm and laser photons which maximizes the signal cross section, and eliminating the gluon radiation by taking into account only two-jet events. Clear signals can be obtained [110] which allow the measurement of $\Gamma(H \rightarrow \gamma\gamma) \times \text{BR}(H \rightarrow b\bar{b})$ with a statistical accuracy of 2% for $M_H = 120$ GeV at an energy $\sqrt{s_{ee}} = 210$ GeV and a luminosity $\mathcal{L}_{\gamma\gamma} = 410 \text{ fb}^{-1}$; Fig. 2.15 (left). Because of the smaller $H \rightarrow b\bar{b}$ branching ratio, the accuracy drops to 7% for $M_H = 160$ GeV. For heavier Higgs particles decaying into WW/ZZ final states, the two-photon width can be measured with a precision $\Delta\Gamma_{\gamma\gamma} \simeq 3\%–10\%$ for $M_H = 200–350$ GeV [79]; Fig. 2.15 (right). The relative phase of the coupling can also be measured and, for $M_H = 200$ GeV, one obtains an accuracy of $\Delta\phi_{\gamma\gamma} \sim 35 \text{ mrad}$ [79].

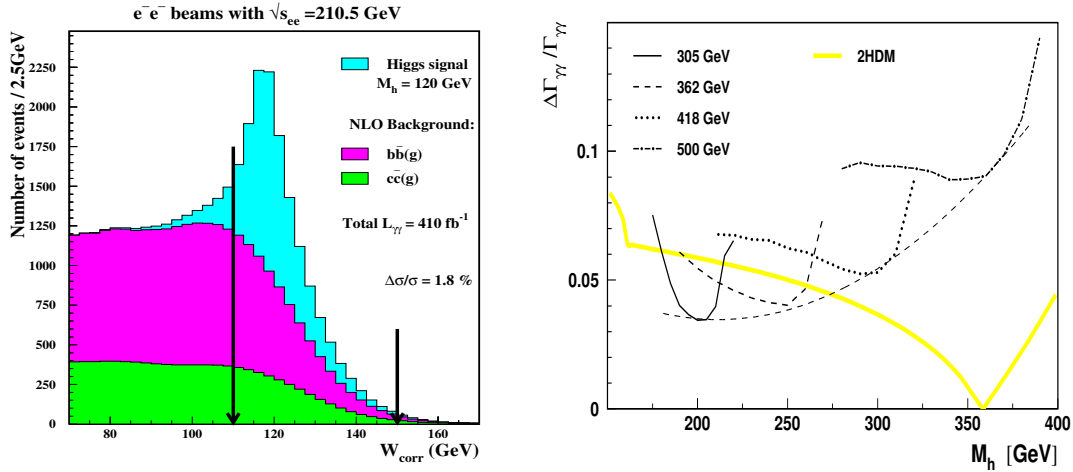


FIGURE 2.15. The reconstructed invariant mass distribution of the $\gamma\gamma \rightarrow H \rightarrow b\bar{b}$ signal and the $b\bar{b}(g)$ and $c\bar{c}(g)$ backgrounds [79] (left) and the expected statistical errors in the determination of the $H\gamma\gamma$ coupling in $\gamma\gamma \rightarrow H \rightarrow WW/ZZ$ (right) with the yellow (thick light) band showing the prediction in a general two-Higgs doublet model [79].

Impact of Higgs coupling measurements

If we combine the Higgs-strahlung and WW fusion processes for single Higgs production, the decay branching ratio measurements, associated Higgs production with top quark pairs and double Higgs production in the strahlung and WW fusion processes, the various couplings associated with the Higgs particle can be determined rather accurately. We can then compare the magnitudes of these couplings with the the SM and check the fundamental prediction

that they are indeed proportional to the particle masses. Relations between various Higgs couplings and particle masses are shown in Fig. 2.16 for the case of a 120 GeV SM Higgs boson with accuracies corresponding to $\mathcal{L} = 500 \text{ fb}^{-1}$ at $\sqrt{s}=300 \text{ GeV}$ for the c, τ, b, W and Z couplings, $\sqrt{s} = 500 \text{ GeV}$ for the λ_{HHH} self-coupling and $\sqrt{s} = 700 \text{ GeV}$ for the $t\bar{t}H$ Yukawa coupling. A summary of the various precision measurements at ILC is given in Table 2.3

An important feature of ILC experiments is that absolute values of these coupling constants can be determined in a model-independent way. This is crucial in establishing the mass generation mechanism for elementary particles and very useful to explore physics beyond the SM. For instance, radion-Higgs mixing in warped extra dimensional models could reduce the magnitude of the Higgs couplings to fermions and gauge bosons in a universal way [56, 57] and such effects can be probed only if absolute coupling measurements are possible. Another example is related to the electroweak baryogenesis scenario to explain the baryon number of the universe: to be successful, the SM Higgs sector has to be extended to realize a strong first-order phase transition and the change of the Higgs potential can lead to observable effects in the triple Higgs coupling [111, 112]. Finally, the loop induced gluonic and photonic decay channels are sensitive to scales far beyond the Higgs mass and can probe new particles that are too heavy to be produced directly [113].

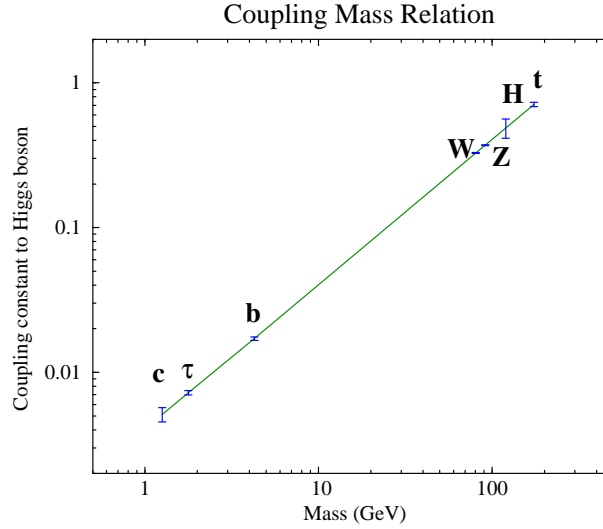


FIGURE 2.16. The relation between the Higgs couplings and the particle masses as determined from the high-precision ILC measurements [4]; on the y axis, the coupling κ_i of the particle i with mass m_i is defined in a such a way that the relation $m_i = v\kappa_i$ with $v \simeq 246 \text{ GeV}$ holds in the SM.

2.3 THE HIGGS BOSONS IN SUSY THEORIES

2.3.1 Decays and production of the MSSM Higgs bosons

The decay pattern of the Higgs bosons of the MSSM [40] is more complicated than in the SM and depends strongly on the value of $\tan\beta$ and the Higgs masses; see Fig. 2.17 where the branching ratios are shown for $\tan\beta = 3$ and 30. The lightest h boson will decay mainly into fermion pairs since its mass is smaller than $\sim 140 \text{ GeV}$, except in the decoupling limit in which it decays like the SM-Higgs boson and thus the WW decays can be dominant.

TABLE 2.3

Precision of the Higgs couplings determination for various particles at the ILC from a global fit for $M_H = 120$ GeV with 500 fb^{-1} data. For c, τ, b, W, Z couplings, $\sqrt{s} = 500$ GeV is assumed while $\sqrt{s} = 500$ (800) GeV is taken for the HHH ($t\bar{t}H$) couplings and 1 ab^{-1} data is assumed (the measurement of λ_{HHH} can be improved by a factor of two at $\sqrt{s} = 1$ TeV). The accuracy for the determination of the Higgs boson mass, total decay width and CP-mixture at $\sqrt{s} = 350$ GeV with 500 fb^{-1} data, are also shown. From Ref. [7].

| coupling | λ_{HHH} | g_{HWW} | g_{HZZ} | $g_{Ht\bar{t}}$ | $g_{Hb\bar{b}}$ | $g_{Hc\bar{c}}$ | $g_{H\tau\tau}$ |
|----------|-----------------|-------------|-------------|-----------------|-----------------|-----------------|-----------------|
| accuracy | ± 0.22 | ± 0.012 | ± 0.012 | ± 0.030 | ± 0.022 | ± 0.037 | ± 0.033 |

| observable | M_H | Γ_H | CP-mixture |
|------------|---------------|-------------|-------------|
| accuracy | ± 0.00033 | ± 0.061 | ± 0.038 |

The fermionic channels are in general also the dominant decay modes of the heavier scalar H and pseudoscalar A bosons, except for the H boson when it is SM-like. For values of $\tan\beta$ much larger than unity, the main decay modes of the three neutral Higgs bosons are decays into $b\bar{b}$ and $\tau^+\tau^-$ pairs with the branching ratios being of order $\sim 90\%$ and 10% , respectively. For large masses, the top decay channels $H, A \rightarrow t\bar{t}$ open up, yet for large $\tan\beta$ these modes remain suppressed. If the masses are high enough, the heavy H boson can decay into gauge bosons or light h boson pairs and the pseudoscalar A particle into hZ final states. However, these decays are strongly suppressed for $\tan\beta \gtrsim 3-5$ as is suggested by the LEP2 constraints. The charged Higgs particles decay into fermions pairs: mainly $t\bar{b}$ and $\tau\nu_\tau$ final states for H^\pm masses, respectively, above and below the $t\bar{b}$ threshold. If allowed kinematically and for small values of $\tan\beta$, the H^\pm bosons decay also into hW final states for $\tan\beta \lesssim 5$.

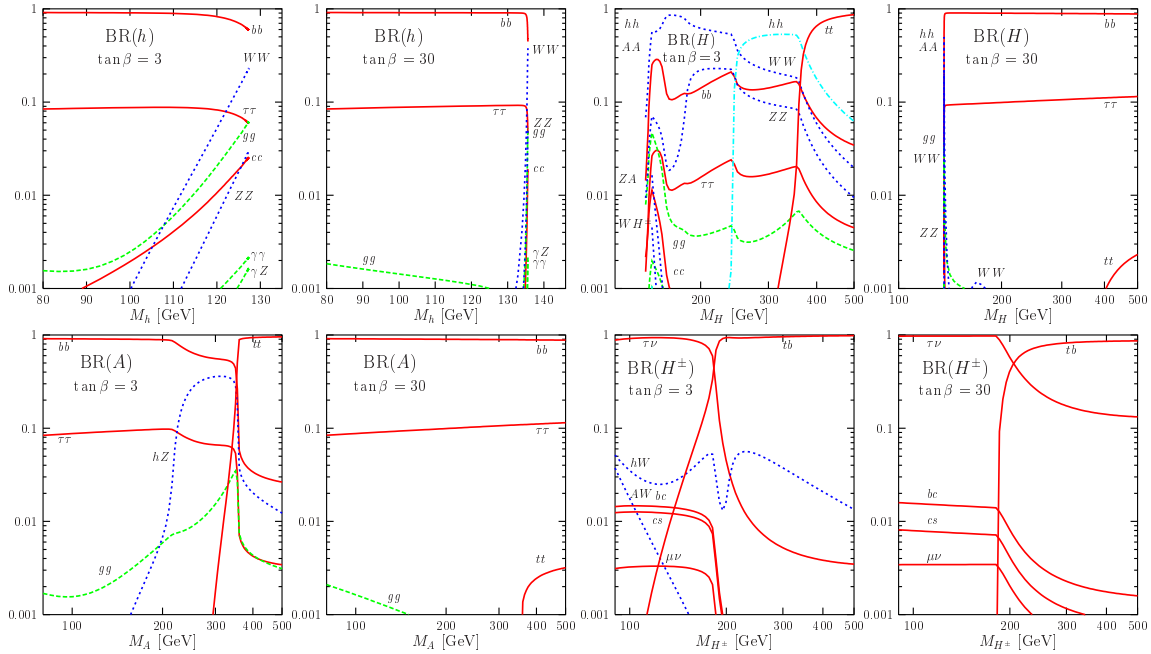


FIGURE 2.17. The decay branching ratios of the MSSM Higgs bosons as functions of their masses for $\tan\beta = 3$ and 30 in the maximal mixing scenario with $M_S = 2$ TeV.

Adding up the various decay modes, the widths of all five Higgs bosons remain very narrow. The total width of one of the CP-even Higgs particles will be close to the SM Higgs boson width, while the total widths of the other Higgs particles will be proportional to $\tan\beta$ and will be of the order of 10 GeV even for large masses and large $\tan\beta$ values.

Other possible decay channels for the MSSM bosons, in particular the heavy H, A and H^\pm states, are decays into supersymmetric particles. In addition to light sfermions, decays into charginos and neutralinos could eventually be important if not dominant. Decays of the lightest h boson into the lightest neutralinos (LSP) can be also important in some parts of the SUSY parameter space; see Ref. [40] for a recent review. These decays can render the search for Higgs particle rather difficult, in particular at hadron colliders.

At the ILC, besides the usual Higgs-strahlung and fusion processes for h and H production, the neutral Higgs particles can also be produced pairwise: $e^+e^- \rightarrow A + h/H$ [114]. The cross sections for the Higgs-strahlung and the pair production as well as the cross sections for the production of h and H are mutually complementary, coming either with a coefficient $\sin^2(\beta - \alpha)$ or $\cos^2(\beta - \alpha)$; Fig. 2.18. The cross section for hZ production is large for large values of M_h , being of $\mathcal{O}(100 \text{ fb})$ at $\sqrt{s} = 500 \text{ GeV}$; by contrast, the cross section for HZ is large for light h [implying small M_H]. In major parts of the parameter space, the signals consist of a Z boson and $b\bar{b}$ or $\tau^+\tau^-$ pairs, which is easy to separate from the backgrounds with b -tagging. For the associated production, the situation is opposite: the cross section for Ah is large for light h whereas AH production is preferred in the complementary region. The signals consists mostly of four b quarks in the final state, requiring efficient b -quark tagging; mass constraints help to eliminate the QCD jets and ZZ backgrounds. The CP-even Higgs particles can also be searched for in the WW and ZZ fusion mechanisms.

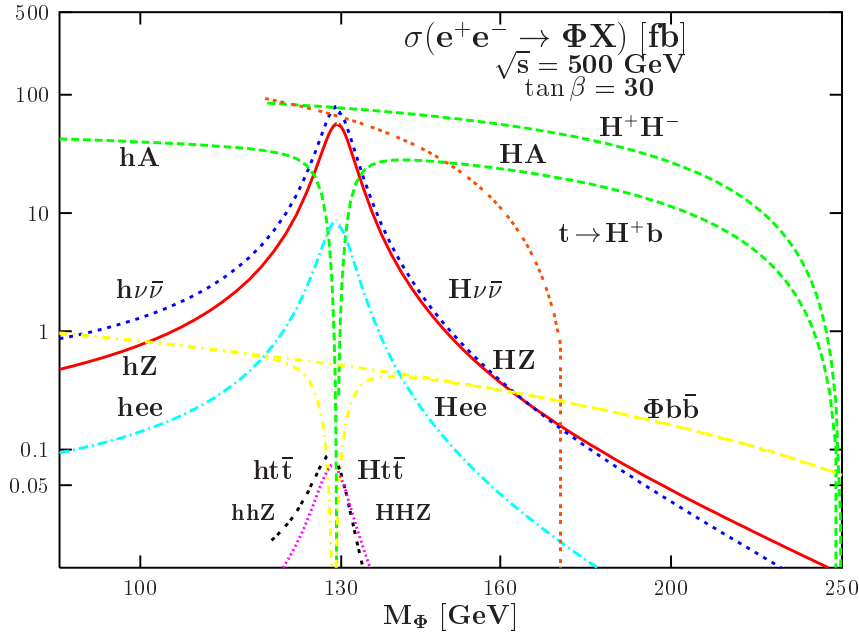


FIGURE 2.18. Production cross sections of the MSSM Higgs bosons in e^+e^- collisions as functions of the masses for $\tan\beta = 30$ and $\sqrt{s} = 500 \text{ GeV}$; from Ref. [40].

In e^+e^- collisions, charged Higgs bosons can be produced pairwise, $e^+e^- \rightarrow H^+H^-$, through γ, Z exchange. The cross section depends only on the charged Higgs mass; it is large

almost up to $M_{H^\pm} \sim \frac{1}{2}\sqrt{s}$. H^\pm bosons can also be produced in top decays; in the range $1 < \tan\beta < m_t/m_b$, the $t \rightarrow H^+b$ branching ratio and the $t\bar{t}$ production cross sections are large enough to allow for their detection in this mode as will be discussed in chapter 4.

The discussion of SUSY Higgs production at the ILC can be briefly summarized in the following three points.

- The Higgs boson h can be detected in the entire range of the MSSM parameter space, either through the Higgs–strahlung [and WW fusion] process or associated production with the pseudoscalar A boson. In fact, this conclusion holds true even at a c.m. energy of 250 GeV and with a luminosity of a few fb^{-1} . Even if the decay modes of the h boson are very complicated, missing mass techniques allow for their detection. For instance, the branching ratios for the invisible h boson decays into the LSP neutralinos can be measured at the percent level as exemplified in Fig. 2.19 for a 350 GeV ILC. The accuracy can be substantially improved by running at lower c.m. energies [80]. The same very detailed tests and precision measurements discussed previously for the SM Higgs boson can be performed for the MSSM h boson, in particular in the decoupling limit.

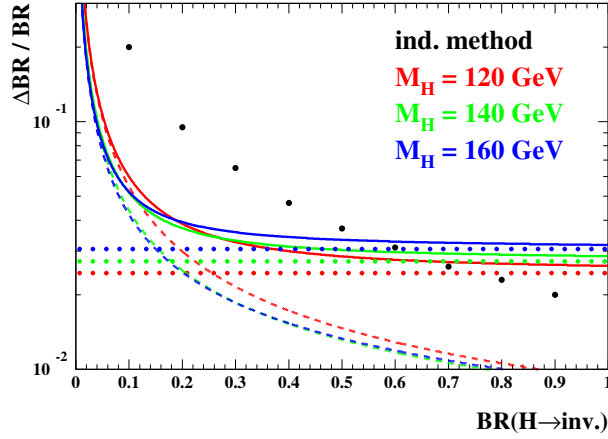


FIGURE 2.19. The expected accuracy on the invisible decay rate as a function of the branching ratio at $\sqrt{s} = 350$ GeV with 500 fb^{-1} data (full lines). The other lines indicate the individual contributions from the measurement of the invisible rate (dashed lines) and the total Higgs–strahlung cross section (dotted lines); the large dots are the result of the indirect method [7]; from Ref. [92].

- All SUSY Higgs bosons can be discovered at an e^+e^- collider if the H , A and H^\pm masses are less than the beam energy; for higher masses, one simply has to increase the c.m. energy, $\sqrt{s} \gtrsim 2M_A$. The various cross section contours for heavy MSSM Higgs production processes are shown in Fig. 2.20 in the $[M_A, \tan\beta]$ plane for $\sqrt{s} = 500$ GeV and 1 TeV [115]. As can be seen, several channels might be observable depending on the value of $\tan\beta$. Note that the additional associated neutral Higgs production processes with $t\bar{t}$ and $b\bar{b}$ allow for the measurement of the Yukawa couplings. In particular, $e^+e^- \rightarrow b\bar{b} + h/H/A$ for high $\tan\beta$ values allow for the determination of this important parameter for low M_A values.

- If the energy is not high enough to open the HA pair production threshold, the photon collider option may become the discovery machine for the heavy Higgs bosons [116, 117]. Since the A, H bosons are produced as s -channel resonances, the mass reach at a photon collider is extended compared to the e^+e^- mode and masses up to 80% of the original c.m. energy can be probed. It has been shown in Ref. [117] that the whole medium $\tan\beta$ region up to about 500 GeV, where only one light Higgs boson can be found at the LHC, can be

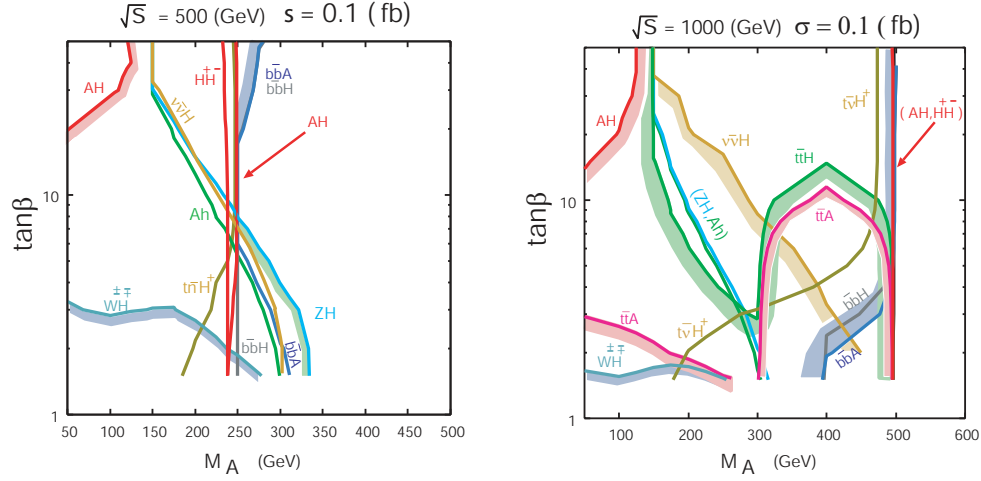


FIGURE 2.20. Cross section contours of various heavy MSSM Higgs production processes in the plane $[M_A, \tan \beta]$ for $\sqrt{s} = 500$ GeV and 1 TeV [115].

covered by the photon collider option with three years of operation with an e^-e^- c.m. energy of 630 GeV; see Fig. 2.21. The photon collider mode is also important to determine the CP properties of the heavy Higgs bosons, either by studying angular correlation of Higgs decay products or by using initial beam polarization. The discrimination between the scalar and pseudoscalar particles can be performed and CP violation can be unambiguously probed.

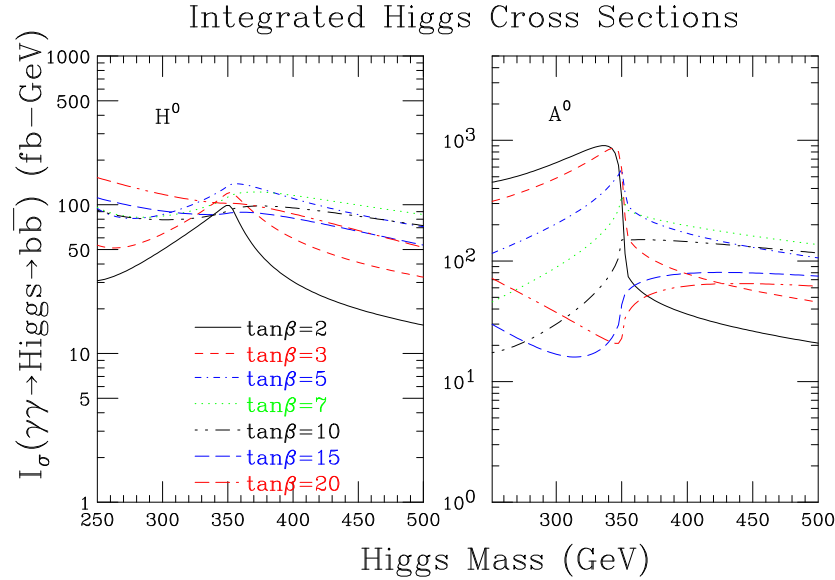


FIGURE 2.21. Effective cross sections for the production of the heavier CP-even (left) and the CP-odd (right) Higgs bosons in $\gamma\gamma$ collisions, $\sigma(\gamma\gamma \rightarrow H/A \rightarrow b\bar{b})$ for several $\tan \beta$ values; from Ref. [117].

2.3.2 Measurements in the MSSM Higgs sector

A number of very important measurements can be performed at the ILC in the MSSM Higgs sector. If the heavier H , A and H^\pm states are kinematically accessible, one can measure their masses and cross sections times decay branching ratios with a relatively good accuracy. In

the pair production process $e^+e^- \rightarrow HA$, a precision of the order of 0.2% can be achieved on the H and A masses, while a measurement of the cross sections can be made at the level of a few percent in the $b\bar{b}b\bar{b}$ and ten percent in the $b\bar{b}\tau^+\tau^-$ channels; see Fig. 2.22 (left).

For the charged Higgs boson, statistical uncertainties of less than 1 GeV on its mass and less than 15% on its production cross section times branching ratio can be achieved in the channel $e^+e^- \rightarrow H^+H^- \rightarrow t\bar{b}t\bar{b}$ for $M_{H^\pm} \sim 300$ GeV with high enough energy and luminosity; Fig. 2.22 (right). These measurements allow the determination of the most important branching ratios, $b\bar{b}$ and $\tau^+\tau^-$ for the H/A and tb and $\tau\nu$ for the H^\pm particles, as well as the total decay widths which can be turned into a determination of the value of $\tan\beta$, with an accuracy of 10% or less. The spin-zero nature of the particles can be easily checked by looking at the angular distributions which should go as $\sin^2\theta$. Several other measurements, such as the spin-parity of the Higgs particles in $H/A \rightarrow \tau^+\tau^-$ decays and, in favorable regions of the parameter space, some trilinear Higgs couplings, can be made.

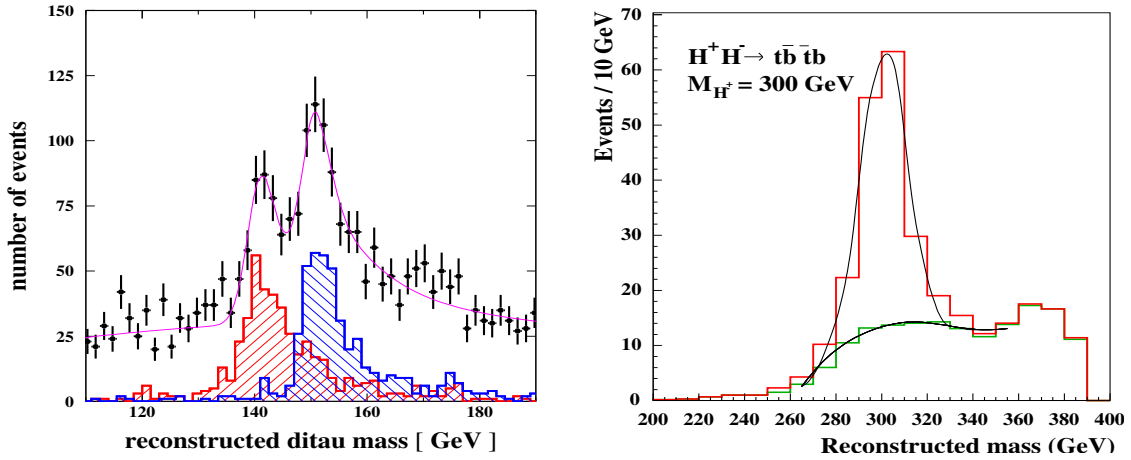


FIGURE 2.22. The reconstructed $\tau\tau$ invariant mass from a kinematic fit in $e^+e^- \rightarrow HA \rightarrow b\bar{b}\tau^+\tau^-$ for $M_A = 140$ GeV and $M_H = 150$ GeV at $\sqrt{s} = 500$ GeV with 500 fb^{-1} data [118] (left) and the di-jet invariant mass distribution for $e^+e^- \rightarrow H^+H^- \rightarrow t\bar{b}t\bar{b}$ for $M_{H^\pm} = 300$ GeV after applying the intermediate W, t and the equal mass final state constraints for 500 fb^{-1} data at $\sqrt{s} = 800$ GeV [7] (right).

The profile of the lighter Higgs boson can be entirely determined. This is particularly the case close to the decoupling regime where the h boson behaves like the SM Higgs particle but with a mass below $M_h \sim 140$ GeV. This is, in fact, the most favorable mass range for precision measurements as the Higgs boson has many decay channels that are accessible in this case. This has been shown in the previous section when we reviewed the precision studies for a SM Higgs boson at the ILC.

A detailed analysis of the deviations of the couplings of the h boson with a mass $M_h = 120$ GeV, from the predictions in the SM has been performed in Ref. [7] using a complete scan of the MSSM $[M_A, \tan\beta]$ parameter space, including radiative corrections. In Fig. 2.23, shown are the 1σ and 95% confidence level contours for the fitted values of various pairs of ratios of couplings, assuming the experimental accuracies at the ILC discussed in the previous section. From a χ^2 test which compares the deviations, 95% of all MSSM solutions can be distinguished from the SM case for $M_A \lesssim 600$ GeV and this number reduces to only 68% for $M_A \lesssim 750$ GeV. In some cases, one is sensitive to MSSM effects even for masses $M_A \sim 1$ TeV,

i.e. beyond the LHC mass reach. If the deviations compared to the SM are large, these precision measurements would also allow for an indirect determination of M_A ; for instance, in the mass range $M_A = 300\text{--}600$ GeV an accuracy of 70–100 GeV is possible on the A mass.

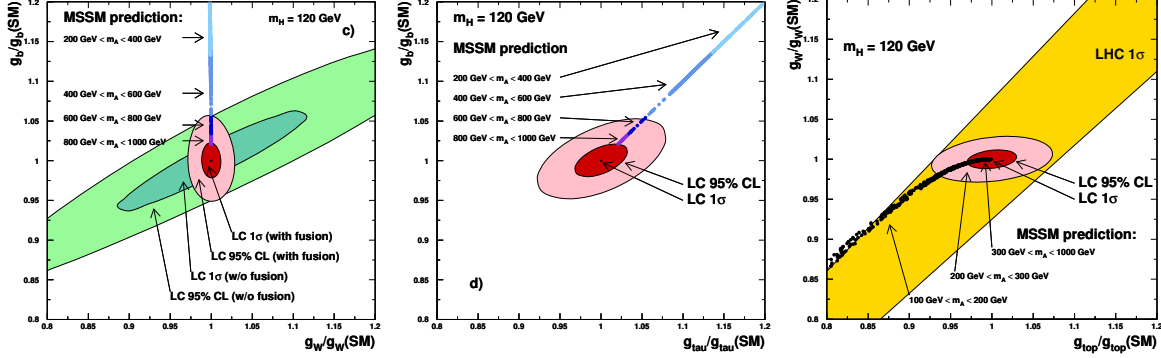


FIGURE 2.23. Determination of the couplings of a SM-like Higgs boson at the ILC and the interpretation within the MSSM. The contours are the couplings of a 120 GeV Higgs boson as measured with 500 fb^{-1} data at $\sqrt{s} = 350$ GeV except for g_{Htt} which uses 800 GeV (here the expectation at the LHC is also shown); from Ref. [7].

This type of indirect determination cannot be made in a convincing way at the LHC as the experimental errors in the various measurements are worse than at the ILC; see Fig. 2.23 where the g_{hWW} and $g_{h\tau\tau}$ contours are displayed. While at the ILC, MSSM effects can be probed for masses close to $M_A = 1$ TeV, there is practically no sensitivity at the LHC. However, the precision measurements at the ILC can gain enormously from other measurements that can be performed only at the LHC. Indeed, the various Higgs couplings are not only sensitive to the tree-level inputs M_A and $\tan\beta$ but also, on parameters that enter through radiative corrections such as the stop and sbottom masses which could be accessible only at the LHC. If, in addition, the A boson is seen at the LHC [which means that $\tan\beta$ is large, $\tan\beta \gtrsim 15$] and its mass is measured at the level of 10%, the only other important parameter entering the Higgs sector at one-loop is the trilinear coupling A_t [and to a lesser extent, A_b and μ] which will be only loosely constrained at the LHC. Nevertheless, using this knowledge and the fact that the top mass can be measured with a precision of 100 MeV at the ILC, one can vastly improve the tests of the MSSM Higgs sector that can be performed at the LHC or at the ILC alone; see Ref. [15] for a discussion on the LHC–ILC complementarity.

2.3.3 The Higgs sector beyond the MSSM

In the MSSM with CP-violation, the three neutral Higgs bosons H_1, H_2, H_3 are mixtures of CP-even and CP-odd states. Because of the sum rule for the Higgs couplings to gauge bosons, $\sum_i g_{H_i VV}^2 = g_{H_{SM}}^2$, the production cross sections in the Higgs-strahlung and WW fusion processes should be large for at least one of the particles and there is a complementarity between H_i single and $H_j H_k$ pair production. In fact, similar to the usual MSSM, the normalized couplings are such that $|g_{H_1 VV}| = |g_{H_2 H_3 V}| \sim 1$ in the decoupling limit $M_{H^\pm} \gtrsim 200$ GeV and at least H_1 is accessible for $\sqrt{s} \gtrsim 300$ GeV, since $M_{H_1} \lesssim 130$ GeV. If two or the three Higgs particles are very close in mass, the excellent energy and momentum resolution on the recoiling Z boson in the Higgs-strahlung process would allow to resolve the coupled

Higgs systems, e.g. from an analysis of the lineshape. The presence of CP-violation can be unambiguously checked by studying the spin-spin correlations in Higgs decays into tau lepton pairs or controlling the beam polarization of the colliding photon beams at the $\gamma\gamma$ option of the ILC; see Ref. [43] for instance.

In the NMSSM, where a complex iso-scalar field is introduced, leading to an additional pair of scalar and pseudoscalar Higgs particles, the axion-type or singlino character of the pseudoscalar A_1 boson makes it preferentially light and decaying into b quarks or τ leptons [50]. Therefore, in some areas of the NMSSM parameter space, the lightest scalar Higgs bosons may dominantly decay into a pair of light pseudoscalar A_1 bosons generating four b quarks or τ leptons in the final state. In fact, it is also possible that H_1 is very light with small VV couplings, while H_2 is not too heavy and plays the role of the SM-like Higgs particle; the decays $H_2 \rightarrow H_1 H_1$ can also be substantial and will give the same signature as above. This is exemplified in Fig. 2.24 where shown are scatter plots for the mass of the SM-like Higgs boson (h_H) and the pseudoscalar-like (h_L) boson, the ratio of h_H coupling to Z bosons (R_H) compared to the SM Higgs coupling, and the branching ratio of the heavy to light Higgs decay ($h_H \rightarrow h_L h_L$) [49]. As seen previously, Higgs-strahlung allows for the detection of the CP-even Higgs particles independently of their decay modes, provided that their couplings to the Z boson are substantial, as it occurs for one CP-even Higgs boson as exemplified in the middle plot of Fig. 2.24. In fact, thanks to the usual sum rule which relates the CP-even Higgs couplings to the those of the SM Higgs, a “no-lose theorem” for discovering at least one Higgs state has been established for ILC while the situation is presently less clear for the LHC and all Higgs particles could escape detection [49, 50].

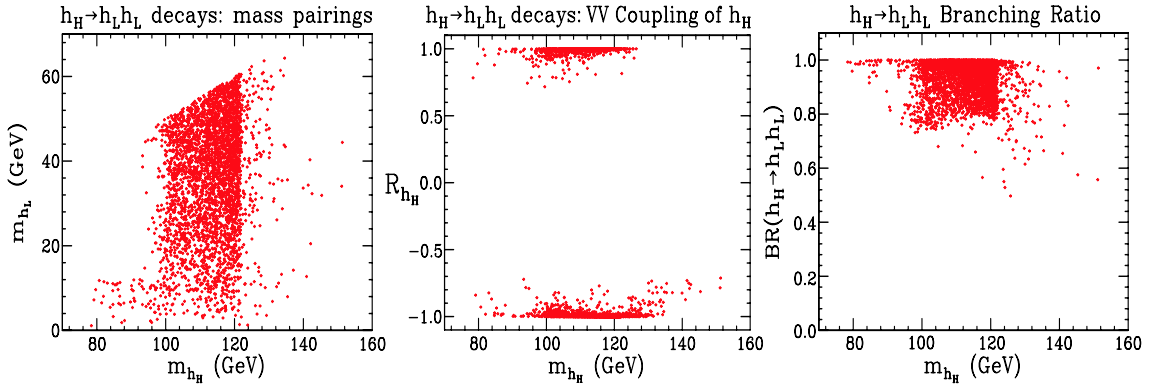


FIGURE 2.24. Scatter plots for the mass of the h_H and h_L boson (left), the normalized couplings to the h_H boson (middle) and the branching ratio of its decays to lighter h_L bosons (right) as function of the Higgs mass; they have been obtained in an NMSSM scan for regions with $h_H \rightarrow h_L h_L$ decays; from [49].

In a general SUSY model, with an arbitrary number of isosinglet and isodoublet scalar fields (as well as a matter content which allows for the unification of the gauge coupling constants), a linear combination of Higgs fields has to generate the W/Z boson masses and thus, from the triviality argument discussed earlier, a Higgs particle should have a mass below 200 GeV and significant couplings to gauge bosons [48]. This particle should be therefore kinematically accessible at the ILC with a c.m. energy $\sqrt{s} \gtrsim 350$ GeV. It can be detected in the Higgs-strahlung process independently of its (visible or invisible) decay modes. If its mass happens to be in the high range, $M_h \sim 200$ GeV, at least its couplings to W, Z bosons and b -quarks (eventually t -quarks at high energies and luminosities), as well as the total

decay widths and the spin-parity quantum numbers can be determined.

We should stress again that even in scenarios with invisible Higgs decays, as would be the case for instance of spontaneously broken R-parity scenarios in which the Higgs particles could decay dominantly into escaping Majorons, $H_i \rightarrow JJ$, at least one CP-even Higgs boson is light and has sizable couplings to the gauge bosons and should be observed by studying the recoil mass spectrum against the Z boson in the Higgs-strahlung process.

From the previous discussions, one can thus conclude that the ILC is the ideal machine for the SUSY Higgs sector, whatever scenario nature has chosen.

2.4 THE HIGGS SECTOR IN ALTERNATIVE SCENARIOS

As discussed in the introductory section, several non-supersymmetric scenarios beyond the SM predict new features which might significantly affect the Higgs sector. To illustrate the large impact that such models can have, we will take as an example the effects of a radion in warped extra dimensional models. Other possibilities will be discussed in chapter 6.

In Randall-Sundrum models [55], a scalar radion field is introduced to stabilize the distance between the SM and the gravity brane. Carrying the same quantum numbers, the Higgs and radion fields can mix and the properties of the Higgs boson will be altered [56, 57]. In particular, Higgs-radion mixing can lead to important shifts in the Higgs couplings which become apparent in the various decay widths. These shifts depend on the radion and Higgs masses, the mixing parameter ξ which is expected to be of order unity and the ratio of the Higgs vacuum expectation value v to the effective new scale $\Lambda \sim 1$ TeV.

The ratio of Higgs partial decay widths in these models to their SM values is illustrated in the left-hand side of Fig. 2.25 for $M_H = 125$ GeV and various values of the radion mass M_ϕ and the ratio v/Λ [56]. As can be seen, while the shifts in the $f\bar{f}/VV$ and $\gamma\gamma$ widths are rather similar, the shift in the $H \rightarrow gg$ partial decay width is different; the width can become close to zero for some values of the mixing. The impact of mixing in $f\bar{f}$ and VV final states is in general smaller and the branching ratios will not be significantly affected as these decays are dominant. This implies that it will be imperative to perform a precise measurement of the Higgs total decay width in order to probe the mixing with radions. At the ILC, the shift in the photon couplings can be probed in $\gamma\gamma \rightarrow H$ production while in the e^+e^- option, the $H \rightarrow gg$ width can be precisely measured. Since the total decay width can be also measured, the absolute values of the Higgs couplings can be unambiguously determined.

The suppression of the Hgg loop induced coupling can occur in other extensions of the SM as well. Besides the MSSM with light top squarks and large trilinear A_t couplings, the $SU(2)_R$ partner of the right-handed top quark in warped extra dimensional models with an extended left-right symmetric structure will also contribute to the Hgg vertex and could interfere destructively with the top quark contribution, leading to a much smaller coupling [113]. In the strongly interacting light Higgs scenario proposed recently [65], the Higgs couplings to gluons, as well as the couplings to fermions and gauge bosons, are also suppressed. Note that the suppression of the Hgg coupling would lead to a decrease of the cross section for the dominant Higgs production mechanism in proton collisions, $gg \rightarrow H$, and would make the Higgs search more complicated at the LHC.

Another important consequence of radion mixing is the decays of the Higgs boson into a pair of radions. Indeed, if the radion is relatively light, the decays $H \rightarrow \phi\phi$ might be kinematically accessible and, for some mixing values, the branching fractions might be substantial.

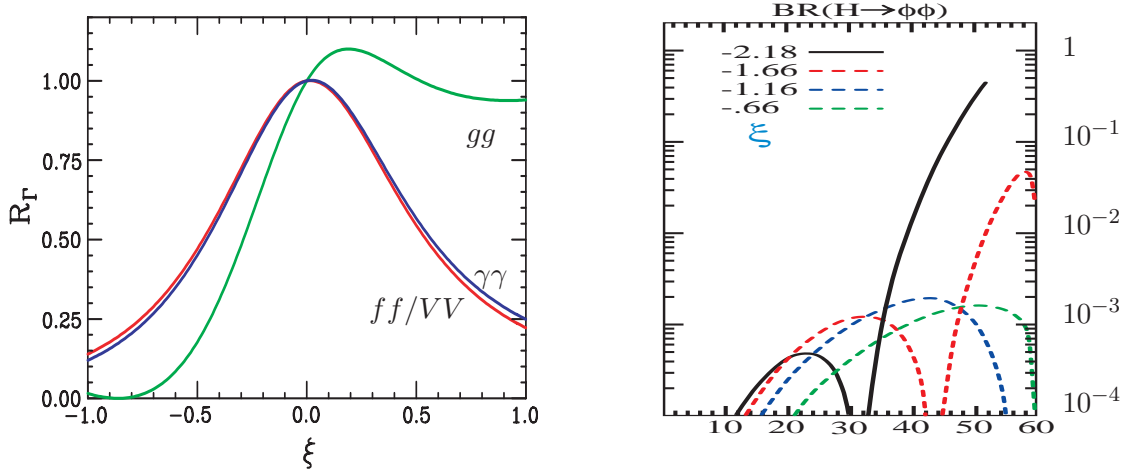


FIGURE 2.25. Left: the ratio R_Γ of Higgs partial widths to their SM values, as a function of the mixing parameter ξ with $M_H = 125$ GeV, $M_\phi = 300$ GeV and $v/\Lambda = 0.2$ [56]. Right: the branching fractions for the decays $H \rightarrow \phi\phi$ as a function of M_ϕ for different ξ values and $M_H = 120$ GeV, $\Lambda = 5$ TeV [57].

This is exemplified in the right-hand side of Fig. 2.25 where $BR(H \rightarrow \phi\phi)$ is displayed as a function of the mixing parameter ξ for $M_H = 120$ GeV and $\Lambda = 5$ TeV [57]. As can be seen, the rate can be very large, in particular for the largest $|\xi|$ values when M_ϕ is close to $\frac{1}{2}M_H$. The detection of the $H \rightarrow \phi\phi$ decay mode could provide the most striking evidence for the presence of non-zero ξ mixing. In the considered mass range, $M_\phi \lesssim 60$ GeV, the radion will mainly decay into $b\bar{b}$ and gg final states, while the $\gamma\gamma$ branching ratio is very small. Observing these final states will be rather difficult at the LHC while in Higgs-strahlung at the ILC, the final state $ZH \rightarrow Z\phi\phi \rightarrow Z + 4$ jets should be easily detectable. Finally, the reverse decay process $\phi \rightarrow HH$ is also possible for radion masses larger than $M_\phi \gtrsim 230$ GeV. The branching fractions, when this decay occurs, can be rather large. For $M_H \sim 120$ GeV, the process $e^+e^- \rightarrow Z\phi \rightarrow ZHH \rightarrow Z + 4b$ would dramatically increase the ZHH production rate at the ILC and would lead to spectacular events; see chapter 6.

Note that in models with large extra dimensions [58], the interaction of the Higgs field and the Ricci scalar curvature of the induced four-dimensional metric also generates a mixing term with the closest Kaluza-Klein graviscalar fields [59]. This mixing results in an effective Higgs decay width, $\Gamma(H \rightarrow \text{graviscalar})$, which is invisible as the graviscalars are weakly interacting and mainly reside in the extra dimension while the Higgs is on the TeV brane. These invisible Higgs decays can be largely dominating. In addition, there is the possibility of Higgs decays into a pair of graviscalars, but the rates are smaller than the ones from mixing. These decays will complicate the Higgs search at the LHC, while they can be easily detected in Higgs-strahlung at the ILC and the branching fractions precisely measured.

Other models also predict large rates for invisible decays of the Higgs boson. An example, besides decays into the lightest neutralinos and Majorons [54] in non minimal SUSY models, is again given by extra dimensional models in which the Higgs bosons decay into the lightest Kaluza-Klein particles which are supposed to form the dark matter in the universe [119]. Finally, in the minimal extension of the Higgs sector with a singlet field S , invisible $H \rightarrow SS$ decays occur and could be the dominant channels [60].

Thus, one can conclude that also in alternative scenarios to supersymmetry, the ILC will be a valuable tool to unravel the electroweak symmetry breaking mechanism.

CHAPTER 3

Couplings of gauge bosons

The Standard Model has been thoroughly tested in the last two decades with the high-precision measurements of LEP, SLC and the Tevatron which have firmly established that it describes correctly the electroweak and strong interactions of quarks and leptons. However, many important aspects of the model, besides the electroweak symmetry breaking mechanism for particle mass generation, need more experimental investigation. This can be done at the ILC in the production of fermion antifermion pairs as well as electroweak gauge bosons, in particular single and pair production of W bosons, which provide the largest cross sections leading to event samples of a few million each with the ILC expected luminosity.

An important task is to measure the interactions amongst gauge bosons much more precisely than it was possible at LEP and the Tevatron and will be possible at the LHC, for instance, determine the trilinear self-couplings of the W and Z bosons at the per-mille level. Anomalous values of these couplings are most precisely measured in the clean environment of an e^+e^- collider and at the highest possible c.m. energy \sqrt{s} . The ILC thus allows to constrain new physics at scales far above the direct reach of the collider through quantum corrections and, alternatively, to probe small effects from operators in an effective Lagrangian that are suppressed by powers of s/Λ^2 where Λ is the scale at which the new physics sets in. The measurement of the quartic gauge boson self-couplings is of utmost importance, especially if no Higgs particles have been observed at the LHC and ILC. In this scenario, the interactions between massive gauge bosons become strong at energies close to 1 TeV and the effective scale for the new interactions needed to restore quantum-mechanical unitarity can be extracted from a precise measurement of anomalous values of these self-couplings.

Another important task, once the top quark and the Higgs boson masses are accurately known, is to measure the value of the effective weak mixing angle $\sin^2 \theta_{\text{eff}}^l$ and the W boson mass M_W and to test more precisely their quantum corrections and the consistency of the model in an unambiguous way. These parameters can be determined with an accuracy that is far better than the one presently available by running the high-luminosity ILC near the Z boson resonance and near the WW threshold and this test can be performed at an unprecedented level of precision. Then, and only then, virtual effects of new physics beyond the SM can be probed in an unambiguous way. Furthermore, observables in fermion pairs produced in e^+e^- collisions at high energy are sensitive to new physics far beyond the center of mass energy. As one example, an ILC running at 500 GeV is sensitive to effects of a heavy Z' boson, that is predicted in many SM extensions, beyond the reach of the LHC and it can, if such a particle has been observed at the LHC, measure its couplings and thus distinguish

between the various models where this new Z' boson occurs.

Finally, the ILC offers the possibility of testing QCD at high energy scales in the experimentally clean and theoretically tractable e^+e^- environment. In particular, it allows a more precise determination of the strong coupling α_s , which is presently known with an error of several percent [35], and the measurement of its evolution with the energy scale. Since the weak and electromagnetic couplings are known with a much higher accuracy, this measurement is very important as the present error on α_s represents the dominant uncertainty on the prediction of the scale for grand unification of the strong, weak and electromagnetic forces.

3.1 COUPLINGS OF GAUGE BOSONS TO FERMIONS

In the SM, fermion pair production, $e^+e^- \rightarrow f\bar{f}$ for $f \neq e$, proceeds at tree-level via the exchange of photons and Z bosons in the s -channel. These processes can thus be used to measure the couplings of fermions to gauge bosons. All cross sections are given by the product of the initial state e^+e^-V and the final state $f\bar{f}V$ couplings. Assuming universality, lepton pair production thus measures the leptonic couplings while quark production measures the product of the leptonic and the quark couplings.

Since weak interactions violate parity, the vector- ($g_{V,f}$) and the axial-vector- ($g_{A,f}$) couplings can vary independently in general. However they can be disentangled experimentally without major problems. The total cross section is proportional to the squared sum of the couplings ($g_{V,f}^2 + g_{A,f}^2$) while several asymmetries like the left-right asymmetry A_{LR}^f with polarized beams or the forward-backward asymmetry A_{FB}^f measure their ratio $g_{V,f}/g_{A,f}$.

The fermion couplings to the Z boson have already been measured with great success at LEP and SLD on the Z -boson resonance [120]. The comparison of their precise measurements with accurate calculations led to the prediction of the top quark mass before it was actually discovered [121] and to the current prediction that the Higgs boson should be light [120].

At $\sqrt{s} \sim 500$ GeV, $e^+e^- \rightarrow f\bar{f}$ samples of a few million events are expected so that the couplings can be measured at the per-mille level accuracy. The main interest in fermion pair production lies in limits on physics beyond the SM. Apart from photons and Z bosons, all other particles that couple to electrons and the final state fermions can be exchanged and thus contribute to the cross section. In a more model independent approach, the virtual effects of new physics can be parameterized in terms of contact interactions using the effective helicity-conserving Lagrangian, with the interaction strength set to $g_*^2/4\pi = 1$,

$$\mathcal{L}_{\text{eff}} = \sum_{i,j=L,R} \eta_{ij} \frac{4\pi}{\Lambda_{ij}^2} \bar{e}_i \gamma^\mu e_i \cdot \bar{f}_j \gamma_\mu f_j. \quad (\text{i})$$

Here, one assumes that the masses of the exchanged particles are so heavy, that details of the propagator are not felt and only the Lorenz structure of the couplings remains visible.

In a detailed experimental analysis it has been shown that fermion pair production at the ILC provides a large sensitivity to the contact interaction scales Λ_{ij} [122]. The limits on the scales that one can extract from the precision measurements are shown in Fig. 3.1 for quark (left) and muon (right) pair production at $\sqrt{s} = 500$ GeV using 1 ab^{-1} of data, e^- polarization and various assumptions for the systematical errors; for muon final states, the significant improvement using e^+ polarization is also displayed. As can be seen, scales of the order of $\Lambda = 20$ to 100 TeV can be reached at this energy, significantly higher than

those obtainable at the LHC; this is shown in the $e^+e^- \rightarrow q\bar{q}$ case as the LHC cannot probe $e^+e^- \mu^+ \mu^-$ couplings. At $\sqrt{s}=1$ TeV, the limits are expected to be approximately 50% larger.

A model dependent application of the precision measurements of fermion pair production, besides probing for instance fermion compositeness and/or anomalous couplings, leptoquarks, etc., is the search for heavy neutral Z' vector bosons. The fermion cross sections and asymmetries are altered by the virtual exchange of the Z' boson and are thus sensitive to its mass and couplings. In general, the ILC precision measurements at $\sqrt{s} = 500$ GeV are more or equally sensitive to the Z' mass as the LHC direct mass reach and more sensitivity is gained at a 1 TeV. If a Z' boson with a mass $M_{Z'} \lesssim 3 - 4$ TeV has been observed at the LHC, the ILC allows to determine the model origin. A more detailed discussion of Z' effects and other applications of ILC precision measurements is given in chapter 6.

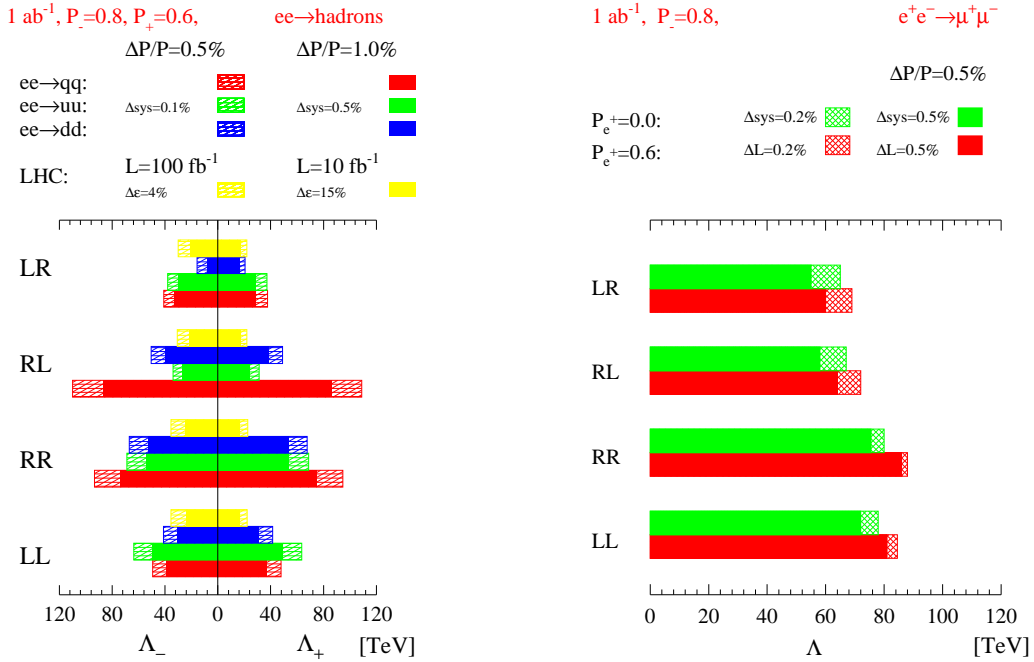


FIGURE 3.1. Sensitivities at the 95% CL of a 500 GeV ILC to contact interaction scales Λ for different helicities in $e^+e^- \rightarrow \text{hadrons}$ (left) and $e^+e^- \rightarrow \mu^+\mu^-$ (right) including beam polarization [122].

Another possibility to measure the fermion couplings to the Z boson is to return to the Z -resonance in the GigaZ option of the ILC [19]. With a luminosity around $\mathcal{L} = 5 \cdot 10^{33} \text{ cm}^{-2} \text{ s}^{-1}$, a billion Z decays can be collected within a few months of running. The most sensitive observable to measure the Z -fermion couplings is the left-right polarization asymmetry $A_{\text{LR}} = \frac{1}{\mathcal{P}} \frac{\sigma_L - \sigma_R}{\sigma_L + \sigma_R}$, where $\sigma_{L,R}$ denotes the cross section for left/right handed polarized electron beams and \mathcal{P} the beam polarization. This asymmetry is sensitive to the ratio of the vector to axial-vector coupling of the electron to the Z boson, $A_{\text{LR}} = 2g_{V,e}g_{A,e}/(g_{V,e}^2 + g_{A,e}^2)$, which in turn measures the effective weak mixing angle in Z decays, $g_{V,e}/g_{A,e} = 1 - 4Q_e \sin^2 \theta_{\text{eff}}^l$.

If e^\pm polarization is available, the cross section for a given beam polarization is given by

$$\sigma = \sigma_u [1 - \mathcal{P}_{e^+} \mathcal{P}_{e^-} + A_{\text{LR}} (\mathcal{P}_{e^+} - \mathcal{P}_{e^-})]. \quad (\text{ii})$$

If the sign of the electron and positron polarization can be flipped independently, four measurements with four unknowns are possible, so that A_{LR} can be measured without the need

for absolute polarimetry. Polarimeters are, however, still needed to measure a possible polarization difference between the left- and the right-handed state and to track any time dependences of the polarization which enters in the polarization product of equation (ii). A_{LR} can be measured with a statistical accuracy of about $\Delta A_{\text{LR}} = 3 \cdot 10^{-5}$. The largest systematic uncertainty by far comes from the knowledge of the beam energy. The slope close to the Z -peak is $dA_{\text{LR}}/d\sqrt{s} = 2 \cdot 10^{-2}/\text{GeV}$ and is due to the γ - Z interference. Not to be dominated by this effect the center of mass energy needs to be known to 1 MeV relative to the Z -mass which has to be calibrated by frequent scans. If the beamstrahlung is the same in the peak running and in the scans for energy calibration, its effect cancels out and beamstrahlung does not contribute to the systematic uncertainty.

Conservatively, a final error of $\Delta A_{\text{LR}} = 10^{-4}$ will be assumed corresponding to $\Delta \sin^2 \theta_{\text{eff}}^l = 1.3 \cdot 10^{-6}$. This is an improvement of more than one order of magnitude compared to the value obtained at LEP/SLD. To achieve this precision, one also needs to know the fine structure constant at the scale M_Z , $\alpha(M_Z^2)$, with a much better precision than presently. Measuring the cross section $\sigma(e^+e^- \rightarrow \text{hadrons})$ to 1% roughly up to the J/Ψ resonance would reduce the uncertainty of the $\sin^2 \theta_{\text{eff}}^l$ prediction to the level of the experimental error [123]. With modest upgrades this is possible using present machines.

If absolute values of the couplings are to be measured, one needs to obtain the Z boson leptonic width Γ_ℓ . The peak cross section $\sigma(e^+e^- \rightarrow \ell^+\ell^-)$ for $\sqrt{s} = M_Z$ is proportional to $\Gamma_\ell^2/\Gamma_{\text{tot}}^2$. Thus, to measure Γ_ℓ , apart from the cross section, the total width of the Z boson needs to be determined from a scan. Many systematic uncertainties enter the determination of Γ_ℓ and the relative knowledge of the beam energy affects the determination of Γ_{tot} while the knowledge of the total luminosity and the selection efficiency directly enter the cross section measurement. The most severe systematics are expected to come from the beam energy spread and from beamstrahlung. Because the second derivative of a Breit-Wigner distribution at the peak is very large, the effective peak cross section is strongly reduced by these effects, which may well limit the Γ_ℓ measurement. A probably optimistic estimate [19] shows a possible improvement of a factor two relative to the LEP measurement.

The b-quark, the isospin partner of the top quark, plays a special role in many models. Its forward-backward asymmetry as measured at LEP is one of the few observables that deviates from the SM prediction by more than two standard deviations [120], a deviation that can be explained, e.g. in extra-dimensional models [124]. At GigaZ, the asymmetry parameter $\mathcal{A}_b = \frac{2g_{V,b}g_{A,b}}{g_{V,b}^2 + g_{A,b}^2}$ can be measured one order of magnitude better than at LEP/SLD and without a dependence on the Zee couplings, revealing if the current deviation is real or simply a statistical fluctuation. Also the measurement of the fraction of $b\bar{b}$ events in hadronic Z decays, R_b , which is proportional to $g_{V,b}^2 + g_{A,b}^2$ can be improved by a factor five.

In addition to the fermion- Z couplings, the W boson mass can be measured at the ILC with a threshold scan to a precision around 6 MeV [125]. Because of a similar structure of the radiative corrections, this observable is usually interpreted together with the coupling measurements. Within a wide range of models, the measurement of M_W can replace the one of Γ_ℓ which is not accurately determined as mentioned above. However, this measurement takes one year of running at $\sqrt{s} \sim 160$ GeV, where not many physics issues can be addressed.

As a possible application of the precision measurements discussed above, Fig. 3.2 displays the projected $\sin^2 \theta_{\text{eff}}^l$ and M_W measurements under different assumptions compared to the prediction of the SM and its supersymmetric extension, the MSSM [41]. Within the SM, a stringent test of the model is possible while for the MSSM the sensitivity is good enough

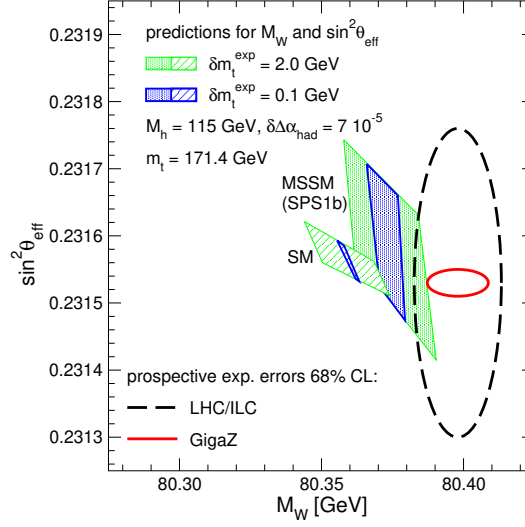


FIGURE 3.2. $\sin^2 \theta_{\text{eff}}^l$ versus M_W for different experimental assumptions compared to the predictions from the SM and the MSSM [41].

to constrain some of its parameters. It can also be seen that the precise top quark mass measurement at the ILC is needed for an optimal sensitivity of the comparison.

3.2 COUPLINGS AMONG GAUGE BOSONS

3.2.1 Measurements of the triple couplings

The couplings among the electroweak gauge bosons are directly given by the structure of the gauge group. This structure can thus directly be determined by a measurement of the gauge boson interactions. W -boson pair production is an especially interesting process in this respect. Without gauge interactions, W^+W^- pairs are produced in e^+e^- collisions via neutrino t -channel exchange. This mechanism violates unitarity and is regulated by the photon and Z boson s -channel exchange processes which involve the triple gauge boson couplings. Since the exact values of the self-couplings, as predicted by the $SU(2)_L \times U(1)_Y$ gauge structure, are needed for unitarity restoration, small changes lead to large variations of the cross section. For this reason, the $e^+e^- \rightarrow W^+W^-$ process is much more sensitive to the triple gauge boson couplings than one would naively expect from cross section estimates.

The triple gauge boson couplings are conventionally parameterized as [126]:

$$\begin{aligned} \mathcal{L}_{WWV} = & g_{WWV} \left[ig_1^V V_\mu (W_\nu^- W_{\mu\nu}^+ - W_{\mu\nu}^- W_\nu^+) + i\kappa_V W_\mu^- W_\nu^+ V_{\mu\nu} + i\frac{\lambda_V}{M_W^2} W_{\lambda\mu}^- W_{\mu\nu}^+ V_{\nu\lambda} \right. \\ & + g_4^V W_\mu^- W_\nu^+ (\partial_\mu V_\nu - \partial_\nu V_\mu) + g_5^V \epsilon_{\mu\nu\lambda\rho} (W_\mu^- \partial_\lambda W_\nu^+ - \partial_\lambda W_\mu^- W_\nu^+) V_\rho \\ & \left. + i\tilde{\kappa}_V W_\mu^- W_\nu^+ \tilde{V}_{\mu\nu} + i\frac{\tilde{\lambda}_V}{M_W^2} W_{\lambda\mu}^- W_{\mu\nu}^+ \tilde{V}_{\nu\lambda} \right], \end{aligned} \quad (\text{iii})$$

using the antisymmetric combinations $V_{\mu\nu} = \partial_\mu V_\nu - \partial_\nu V_\mu$ and their duals $\tilde{V}_{\mu\nu} = \frac{1}{2}\epsilon_{\mu\nu\rho\sigma} V_{\rho\sigma}$. The overall coefficients are $g_{WW\gamma} = e$ and $g_{WWZ} = e \cot \theta_W$. Electromagnetic gauge invariance

TABLE 3.1

Results of the single parameter fits (1σ) to the different triple gauge couplings at the ILC for $\sqrt{s} = 500$ GeV with $\mathcal{L} = 500 \text{ fb}^{-1}$ and $\sqrt{s} = 800$ GeV with $\mathcal{L} = 1000 \text{ fb}^{-1}$; $\mathcal{P}_{e^-} = 80\%$ and $\mathcal{P}_{e^+} = 60\%$ has been used.

| coupling | error $\times 10^{-4}$ | |
|------------------------|------------------------------|------------------------------|
| | $\sqrt{s} = 500 \text{ GeV}$ | $\sqrt{s} = 800 \text{ GeV}$ |
| Δg_1^Z | 15.5 | 12.6 |
| $\Delta \kappa_\gamma$ | 3.3 | 1.9 |
| λ_γ | 5.9 | 3.3 |
| $\Delta \kappa_Z$ | 3.2 | 1.9 |
| λ_Z | 6.7 | 3.0 |
| g_5^Z | 16.5 | 14.4 |
| g_4^Z | 45.9 | 18.3 |
| $\tilde{\kappa}_Z$ | 39.0 | 14.3 |
| $\tilde{\lambda}_Z$ | 7.5 | 3.0 |

requires that $g_1^\gamma = 1$ and $g_5^\gamma = 0$ at zero momentum transfer. In the SM, one has $g_1^V = \kappa_V = 1$, all other couplings are equal to zero. Among the different couplings g_1 , κ and λ are C- and P-conserving, g_5 is C and P-violating but CP-conserving while g_4 , $\tilde{\kappa}$, $\tilde{\lambda}$ violate CP symmetry.

Experimentally, the different types of couplings can be disentangled by analysing the production angle distribution of the W boson and the W polarization structure which can be obtained from the decay angle distributions. Anomalous $WW\gamma$ and WWZ couplings give similar signals in the final state distributions. However they can be disentangled easily at the ILC using beam polarization. Because of the strong dominance of the left-handed electron state, high polarization values are needed for this analysis. This can also be achieved by increasing the effective polarization using polarized positron beams.

An analysis using a fast simulation has been performed at the two energies $\sqrt{s} = 500$ GeV and 800 GeV [127] and the results for single parameter fits are shown in Table 3.1. For the multi-parameter fits, the correlations are modest at $\sqrt{s} = 800$ GeV so that the errors increase by at most 20%, while at $\sqrt{s} = 500$ GeV they are much larger and the errors increase by about a factor two in the multi-parameter fit of the C,P conserving parameters. For the C or P violating parameters, the correlations are small at both energies [127]. In scenarios in which there is no Higgs boson and new strong interactions at high energies occur, the anomalous triple gauge couplings translate into a mass scale for the new physics around 10 TeV, i.e. far beyond the energy where unitarity breaks down in this case [7].

Additional information on the triple gauge couplings can be obtained from the $e\gamma$ and $\gamma\gamma$ options of the ILC. In this case, only the $WW\gamma$ couplings can be measured without ambiguities from the WWZ couplings. It is often claimed that these options are particularly sensitive because of the large cross sections and because the leading contributions depend on the triple gauge couplings. However, in $e\gamma \rightarrow W^- \nu$ and $\gamma\gamma \rightarrow W^+ W^-$, no gauge cancellations occur so that the sensitivity is reduced. Detailed studies have shown that for the coupling κ_γ , the e^+e^- mode is by far superior, while for the coupling λ_γ competitive results can be obtained [128, 129]. Figure 3.3 compares the κ_γ and λ_γ measurements at different machines. Particularly for the coupling κ which, because of its lower mass dimension is interesting to study, the measurement at the ILC is an order of magnitude better than the one at the LHC.

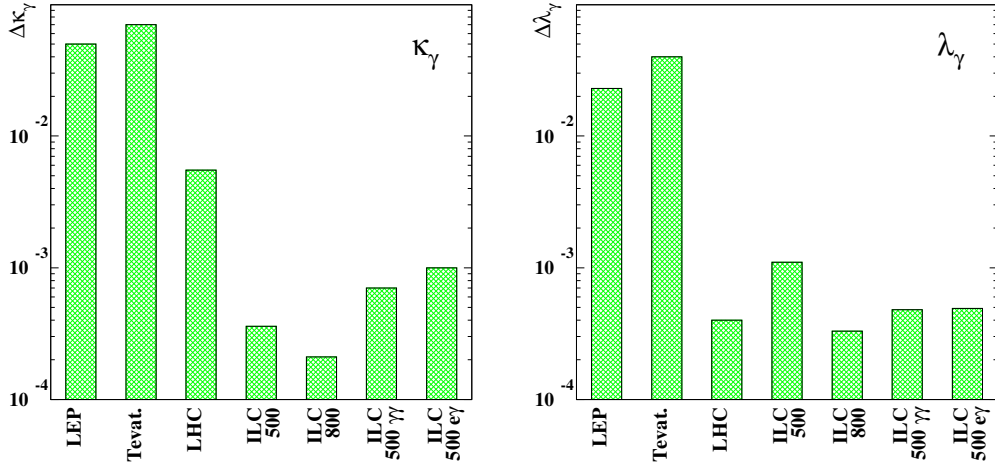


FIGURE 3.3. Comparison of $\Delta\kappa_\gamma$ and $\Delta\lambda_\gamma$ at different machines. For LHC and ILC three years of running are assumed (LHC: 300 fb^{-1} , ILC $\sqrt{s} = 500 \text{ GeV}$: 500 fb^{-1} , ILC $\sqrt{s} = 800 \text{ GeV}$: 1000 fb^{-1}). If available the results from multi-parameter fits have been used.

3.2.2 Measurements of the quartic couplings

In addition to the triple electroweak gauge boson couplings, the ILC is also sensitive to the quartic couplings. Two processes are important in this context: triple gauge boson production, $e^+e^- \rightarrow VVV$, and vector boson scattering, $e^+e^- \rightarrow \ell_1\ell_2 VV'$ with $\ell_{1,2} = e, \nu$ and $V, V' = W, Z$. In vector boson scattering, the underlying process is the quasi-elastic scattering $V_1V_2 \rightarrow V_3V_4$. The subprocesses with initial Z bosons are, however, suppressed as a result of the small Zee couplings. Nevertheless $WZ \rightarrow WZ$ and $ZZ \rightarrow ZZ$ are of some use in the case where no custodial $SU(2)$ invariance is assumed.

In the SM in which a light Higgs boson is absent, unitarity requires that the interaction among gauge bosons becomes strong at high energies. In this case, the physics of EWSB below the symmetry breaking scale is described by the most general effective Lagrangian for the Goldstone bosons required by the spontaneous $SU(2)_L \times U(1)_Y \rightarrow U(1)_Q$ breaking. This Lagrangian describes the physics of longitudinal gauge bosons and its parameters can be probed in their interactions. The most general C and P conserving effective Lagrangian contains 10 dimension-four interactions $L_{1,\dots,10}$ [130]. As the SM accounts for the small deviation of the $\rho = M_W^2/(\cos^2\theta_W M_Z^2)$ parameter from unity, a custodial $SU(2)_c$ symmetry appears to be conserved and, in a first step, one can restrict the analyses to the five $SU(2)_c$ invariant and linearly breaking operators. Three of them contribute to the triple gauge boson couplings, while the remaining two contribute only to the quartic couplings,

$$L_4 = \alpha_4 \text{tr}(V_\mu V_\nu) \text{tr}(V^\mu V^\nu), \quad L_5 = \alpha_5 \text{tr}(V_\mu V^\mu) \text{tr}(V_\nu V^\nu). \quad (\text{iv})$$

where V_μ simplifies to $-ig\frac{\sigma^i}{2}W_\mu^i + ig'\frac{\sigma^3}{2}B_\mu$ (B is the hypercharge gauge boson) in the unitarity gauge. The coefficients α_i are related to scales of new physics Λ_i^* by naive dimensional analysis, $\alpha_i = (v/\Lambda_i^*)^2$. In the absence of resonances that are lighter than $4\pi v$, one expects a strongly interacting symmetry breaking sector at a scale $\Lambda_i^* \approx 4\pi v \approx 3 \text{ TeV}$ which means the coefficients α_i are of order $1/16\pi^2$ unless they are suppressed by some symmetry.

Thus, the quartic electroweak gauge couplings can be parameterized in an almost model-independent way (only the custodial $SU(2)$ symmetry can be assumed for simplicity) by the

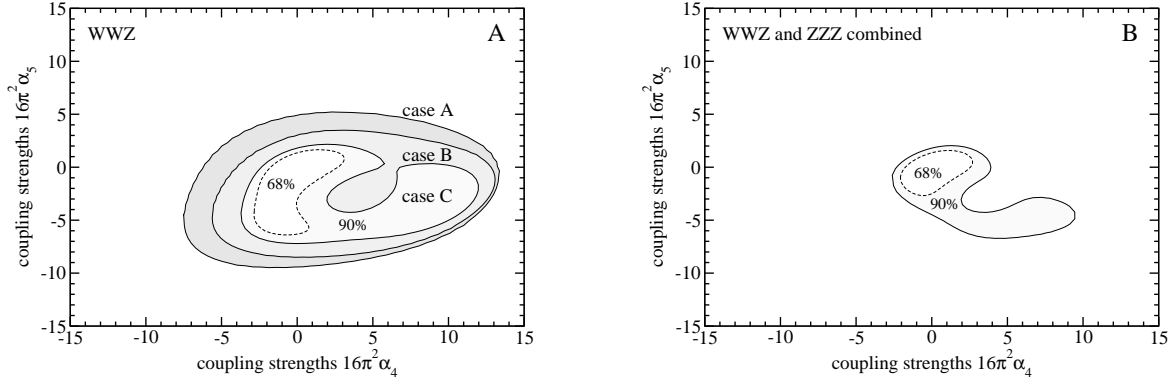


FIGURE 3.4. Expected sensitivity for α_4, α_5 at the ILC with $\sqrt{s} = 1$ TeV and 1 ab^{-1} from the $e^+e^- \rightarrow VVV$ channels [131]. Left: the WWZ channel for unpolarized (A), only e^+ polarized (B) and both e^\pm polarized (C) beams. Right: combined fit using WWZ and ZZZ for e^\pm polarized beams. Lines represent 90% The outer (inner) line represents 90% (68%) confidence level.

operators L_4 and L_5 and their coefficients α_4 and α_5 can be determined or constrained by studying, for instance, quasi-elastic gauge boson scattering at high energies. In fact, the sensitivity of the quartic couplings to the two parameters rises strongly with energy and useful results can be obtained only with the upgrade of the ILC to the energy of 1 TeV.

Within the generic effective-field theory context discussed above, all processes that contain quasi-elastic weak boson scattering, $e^+e^- \rightarrow \ell\ell V^*V^* \rightarrow \ell\ell VV$, and triple weak boson production, $e^+e^- \rightarrow VVV$, have been recently reanalyzed [131]. The study uses complete six-fermion matrix elements in unweighted event samples, fast simulation of the ILC detector and a multidimensional parameter fit of the set of anomalous couplings. It also includes a study of triple weak boson production which is sensitive to the same set of anomalous couplings. In the case where the simplifying assumption of custodial symmetry is used, the results are illustrated in Figs. 3.4 for the $e^+e^- \rightarrow WWZ, ZZZ$ channels and Fig. 3.5a for the combination of both channels assuming a 1 TeV ILC with 1 ab^{-1} of data. As can be seen, an accuracy of the order of $1/(16\pi^2)$ can be obtained on the coefficients α_4 and α_5 .

With the assumption of conserved $SU(2)_c$ symmetry, the LHC obtains similar limits as those shown above. However, since the ILC can, contrary to the LHC, tag the initial and final state gauge bosons, the separation of couplings is possible without the need of this assumption. An example of constraints in this case, including the four-dimension operators L_6 and L_7 which break the custodial symmetry, is shown in Fig. 3.5b where the same energy and luminosity as above is assumed. Despite of the increase of the parameter space, the constraints are only a factor of two to three worse than in the conserved $SU(2)$ case.

Note that the limits on the parameters α_i can be interpreted in terms of heavy resonances; the constraints on the masses of these resonances depend strongly on the assumptions and vary between 1 and 4 TeV [131]. This aspect will be discussed in chapter 6.

3.3 THE STRONG INTERACTION COUPLING

Precision measurements in strong interaction processes will be part of the physics program of the ILC. Among the many aspects of perturbative QCD which can be studied at the collider, the measurement of the strong coupling α_s will represent one of the most important outcome.

The strong coupling α_s can be determined from event shape observables in $e^+e^- \rightarrow q\bar{q}g$

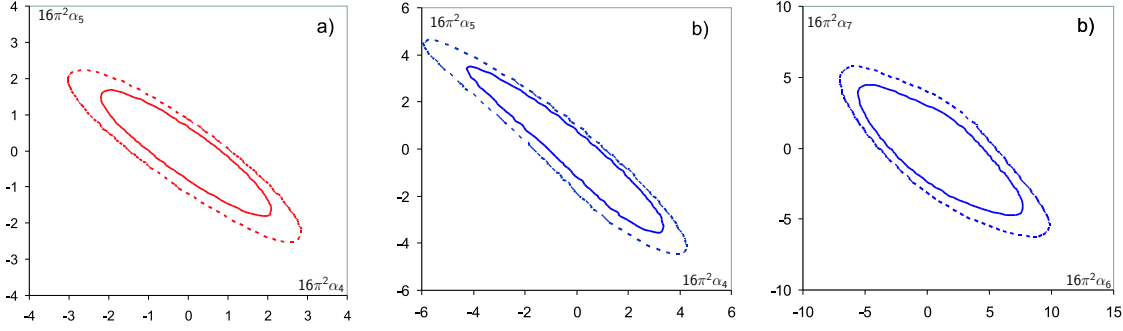


FIGURE 3.5. Limits of α_4 , α_5 assuming $SU(2)_c$ conservation (a) and $\alpha_4 - \alpha_7$ without this assumption (b) from a combined analysis of three-vector-boson production and of vector-boson scattering assuming 1000 fb^{-1} at $\sqrt{s} = 1 \text{ TeV}$. The dashed line represent 90% c.l. and the solid line 68%.

that are sensitive to the three-jet nature of the particle flow; examples of such observables are the thrust, jet masses and jet rates. In this method, one usually forms a differential distribution, applies corrections for detector and hadronization effects and fits a perturbative QCD prediction to the data, allowing α_s to vary. Measurements from LEP and SLC have shown that statistical errors below 0.001 can be obtained with samples of a few tens of thousands hadronic events. With the current ILC design luminosities, hundreds of thousands of $e^+e^- \rightarrow q\bar{q}$ events can be produced each year and a statistical error on $\alpha_s(M_Z)$ below 0.0005 can be achieved [132, 7]. The systematic error, however, is at present a factor ten larger than this value and it is not clear, how much it can be improved by higher order calculations.

The GigaZ option also provides the possibility for a very accurate determination of the value of $\alpha_s(M_Z)$ via the measurement of the inclusive ratio of the Z boson decay widths $R_{\text{had}} = \Gamma_{\text{had}}/\Gamma_\ell$. The current LEP data sample of $1.6 \cdot 10^6$ Z bosons provides an accuracy $\Delta\alpha_s(M_Z) = 0.0025$ from the ratio R_{had} [35]. At GigaZ, the statistical error can be lowered to the level of 0.0004 but systematic errors arising from the hadronic and leptonic event selection will probably limit the precision to $\Delta\alpha_s(M_Z) = 0.0008$ [133]. This would be a very precise and reliable measurement from a single and clean observable which is subject to very small theoretical uncertainties. Especially R_{had} is unaffected by any non-perturbative corrections.

The translation of the measurements of $\alpha_s(M_Z)$ discussed above to other energies, $\alpha_s(Q)$ with $Q \neq M_Z$, requires the assumption that the running of the coupling is determined by the QCD β function. Since the logarithmic decrease of α_s with energy is an essential component of QCD, reflecting the underlying non-Abelian dynamics of the theory, it is important also to test this energy dependence explicitly. Such a test would be particularly interesting if new colored particles were discovered, since deviations from QCD running would be expected at energies above the threshold for pair production of the new particles. Furthermore, extrapolation of α_s to very high energies of the order of $M_U = 10^{16} \text{ GeV}$ can be combined with corresponding extrapolations of the weak and electromagnetic couplings in order to constrain the coupling unification or the GUT scale. Hence, it would be desirable to measure α_s in the same detector, with the same technique and by applying the same treatment to the data, at a series of different energies Q , so as to maximize the lever-arm for constraining the running. This is shown in Fig. 3.6 where simulated measurements of $\alpha_s(Q)$ at $Q = 91, 500$ and 800 GeV are displayed, together with existing measurements in the range $20 \leq Q \leq 200 \text{ GeV}$ [132, 7].

It is therefore clear that ILC data adds significantly to the lever-arm in the energy evo-

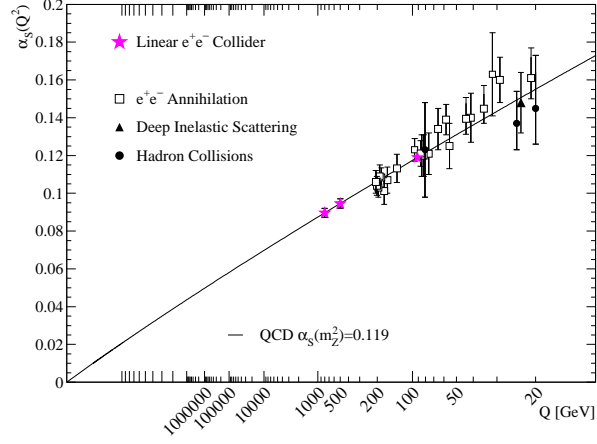


FIGURE 3.6. The evolution of α_s with $1/\ln Q$ from various measurements; the data points are from present ones and the stars denote simulated ILC measurements for $\sqrt{s} = 91, 500$ and 800 GeV.

lution of α_s and allows a substantially improved extrapolation to the GUT scale. This is exemplified in Fig. 3.7 where the evolution of the three gauge couplings is displayed. The measurements at GigaZ will support unification at a scale $M_U \simeq 2 \times 10^{16}$ GeV, with a precision at the percent level. However, the couplings are not expected to meet exactly because of the high threshold effects at the scale M_U . The quantitative evaluation of the discrepancy will provide important constraints on the particle content at the GUT scale.

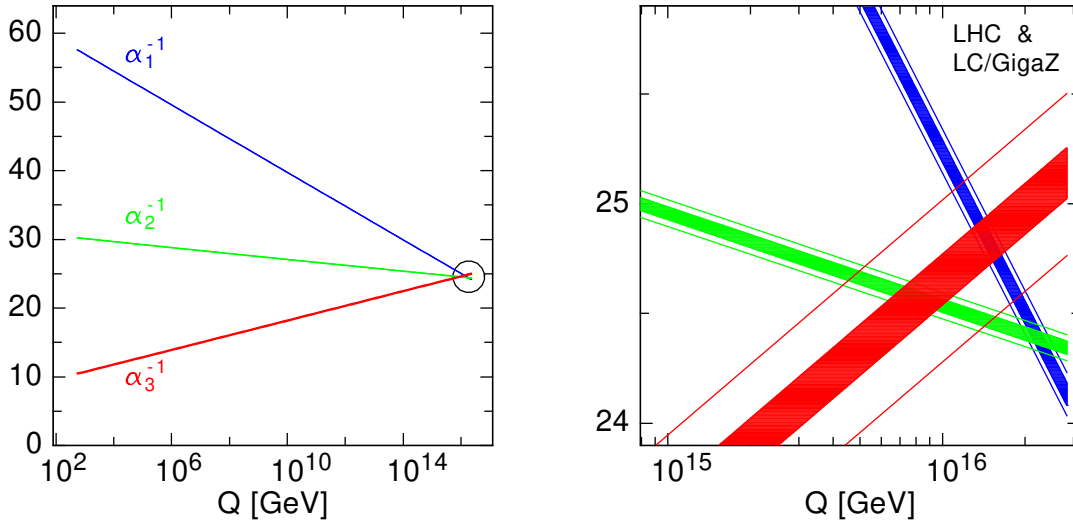


FIGURE 3.7. Extrapolations of the gauge couplings as measured at ILC to the unification scale [134].

Many other aspects of QCD can be addressed at the ILC. In particular, the $\gamma\gamma$ and $e\gamma$ options offer a broad new area of QCD studies in two-photon interactions at high energy and luminosity. Examples are (see also chapter 4 for QCD studies in the process $e^+e^- \rightarrow t\bar{t}$) [7] the total cross section, the photon structure function and the annihilation of virtual photons as a test of BFKL dynamics.

CHAPTER 4

Top quark physics

The top quark is the heaviest particle in the Standard Model and, thus, the most strongly coupled to the electroweak symmetry breaking sector; it is therefore expected to play a fundamental role in the dynamics behind the symmetry breaking mechanism. It might also hold clues in solving the longstanding flavor problem and provide clear indications on new physics beyond the Standard Model. For instance, if the Higgs mechanism should be verified, the measurement of the top quark Yukawa coupling would help to discriminate between SM and non-standard Higgs scenarios. If the new physics beyond the SM is sufficiently decoupled, shifts in the production and decay properties of a SM-like top quark may be the only evidence for it. With the precision ILC measurements, one could have sensitivity to new physics at mass scales far above the electroweak symmetry breaking scale. For example, it has been shown [124, 135] that in warped extra-dimensional models, as the top quark has a wavefunction that is near the TeV brane, its production cross section at the ILC can reveal Kaluza–Klein excitations of gauge bosons with masses up to 10–100 TeV.

Precise and model-independent measurements at the ILC of the top couplings to weak gauge bosons will be sensitive to interesting sources of non-SM physics as many models predict anomalous top quark couplings. In Technicolor and other models with a strongly-coupled Higgs sector, non-standard CP-conserving couplings may be induced at the 5–10% level [136]. In supersymmetric and multi-Higgs models, CP-violating couplings may be induced at the one-loop level, with predictions in the range 10^{-3} – 10^{-2} [137]. Little Higgs or top-seesaw models predict definite shifts in the top quark couplings to the W and Z bosons.

High-precision measurements of the properties and interactions of the top quark are therefore mandatory. The ILC will have broad capabilities to outline the top quark profile with high precision and in a model-independent way. In particular, the $t\bar{t}$ threshold holds the promise of very precise measurements of the top quark mass and total decay width. Both at threshold and in the continuum, the neutral and charged current interactions of the top quark can be very precisely determined. Its vector and axial-vector couplings to the Z boson in the production vertex and to the W boson in the decay vertex, as well as its magnetic and electric dipole moments, could be measured at the one percent level. The high luminosity expected at the ILC will allow to determine the important top quark Yukawa coupling to the Higgs boson with a precision greatly exceeding that foreseen at the LHC.

Finally, if the threshold of new physics is nearby, new decay channels of the top quark, such as decays into a charged Higgs boson in supersymmetric or multi-Higgs doublet models, may be observed and studied in detail in the clean environment of the ILC.

4.1 THE TOP QUARK MASS AND WIDTH

The top quark mass is a fundamental parameter of the SM and also a crucial ingredient of the electroweak precision measurement program, hence the importance to measure it as accurately as possible [138]. In many extensions to the SM in which the Higgs boson mass can be calculated, the theoretical prediction for M_H^2 depends sensitively on m_t . For instance, in the minimal supersymmetric extension of the SM, the radiative corrections grow as m_t^4 [41]. In this case, the expected LHC precision of 1 GeV on m_t translates into a similar uncertainty for the predicted value of the lighter Higgs boson mass M_h [41]. The anticipated accuracy at the ILC is more than an order of magnitude better, obtaining a parametric error small enough to allow for a very incisive comparison of theory and measurement. A smaller uncertainty on m_t also improves the sensitivity to new physics causing anomalous W and Z couplings [139, 137].

Because of its large width, $\Gamma_t \sim 1.5$ GeV, the top quark will decay before it hadronizes, thus non-perturbative effects are expected to be highly suppressed. As a result, the energy dependence of the cross section $\sigma_{t\bar{t}}$ for $e^+e^- \rightarrow t\bar{t}$ can be computed reliably, with an expected increase in rate by a factor of ten as the center-of-mass (CM) energy is varied by 5 GeV around the threshold energy. The location of the rise of the cross section can be used to extract the value of m_t , while the shape and normalization yield information about the total width Γ_t , the strong coupling α_s and eventually, the $t\bar{t}H$ Yukawa coupling $g_{t\bar{t}H}$ [140]. In Ref. [141], three threshold observables: $\sigma_{t\bar{t}}$, the peak of the top momentum distribution, and the forward-backward charge asymmetry, were simultaneously fitted to obtain measurement uncertainties on m_t , Γ_t , α_s of 19 MeV, 32 MeV, and 0.0012, respectively. However this study did not include a complete evaluation of important systematic uncertainties, such as e.g. the determination of the luminosity spectrum or theoretical uncertainties on differential observables. Figure 4.1 (left) demonstrates the sensitivity of the top mass measurement to these observables. It is expected that the top mass can be measured with a statistical uncertainty of 40 MeV in a modest scan of 10 fb^{-1} , a small fraction of a year at typical design luminosities. A longer scan of about 100 fb^{-1} can determine the top width to 2%.

The threshold cross section has been calculated including some of the next-to-next-to-leading logarithmic (NNLL) QCD corrections, as shown in Fig. 4.1 (right) [142, 143]. The full NNLL contribution is not yet available, but the large size of the corrections relative to the NLL terms [144] suggests that the theoretical uncertainty on the cross section will ultimately be approximately $\delta\sigma_{t\bar{t}}/\sigma_{t\bar{t}} \sim \pm 3\%$, but the effect on the mass determination is small.

The high-precision measurements of the ILC at the $t\bar{t}$ threshold will determine a “threshold” (or resonance) mass parameter with an accuracy significantly below 100 MeV. This threshold mass can then be translated into another short-distance mass that is useful as a theory input, such as the $\overline{\text{MS}}$ mass. This translation will give rise to an additional theoretical uncertainty. The current estimate for the combined experimental and theoretical uncertainty in the determination of the top-quark mass is about 100 MeV [145].

A threshold scan will require precise knowledge of the average c.m. energy and the shape of the luminosity spectrum $d\mathcal{L}/dE$ [146]. Schemes for precision measurement of $\langle E_{cm} \rangle$ include the use of beam spectrometers or using physics processes such as Z boson pair production or radiative returns to the Z . The luminosity spectrum is determined by the beam spread, beamstrahlung and initial state radiation (ISR). All three effects will lead to a smearing of the $t\bar{t}$ threshold cross section, resulting in a significant reduction of the effective luminosity and hence the observed cross section, $\sigma^{\text{obs}}(\sqrt{s}) = \mathcal{L}_0^{-1} \int_0^1 \mathcal{L}(x) \sigma(x\sqrt{s}) dx$.

The influence of the three effects is demonstrated in Fig. 4.2. The beam spread will

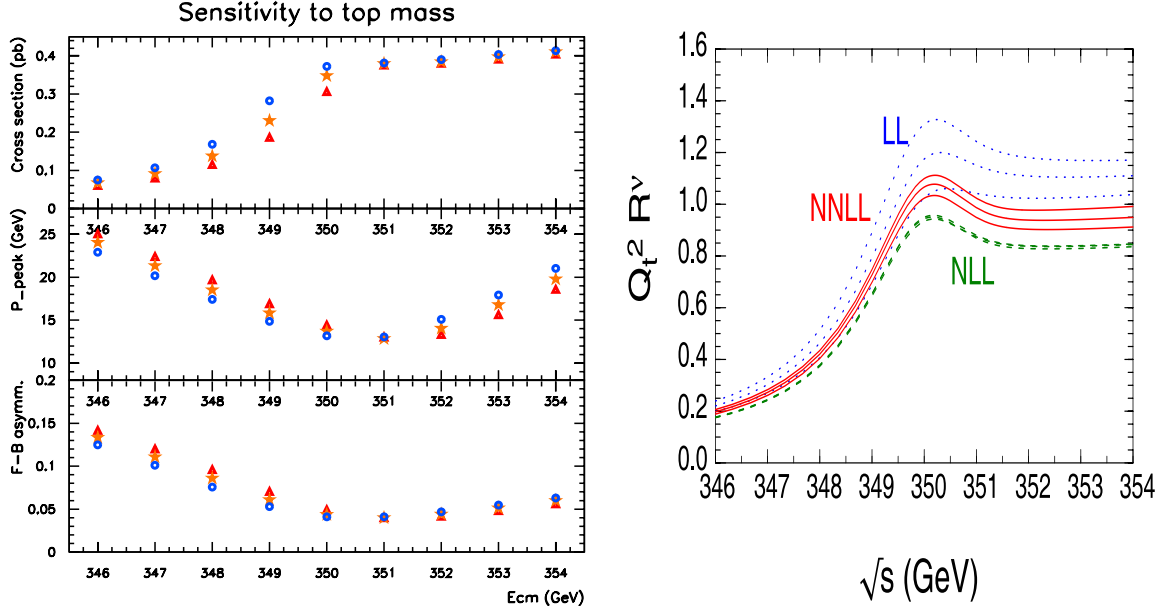


FIGURE 4.1. Left: sensitivity of the observables to the top mass in a c.m.energy scan around the $t\bar{t}$ threshold with the different symbols denoting 200 MeV steps in top mass [141]. Right: dependence of the $e^+e^- \rightarrow t\bar{t}$ cross section on the c.m.energy in various approximations for QCD corrections [143].

typically be $\sim 0.1\%$ and will cause comparably little smearing (though additional beam diagnostics may be required to measure and monitor the beam spread), but beamstrahlung and ISR are very important. The luminosity spectrum will lead to a systematic shift in the extracted top mass which must be well understood; otherwise it could become the dominant systematic error. The proposed method is to analyze the acollinearity of (large angle) Bhabha scattering events, which is sensitive to a momentum mismatch between the beams but insensitive to the absolute energy scale [147]. For this, the envisioned high resolution of the forward tracker will be very important to achieve an uncertainty on the order of 50 MeV.

Including all these contributions, a linear collider operating at the $t\bar{t}$ threshold will be able to measure m_t with an accuracy of $\sim 100 - 200$ MeV. This can be compared with the current accuracy of ~ 2 GeV at the TeVatron and possibly ~ 1 GeV at LHC [12].

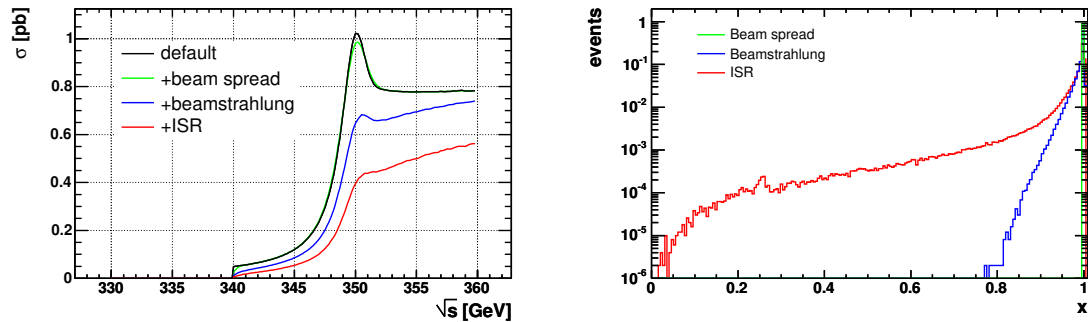


FIGURE 4.2. Left: Smearing of the theoretical $t\bar{t}$ cross section ('default') by beam effects and initial state radiation. Right panel: Simulation of beam spread, beamstrahlung and ISR as distributions of $x = \sqrt{s}/\sqrt{s_0}$ (where $\sqrt{s_0}$ is the nominal c.m. energy of the machine). From Ref. [148].

4.2 TOP QUARK INTERACTIONS

4.2.1 The coupling to the Higgs boson

Near threshold, the $t\bar{t}$ pair interacts, in addition to the QCD potential, via a Yukawa potential associated with Higgs boson exchange. For a low Higgs boson mass, the $t\bar{t}$ cross section is *a priori* sensitive to the top-Higgs Yukawa coupling, g_{tH} [141]. Even more sensitive is the measurement of the $e^+e^- \rightarrow t\bar{t}H$ cross section in the continuum, which is essentially proportional to g_{tH}^2 as discussed in chapter 2.

At the ILC with energies larger than 500 GeV, the process $e^+e^- \rightarrow t\bar{t}H$ with the Higgs decaying to W^+W^- or $b\bar{b}$ has the relatively clean signature of ≥ 6 jets in final state, with 4 b -jets and multi-jet invariant mass constraints, but with backgrounds about three orders of magnitude larger. The dominant backgrounds are radiative top production and/or decay ($t\bar{t}$ +jets) and irreducible $t\bar{t}Z(Z \rightarrow b\bar{b})$ [149]. For Higgs bosons with 120–200 GeV masses, studies with events processed through a realistic detector simulation and involving rather sophisticated event selection procedures, have been performed [102, 101]. They demonstrate that one can measure g_{tH} to 6–10% precision at $\sqrt{s} = 800$ GeV with 1 ab^{-1} data [101]. However, even a 500 GeV ILC can significantly improve our knowledge of the $t\bar{t}H$ Yukawa coupling and accuracies up to 10% can be achieved in the low Higgs mass range [102].

A recent reexamination of the LHC measurement of the coupling suggests it will be challenging to reach this level of precision. However, when combined with ILC results at $\sqrt{s} = 500$ GeV, LHC does better. ILC precision measurement of $\text{BR}(H \rightarrow W^+W^-)$ and $\text{BR}(h \rightarrow b\bar{b})$ replaces theory assumptions in the LHC measurements and leads to a better combined uncertainty of 10–15% or better for a large range of M_H values [15, 67, 102]. Therefore, for a number of years, the combination of results at the LHC and ILC (500 GeV) would yield the most precise determination of the top quark Yukawa coupling.

4.2.2 Couplings to electroweak gauge bosons

Since the charged electroweak current is involved in the top decay, $t\bar{t}$ production in e^+e^- collisions is sensitive to both the neutral and charged gauge boson couplings of the top quark, and in the neutral case, directly sensitive to both the $t\bar{t}\gamma$ and $t\bar{t}Z$ vertices. Because the top quark width, Γ_t , is much larger than Λ_{QCD} , the decay process is not influenced by fragmentation effects and decay products will provide useful information.

The most general $t\bar{t}(\gamma, Z)$ couplings can be written as [150, 151]

$$\Gamma_{t\bar{t}(\gamma, Z)}^\mu = i e \left\{ \gamma^\mu \left[F_{1V}^{\gamma, Z} + F_{1A}^{\gamma, Z} \gamma^5 \right] + \frac{(p_t - p_{\bar{t}})^\mu}{2 m_t} \left[F_{2V}^{\gamma, Z} + F_{2A}^{\gamma, Z} \gamma^5 \right] \right\}, \quad (\text{i})$$

where the only form factors different from zero in the SM are

$$F_{1V}^\gamma = \frac{2}{3}, \quad F_{1V}^Z = \frac{1}{4 \sin \theta_W \cos \theta_W} \left(1 - \frac{8}{3} \sin^2 \theta_W \right), \quad F_{1A}^Z = -\frac{1}{4 \sin \theta_W \cos \theta_W}. \quad (\text{ii})$$

$(e/m_t) \cdot F_{2A}^\gamma$ is the electric dipole moment form factor of the top quark and $(e/m_t) \cdot F_{2A}^Z$ the weak electric dipole moment; $(e/m_t) \cdot F_{2V}^{\gamma, Z}$ are the electric and weak magnetic dipole moments. In the SM, the electric and dipole moment terms violate CP and receive contributions only at the three-loop level and beyond. The CP-conserving form factors are zero at tree-level but receive non-zero $\mathcal{O}(\alpha_s)$ QCD corrections.

TABLE 4.1

The 1σ statistical uncertainties for the real parts of the $(\gamma, Z)t\bar{t}$ form factors obtained from an analysis of the process $e^+e^- \rightarrow t\bar{t} \rightarrow \ell^\pm + \text{jets}$ for $\sqrt{s} = 500$ GeV. Only one coupling at a time is varied.

| Coupling | LO SM Value | $\mathcal{P}(e^-)$ | $\int \mathcal{L} dt$ (fb $^{-1}$) | 1σ sensitivity |
|-----------------|-------------|--------------------|-------------------------------------|-----------------------|
| F_{1A}^γ | 0 | ± 0.8 | 100 | 0.011 |
| F_{1A}^Z | -0.6 | -0.8 | 100 | 0.013 |
| F_{1V}^γ | 2/3 | ± 0.8 | 200 | 0.047 |
| F_{1V}^Z | 0.2 | ± 0.8 | 200 | 0.012 |
| F_{2A}^γ | 0 | +0.8 | 100 | 0.014 |
| F_{2A}^Z | 0 | +0.8 | 100 | 0.052 |
| F_{2V}^γ | 0 | ± 0.8 | 200 | 0.038 |
| F_{2V}^Z | 0 | ± 0.8 | 200 | 0.009 |

In Table 4.1 is shown the 1σ sensitivity limits for the real parts of the $t\bar{t}(\gamma, Z)$ form factors obtained from an analysis of the process $e^+e^- \rightarrow t\bar{t} \rightarrow \ell^\pm + \text{jets}$ at $\sqrt{s} = 500$ GeV [9]. Top quarks are selected and reconstructed, and b quarks are tagged using a detector model with combined efficiency of 20%, and purity of 88%. To extract limits on $F_{1V}^{\gamma, Z}$ and $F_{1A}^{\gamma, Z}$, the angular distribution of the reconstructed top quark can be used. At the the ILC limits on $F_{2A}^{\gamma, Z}$ may be obtained from CP-violating angular asymmetries of the decay leptons, without assuming the tbW couplings to be vanishing [152]. Longitudinal e^- beam polarization can be used to enhance the sensitivity, as well as to obtain independent limits on F_{2A}^γ and F_{2A}^Z , when both are simultaneously kept nonzero. Combinations of decay lepton energy and angular asymmetries can be made sensitive to anomalous couplings either in the production or the decay by a suitable choice of cuts on the lepton energy [153].

$F_{1V}^{\gamma, Z}$ and $F_{2V}^{\gamma, Z}$ are derived from the left-right polarization asymmetry A_{LR} and $F_{2A}^{\gamma, Z}$ from the angular distribution of the reconstructed top quark and the decay angles of the t and \bar{t} . The limits shown in Table 4.1 could be strengthened with positron beam polarization, mostly from the increased $t\bar{t}$ cross section: with $\mathcal{P}_{e^+} = 0.5$, $\sigma(t\bar{t})$ is about a factor 1.45 larger, improving the precision in the measurement of A_{LR} by nearly a factor of 3 [17]. Increasing the c.m. energy to $\sqrt{s} = 800$ GeV improves the limits by a factor 1.3–1.5 [154].

The most general tbW couplings can be parameterized in the form [151]

$$\Gamma_{tbW}^\mu = -\frac{g}{\sqrt{2}} V_{tb} \left\{ \gamma^\mu [f_1^L P_L + f_1^R P_R] - \frac{i \sigma^{\mu\nu}}{M_W} (p_t - p_b)_\nu [f_2^L P_L + f_2^R P_R] \right\}, \quad (\text{iii})$$

where $P_{R,L} = \frac{1}{2}(1 \pm \gamma_5)$. In the limit $m_b \rightarrow 0$, f_1^R and f_2^L vanish and, in the SM, $f_1^L = 1$ and all other form factors are zero at tree-level. The $t\bar{t}W$ vertex can be parameterized similarly.

The f_2^R coupling, corresponding to a V+A tbW interaction, can be measured in $t\bar{t}$ decays with a precision of about 0.01 for $\sqrt{s} = 500$ GeV and 500 fb $^{-1}$ if electron and positron beam polarization are available [151]. This quantity can also be measured at the LHC, but the expected limit is a factor three to eight weaker [155].

The ILC can measure the tbW interaction to significant precision by studying $t\bar{t}$ production below threshold [156]. At c.m. energies below $2m_t$ but still above m_t , the total rate for $e^+e^- \rightarrow W^+W^-b\bar{b}$ is dominated by contributions from the virtual $t\bar{t}$ diagrams in a kinematic configuration where one top is on-shell and the other is off-shell. Other contributions include

single top quark production and, to a smaller extent, non-resonant interfering backgrounds. The rate becomes very sensitive to the tbW interaction, essentially because the narrow width approximation is no longer valid when the top momentum is off-shell.

For simplicity, the analysis focuses on the case of all couplings but f_1^L equal to zero and defines the effective V–A coupling as $g_{tbW} = gV_{tb}f_1^L$. Only the semi-leptonic six-body final state where one W boson decays to a pair of jets and the other into an readily tagged lepton (e , μ or τ), is considered. Combining the below-threshold cross section measurement with the Γ_t extracted from the threshold scan permits extraction of g_{tbW} and Γ_t independently. Under the assumption that the width is measured to an accuracy of 100 MeV, g_{tbW} can be measured to the 3% level, which would represent better than a factor of two improvement compared to the LHC.

Figure 4.3 shows the expected bounds on the SM-like top axial $t\bar{t}Z$ and left-handed tbW interactions and the discriminating power the bounds can place on new physics models. Included in the plot are the 1σ constraints on the independently varied axial $t\bar{t}Z$ coupling from the LHC and ILC [9], and the direct constraints on the left-handed tbW coupling from the LHC [155]. Predicted deviations from a few representative models are also superimposed: a Little Higgs model with T-parity, a model of top-flavor, and a model with a sequential fourth generation whose quarks mix substantially with the third family. The little Higgs model with T-parity has a heavy top quark partner T with a mass assumed to be $m_T = 500$ GeV (the numbers on the plot indicate the strength of the hTt interaction); the top-flavor model has a mixing angle $\sin\phi = 0.9$ (numbers indicate the mass of the heavy Z'). Top-seesaw models generate the same mixing effect as the little Higgs models and, thus, trace out the same line in the plane of deviations in the $t\bar{t}Z$ and tbW as the seesaw model parameters are varied.

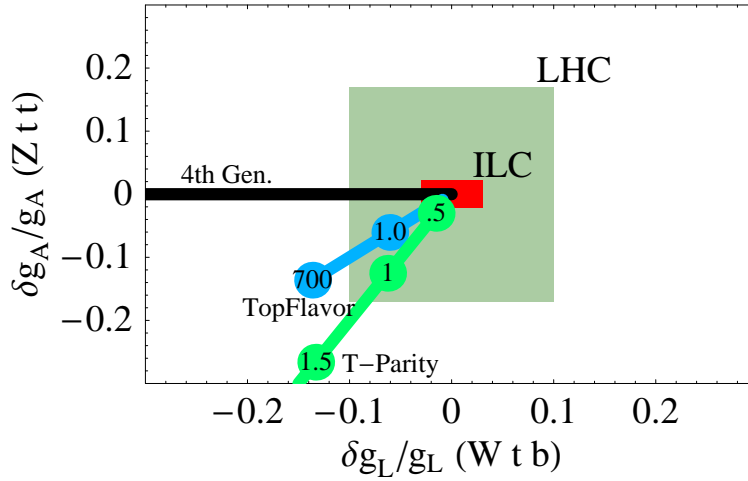


FIGURE 4.3. Expected bounds on axial $t\bar{t}Z$ and left-handed tbW couplings from direct LHC (olive) and ILC (red) measurements; superimposed are predicted deviations from representative models [156].

Finally, the ILC has excellent reach for the measurement of the tensor coupling tZq ; see for instance Ref. [157]. At the ILC, both the anomalous production $e^+e^- \rightarrow tq$ and decay $e^+e^- \rightarrow t\bar{t}, t \rightarrow Vq$ mechanisms can be explored, permitting sensitivity to flavor changing neutral current interactions. With 45% positron and 80% electron polarization at $\sqrt{s} = 500$ GeV, 100 fb $^{-1}$ of data would result e.g. in a sensitivity to $\text{BR}(t \rightarrow \gamma q)$ of 2×10^{-5} . The search sensitivity might be significantly increased if the ILC runs in the $\gamma\gamma$ mode [158].

4.2.3 Couplings to gluons

The ILC can be competitive with and complementary to the LHC in the measurement of the strong top quark coupling to gluons and would allow more refined tests of perturbative QCD [7]. Hard gluon radiation in $t\bar{t}$ events [159] would allow several tests of the strong dynamics of the top quark: test of the flavour-independence of strong interactions, limits on anomalous chromo-electric and/or chromo-magnetic dipole moments [160] and the determination of the running top quark mass. In turn, soft gluon radiation in $t\bar{t}$ events is expected to be strongly regulated by the large top mass and width and would provide additional constraints on the total decay width Γ_t [161]. Color reconnection and Bose-Einstein correlations are also important to study precisely [162] as they may affect the precision with which the top quark mass can be reconstructed kinematically via their multijet decays.

Furthermore, polarized electron and positron beams can be exploited to test symmetries using multi-jet final states. For polarized e^+e^- annihilation to three hadronic jets, one can define the triple product $\mathbf{S}_e \cdot (\mathbf{k}_1 \times \mathbf{k}_2)$, which correlates the e^- beam polarization vector \mathbf{S}_e with the normal to the three-jet plane defined by \mathbf{k}_1 and \mathbf{k}_2 , the momenta of the two quark jets. If the jets are ordered by momentum (flavour), the triple-product is CP-even (odd) and T-odd [163]. In the SM, the contributions to the T-odd form are expected to be very small and limits have been set for the $b\bar{b}g$ system. At the ILC, these observables will provide an additional possibility to search for anomalous effects in the $t\bar{t}g$ system.

4.3 NEW DECAY MODES

Besides the standard channel $t \rightarrow bW$, new decays of the top quark can occur in some extensions of the SM. The prominent example is the top quark decay into a charged Higgs boson, $t \rightarrow bH^+$, in supersymmetric extensions of the SM or in multi-Higgs doublet extensions. This channel has been mentioned in chapter 2 in the context of the MSSM and in this case, the coupling of the H^\pm bosons to top and bottom quarks is a mixture of scalar and pseudoscalar currents and depend only on the ratio of the vev 's of the two Higgs doublet fields $\tan\beta$,

$$g_{H^-tb} \sim m_b \tan\beta(1 + \gamma_5) + m_t \cot\beta(1 - \gamma_5) \quad (\text{iv})$$

The coupling is therefore very strong for small or large $\tan\beta$ values for which the m_t component is not suppressed or the m_b component is strongly enhanced. The branching ratio $\text{BR}(t \rightarrow bH^+) = \Gamma(t \rightarrow bH^+)/[\Gamma(t \rightarrow bW) + \Gamma(t \rightarrow bH^+)]$ is displayed in the left-hand side of Fig. 4.4 as a function of M_{H^\pm} for two values $\tan\beta = 3$ and 30. As can be seen, it is rather substantial being still at the per-mille level for H^+ masses as large as 150 GeV.

Since the cross section for top quark pair production is of the order of $\sigma(e^+e^- \rightarrow t\bar{t}) \sim 0.5$ pb at a $\sqrt{s} = 500$ GeV ILC, the cross section times the branching ratio for the production of one charged Higgs boson is rather large if M_{H^\pm} is not too close to m_t for the decay not to be suppressed by the small phase space. This is shown in the right-hand side of Fig. 4.4 where one can see that, for $M_{H^\pm} \lesssim 150$ GeV, the rates are of the same order of magnitude as the ones from direct pair production, $e^+e^- \rightarrow H^+H^-$, which is displayed for comparison.

In the M_{H^\pm} range under consideration, the main two-body decays of the charged Higgs boson will be into $\tau\nu_\tau$ and $c\bar{s}$ pairs with the former being largely dominating for the chosen $\tan\beta$ values; see Fig. 2.17. This results in a surplus of τ final states over e, μ final states, an apparent breaking of lepton universality. For low values of $\tan\beta$, the three-body decay

modes $H^\pm \rightarrow hW^*$, $AW^* \rightarrow b\bar{b}W$ will lead to multi b and W final states. These signals will be rather easy to be disentangled from the backgrounds in the clean ILC environment.

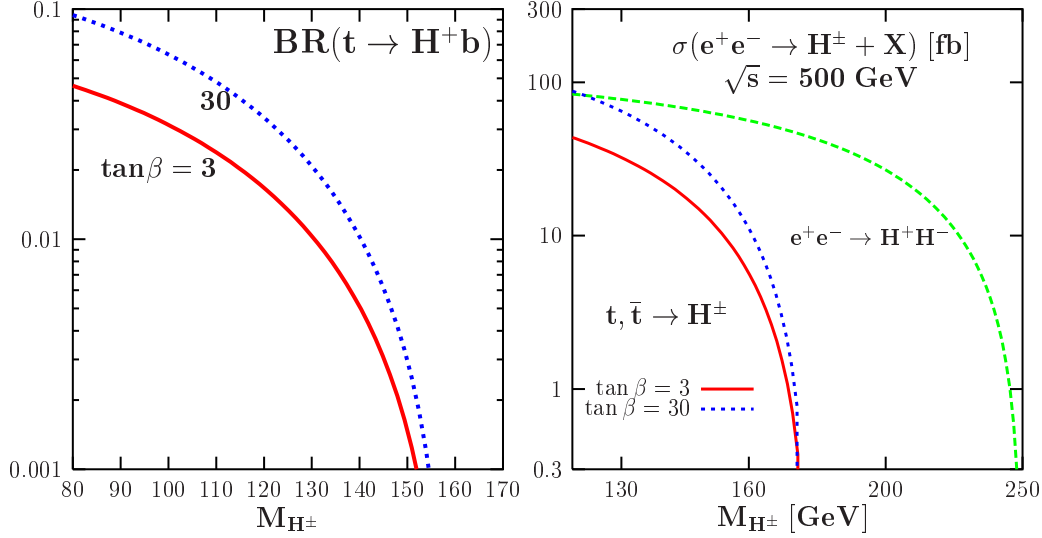


FIGURE 4.4. Left: the branching ratio for the decay $t \rightarrow H^+ b$ as a function of M_{H^\pm} for $\tan\beta = 3$ and 30 in the MSSM. Right: the cross sections times branching ratio for the production of one charged Higgs boson from top decays, $e^+e^- t\bar{t}$ and $t \rightarrow H^+ b$, at the ILC with $\sqrt{s} = 500$ GeV; the direct $e^+e^- \rightarrow H^+H^-$ cross section is shown for comparison. From Ref. [40].

This signal will be first observed at the LHC as it is one of the main discovery channels for charged Higgs bosons. However, the ILC will provide a very important information: the precise measurement of the $t \rightarrow H^+ b$ branching ratio would allow to determine the parameter $\tan\beta$ which is known to be rather difficult to access otherwise; see chapter 5.

In supersymmetric models, another possible and interesting decay mode of the top quark would be into its scalar partner \tilde{t}_1 and the lightest neutralino χ_1^0 which is supposed to form the dark matter in the universe, $t \rightarrow \tilde{t}_1 \chi_1^0$. In the minimal supersymmetric extension with universal masses for the superpartners of the gauge bosons at the high GUT scale, the phase space for this decay is squeezed by the constraints on the \tilde{t}_1 and χ_1^0 masses from LEP and the Tevatron. In non minimal extensions, the decay might be kinematically allowed and, in this case, branching ratios of the order of a few percent would be possible. Since the main decay modes of the top squark in this mass range are the loop induced $\tilde{t}_1 \rightarrow c\chi_0^1$ and the four-body $\tilde{t}_1 \rightarrow b\bar{f}\bar{f}\chi_0^1$ channels, the signal will consist on the missing energy due to the escaping neutralinos. While it is overwhelmed by huge QCD backgrounds at the LHC, this signature should be easy to detect at the ILC.

Finally, flavor changing neutral current (FCNC) decays of the top quark may be also observed. If new quark species exist and do not belong to the standard doublet/singlet assignments of isospin multiplets, they will mix with the top quark, breaking the GIM mechanism and allowing for FCNC top-charm couplings of order $\sqrt{m_t m_c}/M_X^2$ to be induced. In this case, besides breaking the universality of the $V - A$ chiral Wtb current, FCNC top quark decays such as $t \rightarrow c\gamma$ or $t \rightarrow cZ$ may occur at the level of a few permille and can be detected at the ILC [164]. However, the large number of top quarks produced at the LHC allows to search for these rare FCNC decays down to branchings ratio less than 10^{-4} .

CHAPTER 5

Supersymmetry

5.1 INTRODUCTION

5.1.1 Motivations for supersymmetry

Despite its enormous success in describing almost all known experimental data available today, the Standard Model (SM) is widely believed to be an effective theory valid only at the presently accessible energies. Besides the fact that it does not say anything about the fourth fundamental force of nature, the gravitational force, and does not explain the pattern of fermion masses, it has at least three severe problems which call for new physics. Given the high-precision data and the particle content of the SM, the energy evolution of the gauge coupling constants is such that they fail to meet at a common point, the grand unification (GUT) scale. Moreover, the SM does not include any candidate for a particle that is absolutely stable, fairly massive, electrically neutral and having only weak interactions, which accounts for the cold dark matter (DM) that makes up $\approx 25\%$ of the present energy of the universe. Finally, in the SM, the radiative corrections to the Higgs boson mass squared are quadratically divergent and M_H , which is expected to lie in the range of the electroweak symmetry breaking scale, $\mathcal{O}(100)$ GeV, prefers to be close to the cut-off scale beyond which the theory ceases to be valid, the very high GUT or Planck scales.

Supersymmetry (SUSY) [165], which predicts the existence of a partner to every known particle that differs in spin by $\frac{1}{2}$, is widely considered as the most attractive extension of the SM. Firstly, SUSY has many theoretical virtues [166]: it is the first non-trivial extension of the Poincaré group in quantum field theory which, when made local, necessarily includes Einstein's theory of gravity, and it appears naturally in superstring theories. These features may help to reach the ultimate goal of particle physics: the unification of all forces including gravity. However, the most compelling arguments for SUSY are phenomenological ones: when it is realized at low energies, it can solve at once all the above three problems of the SM. Indeed, the main reason for introducing low energy supersymmetric theories in particle physics is their ability to solve naturally the fine-tuning problem [167]: SUSY prevents M_H from acquiring very large radiative corrections as the quadratic divergent loop contributions of the SM particles are exactly canceled by the corresponding loop contributions of their supersymmetric partners. In fact, SUSY allows one to understand the origin of the electroweak symmetry breaking itself in terms of radiative corrections triggered by SUSY breaking [168], which must occur as the newly predicted superparticles have not been observed up to now

and must be thus heavy. In addition, the new SUSY particle spectrum contributes to the evolution of the three gauge couplings and allows their unification at a scale $M_{\text{GUT}} \simeq 2 \cdot 10^{16}$ GeV [169]. Finally, a discrete symmetry called R -parity [170] can be naturally present with the major consequence that the lightest supersymmetric particle (LSP) is absolutely stable; in many cases, this particle has the right properties and the required cosmological relic density to account for the cold DM [171, 172].

5.1.2 Summary of SUSY models

The most economical low-energy globally supersymmetric extension of the SM is the minimal supersymmetric Standard Model (MSSM) [173]. In this model, one assumes the minimal (SM) gauge group, the minimal particle content [i.e., three generations of fermions and their spin-zero partners as well as two Higgs doublet superfields to break the electroweak symmetry in a consistent manner], and R -parity conservation, which makes the LSP absolutely stable. In order to explicitly break SUSY, a collection of soft terms is added to the Lagrangian: mass terms for the gauginos, the SUSY spin- $\frac{1}{2}$ partners of the gauge bosons, mass terms for the sfermions, the spin-0 partners of the SM fermions, mass and bilinear terms for the two Higgs fields and trilinear couplings between sfermion and Higgs fields.

In the most general case, the soft SUSY-breaking terms will introduce a huge number of unknown parameters, $\mathcal{O}(100)$. However, in the absence of complex phases and intergenerational sfermion mixing and if the universality of the two first generations of sfermions is assumed, to cope in a simple way with the severe experimental constraints, this number reduces to $\mathcal{O}(20)$. Furthermore, if the soft SUSY-breaking parameters obey a set of boundary conditions at a high energy scale, all potential phenomenological problems of the general MSSM can be solved with the bonus that, only a handful of new free parameters are present. The underlying assumption is that SUSY-breaking occurs in a hidden sector which communicates with the visible sector only “flavor-blind” interactions, leading to universal soft breaking terms. This is assumed to be the case in the celebrated minimal supergravity (mSUGRA) model [174] or constrained MSSM (cMSSM) which is often used as a benchmark scenario in phenomenological analyses.

Besides the GUT scale which is derived from the unification of the three gauge coupling constants, the cMSSM has only four free parameters plus a sign:

$$m_0, m_{1/2}, A_0, \tan\beta, \text{sign}(\mu),$$

where $m_0, m_{1/2}$ and A_0 are, respectively, the common soft terms of all scalar (sfermion and Higgs) masses, gaugino (bino, wino and gluino) masses and trilinear scalar interactions, all defined at the GUT scale. $\tan\beta$ is the ratio of the vacuum expectation values (vev’s) of the two Higgs doublets at the weak scale and μ is the supersymmetric Higgs(ino) mass parameter. As in the MSSM in general, all soft SUSY-breaking parameters at the weak scale are then obtained via known Renormalization Group Equations (RGEs). The masses of the physical states, the spin- $\frac{1}{2}$ charginos $\chi_{1,2}^\pm$ and neutralinos $\chi_{1,2,3,4}^0$ which are mixtures of the SUSY partners of the gauge and Higgs bosons, the two scalar partners $\tilde{f}_{1,2}$ of the SM fermions and the five MSSM Higgs bosons h, H, A and H^\pm are then obtained by diagonalizing the relevant mass matrices. In this scenario, the LSP is in general the lightest neutralino χ_1^0 .

There are also other constrained MSSM scenarios with only a few basic input parameters, two of them being the anomaly (AMSB) [175] and gauge (GMSB) [176] mediated models in which SUSY-breaking also occurs in a hidden sector but is transmitted to the visible one by

anomalies or by the SM gauge interactions; in the later case, a very light gravitino is the LSP¹. On the other hand, one can slightly depart from the restrictive minimality of the MSSM and interesting examples are the CP violating MSSM [43] where some SUSY parameters can be complex, the NMSSM [49] in which the spectrum is extended to include a singlet superfield and R -parity violating models [178] in which the LSP is not stable.

The Terascale is a mystery that will be revealed by the LHC and the ILC and both machines will have an important role to play in deciphering it. In particular the high precision of the ILC will be necessary to understand the new physics, no matter which scenario nature has chosen. In this chapter, we will mainly focus on the unconstrained and constrained MSSMs defined above as they are very well defined and have been studied in great detail. These models provide us with an excellent testground for the opportunities offered by the high-energy colliders, the ILC in particular, in reaching out to new physics domains.

5.1.3 Probing SUSY and the role of the ILC

To prove and to probe supersymmetry, one not only needs to produce the new particles but also, and this is equally important, to verify its most fundamental predictions in a model independent way. A detailed investigation of the properties of the SUSY and Higgs particle spectrum is thus required and, in particular, one needs to:

- measure the masses and mixings of the newly produced particles, their decay widths and branching ratios, their production cross sections, etc...;
- verify that there are indeed the superpartners of the SM particles and, thus, determine their spin and parity, gauge quantum numbers and their couplings;
- reconstruct the low-energy soft-SUSY breaking parameters with the smallest number of assumptions, that is, in as model independent way as possible;
- ultimately, unravel the fundamental SUSY breaking mechanism and shed light on the physics at the very high energy (GUT, Planck?) scale.

Furthermore, the very precise knowledge of the properties of the lightest SUSY particle and its interactions with the standard and other SUSY particles is mandatory to predict the cosmological relic density of the DM, as well as its rates in direct and indirect detection astroparticle experiments. Achieving this goal would be the decisive test that a particular physics scenario is the solution of the DM puzzle and would lay an additional bridge between collider physics and the physics of the early universe.

In most areas of the MSSM parameter space, in particular in cMSSM type scenarios (except in the focus point scenario to be discussed later in chapter 7), the colored squarks and gluinos turn out to be much heavier than the non-colored sparticles, the sleptons as well as the charginos and neutralinos; see Fig. 5.1. If the masses of the former sparticles do not significantly exceed the TeV scale, as required from naturalness arguments, they can be copiously produced at the LHC either in pairs or in association [12, 13]. They will then decay in potentially long chains which end in the LSP neutralino that signals its presence only via missing energy. These decay chains will involve the other neutralinos and the charginos, and possibly the sleptons, so that one can have access to these weakly interacting particles as well. Typically, one faces a situation in which several SUSY particles are present in the same event, leading to rather complicated final state topologies which are subject to very large

¹In fact, in mSUGRA-like models, one can also have the gravitino being the LSP in large areas of the parameter space [177]; this issue will be discussed in the cosmology chapter.

backgrounds from the SM and, more importantly, from SUSY itself. At the LHC, sparticle mass differences can be determined by measuring the endpoints or edges of invariant mass spectra (with some assumptions on particle identification within the chains) and this results in a strong correlation between the extracted masses; in particular, the LSP mass can be constrained only weakly [15]. Therefore, only in specific constrained scenarios with a handful of input parameters, that some elements of SUSY can be reconstructed in the complicated environment of the LHC.

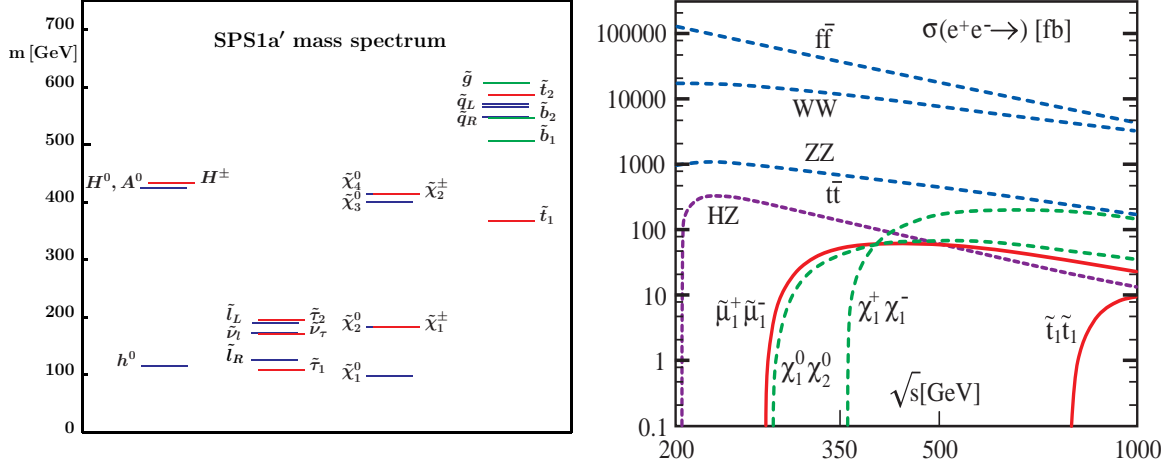


FIGURE 5.1. The spectrum of SUSY and Higgs particles in the benchmark SPS1a' cMSSM point [179] (left) and the production cross sections for various SM and SUSY processes in e^+e^- collisions as a function of the c.m. energy in this scenario (right).

On the other hand, the non-colored SUSY particles (and certainly the lightest Higgs boson) would be accessible at the ILC with a c.m. energy of $\sqrt{s} = 500$ GeV, to be eventually upgraded to 1 TeV. This is, for instance the case in a cMSSM typical scenario called SPS1a' [179] as shown in Fig. 5.1. The cross sections for chargino, neutralino and slepton pair production, when the states are kinematically accessible, are at the level of 10–100 fb, which is only a few orders of magnitude below the dominant SM background processes; Fig. 5.1. Given the expected high-luminosity and the very clean environment of the machine, large samples of events will be available for physics analyses [7, 180]. At the ILC, it will be thus easy to directly observe and clearly identify the new states which appeared only through cascade decays at the LHC. Most importantly, thanks to the unique features of the ILC, tunable energy which allows threshold scans, the availability of beam polarization to select given physics channels and additional collider options such as e^-e^- which allow for new processes, very thorough tests of SUSY can be performed: masses and cross sections can be measured precisely and couplings, mixing angles and quantum numbers can be determined unambiguously. Furthermore, the ILC will provide crucial information which can be used as additional input for the LHC analyses, as would be e.g. the case with the LSP mass. The coherent analyses of data obtained at the LHC and the ILC would allow for a better and model independent reconstruction of the low energy SUSY parameters, connect weak-scale SUSY with the more fundamental underlying physics at the GUT scale, and provide the necessary input to predict the LSP relic density and the connection with cosmology.

To highlight the unique abilities of the ILC to address these issues, we will often use for illustration the cMSSM benchmark SPS1a' point with basic inputs [179]:

$$m_{1/2} = 250 \text{ GeV}, m_0 = 70 \text{ GeV}, A_0 = -300 \text{ GeV}, \tan \beta = 10 \text{ and } \mu > 0,$$

which, using one of the RGE codes (SPHENO) of Ref. [181], leads to the SUSY spectrum of Tab. 5.1. This testcase point is close to the point SPS1a [182] with $m_0 = -A_0 = 100 \text{ GeV}$ and the same $m_{1/2}, \tan \beta$ and μ values, which has been used for detailed LHC [183, 184] as well as ILC analyses, but is not compatible anymore with all collider or cosmological constraints.

TABLE 5.1

Some superparticle and their masses (in GeV) for the cMSSM SPS1a' and SPS1a reference points.

| \tilde{p}/mass | χ_1^0 | χ_2^0 | χ_1^\pm | $\tilde{e}_1/\tilde{\mu}_1$ | $\tilde{e}_2/\tilde{\mu}_2$ | $\tilde{\nu}_e/\tilde{\nu}_\mu$ | $\tilde{\tau}_1$ | $\tilde{\tau}_2$ | $\tilde{\nu}_\tau$ | \tilde{t}_1 | \tilde{b}_1 |
|-------------------------|------------|------------|--------------|-----------------------------|-----------------------------|---------------------------------|------------------|------------------|--------------------|---------------|---------------|
| SPS1a' | 97.7 | 183.9 | 183.7 | 125.3 | 189.9 | 172.5 | 107.9 | 194.9 | 170.5 | 366.5 | 506.3 |
| SPS1a | 96.1 | 176.8 | 176.4 | 143.0 | 202.1 | 186.0 | 133.2 | 206.1 | 185.1 | 379.1 | 491.9 |

5.2 PRECISION SUSY MEASUREMENTS AT THE ILC

5.2.1 The chargino/neutralino sector

The two charginos $\chi_{1,2}^\pm$ and the four neutralinos $\chi_{1,2,3,4}^0$ are obtained by diagonalizing the mass matrices of the charged and neutral gauginos and higgsinos. For charginos, the matrix depends on the wino and higgsino mass parameters M_2 and μ and on $\tan \beta$; for neutralinos, the bino mass parameter M_1 enters in addition. These parameters determine to a large extent the production and decay properties of the χ_i^0, χ_i^\pm states that we will call “inos” for short.

Charginos are produced in pairs, $e^+e^- \rightarrow \chi_i^+ \chi_j^-$, through s -channel γ/Z boson and t -channel sneutrino exchanges; the latter contribution can be suppressed with polarized e_R^-/e_L^+ beams. Neutralino pair production, $e^+e^- \rightarrow \chi_i^0 \chi_j^0$, proceeds through s -channel Z boson and t - and u -channel $\tilde{e}_{L,R}$ exchanges. The ino states decay into lighter charginos and neutralinos and (possibly virtual) gauge or Higgs bosons as well as sfermion–fermion pairs; for the lighter inos, one would then have the topologies $\chi_1^\pm \rightarrow f \bar{f}' \chi_1^0$ and $\chi_2^0 \rightarrow f \bar{f} \chi_1^0$. These final states can be easily detected as the production cross sections are sizable and the backgrounds involving a large amount of missing energy are small.

The chargino masses can be determined in the continuum from the di-jet energy distributions in the process $e^+e^- \rightarrow \chi_1^+ \chi_1^- \rightarrow \ell^\pm \nu q \bar{q}' \chi_1^0 \chi_1^0$, which leads to a mass resolution $\Delta m_{\chi_1^\pm}/m_{\chi_1^0}$ at the permille level. This can serve to optimize a scan around threshold which, because of the steep $\sigma \propto \beta_\chi$ rise of the excitation curve with the velocity, would lead to a mass resolution $\Delta m_{\chi_1^\pm} = \mathcal{O}(50) \text{ MeV}$ for $m_{\chi_1^\pm} \sim 170 \text{ GeV}$; Fig. 5.2. The di-jet mass spectrum in χ_1^\pm decays allows also to determine the chargino–neutralino mass difference with a high precision, $\Delta(m_{\chi_1^\pm} - m_{\chi_1^0}) = \mathcal{O}(50) \text{ MeV}$, from which one can infer the mass of the escaping lightest neutralino. If the chargino happens to be almost degenerate with the LSP neutralino, as is typically the case in AMSB models, one can use ISR photons in the process $e^+e^- \rightarrow \chi_1^+ \chi_1^- \gamma$ to measure both the χ_1^\pm and $\chi_1^\pm - \chi_1^0$ masses from the spectra of, respectively, the photon recoil mass which peaks at $2m_{\chi_1^\pm}$ and the energy of the soft pions from $\chi_1^\pm \rightarrow \chi_1^0 + \pi_{\text{soft}}$ which peaks at $\Delta m_{\chi_1^\pm} - m_{\chi_1^0}$; Fig. 5.2. An uncertainty of a few percent is obtained in both cases.

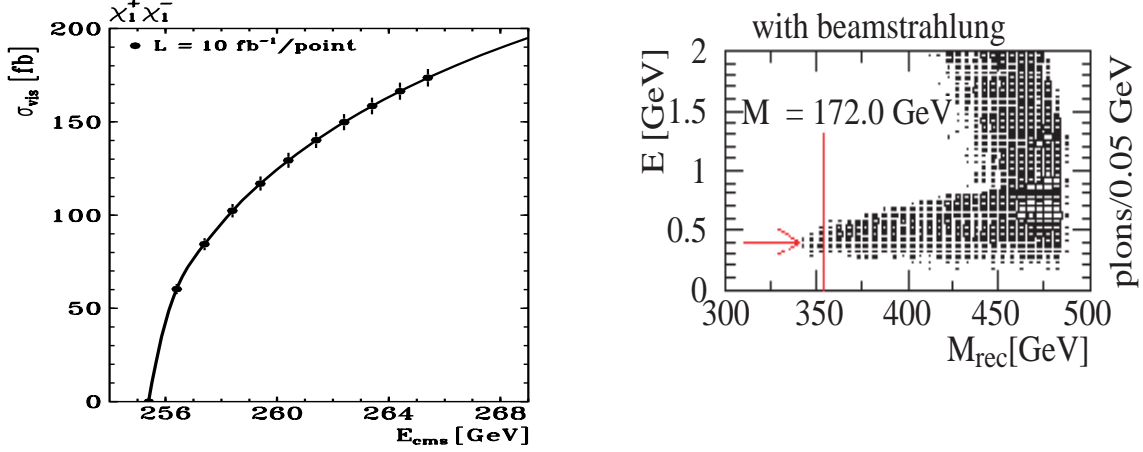


FIGURE 5.2. The cross section for $e_R^+ e_L^- \rightarrow \chi_1^+ \chi_1^- \rightarrow \ell^\pm \nu_\ell \chi_1^0 q \bar{q}' \chi_1^0$ near threshold, with the error bars obtained with a luminosity of 10 fb^{-1} per point [185] (left). The initial state radiated photon recoil mass for the process $e_R^+ e_L^- \rightarrow \chi_1^+ \chi_1^- \gamma \rightarrow \pi^+ \pi^- \gamma \cancel{E}$ (right) [186].

Similarly to the chargino case, the di-lepton mass and energy spectra in the process $e^+ e^- \rightarrow \chi_2^0 \chi_1^0 \rightarrow \ell^+ \ell^- \chi_1^0 \chi_1^0$, allow to determine the mass difference of the two neutralinos at the permille level. In the case where the neutralino χ_2^0 decays dominantly via a real or virtual stau lepton, $\chi_2^0 \rightarrow \tilde{\tau}_1 \tau \rightarrow \tau^+ \tau^- \chi_1^0$, which might occur at high $\tan \beta$ values that lead to light tau sleptons, the resolution on the χ_2^0 mass deteriorates to the level of a few percent. The reason is that the energy of the τ 's cannot be reconstructed because of the missing neutrinos and, in fact, this is also the case for charginos in the decays $\chi_1^\pm \rightarrow \tilde{\tau}_1^\pm \nu_\tau \rightarrow \tau^\pm \nu_\tau \chi_1^0$. A better mass resolution, $\mathcal{O}(100)$ MeV, can be obtained with a threshold scan in scenarios where sleptons are light, even in topologies involving τ 's. For very heavy selectrons the error is larger since only the s -channel Z exchange contribution is present, leading to relatively smaller cross sections and a less steep excitation curve, $\sigma \propto \beta_\chi^3$ because of the Majorana nature of the neutralinos. An exception is when the neutralinos that are produced in mixed pairs have opposite CP parities, in which case the cross section increases steeply in S-waves.

Note that for the verification of the spin- $\frac{1}{2}$ character of the neutralinos and charginos, neither the onset of the excitation curves near threshold nor the angular distributions in the production processes provide unique signals of the spin [187]. However, decay angular distributions of polarized neutralinos/charginos that are pair produced with polarized beams provide an unambiguous determination of the spin- $\frac{1}{2}$ character of the particles albeit at the expense of more involved experimental analyses [187].

The $e^+ e^- \rightarrow \chi_i^+ \chi_j^-$ production cross sections are binomials in the chargino mixing angles $\cos 2\phi_{L,R}$ and the latter can be determined in a model independent way using polarized beams. This is exemplified in the contours shown in Fig. 5.3 for two c.m. energies and assuming $\mathcal{P}_{e^-} = 0.8$ and $\mathcal{P}_{e^+} = 0.5$. At $\sqrt{s} = 500$ GeV, two regions of the plane are selected, but one of them can be removed by moving to lower c.m. energies. For SPS1a, including the uncertainties in the mass measurements, one obtains the 95% CL limited range for the mixing angles $\cos 2\phi_L = [0.62, 0.72]$ and $\cos 2\phi_R = [0.87, 0.91]$. In the CP conserving MSSM, the information obtained from chargino production and decay processes would be sufficient to determine the basic parameters entering the $\chi^\pm - \chi^0$ system with a very good accuracy. Also, we recall that the t -channel $\tilde{\nu}$ exchange can be suppressed using polarized beams and $m_{\tilde{\nu}_e}$

can be measured from the cross section. If too heavy, one can have an indirect sensitivity on multi-TeV sneutrinos and measure their masses [188, 189] unless the $e\chi_1^+\tilde{\nu}$ coupling is small [as for a higgsino χ_i^\pm]. Thus, even if they are well beyond the kinematical reach of the ILC, sleptons can be probed up to masses of $\mathcal{O}(10 \text{ TeV})$ thanks to the achievable high precision.

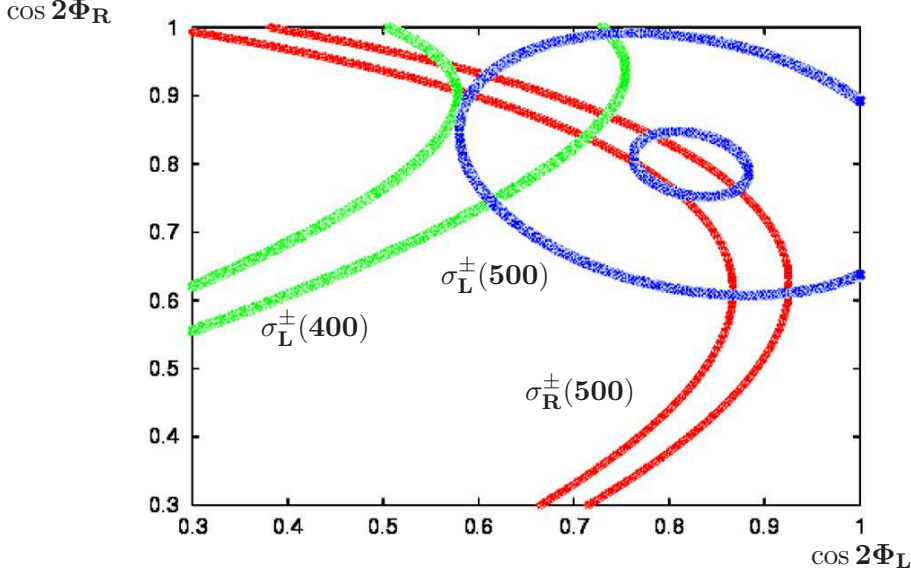


FIGURE 5.3. Contours for the $e^+e^- \rightarrow \chi_1^+\chi_1^-$ production cross section for polarized e^\pm beams in the plane $[\cos 2\phi_L, \cos 2\phi_R]$ at $\sqrt{s} = 400$ and 500 GeV [184].

The neutralino mixing angles can also be determined in pair and mixed production, leading to additional determinations of the basic SUSY parameters. By only using the processes $e^+e^- \rightarrow \chi_1^0\chi_2^0$ and $\chi_2^0\chi_2^0$, the constraints on M_2, μ and $\tan\beta$ can be improved and the parameter M_1 can be determined from the production vertex. This is particularly true in models with CP violation, in which the parameters μ and $M_{1,2}$ have complex phases that can be determined unambiguously in a fully model independent way by combined information from χ^\pm and χ^0 production. In fact, CP violation can be checked directly by measuring CP-odd observables in neutralino production [43, 190].

We note that in the SPS1a or SPS1a' scenarios, and in many SUSY cases, the heavier neutralinos and chargino are not accessible in pair production unless the ILC c.m. energy is upgraded to 1 TeV . However, mixed pair production $e^+e^- \rightarrow \chi_1^0\chi_{3,4}^0$ for instance, might be accessible at energies only at or slightly above $\sqrt{s} = 500 \text{ GeV}$, but the production rates are small and the backgrounds too large. A study at $\sqrt{s} = 750 \text{ GeV}$ with 1 ab^{-1} luminosity shows that the Z/W boson energy spectra in the decays of these heavier ino states allow their reconstruction with mass resolutions of a few GeV. Note also that from the determination of the SUSY parameters in lighter $\chi_{1,2}^0, \chi_1^\pm$ production and decays, one can predict the masses of the heavier ino states with a few percent accuracy.

5.2.2 The slepton sector

The sfermion system is described, in addition to $\tan\beta$ and μ , by three parameters for each sfermion species: the left- and right-handed soft-SUSY breaking scalar masses $M_{\tilde{f}_L}$ and $M_{\tilde{f}_R}$

and the trilinear couplings A_f . Sfermion mixing turns the current eigenstates \tilde{f}_L and \tilde{f}_R into the mass eigenstates \tilde{f}_1 and \tilde{f}_2 , but only in the case of the third generation that this mixing, $\propto m_f$, is important [for the first two sfermion generations, since $m_f \rightarrow 0$, universality can be assumed in general as will be done here]. In the case of $\tilde{\tau}$ s, it is significant at large $\tan\beta$, leading to a $\tilde{\tau}_1$ that is much lighter than the other sleptons.

The production of the second and third generation sleptons in e^+e^- collisions is mediated by s -channel γ/Z exchanges in P-waves with a characteristic rise of the excitation curve, $\sigma \propto \beta_{\tilde{\ell}}^3$. The production of selectrons and electronic sneutrinos proceeds, in addition, through t -channel exchanges of neutralinos or charginos. The channels $e^+e^- \rightarrow \tilde{e}_R^\pm e_L^\mp$ are generated in S-waves with a steep threshold excitation curve, $\sigma \propto \beta_{\tilde{e}}$. Selectrons can also be produced in e^-e^- collisions through neutralino exchange, with steep excitation curves for $\tilde{e}_R^-\tilde{e}_R^-$ and $\tilde{e}_L^-\tilde{e}_L^-$ final states. Thus, different states and their quantum numbers can be disentangled by a proper choice of the beam energy and the polarization. Since in many SUSY scenarios the sleptons are relatively light, their decays are rather simple and involve in general only the light chargino and neutralinos plus leptons. In SPS1a for instance, the decays of all sleptons directly into the LSP, $\tilde{\ell} \rightarrow \ell\chi_1^0$, are the dominant ones.

Slepton masses can be measured in threshold scans or in the continuum. At threshold, $\tilde{\ell}_L^+\tilde{\ell}_L^-$ and $\tilde{\ell}_R^+\tilde{\ell}_R^-$ are excited in a P-wave characterized by a slow rise of the cross section. The experimental accuracy requires higher order corrections and finite sfermion width effects to be included. An example of a simulation for the SPS1a point is shown in Fig. 5.4 for $\tilde{\mu}_R$. Using polarized e^+e^- beams and $\mathcal{L} = 50 \text{ fb}^{-1}$, a highly correlated 2-parameter fit gives $\Delta m_{\tilde{e}_R} = 0.2 \text{ GeV}$ and $\Delta\Gamma_{\tilde{e}_R} = 0.25 \text{ GeV}$; the resolution deteriorates by a factor of ~ 2 for $\tilde{\mu}_R^+\tilde{\mu}_R^-$ production. For $e_R^-e_L^+ \rightarrow \tilde{e}_R^-\tilde{e}_L^+$, the gain in resolution is a factor ~ 4 with only a tenth of luminosity, compared to e^+e^- beams.

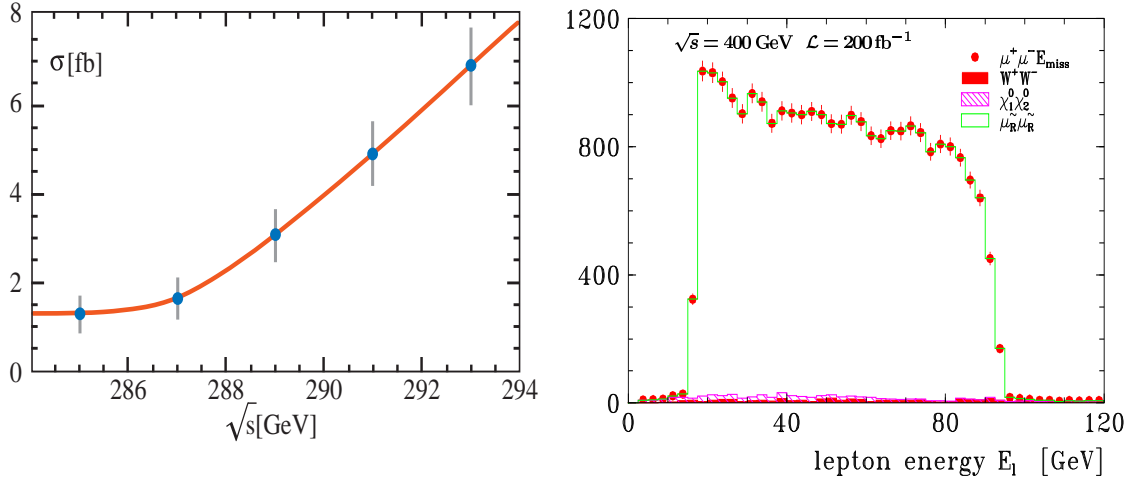


FIGURE 5.4. Slepton mass measurements in SPS1a: Cross sections at threshold for $e_L^+e_R^- \rightarrow \tilde{e}_R^+\tilde{e}_L^-$ including background with 1 fb^{-1} per point [191] (left). Lepton energy spectra in $e_R^-e_L^+ \rightarrow \tilde{\mu}_R^+\tilde{\mu}_R^- \rightarrow \mu^-\chi_1^0\mu^+\chi_1^0$ at $\sqrt{s}=400 \text{ GeV}$ and $\mathcal{L}=200 \text{ fb}^{-1}$ [185] (right).

Above the threshold, slepton masses can be obtained from the endpoint energies of leptons coming from slepton decays. In the case of two-body decays, $\tilde{\ell}^\pm \rightarrow \ell^\pm\chi_i^0$ and $\tilde{\nu}_\ell \rightarrow \ell^\pm\chi_i^\mp$, the lepton energy spectrum is flat with the minimum and maximum energies providing an accurate determination of the masses of the primary slepton and the secondary neutralino/chargino. A simulation of the μ energy spectra of $\tilde{\mu}_R^+\tilde{\mu}_R^-$ production, including

beamstrahlung, initial state radiation, selection criteria and detector resolution, is shown in Fig. 5.4 for the point SPS1a [185]. With a moderate luminosity of 200 fb^{-1} at $\sqrt{s} = 400 \text{ GeV}$, one obtains $m_{\tilde{\mu}_R} = 143 \pm 0.10 \text{ GeV}$ and $m_{\chi_1^0} = 96 \pm 0.10 \text{ GeV}$. If $m_{\chi_1^0}$ is known from chargino/neutralino production, one can improve the slepton mass determination by a factor of two from reconstructed kinematically allowed slepton minima. Similar results are obtained in the case of selectron production in $e^+e^- \rightarrow \tilde{e}_R \tilde{e}_R^*$.

The sneutrino analysis is more involved in scenarios with light states which decay dominantly into invisible channels, $\tilde{\nu}_\ell \rightarrow \nu_\ell \chi_1^0$. The $\tilde{\nu}$ mass resolution could be optimized by looking at the channel $e^+e^- \rightarrow \tilde{\nu}_e \tilde{\nu}_e \rightarrow \nu_e \chi_1^0 e^\pm \chi_1^\mp$. This is exemplified in Fig. 5.5 for scenario SPS1a, where the branching ratio for the $\tilde{\nu}_e \rightarrow \chi_1^\pm e^\mp$ decay is about 10%. The sneutrino mass can be determined to the level $\Delta m_{\tilde{\nu}} = 1.2 \text{ GeV}$, which is comparable to the accuracy obtained from a threshold scan.

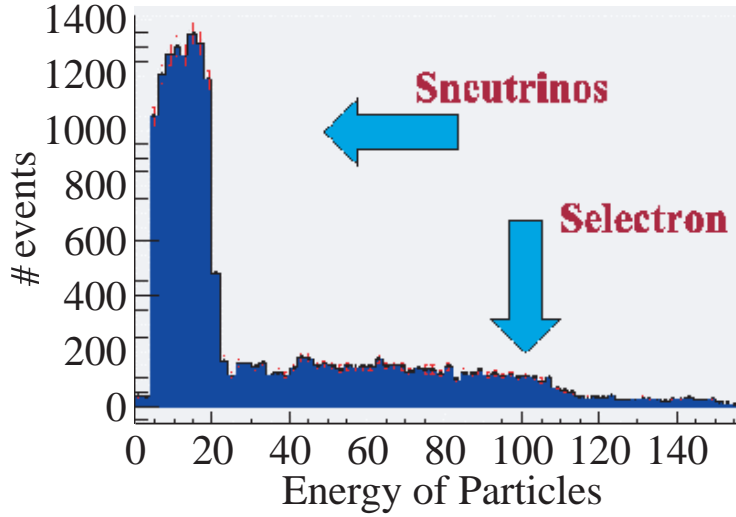


FIGURE 5.5. Lepton energy spectrum for the sneutrino production and decay processes $e^+e^- \rightarrow \tilde{\nu}_e \tilde{\nu}_e \rightarrow \nu_e \chi_1^0 e^\pm \chi_1^\mp \rightarrow e^\pm \mu^\mp + \cancel{e}$ [192].

The $\sin^2 \theta$ law for the angular distribution in the production of sleptons (for selectrons close to threshold) is a unique signal of the fundamental spin-zero character; the P-wave onset of the excitation curve is a necessary but not sufficient condition in this case [187]. Thus, the slepton spin determination is conceptually very simple at the ILC.

As mentioned previously, large mixing effects are in general expected in the stau sector, making as in SPS1a, $\tilde{\tau}_1$ the lightest slepton. The stau masses can be determined using the same methods as described above and, for SPS1a, one obtains $\Delta m_{\tilde{\tau}_1} = 0.3 \text{ GeV}$. Since in scenarios with $\tan \beta \gtrsim 10$, charginos and neutralinos in the decay chain will dominantly lead to additional tau leptons in the final state, it is difficult to disentangle the heavier $\tilde{\tau}_2$ from the background of the lighter $\tilde{\tau}_1$ and the $m_{\tilde{\tau}_2}$ measurement is still an open problem. Another very difficult region is when $\tilde{\tau}_1$ is almost degenerate in mass with the χ_1^0 LSP, a possibility that is important as it corresponds to the co-annihilation region in which the LSP has the required cosmological relic density to make the DM. In this case, the final state τ leptons are very soft and the two-photon processes $e^+e^- \rightarrow \tau\tau ee$ and $e^+e^- \rightarrow c\bar{c}ee, b\bar{b}ee$ with the quarks decaying semi-leptonically, besides $e^+e^- \rightarrow WW \rightarrow \tau\tau\nu\nu$, represent very large backgrounds.

It has been nevertheless shown in detailed simulations that the signal can be detected and accuracies close to 1 GeV can be achieved on the $\tilde{\tau}$ mass for scenarios where $m_{\tau_1} - m_{\chi_1^0} \gtrsim$ a few GeV; the uncertainty drops by a factor of 2 if the c.m. energy is optimized.

In the case of $\tilde{\tau}$ s, the mixing angle $\theta_{\tilde{\tau}}$ can be extracted from two measurements of the cross section $\sigma(e^+e^- \rightarrow \tilde{\tau}_1\tilde{\tau}_1)$ with different beam polarizations [193, 194]. In the SPS1a scenario, one obtains a precision at the percent level, $\cos 2\theta_{\tilde{\tau}} = -0.84 \pm 0.04$ [185]. The value of $\theta_{\tilde{\tau}}$ and the degree of τ polarization in $\tilde{\tau}$ decays depend on the fundamental parameters μ , A_τ and $\tan\beta$, which can therefore be constrained by these measurements. In fact, the dominant decay mode $\tilde{\tau}_1 \rightarrow \chi_1^0\tau$ can also be exploited to determine $\tan\beta$ if it is high enough, by using the polarization of τ leptons which has been shown to be probed at the percent level [193, 194]. τ polarization would allow, for instance, to discriminate between different GUT scenarios [195]. Furthermore, since the trilinear A_τ coupling is enhanced by $\tan\beta$ in the couplings of the heavier scalar and pseudoscalar Higgs bosons to $\tilde{\tau}$ states, this parameter can be measured in the Higgs decays $H, A \rightarrow \tilde{\tau}_1\tilde{\tau}_2$ [196]. Finally, the important parameter $\tan\beta$ can also be measured in $\tau\tau$ fusion to Higgs bosons at the $\gamma\gamma$ option of the ILC [197].

Note that in SUSY models which incorporate heavy right-handed neutrinos, spectacular flavor violating slepton decays such as $\tilde{\tau}_1 \rightarrow \mu\chi_1^0$ may be observed at the ILC [198], in addition to lepton-number changing processes like $e^+e^- \rightarrow \mu^\pm\tau^\mp$ [199].

5.2.3 The squark sector

For the third generation squarks, \tilde{t} and \tilde{b} , the mixing is expected to be important and, as a result of the large top and bottom quark Yukawa couplings, it is possible that the lightest top or bottom squarks are much lighter than the other squarks and kinematically accessible at the ILC. This is for instance the case in SPS1a where $m_{\tilde{t}_1} = 379.1$ GeV and $m_{\tilde{b}_1} = 491.9$ GeV in which case \tilde{t}_1 , and to a lesser extent \tilde{b}_1 , can be produced at $\sqrt{s} = 1$ TeV. In fact, to achieve electroweak baryogenesis in the MSSM (see chapter 7, the right-handed top squark must be lighter than the top quark in order that a strong first order transition is realized, while the other stop eigenstate is very heavy. The \tilde{t}_1 state may escape detection at the LHC because of the huge backgrounds, while it can easily be observed at the ILC; Fig. 5.6 [200]. Thus, there is a possibility that the stop sector can be studied only at the ILC.

The phenomenology of the \tilde{t} and \tilde{b} states is analogous to that of the $\tilde{\tau}$ system. The masses and mixing angles can be extracted from production cross sections measured with polarized beams. For stop pair production with different beam polarizations, $\sigma(e_R^-e_L^+ \rightarrow \tilde{t}_1\tilde{t}_1)$ and $\sigma(e_L^-e_R^+ \rightarrow \tilde{t}_1\tilde{t}_1)$ have been studied for $\tilde{t}_1 \rightarrow b\chi_1^\pm$ and $\tilde{t}_1 \rightarrow c\chi_1^0$ decay modes including full statistics SM background. We mention here a simulation using SIMDET in a dedicated “light-stop” scenario with $m_{\tilde{t}_1} = 210$ GeV and $m_{\chi_1^0} = 121.2$ GeV [200] for which the decay $\tilde{t}_1 \rightarrow b\chi_1^\pm$ is not open and the SUSY background is thus small. The charm tagging, helps to enhance the signal from the decay $\tilde{t}_1 \rightarrow c\chi_1^0$. The results, shown in the left panel of Fig. 5.6 provide high accuracies on the \tilde{t}_1 mass $\Delta m_{\tilde{t}_1} \sim 0.7$ GeV and mixing angle $\Delta \cos \theta_{\tilde{t}} \sim 0.01$.

Similarly to the $\tilde{\tau}$ case, the measurement of top quark polarization in squark decays can provide information on $\tan\beta$. For this purpose the decay $\tilde{b}_1 \rightarrow t\chi_1^\pm$ is far more useful than $\tilde{t}_1 \rightarrow t\chi_i^0$ since in the latter the top polarization is only weakly sensitive to high $\tan\beta$ values. A feasibility study of the reaction $e_L^+e_R^- \rightarrow \tilde{b}_1\tilde{b}_1 \rightarrow t\chi_1^- + \bar{t}\chi_1^+$ has been performed in Ref. [194] where a fit to the angular distribution with respect to the angle between \tilde{b}_1 and a final quark in the top rest frame, allows for a nice measurement of the polarization. One can then derive the value of $\tan\beta$ as illustrated in Fig. 5.6 where one obtains $\tan\beta = 17.5 \pm 4.5$ in the studied

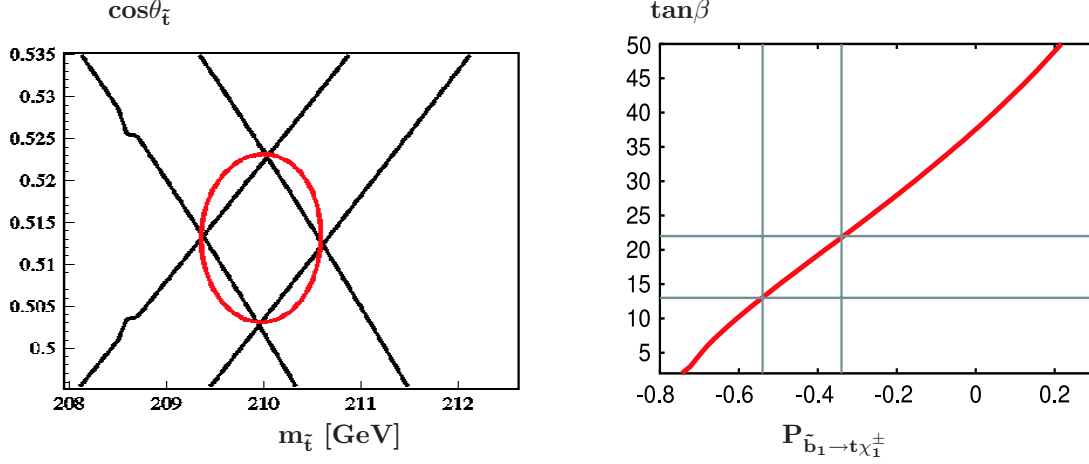


FIGURE 5.6. Left: Contours of $\sigma(e_R^- e_L^+ \rightarrow \tilde{t}_1 \tilde{t}_1)$ and $\sigma(e_L^- e_R^+ \rightarrow \tilde{t}_1 \tilde{t}_1)$ as a function of $m_{\tilde{t}_1}$ and $\cos\theta_{\tilde{t}_1}$ for $\sqrt{s} = 500$ GeV and $\mathcal{L} = 2 \cdot 500 \text{ fb}^{-1}$ [200]. Right: $\tan\beta$ as a function of top polarization as obtained from a simulation in Ref. [194].

scenario with an input value of $\tan\beta = 20$. After fixing $\tan\beta$, measurements of the stop mass and mixing angle allows to determine the trilinear coupling A_t at the 10% level.

Finally, first and second generation squarks, which will be produced copiously and studied at LHC, might be accessible at ILC only at energies $\sqrt{s} \gtrsim 1$ TeV. Compared to the LHC, \tilde{q} pair production at the ILC if kinematically possible would allow for better mass measurements and a check of their charge, spin and chirality numbers.

5.2.4 Measurements in other scenarios/extensions

So far, we have only discussed the prominent features of the MSSM with gravity mediated SUSY-breaking. Interesting and important studies can also be performed at the ILC in variants of the MSSM in which some underlying basic assumptions are relaxed or in SUSY models with different breaking patterns. In the following, we will briefly summarize some of the studies which can be made at the ILC.

In Gauge mediated SUSY breaking models [176], the LSP is the lightest gravitino \tilde{G} which has a very small mass, leading to NLSP decay lengths ranging from micro-meters to tens of meters. This NLSP is in general either the lightest neutralino which decays into a gravitino and a photon, $\chi_1^0 \rightarrow \tilde{G}\gamma$, and produces displaced photons not pointing to the interaction vertex, or the $\tilde{\tau}_1$ with decays $\tilde{\tau}_1 \rightarrow \tilde{G}\tau$. The phenomenology of the other SUSY particles, and even that of the NLSP if its lifetime is large and decays outside the detector, is the same as in gravity mediated models but with different spectra. Detailed simulations [7] show that a signal with displaced photons can be observed for NLSP masses close to the production kinematical limit and that various techniques [such as tracking, pointing calorimetry and photon counting] allow to measure the decay length over a large range and determine the SUSY scale. From the rest of the SUSY spectrum, a precise determination of the GMSB parameters is possible. The scenario with $\tilde{\tau}_1$ NLSP has also been studied [201] and it has been shown that in many cases that the long $\tilde{\tau}$ lifetime allows a precise determination of $m_{\tilde{G}}$.

In Anomaly mediated SUSY breaking models [175], the most characteristic feature is that the LSP neutralino is wino like and is nearly mass degenerate with the lightest chargino χ_1^\pm .

As mentioned previously, chargino $e^+e^- \rightarrow \chi_1^+\chi_1^-$ production will be then a difficult process and one should rely on new search strategies [186, 188], depending on the χ_1^\pm lifetime and decay modes which are related to the small mass difference $m_{\chi_1^+} - m_{\chi_1^0}$. Signatures like ISR photons, heavy ionizing particle, terminating tracks decaying to pions, etc., can be used for detection. Chargino with masses very close to the beam energy can be observed. Another interesting feature of AMSB models is the near mass degeneracy of $\tilde{\ell}_L$ and $\tilde{\ell}_R$ which can be tested precisely at the ILC.

The MSSM with R-parity breaking [178] is an interesting scenario as it provides a nice framework to describe [202] the mass and the mixing patterns of the SM light neutrinos. The LSP is not anymore stable and does not provide a DM candidate and, since astrophysical constraints do not apply, it can be a priori any SUSY particle. Nevertheless, the LSP is generally again the χ_1^0 or the $\tilde{\tau}_1$ and, depending on whether \mathcal{R}_p couplings are lepton or baryon number violating, it will decay either into leptons or jets. For small \mathcal{R}_p couplings, as required by data in the leptonic and light quark sectors, the production and decay characteristics of the SUSY particles are identical to the usual MSSM, except for the LSP decays which lead to visible particles and not missing energy. The signatures with multi-lepton or/and multi-jet final states have been shown to be straightforwardly observable using the over-constrained kinematics of the final states, and easily recognizable from the SM and usual MSSM expectations [7]. For large \mathcal{R}_p couplings, interesting new signals, such as single production of sneutrinos $e^+e^- \rightarrow \tilde{\nu} \rightarrow \ell^+\ell^-, \nu\chi_1^0, \ell^\pm\chi_1^\pm$ might occur and extend significantly the accessible mass reach of the ILC. Significant \mathcal{R}_p couplings can be present in the third generation sfermion sector, in particular for \tilde{t}_1 , leading to an interesting phenomenology and new signatures which can be also precisely probed at the ILC.

The next-to minimal SSM, is a very interesting extension of the MSSM as it solves the problem of the μ parameter, which is a SUSY parameter but with values of the order of the SUSY-breaking scale. By adding a singlet superfield S in the superpotential, $W \supset \lambda H_1 H_2 S - \frac{1}{3}\kappa S^3$ [49]. The scalar component of S develops a vev $x = \langle S \rangle$ which generates an effective μ -term, $\mu = \lambda x$. The fermionic component of the extra superfield, the singlino, will mix with the neutral gauginos and higgsinos, leading to a 5×5 neutralino mass matrix which will depend on M_1 , M_2 , $\tan\beta$, x and the trilinear couplings λ and κ . In some regions of the parameter space, the singlino χ_S^0 may be the LSP and can be searched for in associated production with the usual neutralinos, $e^+e^- \rightarrow \chi_S^0\chi_i^0$. If the singlino dominated LSP has small couplings to the other neutralinos, the usual SUSY production processes will lead to signatures involving displaced vertices due to the decay of the NLSP neutralino into the singlino which would signal the extended structure [203]. Another possibility of discriminating the MSSM from the NMSSM when the spectra look identical but the neutralino-singlino mixing is substantial, would be to study the summed up production cross sections for the four neutralinos, $\sum \sigma(e^+e^- \rightarrow \chi_i^0\chi_i^0)$, if they are all kinematically accessible [204].

The CP violating MSSM [43] has been already mentioned previously. In the chargino and neutralino sectors, the phases of μ , M_1 and M_2 can be determined from the precise measurement of the χ^0, χ^\pm masses and mixing angles, even if only the light states are accessible kinematically; the availability of beam polarization [17] is crucial here. In the sfermion sector, the phases of the trilinear couplings A_f and μ can be studied in the production and decays of the third generation \tilde{t}, \tilde{b} and $\tilde{\tau}$ states.

Other scenarios, such as those inspired by superstring models or incorporating right-handed sneutrinos or heavy right-handed neutrinos, have been also discussed.

5.3 DETERMINING THE SUSY LAGRANGIAN

5.3.1 A summary of measurements and tests at the ILC

Let us first summarize the results of the SPS1a sparticle mass measurements to highlight the high precision that can be achieved at the ILC. These are displayed in Tab. 5.2 from Ref. [185], where quoted are the best values expected from either production in the continuum or in threshold scans. In most cases, they are based on realistic Monte Carlo and detector simulations with reasonable assumptions on the ILC performance. Only for the heavy χ^0 , χ^\pm and \tilde{t}_1 states some plausible estimates are made. Typical accuracies in the percent to the permille range are expected.

It should be pointed out once more that the ILC provides much more valuable information than sparticle masses. Accurate values on sparticle mixing angles and couplings can also be obtained and the spin–quantum numbers can be easily determined. Other aspects, such as the chirality of the sleptons, the Majorana nature of the neutralinos, the presence of CP–violation, etc., can be directly verified. All these precision measurements serve as a valuable input to explore SUSY scenarios in a model independent way. For some of these studies, the polarization of both electron and positron beams is very important [17].

TABLE 5.2

Sparticle masses and their expected accuracies at the ILC in SPS1a' [185, 179].

| | m [GeV] | Δm [GeV] | Comments |
|------------------|-----------|------------------|---|
| χ_1^\pm | 183.7 | 0.55 | simulation threshold scan, 100 fb ⁻¹ |
| χ_2^\pm | 415.4 | 3 | estimate $\chi_1^\pm \chi_2^\mp$, spectra $\chi_2^\pm \rightarrow Z \chi_1^\pm, W \chi_1^0$ |
| χ_1^0 | 97.7 | 0.05 | combination of all methods |
| χ_2^0 | 183.9 | 1.2 | simulation threshold scan $\chi_2^0 \chi_2^0$, 100 fb ⁻¹ |
| χ_3^0 | 400.5 | 3–5 | spectra $\chi_3^0 \rightarrow Z \chi_{1,2}^0, \chi_2^0 \chi_3^0, \chi_3^0 \chi_4^0$, 750 GeV, $\gtrsim 1$ ab ⁻¹ |
| χ_4^0 | 413.9 | 3–5 | spectra $\chi_4^0 \rightarrow W \chi_1^\pm, \chi_2^0 \chi_4^0, \chi_3^0 \chi_4^0$, 750 GeV, $\gtrsim 1$ ab ⁻¹ |
| \tilde{e}_R | 125.3 | 0.05 | $e^- e^-$ threshold scan, 10 fb ⁻¹ |
| \tilde{e}_L | 189.9 | 0.18 | $e^- e^-$ threshold scan 20 fb ⁻¹ |
| $\tilde{\nu}_e$ | 172.5 | 1.2 | simulation energy spectrum, 500 GeV, 500 fb ⁻¹ |
| $\tilde{\mu}_R$ | 125.3 | 0.2 | simulation energy spectrum, 400 GeV, 200 fb ⁻¹ |
| $\tilde{\mu}_L$ | 189.9 | 0.5 | estimate threshold scan, 100 fb ⁻¹ |
| $\tilde{\tau}_1$ | 107.9 | 0.24 | simulation energy spectra, 400 GeV, 200 fb ⁻¹ |
| $\tilde{\tau}_2$ | 194.9 | 1.1 | estimate threshold scan, 60 fb ⁻¹ |
| \tilde{t}_1 | 366.5 | 1.9 | estimate b -jet spectrum, $m_{\min}(\tilde{t}_1)$, 1TeV, 1000 fb ⁻¹ |

A very important test to be performed at the ILC is the fundamental SUSY identity between the gauge couplings g and the corresponding gaugino Yukawa couplings \hat{g} in the electroweak and strong sectors. The cross sections of the first generation sleptons are sensitive to the SUSY Yukawa couplings $\hat{g}(e\tilde{e}\chi^0)$ and $\hat{g}(e\tilde{\nu}\chi^\pm)$ and, from the measurement of \tilde{e}_R , \tilde{e}_L and $\tilde{\nu}$ production rates, one can test the SUSY identity in the electroweak sector [191, 192]. For \tilde{e} production, beam polarization is crucial for disentangling the SU(2) and U(1) couplings: taking into account uncertainties from the selectron mass and the neutralino parameters, the couplings \hat{g} and \hat{g}' , can be extracted with a precision of 0.7% and 0.2%, respectively, at a 500 GeV collider with 500 fb⁻¹ in the SPS1a scenario [192]. Sneutrino production is only sensitive to the SU(2) coupling \hat{g} , but here, the dominantly invisible $\tilde{\nu}_e$ decay limits the expected precision to 5% [192]. The equality of the gauge and SUSY Yukawa couplings in

the $SU(3)$ sector can be checked only if the squarks and gluinos are also relatively light, in which case the associated production of squarks and gluinos, $e^+e^- \rightarrow q\tilde{q}\tilde{g}$ can be used [192].

Note that the identity between the Yukawa and the electroweak gauge couplings can also be tested in chargino/neutralino pair production [204]; this is worth noting as this method works also in the case where the sleptons are too heavy to be directly accessible.

5.3.2 Determination of the low energy SUSY parameters

Once masses and mixing angles of superparticles have been measured, the Lagrangian SUSY breaking parameters can be then determined. We briefly summarize below the procedure, ignoring higher order effects to simplify the picture.

From chargino–neutralino measurements, one obtains $M_{1,2}, \mu$ and $\tan \beta$ [204, 205]:

$$\begin{aligned} M_1 &= [\Sigma_i m_{\tilde{\chi}_i^0}^2 - M_2^2 - \mu^2 - 2M_Z^2]^{1/2}, & M_2 &= M_W[\Sigma - \Delta[\cos 2\phi_R + \cos 2\phi_L]]^{1/2} \\ |\mu| &= M_W[\Sigma + \Delta[\cos 2\phi_R + \cos 2\phi_L]]^{1/2}, & \tan \beta &= [(1 + \Delta')/(1 - \Delta')]^{1/2} \end{aligned}$$

with $\Delta = (m_{\tilde{\chi}_2^\pm}^2 - m_{\tilde{\chi}_1^\pm}^2)/4M_W^2$, $\Delta' = \Delta(\cos 2\phi_R - \cos 2\phi_L)$ and $\Sigma = (m_{\tilde{\chi}_2^\pm}^2 + m_{\tilde{\chi}_1^\pm}^2)/2M_W^2 - 1$.

It has been demonstrated in detail [204] that using the chargino/neutralino sector, the four parameters can be determined from the measurement of the ino masses and mixing angle even if only the light states are accessible kinematically.

The sfermion mass parameters and trilinear couplings are obtained through

$$\begin{aligned} m_{\tilde{f}_{L,R}}^2 &= M_{\tilde{f}_{L,R}}^2 + M_Z^2 \cos 2\beta (I_{L,R}^3 - Q_f \sin^2 \theta_W) + m_f^2 \\ A_f - \mu(\tan \beta)^{-2I_3^f} &= (m_{\tilde{f}_1}^2 - m_{\tilde{f}_2}^2)/(2m_f) \cdot \sin 2\theta_{\tilde{f}} \end{aligned}$$

Parameter determination from the Higgs sector is more involved as one needs to include the large radiative corrections that are present. In any case, the expected precise measurement of the lightest h boson mass at the ILC, $\Delta M_h \sim 50$ MeV, allows to severely constrain and with some assumptions to determine some parameters in the stop sector, such as the trilinear coupling A_t and the heavier stop mass $m_{\tilde{t}_2}$ (which are difficult to measure at the LHC), if they cannot be accessed directly at ILC [138].

In view of the high accuracy that is achievable at the ILC an even more involved approach is required and the radiative corrections to the previous relations need to be implemented. This leads to a highly non-linear system of relations which has to be solved numerically; several codes which do this job [206, 207] are available. In Tab. 5.3, we display values of SUSY parameters that can be derived for the general MSSM in SPS1a [206] using mass measurements at the ILC given previously and the LHC [184] after a global fit. As expected, a very high precision is achieved in the gaugino and slepton sectors, while the gluino and squark (except for \tilde{t}_1) sectors are the territory of LHC. However, the precision measurements at the ILC also allow for mass predictions for heavier sparticles. Providing such mass predictions lead to an increase in statistical sensitivity for observing these heavier particles in the decay chains at the LHC. Verifying subsequently the predicted particle masses at the LHC leads to a powerful test of the underlying model. On the other hand, fitting this information back to the ILC analyses enhances the accuracy of the parameter determination [184].

TABLE 5.3

Results for the MSSM parameter determination in SPS1a [206] and SPS1a' [179] using the mass measurements at the ILC and the LHC [184] after a global fit; the central values are approximately reproduced. Not that the two analyses use different sets of measurements, assume slightly different accuracies and treat differently the theoretical errors; this explains the slight discrepancies in the outputs.

| | ΔLHC | ΔILC | $\Delta\text{LHC+ILC}$ | SPS1a | $\Delta\text{LHC+ILC}$ | SPS1a' |
|----------------------|--------------------|--------------------|------------------------|--------|------------------------|--------|
| $\tan\beta$ | ± 9.1 | ± 0.3 | ± 0.2 | 10 | ± 0.3 | 10 |
| μ | ± 7.3 | ± 2.3 | ± 1.0 | 344.3 | ± 1.1 | 396 |
| M_A | fixed 500 | ± 0.9 | ± 0.8 | 399.1 | ± 0.8 | 372 |
| A_t | ± 91 | ± 2.7 | ± 3.3 | -504.9 | ± 24.6 | -565.1 |
| M_1 | ± 5.3 | ± 0.1 | ± 0.1 | 102.2 | ± 0.1 | 103.3 |
| M_2 | ± 7.3 | ± 0.7 | ± 0.2 | 191.8 | ± 0.1 | 193.2 |
| M_3 | ± 15 | fixed 500 | ± 11 | 589.4 | ± 7.8 | 571.7 |
| $M_{\tilde{\tau}_L}$ | fixed 500 | ± 1.2 | ± 1.1 | 197.8 | ± 1.2 | 179.3 |
| $M_{\tilde{e}_L}$ | ± 5.1 | ± 0.2 | ± 0.2 | 198.7 | ± 0.18 | 181.0 |
| $M_{\tilde{e}_R}$ | ± 5.0 | ± 0.05 | ± 0.05 | 138.2 | ± 0.2 | 115.7 |
| $M_{\tilde{Q}^3_L}$ | ± 110 | ± 4.4 | ± 39 | 501.3 | ± 4.9 | 471.4 |
| $M_{\tilde{Q}^1_L}$ | ± 13 | fixed 500 | ± 6.5 | 553.7 | ± 5.2 | 525.8 |
| $M_{\tilde{d}_R}$ | ± 20 | fixed 500 | ± 15 | 529.3 | ± 17.3 | 505.7 |

5.3.3 Reconstructing the fundamental SUSY parameters

Although low energy SUSY is characterized by energy scales of $\mathcal{O}(1 \text{ TeV})$, the roots for all the phenomena we will observe experimentally in this range may go to energies near the GUT or Planck scales. Fortunately, SUSY provides us with a stable bridge between these two vastly different energy regions: RGEs by which parameters from low to high scales are evolved based on nothing but experimentally measured quantities. This procedure, which has very successfully been pursued for the three gauge couplings, can be expanded to the soft-SUSY breaking parameters: gaugino and scalar masses and trilinear couplings. This bottom-up approach makes use of the low-energy measurements to the maximum extent possible and allows to reconstruct the fundamental theory at the high scale in a transparent way.

In this approach, the combination of measurements performed at both the LHC and the ILC will be crucial. As a matter of fact, most of the strongly interacting particles are too heavy and will not be accessible at the ILC, while they will be copiously produced and their masses measured at the LHC. In turn, the precision of the LHC measurements alone will not be sufficient for a comprehensive and high-precision picture of SUSY at the weak scale; in fact, some of the low energy SUSY-breaking parameters cannot be constrained at all. Thus, only the LHC-ILC tandem can provide us with such a picture and allows the reconstruction of the fundamental SUSY theory at the high scale.

This discussion will be again illustrated using a cMSSM scenario. Adding the measurements of the masses of the heavy states [the colored $\tilde{q}_L, \tilde{q}_R, \tilde{b}_1$ and \tilde{g} and the heavy electroweak $\chi_{3,4}^0, \chi_2^\pm$ states] which can be performed at the LHC at the percent level provided a very high luminosity is collected, and the ILC measurements discussed previously, one can determine to a high precision the soft SUSY-breaking gaugino mass parameters $M_{1,2,3}$ and the sfermion mass parameters $m_{\tilde{f}_{L,R}}$. One can then evolve these parameters using standard RGEs up to the GUT scale, the value of which is derived from the measurement of the gauge coupling

constants at the Giga-Z option of the ILC. In SPS1a', one obtains (ignoring threshold effects) $M_{\text{GUT}} = (2.47 \pm 0.02) \cdot 10^{16}$ GeV, which leads to a common value of $\alpha_{\text{GUT}}^{-1} = 24.17 \pm 0.06$. This is shown in Fig. 5.7, where the thickness of the curves reflect the 1σ errors.

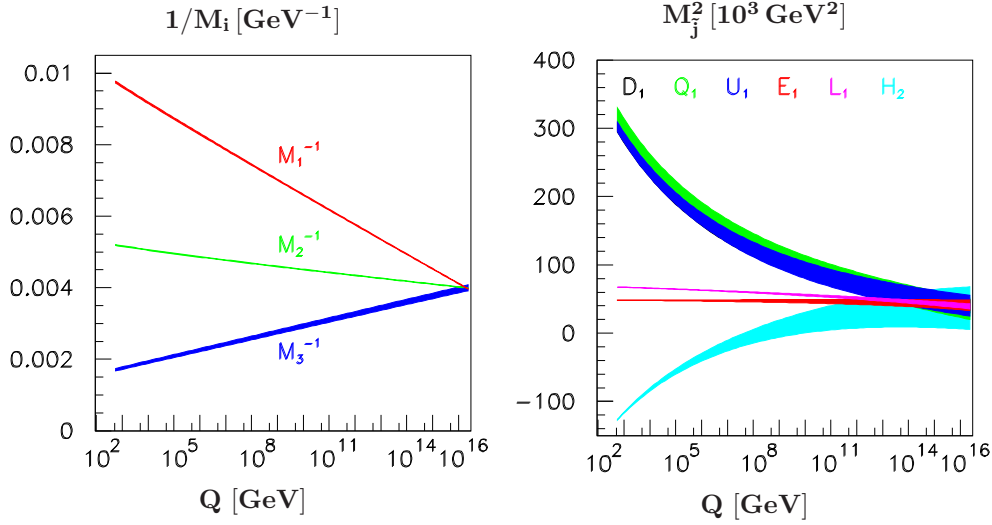


FIGURE 5.7. Evolution from low to high scales of gaugino and scalar mass parameters in the cMSSM point SPS1a'; the widths of the bands indicate the 1σ CL [208].

Note that while the parameters are determined accurately in the gaugino and slepton sectors, the errors are larger for squarks. Nevertheless, one can see that the two sets unify nicely, providing a strong confidence that we are indeed in a cMSSM-type scenario.

One can then derive the basic parameters of the model at the scale M_{GUT} . A global fit of all the SUSY parameters obtained from measurements at the LHC and the ILC as given in Tab. 5.3, can be used to determine the GUT values of the common gaugino and scalar masses m_0 and $m_{1/2}$, the universal trilinear coupling A_0 as well as the value of $\tan\beta$. The result of a fit performed in Ref. [206] for the SPS1a scenario is shown in Tab. 5.4, with the sign of μ fixed to its true value, i.e. $\mu > 0$; for further analyses, see e.g. Ref. [207]. At the LHC, these fundamental parameters can be determined at the percent level but the ILC improves the determination by an order of magnitude; a very accurate picture is achieved when the LHC and ILC data are combined.

TABLE 5.4

Summary of the cMSSM fit in SPS1a (with $\mu > 0$ fixed) and SPS1a' based on the parameter values of Tab. 5.3 at the LHC, ILC and their combination. The same warnings on the differences between the two analyses as in the caption of Table 5.3 hold also in this context.

| | SPS1a | LHC | ILC | LHC+ILC | SPS1a' | $\Delta_{\text{LHC+ILC}}$ |
|-------------|-------|-------------------|-------------------|-------------------|--------|---------------------------|
| m_0 | 100 | 100.03 ± 4.0 | 100.03 ± 0.09 | 100.04 ± 0.08 | 70 | 0.2 |
| $m_{1/2}$ | 250 | 249.95 ± 1.8 | 250.02 ± 0.13 | 250.01 ± 0.11 | 250 | 0.2 |
| $\tan\beta$ | 10 | 9.87 ± 1.3 | 9.98 ± 0.14 | 9.98 ± 0.14 | 10 | 0.3 |
| A_0 | -100 | -99.29 ± 31.8 | -98.26 ± 4.43 | -98.25 ± 4.13 | -300 | 13 |

5.3.4 Analyses in other GUT scenarios

The case of the cMSSM discussed previously demonstrates that high-precision measurements allow us to reconstruct physical scenarios near the Planck scale. This can be done in many other GUT scenarios and the example of string effective theories is briefly discussed below. another example, left–right symmetric models which incorporate the seesaw mechanism to generate the small neutrino masses will be discussed in chapter 7.

Heterotic string theories give rise to a set of 4-dimensional dilaton S and moduli T superfields after compactification. The vacuum expectation values of S and T , generated by non–perturbative effects, determine the soft supersymmetry breaking parameters. The properties of the theories are quite different for dilaton and moduli dominated scenarios, quantified by the mixing angle θ . This angle θ characterizes the \tilde{S} and \tilde{T} components of the wave function of the Goldstino, which is associated with the breaking of supersymmetry. The mass scale is set by the second parameter of the theory, the gravitino mass $m_{3/2}$.

In leading order, the masses [209] are given by, $M_i \propto -g_i^2 m_{3/2} \langle S \rangle \sqrt{3} \sin \theta$ and $M_j^2 \propto m_{3/2}^2 (1 + n_j \cos^2 \theta)$ for the gaugino and scalar sectors, respectively. A dilaton dominated scenario, $\sin \theta \rightarrow 1$, leads to universal boundary conditions of the soft–SUSY breaking parameters while in moduli dominated scenarios, $\cos \theta \rightarrow 1$, the gaugino masses are universal but not the scalar masses. The breaking is characterized by integer modular weights n_j which quantify the couplings between matter and moduli fields. Within one generation, significant differences between left and right sfermions and between sleptons and squarks can occur.

The results [208] for the analysis of a mixed dilaton/moduli superstring scenario with dominating dilaton component, $\sin^2 \theta = 0.9$, and with different couplings of the moduli field to the (L,R) sleptons, the (L,R) squarks and to the Higgs fields corresponding to the O–I representation $n_{L_i} = -3$, $n_{E_i} = -1$, $n_{H_1} = n_{H_2} = -1$, $n_{Q_i} = 0$, $n_{D_i} = 1$ and $n_{U_i} = -2$, are presented in Fig. 5.8. The gravitino mass is set to 180 GeV in this analysis. Given this set of superstring induced parameters, the evolution of the gaugino and scalar mass parameters can be exploited to determine the modular weights n . Fig. 5.8 demonstrates how stringently this theory can be tested by analyzing the integer character of the entire set of weights.

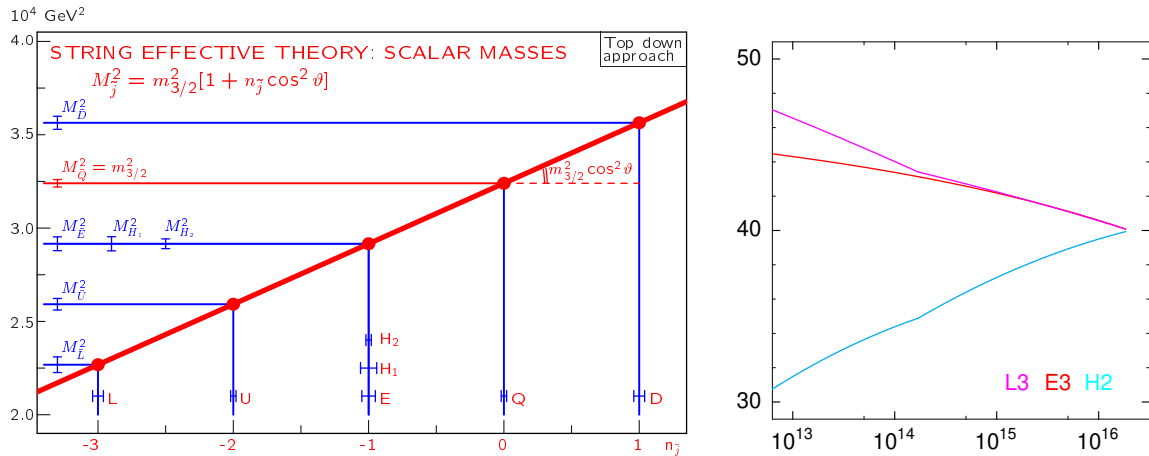


FIGURE 5.8. Left: the linear relation between integer modular weights and scalar mass parameters in string effective theories [208]. Right: impact of the heavy right–handed neutrino mass on the evolution of the scalar mass parameters in left–right symmetric theories [210].

Thus, high-precision measurements at the ILC may provide access to crucial low and high-scale parameters which allow to discriminate between various theories beyond the SM.

Another example of model parameterization at the very high scale is provided by left–right symmetric extensions of the SM. The complex structure observed in the neutrino sector requires the extension of the MSSM by a superfield including the right–handed neutrino field and its scalar partner. If the small neutrino masses are generated by the seesaw mechanism [211], a similar type of spectrum is induced in the scalar sneutrino sector, splitting into light TeV scale and very heavy masses. The intermediate seesaw scales will affect the evolution of the soft mass terms which break the supersymmetry at the high (GUT) scale, particularly in the third generation with large Yukawa couplings.

If sneutrinos are lighter than charginos and the second lightest neutralino, as encoded in SPS1a', they decay only to invisible $\nu\tilde{\chi}_1^0$ final states, but sneutrino masses can be measured in chargino decays to sneutrinos and leptons. These decays develop sharp edges at the endpoints of the lepton energy spectrum for charginos produced in e^+e^- annihilation. Sneutrinos of all three generations can be explored this way [210]. As seen before, the errors for the first and second generation sneutrinos are expected at the level of 400 MeV, doubling for the more involved analysis of the third generation.

This will provide us with the opportunity to measure, indirectly, the intermediate seesaw scale of the third generation [210]. This can be illustrated in an SO(10) model in which the Yukawa couplings in the neutrino sector are proportional to the up–type quark mass matrix. The masses of the right–handed Majorana neutrinos are hierarchical, $\propto m_{\text{up}}^2$, and the mass of the heaviest neutrino is given by $M_{R_3} \sim m_t^2/m_{\nu_3}$ which, for $m_{\nu_3} \sim 5 \times 10^{-2}$ eV, amounts to $\sim 6 \times 10^{14}$ GeV, i.e., a value close to the GUT scale.

Since the ν_R is unfrozen only beyond $Q = M_{\nu_R}$ the impact of the left–right extension will be visible in the evolution of the scalar mass parameters only at very high scales. The effect of ν_R can be manifest only in the third generation where the Yukawa coupling is large enough; the evolution in the first two generations can thus be used to calibrate the assumption of universality for the scalar mass parameters at the unification scale. In Fig. 5.8 the evolution of the scalar mass parameters in the third generation and the Higgs mass parameter are displayed. The lines include the effects of the right–handed neutrino which induce the kinks. Only the picture including $\nu_R, \tilde{\nu}_R$ is compatible with the assumption of unification.

The kinks in the evolution of $M_{\tilde{L}_3}^2$ shift the physical masses [squared] of the $\tilde{\tau}_L$ and $\tilde{\nu}_{\tau L}$ particles of the third generation by the amount $\Delta_\nu[M_R]$ compared with the slepton masses of the first two generations. The measurement of $\Delta_\nu[M_{R_3}] \propto m_{\nu_3} M_{R_3} \log(M_{GUT}^2/M_{R_3}^2)$ can be exploited to determine the neutrino seesaw scale of the third generation, $M_{R_3} = 3.7\text{--}6.9 \times 10^{14}$ GeV [210], in the LR extended SPS1a' scenario with an initial value of 6×10^{14} GeV.

Thus, this analysis provides us with a unique possibility of indirectly verifying the seesaw mechanism and estimate of the high-scale ν_R seesaw mass parameter M_{R_3} . This would have an impact in explaining the baryon asymmetry of the universe if it is triggered by leptogenesis as will be discussed in chapter 7.

CHAPTER 6

Alternative scenarios

6.1 GENERAL MOTIVATION AND SCENARIOS

Besides supersymmetric models, there are many proposals for physics scenarios beyond the Standard Model. These alternative scenarios involve new dynamics on the electroweak symmetry breaking and/or new concepts on space-time and their main motivation is, in most cases, to provide a solution to the naturalness problem. Since this problem is connected with the stability of the electroweak symmetry breaking scale, and the new ingredients are closely related to the physics of the Higgs sector, its solution necessarily involves new particles and/or new interactions at the Terascale. Furthermore, these models need to address the question of the dark matter which calls for a new stable particle with a mass near the EWSB scale. Among the plethora of scenarios which have been proposed, some examples are as follows:

Models with large extra dimensions [58]: If there is an extra dimensional space where only gravitons can propagate, the weakness of the gravitational interaction can be explained. In this case, the four-dimensional Planck mass is a fictitious mass scale, and the fundamental gravity mass scale in the higher dimension can be close to the TeV scale. A characteristic collider signal is Kaluza–Klein (KK) graviton emission where topologies with missing energy are expected at the LHC and ILC. KK graviton exchange in fermion pair production will play an important role to confirm the gravitational nature of the new particles.

Warped extra-dimension models [55]: In the setup proposed by Randall and Sundrum (RS), two three-dimensional branes are placed at different points in the fifth dimensional direction, and the space-time between two branes is part of a five-dimensional anti-de Sitter space. In this case, the mass scale on the SM brane is exponentially suppressed compared to that on the Planck brane. The weakness of gravitation is explained by the suppression of the graviton wave function at the SM brane. The KK modes of the graviton, however, can couple strongly to the SM particles, and these may be produced as spin-two resonances at the LHC and ILC. Their effects may also appear indirectly in SM particle production processes. Note that five-dimensional RS models are dual to strongly coupled four-dimensional models.

Universal extra dimension (UED) models [212]: In these models, all SM particles are assumed to propagate in a flat extra-dimensional space. With a suitable orbifold compactification, one can construct a phenomenologically viable model. These models look like a bosonic supersymmetric theory since the first KK modes play the role of superpartners in SUSY models but with the wrong spins. One can introduce a KK parity which makes the lightest first KK particle absolutely stable and a potential dark matter candidate.

Strong interaction models: Within the SM and its supersymmetric extensions, the Higgs field is introduced as a fundamental degree of freedom. Dynamical electroweak symmetry breaking is rooted in new strong interactions, not necessarily involving a Higgs boson [26]. If global symmetries of these interactions are broken spontaneously, a set of Goldstone bosons will be generated, such as pions after breaking chiral symmetries in QCD. By absorbing these Goldstones, longitudinal degrees of freedom and masses are generated for gauge bosons. Several scenarios have been developed along this path quite early [62, 63] as an alternative to the standard Higgs mechanism and more recently [61] in a variant responding to the success of the light Higgs picture in accounting for the high-precision electroweak data.

Little Higgs models [61]: These are models with a composite Higgs boson but, unlike traditional Technicolor models [63], the dynamical scale is around 10 TeV and the physical Higgs boson is considered to be a part of composite field. The quadratic divergence of the Higgs boson mass renormalization is canceled at the one-loop level by extra gauge bosons and top partners with a carefully chosen global and gauge symmetry structure. An interesting class of little Higgs models are those with T parity [213] in which the new particles can be much lighter than 1 TeV without conflict with the precision electroweak data. In particular, the lightest T-odd particle, a heavy photon, can be even lighter than a few hundred GeV.

There is a variety of possibilities in each of the above scenarios. In models with extra dimensions, phenomenological implications depend on which particles are allowed to propagate in the extra dimensions. The Higgsless model proposed in Ref. [66] is one type of a five-dimensional model. There are also proposals where the idea of extra space dimensions is combined with low energy supersymmetry. Some models in warped extra dimensions can be considered to be the dual description of strongly coupled conformal field theories [214] and composite Higgs scenarios have been proposed based on this duality [215].

The above alternative models introduce new particles and interactions at the TeV scale and new signals are expected at the LHC experiment. If some signals are indeed observed, the nature of the new physics could be determined by various precise measurements at the ILC. In this respect, indirect searches for new physics effects in SM and Higgs processes are also important at the ILC. In the following, typical examples of ILC studies are presented.

6.2 EXTRA DIMENSIONAL MODELS

6.2.1 Large extra dimensions

In the models with large extra dimensions, the effective four-dimensional Planck mass M_P is related to the fundamental gravity mass scale M_D in the $4 + \delta$ dimensional space-time by $M_P^2 = V_\delta M_D^{2+\delta}$ where V_δ is the volume of the extra-dimensional space. For example, taking $M_D = 1$ TeV, the size of the extra dimension is 0.1 mm to 1 fm for $\delta = 2$ to 6. The KK modes of the graviton have, therefore, an almost continuous spectrum.

At the ILC, the observation of a single photon with missing energy due to the emission of a KK graviton in the reaction $e^+e^- \rightarrow G_{KK}\gamma$ is a robust signal of the model. The sensitivity to the scale M_D in this channel is shown in Table 6.1 for polarized and unpolarized e^\pm beams. Beam polarization is very effective in this case as the main background process, $e^+e^- \rightarrow \nu\bar{\nu}\gamma$, can be suppressed significantly. The search limit for the scale M_D is similar to that obtained in gluon and KK graviton emission at the LHC. Note that there are severe cosmological and astrophysical [216] bounds on the mass M_D in this scenario; a recent analysis [217]

of astrophysical data sets a lower limit of several hundred TeV in the case of two extra dimensions. The limit is weaker for a larger number of extra dimensions and the constraints are not strong for $\delta \geq 4$.

TABLE 6.1

The sensitivity at the 95% CL in the mass scale M_D (in TeV) for direct graviton production in the polarized and unpolarized $e^+e^- \rightarrow \gamma G_{KK}$ process for various δ values assuming a 0.3% normalization error [7].

| δ | 3 | 4 | 5 | 6 |
|---|-----|-----|-----|-----|
| $M_D(\mathcal{P}_{e^-} = \mathcal{P}_{e^+} = 0)$ | 4.4 | 3.5 | 2.9 | 2.5 |
| $M_D(\mathcal{P}_{e^-} = 0.8)$ | 5.8 | 4.4 | 3.5 | 2.9 |
| $M_D(\mathcal{P}_{e^-} = 0.8, \mathcal{P}_{e^+} = 0.6)$ | 6.9 | 5.1 | 4.0 | 3.3 |

Once the missing energy signal is observed, the next step would be to confirm its gravitational nature and determine the number of extra dimensions. The ILC will play an essential role here. The number of extra dimensions can be determined from the energy dependence of the production cross section. In the left-hand side of Fig. 6.1, it is shown that its measurement at two collider energies, $\sqrt{s} = 500$ GeV and 800 GeV, can discriminate between scenarios with different numbers of extra dimensions. Additional information on the number of extra dimensions can also be obtained from the missing mass distribution.

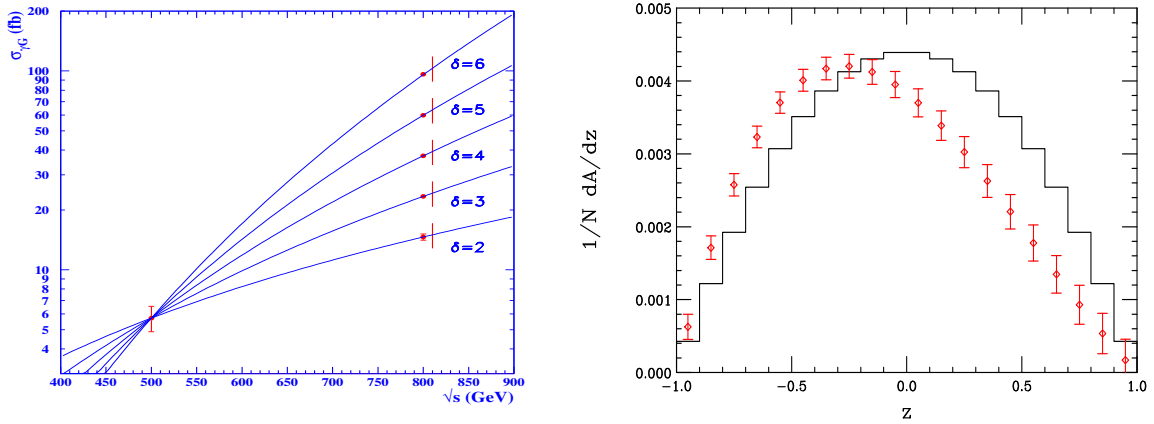


FIGURE 6.1. Left: determination of the number of extra-dimensions at the ILC at two center of mass energies $\sqrt{s} = 500$ and 800 GeV [218]. Right: the differential azimuthal asymmetry distribution for $e^+e^- \rightarrow \ell^+\ell^-$ at 500 GeV ILC with 500 fb $^{-1}$ data in the SM (histogram) and in the LED model with a cut-off of 1.5 TeV (data points); e^\pm are assumed to be 80% and 60% polarized, respectively [219].

An alternative signal for the presence of extra dimensions is provided by KK-graviton exchange in processes such as $e^+e^- \rightarrow f\bar{f}$. The mass reach in this channel is similar to that obtained in KK-graviton emission. Since many new physics models can generate deviations in this reaction, it is important to discriminate the extra-dimensional model from other scenarios. s -channel KK-graviton exchange has the characteristic signature of spin-two particle in the angular distributions of the $e^+e^- \rightarrow f\bar{f}, WW$ and HH production processes [220]. Furthermore, if both electron and positron are transversely polarized, the azimuthal asymmetry distribution provides a powerful tool to identify the spin-two nature of the virtually exchanged particle [17, 219] as shown in the right-hand side of Fig. 6.1.

6.2.2 Warped extra dimensions

In the original proposal of Randall and Sundrum [55], only the graviton was assumed to propagate in the extra-dimensional space and the SM fields were confined on the TeV brane. In this model, the mass scales of the dimensionful parameters in the action are set by the Planck scale, but the physical mass scales on the TeV (or SM) brane are reduced by the warp factor of $e^{-\pi k r_c}$ where $k r_c \sim 11$ to explain the hierarchy between the weak and Planck scales. A characteristic signal of this extension is the presence of the graviton KK modes near the TeV scale. In fact, the model is specified by two parameters, for instance, the mass of the first KK mode and k/M_* where M_* is the four-dimensional reduced Planck mass. KK graviton resonances can be searched for through the Drell-Yan process at the LHC and the mass reach can be 3–4 TeV, covering most of the interesting parameter space of the model [221].

If such resonances are indeed observed at the LHC, one needs to establish their gravitational nature. The spin of the resonance can be determined from the angular distribution of the final lepton pairs at the LHC and ILC [221, 222]. The search reach through contact interactions at the ILC with a c.m. energy of 500 GeV is similar to the LHC direct search reach and a 1 TeV ILC can significantly extend the discovery limit [15].

Another important property which has to be verified is the universal structure of the graviton couplings to other particles. For this purpose, the branching ratios of the resonances have to be determined precisely. An ultimate confirmation of the model would be provided by the s -channel production of the KK graviton state at the ILC as shown in Fig. 6.2. From line-shape analyses, the two independent parameters, the first KK mode mass and the ratio k/M_* , can be precisely determined along with the various decay branching ratios.

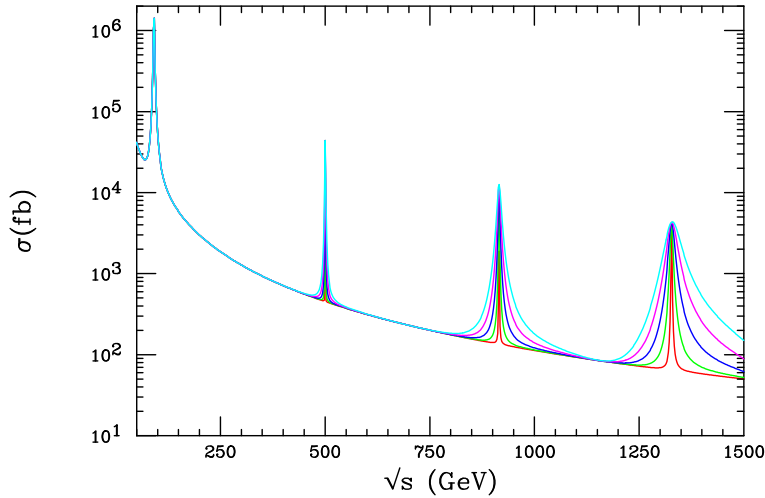


FIGURE 6.2. Graviton resonance production at the ILC in $e^+e^- \rightarrow \mu^+\mu^-$ in the RS model with the mass of the first KK mode taken to be 500 GeV; the exchange of a KK tower is included and the ever widening resonances correspond to increasing the value of k/M_* in the range of 0.01–0.1. From Ref. [221].

In RS models, one would expect the presence of a radion which will mix with the Higgs boson whose properties could be significantly altered. The Higgs couplings to various particles, for instance, could be reduced at the level of a few 10%. These effects can be easily identified with the precision ILC measurements as discussed in chapter 2. The radion has substantial couplings to the W/Z bosons and can be produced in the Higgs-strahlung $e^+e^- \rightarrow \phi Z$ or

WW fusion $e^+e^- \rightarrow \phi\nu_e\bar{\nu}_e$ processes. If it is relatively heavy, $M_\phi \gtrsim 2M_H$, it could decay into two Higgs bosons with large rates. This is illustrated in the left-hand side of Fig. 6.3 where $\text{BR}(\phi \rightarrow HH)$ is displayed as a function of the Higgs–radion mixing parameter ξ . Besides the dominating $\phi \rightarrow WW, ZZ$ decay modes, the channels $\phi \rightarrow HH$ can reach branching fractions of $\mathcal{O}(30\%)$ leading to a significant excess of Higgs pairs compared to the SM. Other decay channels of the radion, such as $\phi \rightarrow t\bar{t}$ and gg , besides WW and ZZ decays, can reach the level of few ten percent when kinematically accessible. These decays could also be probed at the ILC and the branching fractions measured very precisely.

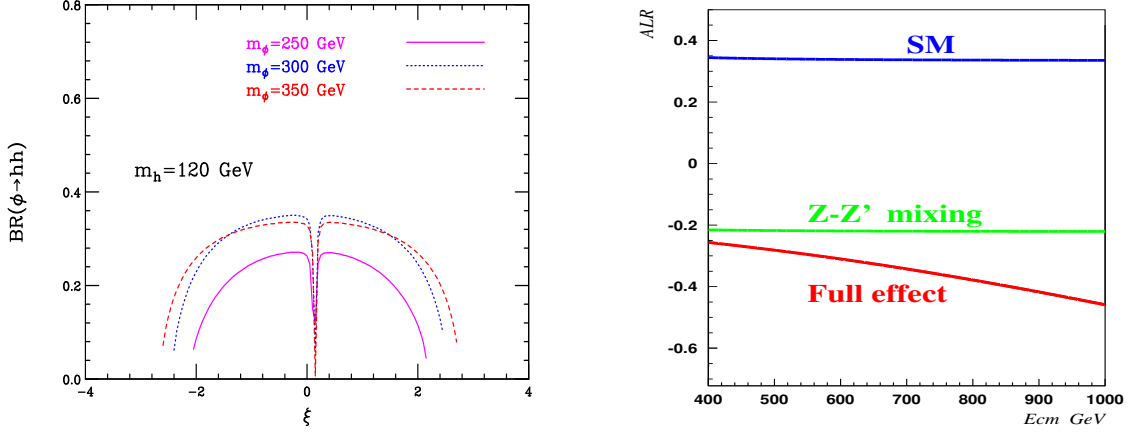


FIGURE 6.3. Left: the $\phi \rightarrow HH$ branching ratios as functions of the parameter ξ for $M_H = 120$ GeV and $\Lambda = 5$ TeV for several values of M_ϕ [57]. Right: the energy dependence of the left–right polarization asymmetry for $t\bar{t}$ production at the ILC in the SM and in the RS scenario in the pure Z – V_{KK} mixing case and taking also into account the virtual KK exchange [124].

The version of the RS model with bulk matter offers the possibility of generating the large mass hierarchies prevailing among SM fermions if they are placed differently along the extra dimension [223]. An interesting aspect of this scenario is related to the KK excitations of gauge bosons. If the SM symmetry is enhanced to $SU(2)_L \times SU(2)_R \times U(1)$, the high-precision data can be fitted while keeping the KK masses down to values as low as 3 TeV. Since the third generation fermions should be localized closer to the TeV-brane to get higher masses, their couplings to the KK gauge bosons are larger and generate more important effects in the t and b sectors. In particular, the stronger b couplings induce a large mixing between the Z and KK bosons which allows to resolve the LEP anomaly on the asymmetry A_{FB}^b [120]. With the high precision in the measurement of the production rates and polarization/angular asymmetries in the $e^+e^- \rightarrow t\bar{t}$ and $b\bar{b}$ processes, KK excitations exchanged in the s -channel can be probed even for masses up to ~ 20 TeV [124]. This is exemplified in Fig. 6.3 (right) where the deviations in the left–right asymmetry A_{LR}^t in $e^+e^- \rightarrow t\bar{t}$ are displayed as a function of \sqrt{s} for fermion localizations and couplings which resolve the A_{FB}^b anomaly with a KK mass of 3 TeV. With the ILC accuracy, a measurement of 10% of the KK mass can be achieved. Additional information on the KK couplings can be obtained from a more precise measurement of A_{FB}^b , A_{LR}^b and $\Gamma(Z \rightarrow b\bar{b})$ at the GigaZ option of the ILC.

Note that in such models, there may be also new fermions with not too large masses. For instance, the $SU(2)_R$ partner of t_R , b'_R , typically reaches KK masses as low as a few hundred GeV and can be thus produced and studied in detail at the ILC. This new quark might affect dramatically the production rates of the Higgs boson at the LHC as discussed earlier.

6.2.3 Universal extra dimensions

Universal extra dimensions (UED) [212] is the model which resembles the most to the original Nordström–Kaluza–Klein scenario. All SM particles are assumed to propagate in a flat extra-dimensional space which is compactified to an orbifold. In the minimal version, the extra one-dimensional space is compactified in the form of an S_1/Z_2 orbifold, where a circle S_1 is divided in half by Z_2 projection. Viewed as a four dimensional theory, the UED model introduces a Kaluza–Klein tower for each SM particle. The common mass of the n th KK states is roughly given by n/R where R is the compactification radius, but radiative corrections and boundary terms lift the initial mass degeneracy of the n th KK states.

In UED models, momentum conservation in the fifth dimension is replaced by a conserved parity, called KK-parity [224, 225]. The zero modes, i.e. the SM particles, are even under this parity but the lightest massive modes are odd. This has the major consequence that the lightest KK particle (LKP), which in general corresponds to the KK hypercharge gauge boson, is absolutely stable. It gives missing transverse energy signals at colliders and is a good dark matter candidate as will be discussed in chapter 7. Another important consequence of this parity is that $n = 1$ KK particles are only produced in pairs. This suppresses their virtual corrections to SM processes, allowing the UED scale $1/R$ to be as low as 300 GeV without conflicting with high-precision electroweak data.

From the previous discussion, one concludes that the situation in UED models is quite analogous to the minimal supersymmetric SM extension with conserved R-parity, except that here, the lightest particle is a spin-one particle, a heavy photon. Thus, if only the first massive KK modes are produced, UED models would look very much like a subset of SUSY models in terms of their collider signatures. Even if one detects a few of the second level KK modes, it is not obvious that this will discriminate the signatures from an extended SUSY model. The crucial discriminators, of course, are the spins of the heavy partner particles. At the LHC, distinguishing these spins is a significant experimental challenge. The ILC will play an important role in this context as the spin difference between superpartners and KK excitations can be determined in detailed angular distribution studies and threshold scans. This is exemplified in Fig. 6.4 where the threshold excitation curve and the angular distribution in the case of $e^+e^- \rightarrow \mu_{R1}^+ \mu_{R1}^-$ for the first muon KK excitation in UED models is compared to smuon pair production in the MSSM, $e^+e^- \rightarrow \tilde{\mu}_R^+ \tilde{\mu}_R^-$ [187].

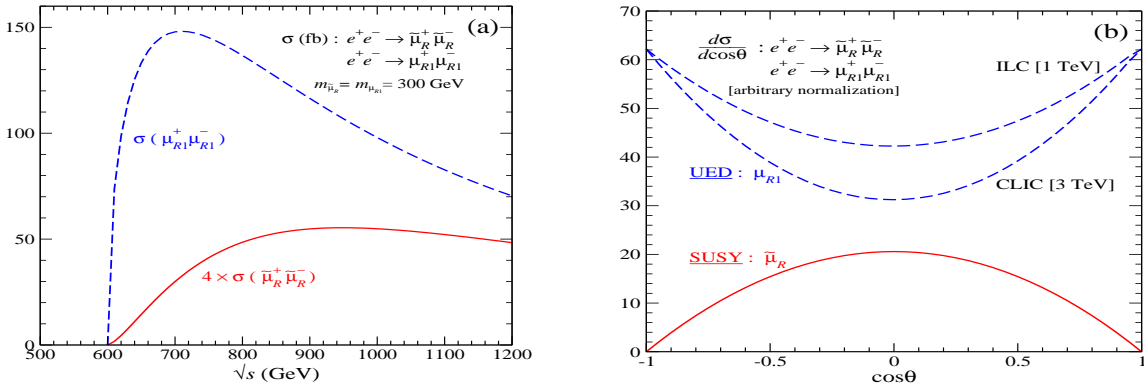


FIGURE 6.4. The threshold excitation for smuons (a) and the angular distribution (b) in the case of smuons in the MSSM and the first KK excitation μ_{R1}^\pm in UED in pair production at the ILC; from Ref. [187].

6.3 STRONG INTERACTION MODELS

6.3.1 Little Higgs models

To interpret the Higgs boson as a (pseudo-)Goldstone boson has been a very attractive idea for a long time. The interest in this picture has been renewed within the little Higgs scenarios [61], that have recently been developed to generate the electroweak symmetry breaking dynamically by new strong interactions. Little Higgs models (LHMs) are based on a complex system of symmetries and symmetry breaking mechanisms. Three points are central in realizing the idea: (i) the Higgs field is a Goldstone field associated with the breaking of a global symmetry G at an energy scale of order $\Lambda_s \sim 4\pi f \sim 10$ to 30 TeV, with f characterizing the scale of the symmetry breaking parameter; (ii) in the same step, the gauge symmetry $G_0 \subset G$ is broken down to the SM gauge group, generating masses for heavy vector bosons and fermions which cancel the standard quadratic divergencies in the radiative corrections to the light Higgs mass; since the masses of these new particles are generated by the breaking of the gauge symmetry G_0 they are of the intermediate size $M \sim gf \sim 1$ to 3 TeV; (iii) the Higgs bosons acquire a mass finally through radiative corrections at the standard electroweak scale of order $v \sim g^2 f / 4\pi \sim 100$ to 300 GeV.

Thus, three characteristic scales are encountered in these models: the strong interaction scale Λ_s , the new mass scale M and the electroweak breaking scale v , ordered in the hierarchical chain $\Lambda_s \gg M \gg v$. The light Higgs boson mass is protected at small value by requiring the collective breaking of two symmetries. In contrast to the boson–fermion symmetry that cancels quadratic divergencies in supersymmetry, the cancellation in LHMs operates in the bosonic and fermionic sectors individually, the cancellation ensured by the symmetries among the couplings of the SM fields and new fields to the Higgs field.

A generic feature of LHMs is the existence of extra gauge bosons, Higgs particles and partners of the top quark. The masses of these new particles are constrained by electroweak precision measurements. Although the precise values depend on the specific model under consideration, these are usually beyond a few TeV, so that their direct production is kinematically not accessible at the ILC. If one introduces T-parity, these masses can be below the TeV scale, but T-odd particles should be pair produced. Even if the new particles are beyond the kinematical reach of the ILC, indirect searches for effects of LHMs is possible in SM processes such as $e^+e^- \rightarrow f\bar{f}, t\bar{t}, ZH$ and $\gamma\gamma \rightarrow H$.

An example of indirect search of the new states at the ILC is shown in the left-hand side of Fig. 6.5. The figure displays the limit on the vev f associated with $SU(5) \rightarrow SO(5)$ symmetry breaking in LHMs as derived from the $e^+e^- \rightarrow f\bar{f}$ processes with a center of mass energy $\sqrt{s} = 500$ GeV and an integrated luminosity of 500 fb^{-1} . Two new mixing angles s and s' specify the gauge symmetry breaking of $[SU(2) \times U(1)]^2 \rightarrow SU(2)_L \times U(1)_Y$. For comparison, the LHC search reach for the heavy gauge boson Z_H is also shown. As can be seen, the indirect searches at the ILC can extend the LHC search limit substantially. A similar search can be performed in the $e^+e^- \rightarrow ZH$ process but with less sensitivity.

In order to cancel the quadratic divergence in the Higgs mass in LHMs, the top quark sector has to be extended. The ordinary top quark is identified as one light combination of the extended top sector so that there could be sizable deviations in the top coupling to W/Z bosons. In Fig. 6.5 (right), the correction to the $t\bar{t}Z$ coupling is shown in the case of LHMs with T-parity. The displayed ILC search limit indicates that most of the interesting parameter region is covered by future high-precision top quark measurements.

ALTERNATIVE SCENARIOS

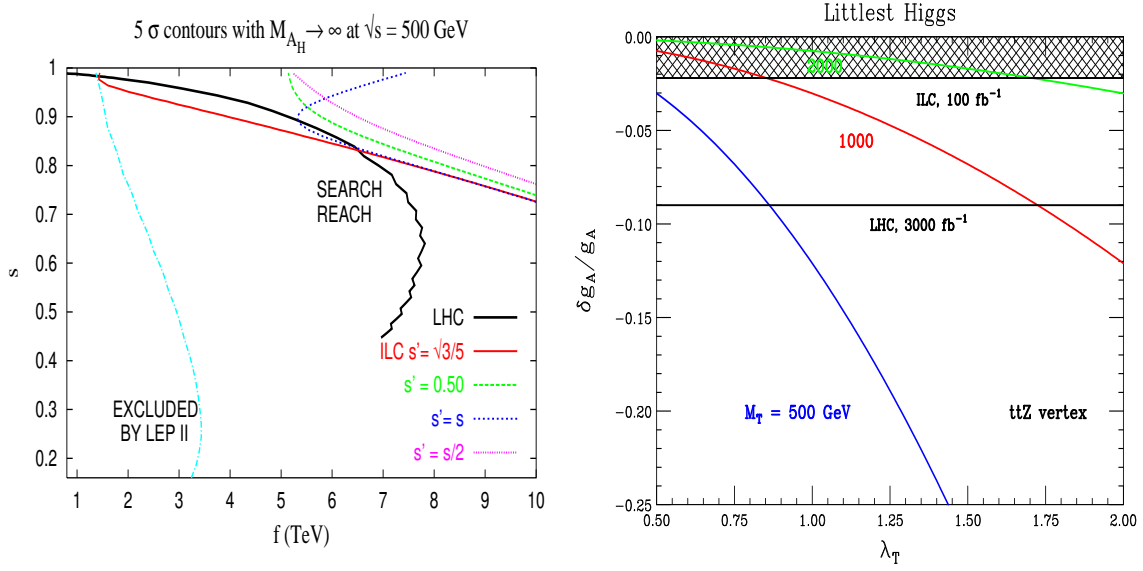


FIGURE 6.5. Left: the ILC search reach in LHMs, as derived from the process $e^+e^- \rightarrow f\bar{f}$, is compared to the LHC reach in heavy Z' boson searches; the decoupling limit of the heavy photon is taken [226]. Right: the corrections to the $t\bar{t}Z$ coupling in LHMs with conserved T-parity for two values of the heavy top quark partner compared to the (super)LHC and ILC sensitivities [227].

Even if T-parity is not imposed, a pseudo-axion might be light enough to be accessible at the ILC in the case where LHMs possess a spontaneously broken approximate U(1) symmetry as in the simplest model [228]. In such a case the pseudo-axion η could be produced in association with the Higgs boson, $e^+e^- \rightarrow H\eta$ and would decay via $\eta \rightarrow HZ$. This is exemplified in Fig. 6.6 (left) where the cross section for the $e^+e^- \rightarrow \eta H \rightarrow HHZ$ process is shown as a function of \sqrt{s} for scenarios with and without the contribution of a Z' boson [64]. The new contributions increase the ZHH rate by an order of magnitude compared to the SM. A relatively light η boson could also be produced in association with top quark pairs, $e^+e^- \rightarrow t\bar{t}\eta$ and the signal in which the η resonance dominantly decays into $b\bar{b}$ pairs could be easily observed at the ILC as shown in Fig. 6.6 (right) for several M_η values.

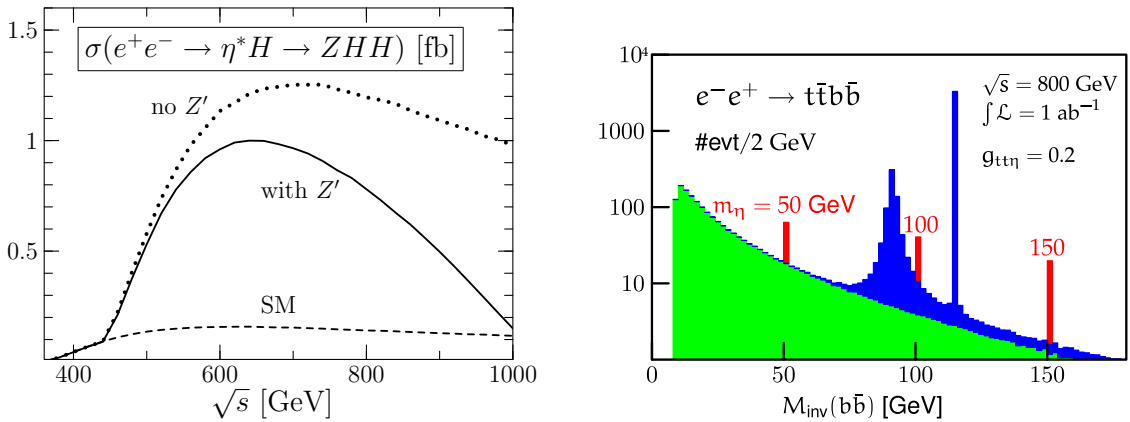


FIGURE 6.6. Left: the cross section of double Higgs production with and without Z' exchange compared with the SM prediction in the simplest LHM for $M_H \sim 130$ GeV and $M_\eta \sim 300$ GeV. Right: the reconstructed $b\bar{b}$ invariant mass in the process $e^+e^- \rightarrow t\bar{t}\eta \rightarrow t\bar{t}b\bar{b}$ compared to the SM background; the peaks correspond to Z, H production and to the η resonance for several M_η values. From Ref. [64].

6.3.2 Strong electroweak symmetry breaking

If no Higgs boson will be observed with mass below 1 TeV, quantum-mechanical unitarity demands strong interactions between the electroweak gauge bosons, becoming effective at energies $(8\pi/\sqrt{2}G_F)^{1/2} \simeq 1.2$ TeV, to damp the growth of the amplitudes for (quasi-)elastic massive gauge boson scattering processes [38].

As discussed in chapter 3, the new interactions between the weak bosons can be expanded in a series of effective interaction terms with rising dimensions [130]. Scattering amplitudes are expanded correspondingly in a series characterized by the energy coefficients s/Λ_*^2 . Demanding CP and isospin invariance, for instance, only two new dimension-four interaction terms (out of the 10 terms present in the general case) must be included in the expansion, L_4 and L_5 , with coefficients $\alpha_{4,5} = v^2/\Lambda_{*4,5}^2$ with scale parameters bounded from above by the value $4\pi v \sim 3$ TeV. The parameters α_i can be measured in the quasi-elastic VV scattering processes $e^+e^- \rightarrow \ell\ell VV$ and triple gauge boson production $e^+e^- \rightarrow VVV$, as the new interaction terms affect the total cross sections and the final state distributions.

As can be seen from Figs. 3.4 and 3.5 of chapter 3, at $\sqrt{s} = 1$ TeV with 1 ab⁻¹ data, the entire range of Λ_* values can be covered, $\Lambda_* \leq 4\pi v \simeq 3$ TeV. These values can be conveniently re-expressed in terms of the maximal mass of the heavy resonances associated with the new interactions the measurement can be sensitive to, under the most favorable conditions; Fig. 6.7 (left). In Table 6.2, displayed are the combined results obtained in the full analysis of Ref. [131] for the sensitivity on the scale Λ_* for all possible spin/isospin channels. In the left-hand side of the table, a conserved $SU(2)_c$ is assumed and in this case, only the channels with even $I+J$ couple to weak boson pairs; in the right-hand side, shown are the results without this constraint. In each case, a single resonance with maximal coupling was assumed to be present. As one can see, scales from ~ 1.5 to ~ 6 TeV can be probed.

TABLE 6.2

Accessible scales Λ_* in TeV for all possible spin/isospin channels from a complete analysis of vector boson scattering processes at 1 TeV the ILC, assuming a single resonance with optimal properties [131]. The numbers in the left-(right-)hand side are with (without) assuming the custodial symmetry.

| Spin | I=0 | I=1 | I=2 | I=0 | I=1 | I=2 |
|------|------|------|------|------|------|------|
| 0 | 1.55 | – | 1.95 | 1.39 | 1.55 | 1.95 |
| 1 | – | 2.49 | – | 1.74 | 2.67 | – |
| 2 | 3.29 | – | 4.30 | 3.00 | 3.01 | 5.84 |

Alternatively, when resonances below the scale Λ_* are present, the vector boson pair production amplitude can be unitarised by a Omnès rescattering factor with one contribution reproducing the low energy theorem $\delta_{\text{LET}}(s) = s/(8\Lambda_{\text{EWSB}}^2)$ for Goldstone boson scattering at threshold far below any resonance and a second contribution from a resonance $\delta_\rho(s) = 3\pi/8 \cdot (\tanh(s - M_\rho^2)/(M_\rho\Gamma_\rho) + 1)$. A study performed in Ref. [229] has shown that W^+W^- production at the ILC with $\sqrt{s} = 800$ GeV and $\mathcal{L} = 500\text{fb}^{-1}$ is competitive with the LHC. As shown in the right-hand side of Fig. 6.7, there is a 6σ exclusion limit for the LET and one can exclude a ρ -like resonance of 2.5 (1.6) TeV at the 16 (33) σ level.

A concrete example of models with a strong EWSB sector is the BESS model [231], which includes most Technicolor models [63]. It assumes a triplet of new vector resonances $V^{\pm,0}$, similar to the ρ or techni- ρ , which mix with the W/Z bosons with a mixing $\propto g/g''$, where g'' is the self-coupling of the $V^{\pm,0}$ state. The $f\bar{f}V^{\pm,0}$ couplings are determined by a second

ALTERNATIVE SCENARIOS

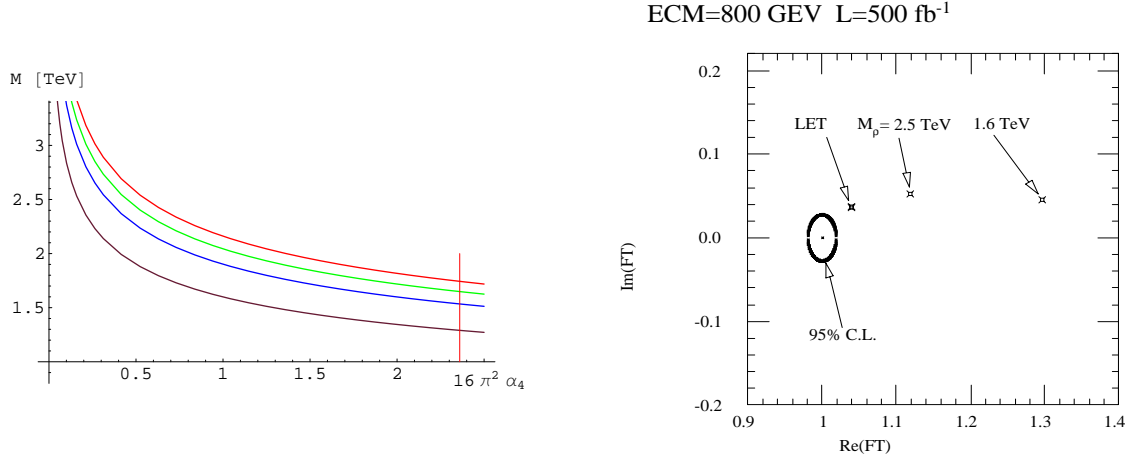


FIGURE 6.7. Left: dependence of the mass of a singlet vector resonance on α_4 for different values of $\Gamma_\pi/M_\pi = 1.0$ (red), 0.8 (blue), 0.3 (brown) [131]. Right: sensitivity for a resonance form factor at a 800 GeV ILC with 500 fb^{-1} data assuming perfect charm tagging [229].

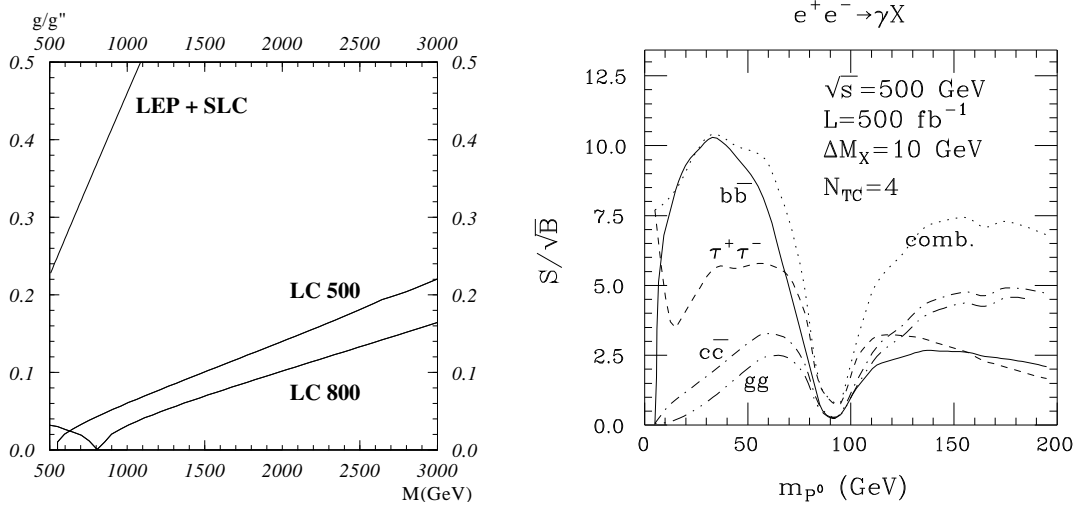


FIGURE 6.8. Left: the 95% C.L. contours for the BESS model parameters from the ILC at $\sqrt{s} = 500$ and 800 GeV compared to present constraints. Right: statistical significance for a P^0 signal in various tagged channels as a function of m_{P^0} at $\sqrt{s} = 500$ GeV with 500 fb^{-1} data. From Ref. [230].

parameter b . A variant of the model, the degenerate BESS, is when the axial and vector resonances are almost degenerate in mass. As many scenarios of dynamical EWSB, it predicts the presence of pseudo Nambu Goldstone bosons (PNGBs).

The vector resonances of the BESS model can be observed in $e^+e^- \rightarrow W^+W^-$ in the general or in $e^+e^- \rightarrow f\bar{f}$ in the degenerate cases. Combining all possible observables in these two channels and using beam polarization, the sensitivity of the ILC on the parameters of the general model is larger than the one expected at the LHC. In the degenerate case, the ILC sensitivity is shown in Fig. 6.8 (left) and if a resonance below 1 TeV is observed at the LHC, one can study it in detail and attempt to split the two nearly degenerate resonances and measure their widths [230]. In addition, the lightest PNGB P^0 can be produced at the ILC e.g. in the reaction $e^+e^- \rightarrow \gamma P^0$ as shown in Fig. 6.8 (right); unlike at the LHC, low P^0 masses can be probed and rates for interesting decay modes can be measured [230].

6.3.3 Higgsless scenarios in extra dimensions

Also in theories with extra space dimensions, the electroweak symmetry can be broken without introducing a fundamental scalar field, leading to Higgsless theories [66]. Since in five-dimensional theories the wave functions are expanded by a fifth component, the electroweak symmetry can be broken by applying appropriately chosen boundary conditions to this field component. This scalar component of the original five-dimensional gauge field is absorbed to generate the massive KK towers of the gauge fields in four dimensions. The additional exchange of these towers in WW scattering damps the scattering amplitude of the SM and allows, in principle, to extend the theory to energies beyond the $\mathcal{O}(1)$ TeV unitarity bound of Higgsless scenarios. However, it is presently unclear whether realistic models of this type can be constructed that give rise to small enough elastic WW scattering amplitudes compatible with perturbative unitarity [232].

Higgsless models can be best tested at the ILC if the energy is pushed to its maximum. Unlike for Technicolor models, one expects that the masses of the new vector bosons, collectively called V_1 , are below the TeV scale and thus kinematically accessible. In this case, they can be produced in the W/Z fusion processes $e^+e^- \rightarrow V_1^\pm e^\mp \nu_e$ and $e^+e^- \rightarrow V_1^0 \nu_e \bar{\nu}_e$ for the charged and neutral states, respectively. The cross sections for these processes, as well as the one for the associated production process $e^+e^- \rightarrow V^\pm W^\mp$, are shown as a function of the V_1 mass in the left-hand side of Fig. 6.9 for c.m. energies of $\sqrt{s} = 500$ GeV and $\sqrt{s} = 1$ TeV and compared to the SM $W^\pm W^\mp Z$ continuum background [233]. One can see that the rates are rather large, exceeding the femtobarn level for V_1 masses close to $M_{V_1} = 800$ GeV at a 1 TeV c.m. energy, before experimental cuts and efficiencies are applied. Thanks to the clean environment, the dominant hadronic decays of the W/Z bosons can be used and the invariant masses of the V_1 resonances can be easily reconstructed. This provides an extra handle for suppressing the SM background as shown in the right-hand side of Fig. 6.9 where the WZ invariant mass distribution for the signal of Higgsless models and the SM background are compared for the same two c.m. energies and several values of the resonance masses. Thus, the ILC has a real potential to test some of the generic predictions of Higgsless models.

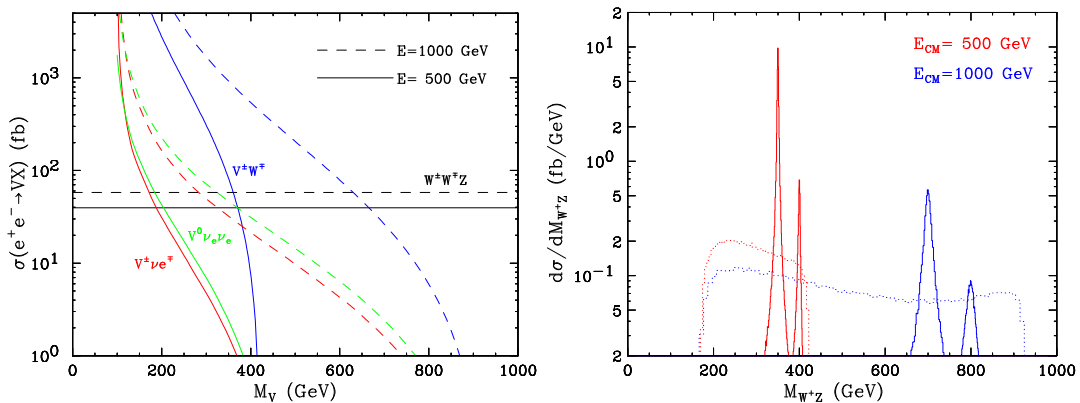


FIGURE 6.9. Left: the production cross sections for the new gauge bosons V_1 and the continuum SM background at the ILC. Right: the WZ invariant mass distribution for the signal in Higgsless models and the SM background. In both cases, the c.m. energy is $\sqrt{s} = 500$ GeV and 1 TeV. From Ref. [233].

6.4 NEW PARTICLES AND INTERACTIONS

New gauge and/or matter particles, not necessarily related to the electroweak symmetry breaking mechanism, are predicted in many extensions of the Standard Model. If any signals for these new particles are seen, it will be crucial to distinguish among the variety of possible new states. Total cross sections, angular distributions and the final polarization can be used to discriminate among the different possibilities; longitudinally polarized beams allow for additional methods to unravel the helicity structure of the new underlying interactions. If new states are directly or indirectly accessible, the ILC will be the ideal instrument to determine their characteristics as will be briefly illustrated below.

6.4.1 New gauge bosons

Gauge bosons in the intermediate TeV scale are motivated by many theoretical approaches [234]. For instance, the breaking of GUTs based on $SO(10)$ or E_6 symmetries, may leave one or several $U(1)$ remnants unbroken down to TeV energies, before the symmetry reduces to the SM symmetry. In the case of the E_6 model, one has the possible breaking pattern:

$$E_6 \rightarrow SO(10) \times U(1)_\psi \rightarrow SU(5) \times U(1)_\chi \times U(1)_\psi \rightarrow SM \times U(1)'$$

and the new Z' corresponding to the final $U(1)'$ remnant, is a linear combination of the gauge bosons of the $U(1)$'s generated in the two-step symmetry breaking, $Z' = Z_\chi \cos \beta + Z_\psi \sin \beta$. The value $\beta = \arctan(-\sqrt{5/3})$ would correspond to a Z'_η originating from the direct breaking of E_6 to a rank-5 group in superstrings inspired models. Another interesting option is left-right (LR) models, based on the group $SU(2)_R \times SU(2)_L \times U(1)_{B-L}$ in which the new Z'_{LR} will couple to a linear combination of the right-handed and B-L currents with a parameter $\alpha_{LR}^2 \sim 3g_R^2/g_L^2 - 1$. The value $\alpha_{LR} \sim \sqrt{2}$ corresponds to a LR symmetric model with equal $SU(2)_R$ and $SU(2)_L$ couplings, $g_R = g_L$. As has been discussed previously, new gauge bosons also appear in little Higgs models and, in extra-dimensional models, the Kaluza-Klein excitations of the electroweak gauge bosons can have masses in the range of a few TeV.

Such intermediate gauge bosons can be searched for at the LHC in the Drell-Yan process, $q\bar{q} \rightarrow Z' \rightarrow \ell^+\ell^-$ with $\ell = e, \mu$, and masses up to about 5 TeV can be reached in general [12, 13]. If Z' bosons are found at the LHC, the role of the ILC will be twofold. First, by analyzing the effect of virtual Z' s -channel exchange on the cross sections and angular distributions of fermion pair production, $e^+e^- \rightarrow f\bar{f}$, the sensitivity to new gauge boson scales can be extended significantly. Second, the couplings of the new Z' boson to SM fermions can be determined very precisely using forward-backward asymmetries and the polarization dependence of the cross sections. The various models could be then clearly discriminated and the nature of the underlying gauge symmetry or model could be identified.

By studying the interference between the γ, Z and the Z' boson exchange contributions in the process $e^+e^- \rightarrow f\bar{f}$, the effects of the new gauge boson can be probed for masses in the multi-TeV range [235]. Already at a $\sqrt{s} = 500$ GeV ILC, the mass reach is comparable to that of the LHC as exemplified in the left-hand side of Fig. 6.10 for several models. This is particularly the case for Z'_{LR} boson and the KK excitations where the mass reach exceeds 5 TeV and 10 TeV, respectively. The sensitivity will be significantly increased when the ILC will be upgraded to $\sqrt{s} = 1$ TeV if the same integrated luminosity is collected.

The Z' mass reach can also be further extended using the GigaZ option of the ILC. Precision electroweak measurements at the Z pole provide a complementary information as they are sensitive to the mixing between the Z and the Z' bosons which is expected to be

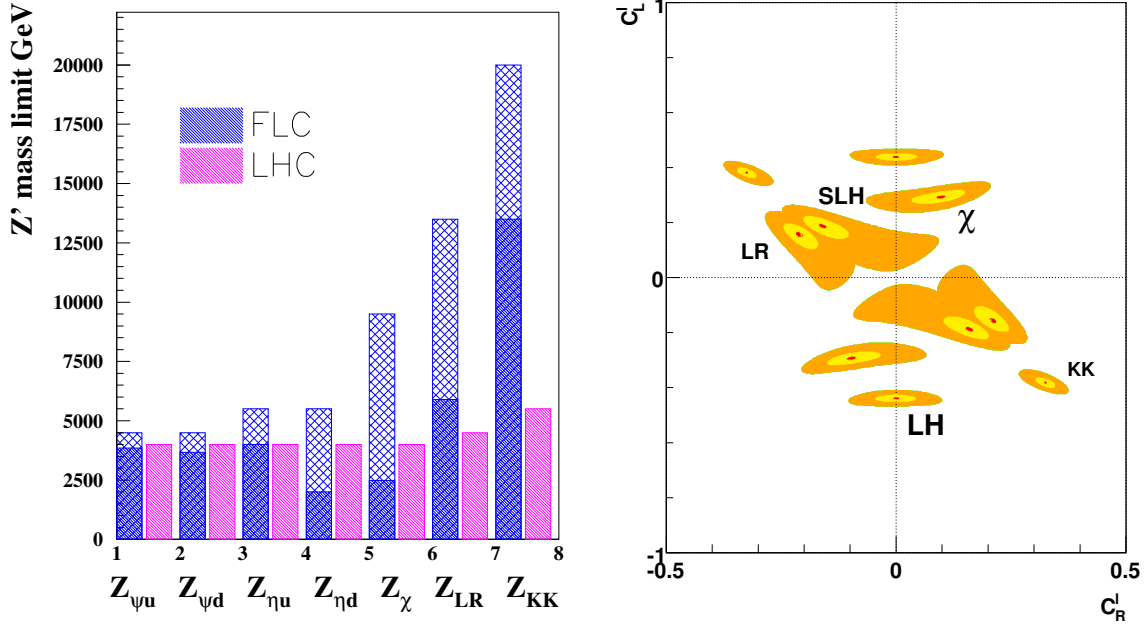


FIGURE 6.10. Left: the mass range covered by the LHC and the ILC (FLC) for a Z' boson in various scenarios; for the ILC the heavy hatched region is covered by exploiting the GigaZ option (sensitive to the Z - Z' mixing) and the high energy region (sensitive to the γ , Z - Z' interference) [15, 236]. Right: the ILC resolving power (95% CL) for $M_{Z'} = 1, 2$ and 3 TeV for left- and right-handed leptonic couplings (c_L^l and c_R^l) based on the leptonic observables σ_{pol}^μ , A_{LR}^μ and A_{FB}^μ ; the smallest (largest) regions correspond to $M_{Z'} = 1$ TeV (3 TeV) [237]. In both figures $\sqrt{s} = 500$ GeV and $\mathcal{L} = 1 \text{ ab}^{-1}$ are assumed.

proportional to the Z/Z' mass ratio. With precisely determined top and Higgs boson masses at the ILC, the Z' mass reach can be significantly larger than the LHC direct Z' search limit for some models, as also illustrated in the left-hand side of Fig. 6.10.

In a second step, the couplings of the Z' boson need to be probed and the model origin determined. An example of chiral coupling determination in several extended models is shown in the right-hand side of Fig. 6.10. Here, Z' bosons originating from the E_6 χ model (χ), a left-right symmetric model (LR), the littlest Higgs model (LH), the simplest little Higgs model (SLH), and KK excitations originating from theories of extra dimensions (KK) are considered. Only leptonic observables have been taken into account and electron and positron beam polarizations are assumed to be 80% and 60%, respectively. As can be seen, for $M_{Z'} = 2$ TeV, the various models can be clearly distinguished. This is a very important step to identify the underlying theory if a new vector resonance is observed at the LHC.

Finally, new charged gauge bosons W' also appear in extensions of the SM such as left-right symmetric models. These particles can be produced at the LHC up to masses of the order of 5 TeV in some cases. Complementing the LHC detection of these states, the ILC could allow to reconstruct the W' couplings. A detailed simulation [238] shows that W' bosons can be observed via their virtual effects in the process $e^+e^- \rightarrow \nu\bar{\nu}\gamma$ and, at $\sqrt{s} = 500$ GeV with 1 ab^{-1} data, masses up to $M_{W'} \sim 1.3$ TeV in left-right models and up to $M_{W'} \sim 5$ TeV for a SM-like heavy W' and the KK excitation of the W boson, can be probed if the systematical errors are assumed to be smaller than 0.1%. The sensitivity can be slightly improved by considering the $e\gamma \rightarrow \nu q + X$ process in the $e\gamma$ option of the ILC. In the case where a heavy SM-like W' boson with a mass of 1.5 TeV is observed, its couplings to quarks and leptons could be measured with an accuracy of a few percent in some cases [238].

6.4.2 Exotic fermions

Many theories beyond the SM such as GUTs or extra-dimensional require the existence of new matter particles with the possibility of new interactions not contained in the SM; for a review, see e.g. Ref. [239]. Examples of new elementary fermions include sequential fourth generation fermions, vector-like fermions with both left- and right-handed components in weak isodoublets, mirror fermions which have the opposite chiral properties as the SM fermions and isosinglet fermions such as the SO(10) Majorana neutrino. Exotic fermions, i.e. fermions that have the usual lepton/baryon but non-canonical $SU(2)_L \times U(1)_Y$ quantum numbers, occur naturally in GUT models that contain a single representation into which a complete generation of SM quarks and leptons can be embedded. For instance, in the E_6 group, each fermion generation lies in the **27** representation, which contains 12 new fermions in addition to the 15 chiral fermions of the SM. It is conceivable that these new fermions acquire masses not much larger than the EWSB scale, if these masses are protected by some symmetry. In fact, this is necessary if the associated new gauge bosons are relatively light.

Except for singlet neutrinos, the new fermions couple to the photon and/or to the weak gauge bosons W/Z with full strength; these couplings allow for pair production, $e^+e^- \rightarrow F\bar{F}$, with practically unambiguous cross sections and, masses very close to the kinematical limit, $m_F \sim \frac{1}{2}\sqrt{s}$, can be probed; see Fig. 6.11 (left). In general, the new fermions will mix with their SM light partners which have the same conserved quantum numbers. This mixing, which is expected to be small $\xi \lesssim 0.1$ from LEP constraints, gives rise to new currents which determine the decay pattern of the heavy fermions, $F \rightarrow fZ/f'W$.

The mixing also allows for the single production of the new fermions, $e^+e^- \rightarrow F\bar{f}$. In the case of quarks and second/third generation leptons, single production proceeds only via s -channel Z exchange and the rates are moderate. For the first generation neutral and charged leptons, one has additional t -channel exchanges which significantly increase the production cross sections; see Fig. 6.11 (right). For not too small mixing, lepton masses close to the center of mass energy can be produced. A full simulation [240] of the processes $e^+e^- \rightarrow N\nu_e \rightarrow e^\pm W^\mp \nu_e$ and $e^+e^- \rightarrow E^\pm e^\mp \rightarrow e^\pm e^\mp Z$, taking into account the dominant backgrounds and detector efficiencies, shows that for $M_{N,E} = 350$ GeV, mixing angles down to $\xi \sim 0.002$ and 0.01 can be probed at a 500 GeV ILC with 500 fb^{-1} data in, respectively, the neutral and charged lepton case.

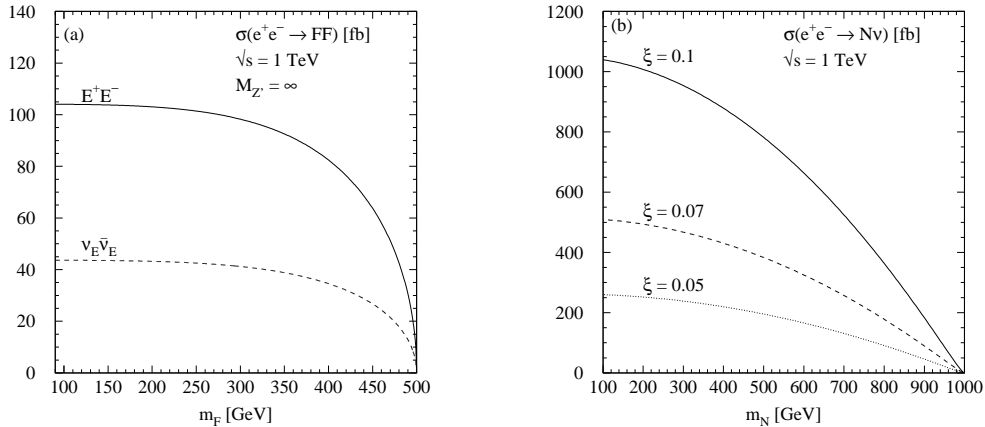


FIGURE 6.11. The production cross sections for new heavy leptons at $\sqrt{s} = 1$ TeV: pair production (left) and single neutrino production for various mixing angles (right). From Ref. [241].

6.4.3 Difermions

Difermions are new spin-zero or spin-one bosons that have unusual baryon and/or lepton quantum numbers [239]. Examples are leptoquarks with $B = \pm 1/3$ and $L = \pm 1$, diquarks with $B = \pm 2/3$ and $L = 0$ and dileptons with $B = 0$ and $L = \pm 2$. They occur in models of fermion compositeness as well as in some GUT models such as E_6 where a colored weak isosinglet new particle can be either a leptoquark or a diquark. In the case of leptoquarks, starting from an effective Lagrangian with general $SU(3) \times SU(2) \times U(1)$ invariant couplings and conserved B and L numbers, one obtains 5 scalar and 5 vector states with distinct SM transformation properties. In addition to the usual couplings to gauge bosons, difermions have couplings to fermion pairs which determine their decays. In supersymmetric models with R -parity violation, the scalar partners of sfermions may be coupled to two fermions giving rise to production and decay mechanisms that are analogous to those of difermions.

Leptoquarks can be produced in pairs at e^+e^- colliders [242, 243] through gauge boson s -channel exchange; significant t -channel quark exchange can also be present in some channels if the quark-lepton-leptoquark coupling squared λ^2/e^2 are not too small. Depending on the charge, the spin and isospin of the leptoquark, the cross sections can vary widely as shown in the left-hand side of Fig. 6.12 for $\sqrt{s} = 500$ and 800 GeV. In a detailed simulation, it has been shown that scalar and vector leptoquark masses very close to the beam energy can be detected with the exception of the $^{-1/3}S_0$ state which can be probed only for masses $\sim 40\%\sqrt{s}$ because of the lower cross section [243]. Once the leptoquarks have been observed, besides the total cross sections, the study of the angular distribution gives an additional handle on the spin and the relative size of the couplings to gauge bosons and fermions.

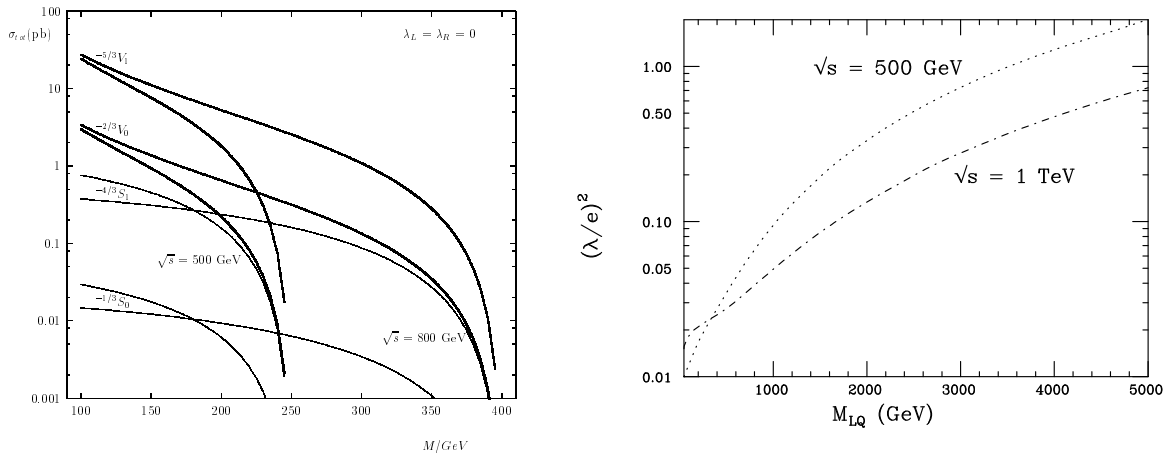


FIGURE 6.12. Left: total cross sections for various leptoquark pair production at the ILC with $\sqrt{s} = 500$ and 800 GeV with vanishing Yukawa couplings and including the corrections due to beamstrahlung and ISR [243]. Right: 95% CL indirect $^{-1/3}S_0$ leptoquark discovery regions (to the left of the curves) at $\sqrt{s} = 500$ GeV and 1 TeV with 50 and 100 fb^{-1} data [244].

Single production of scalar and vector leptoquarks can also occur [242], in particular for those states coupling to first generation leptons which can be produced with large rates in $e\gamma$ initiated subprocesses. Though suppressed by the unknown Yukawa coupling to quark-lepton pairs λ/e , these processes could allow to extend the kinematical reach to masses up to $\sim \sqrt{s}$. First generation leptoquarks can also be observed at the ILC in $e\gamma$ option: the rates are much larger than in the e^+e^- option but the mass reach is slightly lower due to the reduced energy.

One can also indirectly probe the existence of very heavy leptoquarks that are not kinematically accessible at a given c.m. energy in the $e^+e^- \rightarrow q\bar{q}$ process as t -channel leptoquark exchange can contribute significantly to the cross section, provided the Yukawa coupling is sufficiently large. From the total cross section and angular distribution measurements at $\sqrt{s} = 500$ GeV, one can probe the E_6 leptoquark $^{-1/3}S_0$ for $M_S \sim 4$ TeV and $\lambda/e \sim 1$ with only 50 fb^{-1} data as shown in Fig. 6.12 (right) [244]. The effects of a 2 TeV state with couplings as low as $\lambda/e \sim 0.1$, can be probed at $\sqrt{s} = 1$ TeV and $\mathcal{L} = 100 \text{ fb}^{-1}$.

Dileptons, like doubly charged Higgs bosons, would lead to the spectacular four lepton signature if they are pair produced, $e^+e^- \rightarrow L^{++}L^{--} \rightarrow 4\ell^\pm$. Because of the large electric charge $Q_{\ell\ell} = 2$, the rates are significant in the e^+e^- mode of the ILC and even more in the $\gamma\gamma$ mode as $\sigma \propto Q_{\ell\ell}^4$. They can also be singly produced and, in particular, they could appear as s -channel resonances in e^-e^- collisions for mass close to the c.m. energy. Diquarks can be pair produced in e^+e^- collisions for masses smaller than $\frac{1}{2}\sqrt{s}$ and lead to an excess of four-jet events which could be easily searched for in contrast to the LHC.

6.4.4 Compositeness

As a possible physical scenario, strongly interacting electroweak bosons at energies of order 1 TeV could be interpreted as a signal of composite substructures of these particles at a scale of 10^{-17} cm. Moreover, the proliferation of quarks and leptons could be taken as evidence for possible substructures in the fermionic sector. In this picture, masses and mixing angles are a consequence of the interactions between a small number of elementary constituents, in analogy to the quark/gluon picture of hadrons. Although no satisfactory theoretical formalism has been set up so far, one can describe this scenario in a purely phenomenological way.

Compositeness in the fermion sector can be tested at the ILC through the measurement of the $e^+e^- \rightarrow q\bar{q}$ and $\ell^+\ell^-$ cross sections and asymmetries and the search for four-fermion contact interactions generated by the exchange of the fermion subconstituents. As discussed in chapter 3, compositeness scales Λ up to 100 TeV can be probed at the ILC; Fig 3.1.

The existence of excited fermions is a characteristic signal of substructure in the fermionic sector: if the known fermions are composite objects, they should be the ground state of a rich spectrum of excited states which decay down to the former states via a magnetic dipole type de-excitation. In this case, decays to a light partner fermion and a photon with branching ratios of the order of 30% is possible. These decays constitute a characteristic signature of excited fermions and discriminate them from the exotic fermions discussed above.

The pair production of excited fermions [245] follows the same pattern as for the exotic fermions and, for excited leptons, the cross sections are similar to those shown in Fig. 6.11 (left) generating event samples that allow for an easy discovery of these states for masses smaller than the beam energy. Single production of excited fermions at the ILC [245] is also similar to that of exotic fermions, with the notable exception of single production of excited electrons which, in e^+e^- collisions, is strongly enhanced by t -channel photon exchange. This state can also be produced as an s -channel resonance in $e\gamma$ collisions. The single production of excited electronic neutrinos in e^+e^- collisions is also enhanced by t -channel W exchange and leads to the interesting signature of an isolated monochromatic photon and missing energy.

CHAPTER 7

Connections to cosmology

Dark matter has been established as a major component of the universe. We know from several independent observations, including the cosmic microwave background, supernovas and galaxy clusters, that DM is responsible for $\sim 20\%$ of the energy density of the universe. Yet, none of the SM particles can be responsible for it and the observation of DM, together with neutrino masses, is likely the first direct signal of new physics beyond the SM. Several particles and objects have been nominated as candidates for DM. They span a wide range of masses, from 10^{-5} eV, in the case of axions, to 10^{-5} solar masses, for primordial black holes. Cosmology tells us that a significant fraction of the universe mass consists of DM, but does not provide clues on its nature. Particle physics tells us that new physics must exist at, or just beyond, the electroweak scale and new symmetries may result in new, stable particles. Establishing the inter-relations between physics at the microscopic scale and phenomena at cosmological scale will represent a major theme for physics in the next decades.

The ILC will be able to play a key role in elucidating these inter-relations. Out of these many possibilities, there is a class of models which is especially attractive since its existence is independently motivated and DM, at about the observed density, arises naturally. These are extensions of the SM which include an extra symmetry protecting the lightest particle in the new sector from decaying into ordinary SM states. The lightest particle becomes stable and can be chosen to be neutral. Such a particle is called a weakly interacting massive particle (WIMP) and arises in theories beyond the SM, such as supersymmetry with conserved R-parity but also in extra dimensional models with KK-parity.

Current cosmological data, mostly through the WMAP satellite measurements of the CMB, determine the DM density in the universe to be

$$\Omega_{\text{DM}} h^2 = 0.111 \pm 0.006,$$

which is already a determination to 6% accuracy. The accuracy is expected to be improved to the percent level by future measurements by the Planck satellite [246]. The next decades promise to be a time when accelerator experiments will provide new breakthroughs and highly accurate data to gain new insights, not only on fundamental questions in particle physics, but also in cosmology, when studied alongside the observations from satellites and other experiments. The questions on the nature and the origin of DM offer a prime example of the synergies of new experiments at hadron and lepton colliders, at satellites and ground-based DM experiments. In this context, the ILC will play a major role as will be discussed here.

Explaining the baryon asymmetry of the universe is another outstanding problem in cosmology. Both the WMAP experiment and the theory of primordial nucleosynthesis indicate

that the baryon-to-entropy ratio of the present universe is $\sim 10^{-10}$. This asymmetry has to be created after the inflationary period which likely occurred in the evolution of the universe. In order to generate the baryon asymmetry after inflation, the three Sakharov conditions are required, namely, baryon number violation, C and CP violation and a deviation from thermal equilibrium [247]. Two main approaches for generating the baryon asymmetry in our universe have been proposed: baryogenesis mediated by leptogenesis and electroweak baryogenesis. Both options need the introduction of new physics beyond the SM and can be formulated in the context of supersymmetric models. This is, therefore, another aspect that is highlighting an interface between collider particle physics and cosmology. Also in this fundamental issue, the ILC might play a key role.

7.1 DARK MATTER

7.1.1 DM and new physics

Since there is no WIMP candidate within the SM, cold DM is a clear evidence for physics beyond the SM and in chapters 5 and 6, we discussed SM extensions in which appropriate DM candidates exist. These particles are in general electrically neutral, relatively massive and absolutely stable; in addition, they have rather weak interactions in such a way that their cosmological relic density, which is inversely proportional to their annihilation cross section $\sigma_{\text{ann}} \equiv \sigma(\text{WIMP} + \text{WIMP} \rightarrow \text{SM particles})$, falls in the range required by WMAP.

Supersymmetry: a standard way to suppress unwanted interactions leading to unreasonable proton decay rates in SUSY models is to impose R-parity. By virtue of this symmetry, the lightest supersymmetric particle (LSP) is absolutely stable and represents a good candidate for cold DM [171, 172]. In particular, the lightest neutralino is considered to be the prime candidate, but other interesting possibilities are the axino and the gravitino. A detailed description of SUSY dark matter is given in the next two sections.

Models of extra dimensions: which introduce a KK tower for each SM particle. In universal extra-dimensional (UED) models, a discrete quantity called KK-parity is conserved so that the lightest KK particle (LKP), generally corresponding to the KK hypercharge gauge boson, is stable and is a DM candidate [224, 225]. In warped Randall-Sundrum (RS) models embedded in GUTs, a Z_3 symmetry ensures also that the lightest KK state (LZP), the excitation of a Dirac right-handed neutrino, could be stable and a good DM candidate [119] as a result of a baryon number symmetry. These two options will be briefly discussed here.

Little Higgs models: in a class of which, a discrete symmetry called T-parity can be introduced [213] which forbids direct interactions between new heavy gauge bosons and ordinary fermions. The lightest T-odd particle (LTP) is a heavy partner of a U(1) gauge boson and is a good DM candidate [248]; in this respect, these models are four-dimensional reminiscent of UED models mentioned above. Note, however, that it has been recently pointed out that T-parity might be broken by anomalies in some cases [249].

As in these examples, a new continuous or discrete symmetry has to be introduced in order that a new physics model incorporates an electrically neutral particle that is absolutely stable to be an appropriate DM candidate. If thermal production of these particles is assumed in the early universe, their mass and their interactions, which enter in the annihilation cross section, are constrained by the relic density. In most cases, the resulting mass range turns out to be roughly in the vicinity of the electroweak symmetry breaking scale. It is therefore

generally expected that such DM particles can be detected at the LHC in the decay products of the new colored particles that are also present in the new physics model and which can be copiously produced [250]. A characteristic signal of DM particle production is, thus, cascade decays with large missing transverse energy due to the escaping WIMPS, just as in the SUSY case. In order to distinguish between different possibilities and identify unambiguously the DM particle, one needs to determine its mass, spin and other quantum numbers as well as the model parameters that are relevant in the calculation of its thermal relic abundance and its detection rates in astrophysical experiments. In fact, there are four main steps in the physics program which allows for a complete understanding of the nature of the DM candidate:

- discover the WIMP candidate in collider physics experiments in missing energy events (and in direct detection experiments) and measure precisely their mass,
- determine the physics of the new model that leads to the WIMP,
- determine precisely the parameters of this model and predict the relic density as well as the direct and indirect detection cross sections in astrophysical experiments,
- observe the DM particle in astroparticle physics experiments and measure products of cross sections and densities to reconstruct the density distribution of DM.

This ambitious program of precision measurements should reveal what the DM particle is and how it is distributed in the universe. If the determination of the properties of the DM particle matches cosmological observations to high precision, then (and only then) we will be able to claim to have determined what DM is. Such an achievement would be a great success of the particle physics/cosmology connection and would give us confidence in our understanding of the universe.

The high precision measurements to be performed at the ILC will play a significant role in this context. This is demonstrated for SUSY dark matter in the following sections.

7.1.2 SUSY dark matter

In the MSSM, the LSP neutralino is an ideal cold DM candidate [171, 172]. In some areas of the SUSY parameter space, the χ_1^0 cosmological relic density falls in the range required by WMAP. In particular, in the constrained MSSM, there are generally four regions in which this constraint (together with the constraints from collider physics) is satisfied [172]:

- 1) Scenarios where both m_0 and $m_{1/2}$ are rather small, the “bulk region”, are most natural from the point of view of EWSB but are severely squeezed by bounds from colliders searches.
- 2) The “focus point” region occurs at $m_0 \gg m_{1/2}$, and allows χ_1^0 to have a significant higgsino component, enhancing its annihilation cross sections into final states containing gauge and/or Higgs bosons; this solution generally requires multi-TeV scalar masses.
- 3) In the “co-annihilation” region, one has near mass degeneracy between the LSP and the lightest stau $m_{\chi_1^0} \simeq m_{\tilde{\tau}_1}$, leading to enhanced destruction of sparticles since the $\tilde{\tau}_1$ annihilation cross section is much larger than that of the LSP; this requires $m_{1/2} \gg m_0$.
- 4) If $\tan \beta$ is large, the s -channel exchange of the CP-odd Higgs boson A can become nearly resonant, the “ A -funnel” region, again leading to an acceptable relic density.

Fig. 7.1 (left) summarizes the areas in the $[m_0, m_{1/2}]$ cMSSM parameter space for $A_0 = 0$ and $\mu > 0$ in which all constraints from collider searches and high-precision measurements are imposed and the LSP abundance matches the WMAP constraint [251, 252]; their precise locations vary with $\tan \beta$ and thus the $m_0, m_{1/2}$ axes are given without units. Note that a fifth possible region is when $2m_{\chi_1^0} \sim M_h$ and the s -channel h exchange is nearly resonant allowing

the neutralinos to annihilate efficiently [253]; this “ h -pole” region, in which the inos are very light and can be studied in detail at the ILC, is however squeezed by the LEP2 lower limit on M_h [34]. Another possibility in the unconstrained MSSM is the stop co-annihilation region [254], with a small $\tilde{t}_1 - \chi_1^0$ mass difference, which is important for scenarios of electroweak baryogenesis in the MSSM [255]; it will be discussed later in this chapter.

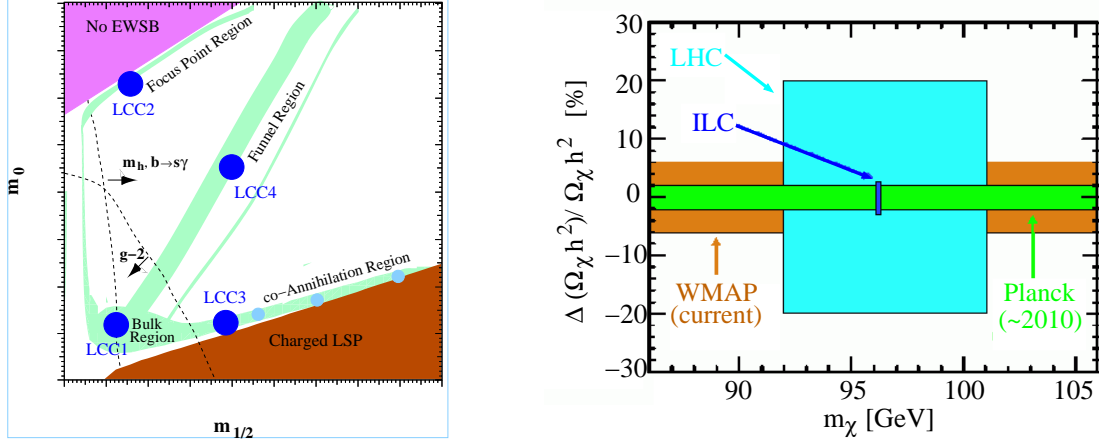


FIGURE 7.1. Left: the DM-favored regions in the cMSSM $[m_{1/2}, m_0]$ parameter space with all experimental and theoretical constraints imposed [251, 252]. Right: accuracy of WMAP and expected accuracy of Planck compared to the LHC and ILC accuracies in the determination of the LSP neutralino mass and the cosmological relic density in the cMSSM point SPS1a' [256].

As seen previously, SUSY particles can be produced abundantly at the LHC and the ILC. However, to determine the predicted WIMP relic density, one must experimentally constrain all processes contributing to the LSP pair annihilation cross section. This requires detailed knowledge, not only of the LSP properties, but also of all other particles contributing to their annihilation. This is not a simple task and all unknown parameters entering the determination of $\Omega_\chi h^2$ need to be experimentally measured or shown to have marginal effects. The very high precision that can be achieved at the ILC, eventually combined with measurement for squarks, gluinos and the heavy Higgs bosons at the LHC, will allow to achieve this goal. The results of a study in the cMSSM SPS1a' scenario are summarized in Fig. 7.1 (right), where the expected precision at ILC and LHC are compared with the satellite determination of $\Omega_\chi h^2$. The figure shows that the ILC will provide a percent determination of $\Omega_\chi h^2$ in the case under study, matching WMAP and even the very high accuracy expected from Planck.

Other SUSY WIMP candidates such as the axino [257] or the gravitino [177] are also possible. If DM is composed of the lightest SUSY particle, the ILC, in some cases when some information from the LHC is added, will be able to determine the mass and the properties of the LSP and pin down its relic density.

7.1.2.1 Neutralino DM scenarios at the ILC

To quantify the prospects for determining the neutralino DM relic density at the ILC and the connection of the ILC with cosmology (LCC), four benchmark cMSSM scenarios which correspond to the four areas discussed above and in which the model is compatible with WMAP data (for the first scenario, see the next footnote however), Fig. 7.1 (left) with their basic input parameters given in Tab. 7.1, have been selected:

- LCC1:** this is simply the SPS1a point with light sleptons with masses just above the LSP mass¹. The important DM annihilation process is through t -channel $\tilde{\ell} = \tilde{e}, \tilde{\mu}, \tilde{\tau}$ exchange, so that the masses $m_{\tilde{\ell}}$ need to be very accurately measured. This is indeed the case at a 500 GeV ILC as shown previously.
- LCC2:** in which all sfermions are too heavy to be observed either at the ILC or at the LHC while all charginos and neutralinos can be produced at the LHC and then measured at the ILC. The main contribution to DM is when these states are exchanged in the t -channel of LSP annihilation into gauge and Higgs bosons and thus, $\Omega_{\chi} h^2$ strongly depends on the gaugino–higgsino mixing which needs to be measured accurately.
- LCC3:** in this scenario the $\tilde{\tau}_1$ and the χ_1^0 LSP are very close in mass, $m_{\tilde{\tau}_1} - m_{\chi_1^0} = 10.8$ GeV, so that co-annihilation dominates annihilation of SUSY particles in the early universe. Here, only these two particles (and χ_2^0) are light enough to be accessible at the 500 GeV ILC, but their important mass difference can be measured with an error of 1 GeV.
- LCC4:** here, LSP annihilation occurs mainly through the exchange of the A boson which has a mass $M_A = 419$ GeV; the measurements of M_A and the total width Γ_A are crucial and, at the ILC, they can be performed only at $\sqrt{s} = 1$ TeV. Most of the SUSY spectrum (except for $\tilde{\tau}_1$ and χ_1^0) is anyway heavy and can be produced only at a 1 TeV machine.

TABLE 7.1

cMSSM parameter sets for four illustrative scenarios of χ_1^0 DM (with $\text{sign}(\mu) > 0$ and $A_0 = 0$ except for LCC1 where $A_0 = -100$ GeV). The accuracy in the determination of the LSP mass and the relic density at the ILC are also shown (and compared to that obtained from LHC measurements only).

| Point | m_0 | $m_{1/2}$ | $\tan \beta$ | $m_{\chi_1^0}$ | ΔILC | $\Omega_{\chi} h^2$ | ΔILC | (ΔLHC) |
|-------|-------|-----------|--------------|----------------|---------------------|---------------------|---------------------|-------------------------|
| LCC1 | 100 | 250 | 10 | 96.1 | ± 0.05 | 0.192 | $\pm 0.24\%$ | (7.2%) |
| LCC2 | 3280 | 300 | 10 | 107.9 | ± 1.0 | 0.109 | $\pm 7.6\%$ | (82%) |
| LCC3 | 213 | 360 | 40 | 142.6 | ± 0.1 | 0.101 | $\pm 18\%$ | (167%) |
| LCC4 | 380 | 420 | 53 | 169.1 | ± 1.4 | 0.114 | $\pm 19\%$ | (405%) |

Many detailed studies of the determination of the DM density from collider measurements in scenarios close to the LCC ones have been performed [183, 250, 258]. A particular focus has been put recently on the LCC3 $\tilde{\tau}_1$ – χ_1^0 co-annihilation point [258] which is known to be difficult and very demanding for ILC detectors as an optimal detection of energetic electrons in the very forward region and a very efficient rejection of the $\gamma\gamma$ background is required. Here, we will rely on a recent comprehensive analysis performed in Ref. [252] to summarize the main results. In this study, the four LCC points have been described in terms of 24 effective MSSM parameters to be as model independent as possible, over which full scans [using a Markov Chain Monte Carlo algorithm] are performed to determine the MSSM models that are compatible with the experimental measurements. The neutralino relic density calculated using `microMRGAS` [259] and the precision from the ILC measurements are summarized for these points in the right-handed column of Tab. 7.1. The accuracies range from less than 1% in the LCC1/SPS1a scenario to 20% in the difficult LCC3 co-annihilation and LCC4

¹As discussed earlier, this point is ruled out as it gives a relic density that is outside the WMAP range, $\Omega_{\chi} h^2 = 0.19$. However, since the corresponding phenomenology is rather close to that of the SPS1a' point (see for instance Tabs. 5.3 and 5.4) which has the correct relic density, $\Omega_{\chi} h^2 = 0.115$, we will keep this problematic point for illustration. The accuracy in the determination of the relic density is different in the two scenarios, though, and in SPS1a' one obtains Ωh^2 at the percent level only.

“A-pole” scenarios; a few percent accuracy is reached in the LCC2 “focus-point” scenario. The analysis also leads to the probability distributions of predictions for $\Omega_\chi h^2$, using the various expected measurements, which are shown in Fig. 7.2. The ILC measurements at $\sqrt{s} = 500$ GeV and 1 TeV for various sparticle masses and mixings, taking into account LHC data, are compared to those which can be obtained using LHC data alone (after a qualitative identification of the model), which in most cases needs ILC data. As can be seen, the gain in sensitivity by combining LHC and ILC data is spectacular.

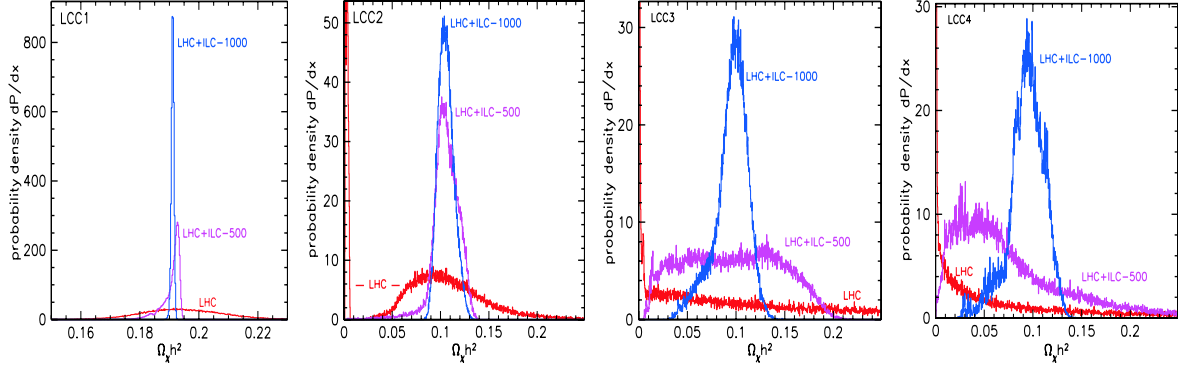


FIGURE 7.2. Probability distribution of predictions for $\Omega_\chi h^2$ from measurements at the ILC with $\sqrt{s}=0.5$ and 1 TeV, and LHC (after qualitative identification of the model); from Ref. [252].

Once the DM relic density is precisely obtained, one can turn to the prediction (or the verification, if they have already been measured in astroparticle experiments) of the cross sections in direct and indirect detection of the DM. For both techniques, the detection rates are convolutions of microscopic cross sections that can be “determined” in particle physics experiments with densities that can be measured in astrophysical experiments. In indirect detection, one looks for, e.g., high energy neutrinos or photons originating from the annihilation of neutralinos in our galaxy and the rate is directly proportional to the annihilation cross sections which enter in the determination of the DM relic density; however, the distribution of DM has several orders of magnitude uncertainty. In direct detection, i.e. in the search of the elastic scattering of ambient neutralinos off a nucleus in a laboratory detector, the astrophysical uncertainty is only a factor of two while the LSP–nucleon scattering cross section has inherent uncertainties from strong interactions that are larger.

Nevertheless, if the modeling of the DM distribution and of the π –nucleon interaction can be improved, a precise determination of the detection rates can be performed by reconstructing the microscopic cross sections using precision SUSY parameter measurements at the ILC and at the LHC for the squark sector. This is clearly the case for the LSP annihilation cross section which is similar to that giving $\Omega_\chi h^2$ but also for the LSP–nucleon cross section when it is dominated by Higgs exchange diagrams. In turn, the determination of the microscopic LSP cross sections from ILC data could allow to significantly constrain in a general way the distribution of DM in the galaxy; see Ref. [252] for a discussion and a detailed study.

7.1.2.2 Gravitino DM at the ILC

SUSY particles other than the lightest neutralinos can also form the DM in the Universe. While LSP sneutrinos have been ruled out by direct WIMP searches [172], the possibility of the axino [257] or the gravitino [177] DM is still open. In many scenarios, one can arrange so

that these WIMPs have the required relic density by choosing appropriate values of the masses and the reheat temperature after the phase of inflation, for instance. These particles have extremely weak couplings to ordinary matter and cannot be observed directly in astrophysical experiments; in contrast, they can be studied at the ILC. Here, we briefly discuss the scenario of a gravitino LSP and its implication for the ILC.

In mSUGRA-type models, the mass of the gravitino and those of the SM superpartners \tilde{P} are given by $m_{\tilde{G},\tilde{P}} = \kappa_{\tilde{G},\tilde{P}} \cdot F/M_P$ where $M_P \simeq 2.4 \cdot 10^{18}$ GeV is the reduced Planck mass, $F \sim (10^{11} \text{ GeV})^2$ is the square of the SUSY breaking scale; $\kappa_{\tilde{G}} = \frac{1}{\sqrt{3}}$ while $\kappa_{\tilde{P}}$ is model-dependent and is expected to be $\mathcal{O}(1)$. The gravitino can be therefore the LSP with a mass in the range $m_{\tilde{G}} \propto 10\text{--}100$ GeV. However, its couplings to matter are very strongly suppressed by a factor $1/M_P$ and, thus, the gravitino is a super-WIMP that cannot be directly observed in astrophysical experiments.

In the early universe, gravitinos are generated via thermal production through processes involving SM and SUSY particles in the thermal bath and also in non-thermal decay processes of superparticles which are out of equilibrium. These superparticles will first decay into the NLSP, which can be either a neutralino, a charged slepton (generally a $\tilde{\tau}$) or a sneutrino, that first freezes out and then decays into the gravitino whose relic density is given by $\Omega_{\tilde{G}} h^2 = m_{\tilde{G}}/m_{\text{NLSP}} \cdot \Omega_{\text{NLSP}} h^2$. Since the next-to LSP decays gravitationally, $\text{NLSP} \rightarrow \tilde{G} + X$, its lifetime is in principle of order $\tau_{\text{NLSP}} \propto M_P^2/M_{\text{EWSB}}^3 = 10^2\text{--}10^8$ s and thus very long. It is therefore constrained by cosmology, in particular by primordial nucleosynthesis (BBN) and cosmic microwave background (CMB) data, and can eventually be tested at colliders by the measurement of the NLSP mass and lifetime.

Gravitinos with masses in the range $m_{\tilde{G}} \propto 10\text{--}100$ GeV are also good DM candidates. However, strong constraints from BBN and in particular recent data from the abundance of primordial light elements such as Lithium, impose that the mass difference between the NLSP and the gravitino should be relatively large. In the case where the NLSP is the $\tilde{\tau}$ slepton, the constraints are shown in the left-hand side of Fig. 7.3 [260]. For stau leptons with masses below $m_{\tilde{\tau}} \lesssim 400$ GeV, a gravitino mass of $m_{\tilde{G}} \lesssim 10$ GeV is required; the $\tilde{\tau}$ lifetime is also restricted to be in the $10^3\text{--}10^5$ s range. Note, however, that these bounds might be somewhat relaxed with a better theoretical understanding of the bound state effects of Li production and/or by possible entropy production after $\tilde{\tau}$ decoupling. Furthermore, all problems from BBN constraints can be easily solved if one allows for a tiny amount of R-parity violation; in this case there is no constraint on the $\tilde{\tau}$ mass and, for a successful thermal leptogenesis, one needs $m_{\tilde{G}} \gtrsim 5$ GeV for the gravitino [261].

At the ILC, a detailed study [201] has been performed in an mSUGRA-like scenario [262] in which $m_{3/2} = m_0 = \frac{1}{22}m_{1/2} \sim A_0 = 20$ GeV, $\tan\beta = 15$ and $\mu > 0$, leading to stau and gravitino masses of $m_{\tilde{\tau}_1} = 157.6$ GeV and $m_{\tilde{G}} = 20$ GeV; the stau lepton has a lifetime $\tau_{\tilde{\tau}_1} = 2.6 \cdot 10^6$ s, i.e. approximately one month, and is stopped in the detector². Assuming a c.m. energy $\sqrt{s} = 500$ GeV and a luminosity $\mathcal{L} = 100 \text{ fb}^{-1}$ and, thanks to the relatively large cross section $\sigma(e^+e^- \rightarrow \tilde{\tau}_1\tilde{\tau}_1 + X) \sim 300 \text{ fb}$, a very clean environment and good detector (tracking, momentum and energy resolution, etc.) performance, one can achieve very precise measurements. The stau mass can be determined from the mean value of the $\tilde{\tau}$ momentum with an accuracy of $\Delta m_{\tilde{\tau}_1} \simeq 200$ MeV. The lifetime can be determined from a fit to the decay time distribution shown in the right-hand side of Fig. 7.3 and one

²Again, this scenario cannot be considered to be realistic in view of the BBN bounds discussed above. However, most of the obtained results may be readily taken up for a more viable scenario.

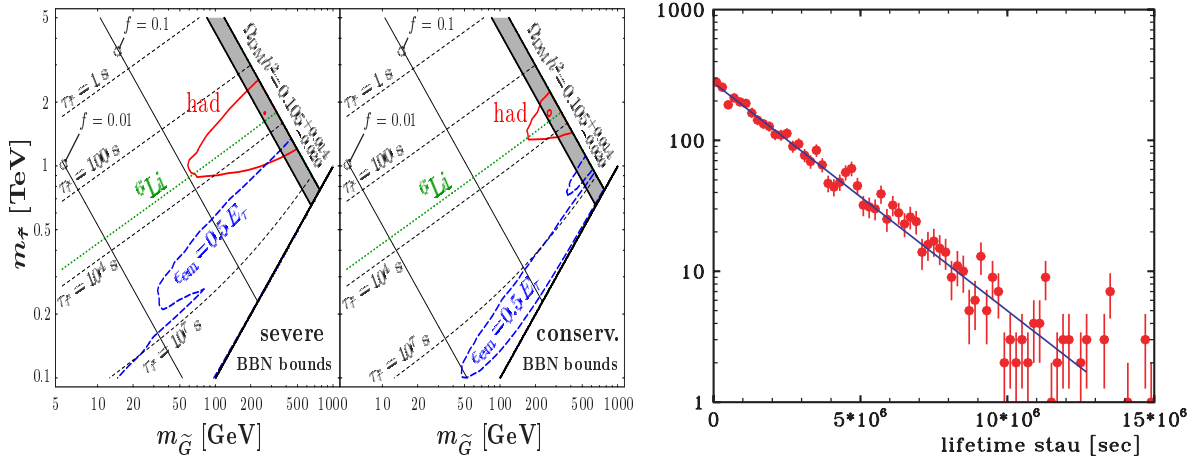


FIGURE 7.3. Left: Cosmological constraints on the masses of the gravitino LSP and the stau NLSP from severe and conservative BBN constraints; the thick solid (red) and thick dashed (blue) curves are for the BBN bounds from late hadronic and electromagnetic energy injection, respectively, and the regions inside or to the right of the corresponding curves are excluded [260]. The $\tilde{\tau}$ lifetime distribution in the decay $\tilde{\tau}_1 \rightarrow \tau \tilde{G}$ at the ILC with $\sqrt{s} = 500$ GeV and $\mathcal{L} = 100 \text{ fb}^{-1}$ (right); from Ref. [201].

obtains $\tau_{\tilde{\tau}_1} = (2.6 \pm 0.05) \cdot 10^6 \text{ s}$. Assuming the usual gravitational coupling, one then obtains the gravitino mass from the $\tilde{\tau}$ mass and lifetime with a very good accuracy, $\Delta m_{\tilde{G}} = \pm 200$ MeV. In fact, one can also measure directly the gravitino mass from the recoil of the tau lepton in the decay $\tilde{\tau}_1 \rightarrow \tau \tilde{G}$ and an accuracy of ± 4 GeV can be achieved. This allows the unique opportunity to have an independent access in a microscopic experiment to the value of the reduced Planck scale, $M_P \simeq (2.4 \pm 0.5) \cdot 10^{18} \text{ GeV}$ and, hence, to Newton's constant, $G_N = 1/(8\pi M_P^2)$. Therefore, also in this scenario, precision measurements at the ILC would allow to derive very important informations on cosmological phenomena.

Note that in scenarios in which a small amount of R-parity violation is introduced in order to avoid BBN constraints, the $\tilde{\tau}$ state will have two-body \tilde{R}_p decays, yielding visible tracks in the detector macroscopic times later; however, in this case, one cannot determine the Planck mass anymore [261].

7.1.3 DM in extra dimensional scenarios

An interesting feature in the simplest version of universal extra dimension (UED) models discussed in chapter 6, is the presence of a discrete conserved quantity, the so called KK-parity $(-1)^n$ where n is the KK level. KK parity ensures the presence of a stable massive particle, the LKP, which can be a cold DM candidate [225]. Several possible LKP candidates are the first KK excitations of Higgs or gauge bosons, such as the particle corresponding to the hypercharge gauge boson B_1 which is naturally obtained in minimal UED (MUED) models, and the KK excitation of a neutrino. In warped extra dimensional models embedded in a GUT, the Z_3 symmetry introduced to prevent rapid proton decay also guarantees the stability of the lightest KK fermion, a right-handed neutrino [119]. This particle is called the LKP and can be also a good cold DM candidate. In the following, we briefly discuss the two options of a B_1 LKP and a ν_R LKP, and their implications at the ILC.

7.1.3.1 DM in universal extra dimensions

In MUED models, the LKP naturally turns out to be the KK partner of the hypercharge gauge boson and, if only annihilation processes are considered, its cosmological relic density is typical of a WIMP candidate. In order to explain all of the DM, the B_1 mass should be in the range $M_{B_1} = 600\text{--}800$ GeV, depending on the rest of the KK spectrum. The mass is clearly too large for this particle to be produced at the ILC. However, it has been realized that one needs to include co-annihilation processes with the SU(2) singlet KK leptons, which in MUED are the lightest among the remaining $n = 1$ KK particles, as well as the influence of gravitons on the final relic density results.

The left-hand of Fig. 7.4 shows the relic density of the LKP as a function of the inverse of the size of the extra dimension R^{-1} , in the MUED model [263]. The lines marked “a,b,c” are for the results obtained when considering only their annihilation with various assumptions on the KK mass spectrum, while the dotted line is the result from the full calculation in MUED, including all co-annihilation processes and with the proper choice of masses. The green horizontal and the blue vertical bands are, respectively, for the WMAP preferred range and the R^{-1} regions disfavored by precision data. As can be seen, LKP particles in the mass range close to 500 GeV are compatible with DM. In the right-hand side of Fig. 7.4, shown is the change in the cosmologically preferred value for R^{-1} as a result of varying away from their nominal MUED values the KK masses of the different particles: three generations of SU(2) singlet and doublet KK leptons and quarks as well as KK gluons and gauge bosons. As can also be seen, visible KK states in the vicinity of $R^{-1} = 500$ GeV are also possible.

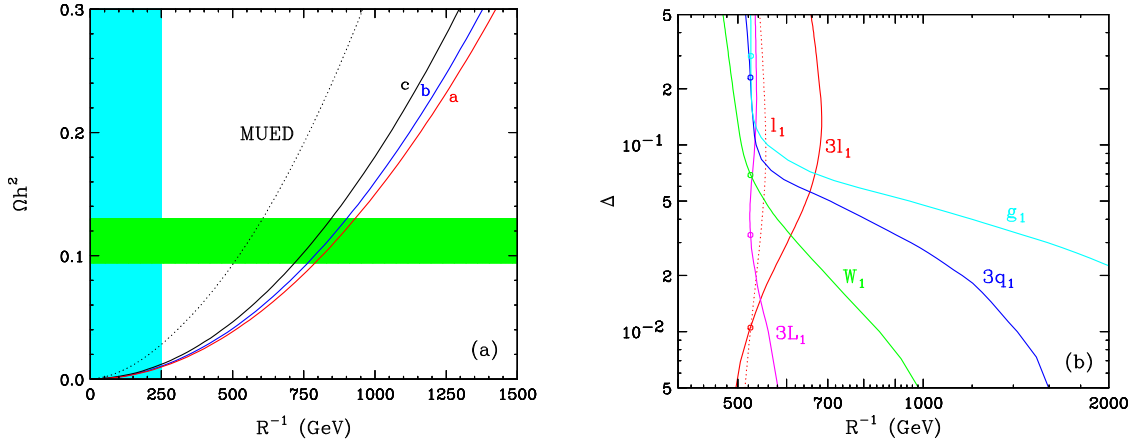


FIGURE 7.4. Left: relic density of the LKP as a function of R^{-1} in the MUED model with and without co-annihilation. Right: the change in the cosmologically preferred value for R^{-1} as a result of varying the different KK masses away from their nominal MUED values. From Ref. [263].

Thus, if the energy of the ILC is slightly raised or the KK masses compatible with DM are lowered by some mechanism, the new particles can be produced at the ILC. At least the lighter KK states are accessible as the mass difference with the LKP can be small to allow for co-annihilation. In many cases, the signals will mimic those of SUSY particles, in particular the presence of missing transverse energy. The determination of the mass and mixing of these particles, as well as their spin and CP-quantum numbers [which are important in this context as the LKP is a spin-one boson while the LSP neutralino in SUSY models is a Majorana fermion], will allow to discriminate between the two scenarios [187, 264].

7.1.3.2 DM in warped extra dimensions

As discussed in chapter 6, the most promising and realistic warped extra-dimensional scenarios need the electroweak gauge group to be extended to $SU(2)_L \times SU(2)_R \times U(1)_X$. In this context, KK Dirac neutrinos charged under the $SU(2)_R$ group are necessary parts of the models. Implementing baryon number conservation in these warped GUT models leads to a KK right-handed neutrino ν_R that is absolutely stable and thus, a potential candidate for cold DM [119]. In fact, even in the absence of this additional symmetry, ν_R can be stable at cosmological scales if the couplings involved in its decay are strongly suppressed, which can occur also if it has a large annihilation cross section, providing the correct relic density.

In a RS scenario embedded in the $SO(10)$ GUT group, the ν_R has no direct couplings to the Z boson but a small $Z\bar{\nu}_R\nu_R$ coupling is induced by the mixing between the Z – Z' mixing. The Z' boson couples with full strength to the ν_R LKP state but, as it must be heavier than $M_{KK} \sim 3$ TeV, the resulting interactions are rather weak. These arguments make that, although of the Dirac type, KK right-handed neutrinos with masses in the range of 1 GeV to 1 TeV can have the required relic abundance without being in conflict with the bounds from direct detection experiments [265]. The DM density is shown in Fig. 7.5 as a function of the LKP mass for two values of the $SO(10)$ coupling g_{10} and two different localizations of the left-handed neutrino ν_L (which also mixes with ν_R); the masses of the KK gauge bosons are assumed to be $M_{KK} = 3, 6$ and 12 TeV while the SM Higgs mass is fixed to be $M_H = 300$ GeV. One notices the effect of the Z , Higgs and Z' resonances which allow for the relic density to be compatible with the WMAP range. Since all KK fermions belonging to the multiplet containing the right-handed top quark, except for its KK mode, are expected to be light compared to the KK gauge bosons and close in mass to the LKP, co-annihilation with the KK leptons for instance can play a non-negligible role [265].

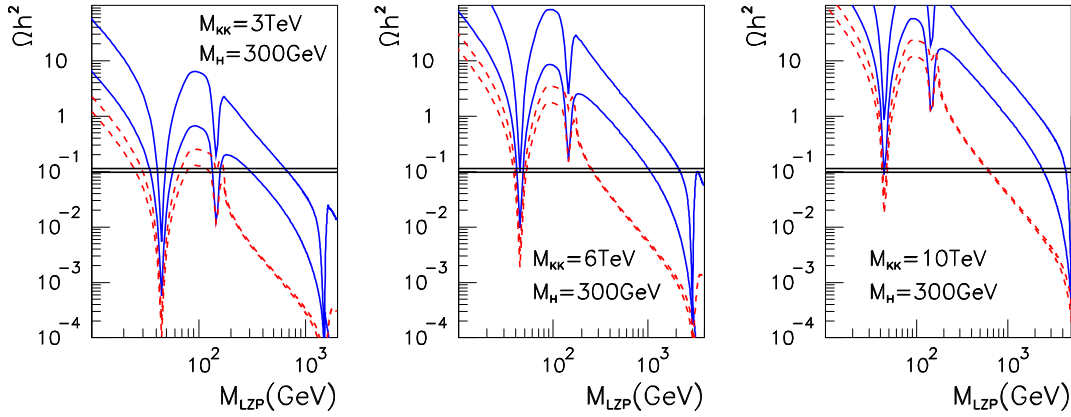


FIGURE 7.5. The relic density of the LKP in annihilation for three M_{KK} values, $g_{10} = 0.3$ (dashed) and 1.2 (solid lines) and two values of $c_{\nu_L} = 0.9$ (lower) and -0.1 (upper curves); from Ref. [265].

If the LKP and the KK fermions which are in the same multiplet have not too large masses, the ILC will be the ideal instrument to produce them and to study in great detail their properties. Again, threshold scans would allow for precise mass measurements and the study of the cross sections as well as various production and decay distributions would allow for the determination of the couplings and spins of the particles. These measurements could be then used to predict the DM density and compare it with the experimental value.

7.2 THE BARYON ASYMMETRY

7.2.1 Electroweak baryogenesis in the MSSM

Electroweak baryogenesis is an interesting possibility where the baryon asymmetry of the universe is generated at the electroweak phase transition. Since the relevant energy scale is the weak scale, this scenario has potential impacts on the Terascale physics. As a strong first-order phase transition is a necessary condition of successful electroweak baryogenesis, the Higgs sector should be extended from the minimal one Higgs doublet SM in which, in view of the current bound on the Higgs boson mass, it is not the case. A strong first-order phase transition is possible in various extensions of the Higgs sector such as the SM supplemented with a scalar singlet field, the two Higgs doublet model, the MSSM and the next-to-minimal supersymmetric Standard Model (NMSSM).

The electroweak baryogenesis scenario in the MSSM has been studied in detail in the literature; see Refs. [266] for reviews. In order to account for the observed amount of baryon asymmetry, a rather specific choice of SUSY parameters is required. First, one of the top squarks, mostly right-handed, has to be lighter than the top quark in order that a strong first-order phase transition is realized. The mass of the other stop, on the other hand, becomes larger than 1 TeV. A new source of CP violation necessary for the generation of the baryon asymmetry is provided by the CP phases of the chargino and neutralino mass matrices. Since the new phases contribute to the electron and neutron electric dipole moments, scalar fermions of the first and second generations should be heavier than a few TeV, while charginos and neutralinos can be in the few 100 GeV range. Finally, the lightest Higgs boson mass is predicted to be close to the present experimental bound, $M_H \sim 114$ GeV. If the lightest neutralino is to account for the DM in this scenario, the mass difference between the light stop and the LSP should not be large, and stop-neutralino co-annihilation [254] is the primary mechanism which generates an LSP relic abundance which matches the WMAP value.

These features are important to test this scenario at the LHC and ILC [267, 255]. The discovery of a light top squark and a SM-like Higgs boson with a mass close to 120 GeV would be a strong indication that electroweak baryogenesis is the mechanism for the generation of the baryon asymmetry. In order to confirm this picture, one needs to determine that \tilde{t}_1 is mainly right-handed and check that the masses and compositions of the charginos and neutralinos are compatible with the required values and finally, compute the DM relic abundance so as to compare with cosmological observations. If $\tilde{t}-\chi_1^0$ co-annihilation is relevant, it is important to determine the stop-neutralino mass difference very precisely. A detailed analysis of the stop, chargino and neutralino sectors at the ILC has been performed for this scenario in Ref. [255]. It is found that the experimental accuracies in the measurements of the stop and ino parameters, as discussed in chapter 5, allow to determine the strength of the phase transition with a reasonable precision, $\Delta_{\text{exp}}[v(T_c)/T_c] \lesssim 10\%$, if the theoretical error is ignored. The second crucial ingredient for electroweak baryogenesis, the CP-violating source responsible for the baryon asymmetry, remains however unconstrained as only an upper bound on the phase of the μ parameter, $|\phi_\mu| \lesssim 0.7$, can be derived.

In addition, the collider measurements can be used to predict rather precisely the DM relic density. By determining the stop and lightest neutralino masses and the stop mixing parameters, the stop-neutralino co-annihilation cross section can be strongly constrained and the DM relic density predicted with a precision of the same order as current astrophysical results. This is exemplified in Fig. 7.6 which shows the accuracy in the determination of the

DM abundance as a function of the stop mass in the electroweak baryogenesis scenario of Ref. [255]. While an experimental error $\Delta m_{\tilde{t}_1} = 1.2$ GeV (grey dots) leads to a relatively loose constraint, a precision $\Delta m_{\tilde{t}_1} = 0.3$ GeV (dark dots) matches the original scenario used as input (the red star) and the 1σ and 2σ WMAP constraints (horizontal shaded bands). Refinements in the determination of the stop mass can thus improve this result significantly.

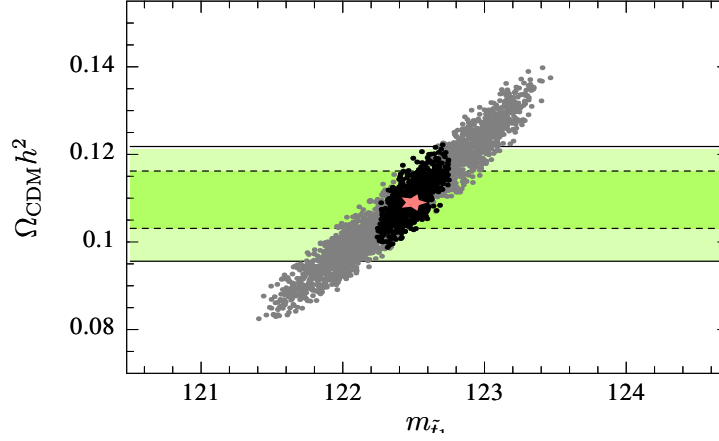


FIGURE 7.6. The DM abundance $\Omega_{\chi} h^2$ as a function of the stop mass for the electroweak baryogenesis scenario, taking into account experimental errors for stop, ino and Higgs measurements at the ILC; the dots correspond to a scan over the 1σ region allowed by these errors; from Ref. [255].

In non-SUSY scenarios, a strong first-order electroweak phase transition needed to generate the baryon asymmetry can also be made possible. For instance, this phase transition can be induced if the SM effective theory with one Higgs doublet Φ is augmented with a dimension-six Higgs operator [111], leading to a scalar Higgs potential of the form

$$V = \lambda(\Phi^\dagger\Phi - \tfrac{1}{2}v^2)^2 + \tfrac{1}{\Lambda^2}(\Phi^\dagger\Phi - \tfrac{1}{2}v^2)^3.$$

This additional term can be generated by strong dynamics at the TeV scale or by integrating out heavy particles such as an additional singlet scalar field [268] or the heavier Higgs particles of a general two-Higgs doublet model [112].

At zero-temperature, the CP-even Higgs state can be expanded in terms of its usual vev, $\langle\varphi\rangle = v_0 \simeq 246$ GeV and the physical Higgs boson field $\Phi = \varphi/\sqrt{2} = (H + v_0)/\sqrt{2}$. From the requirement that the phase transition is first order and that the minimum at zero-temperature is a global minimum, one obtains, respectively, an upper and a lower bound on the cut-off Λ for a given Higgs mass. For a low cut-off scale, $\Lambda \lesssim 1$ TeV, the required electroweak phase transition can be achieved for Higgs masses $M_H \gtrsim 114$ GeV [111].

As a concrete example of a possible origin of the dimension-six operator, one can have a scalar singlet N coupled to the Higgs field via an interaction of the form $\zeta^2\Phi^\dagger\Phi N^2$. If the singlet field has a mass m_N that is larger than the weak scale, it can be integrated out and gives rise to the additional Higgs interactions, $\Delta V \propto \zeta^2/m_N^2 \cdot |\Phi|^6$. The baryogenesis condition of the non-erasure of the generated baryon asymmetry is $R = \langle vT_c \rangle/T_c \gtrsim 1$ where T_c is the critical temperature at which the origin and the non-trivial minimum at $\langle v(T_c) \rangle$ become degenerate. The dependence of this ratio on the parameter ζ in the $\Phi^\dagger\Phi N^2$ interaction is displayed in Fig. 7.7 for several values of the Higgs mass M_H . As can be seen, R values larger than unity can be obtained for Higgs masses as large as $M_H \sim 200$ GeV.

Since the Higgs potential is altered by the dimension–six operator with a low–scale cutoff, large shifts in the Higgs boson self–couplings from their SM values are generated. For instance, the trilinear Higgs coupling becomes $\lambda_{HHH} \equiv \mu = 3M_H^2/v_0 + 6v_0^3/\Lambda^2$ and the SM value μ_{SM} is recovered only for $\Lambda \rightarrow \infty$. In Fig. 7.7, the deviation of the trilinear Higgs coupling normalized to its SM value, $\mu/\mu_{\text{SM}} - 1$, is displayed in the $[M_H, \Lambda]$ plane and one sees that shifts of order unity can be obtained. This is particularly true in the allowed regions (delimited by the dashed lines) for the cut–off scale and the Higgs mass.

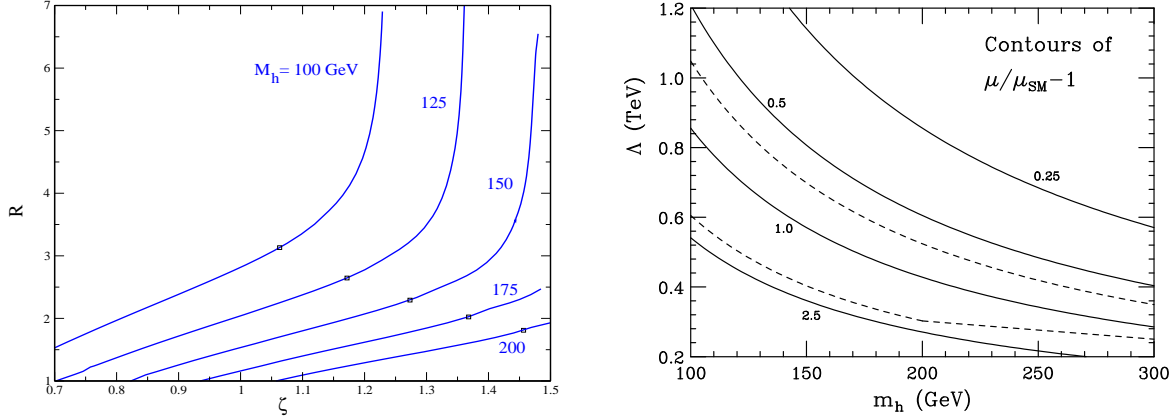


FIGURE 7.7. Left: the ratio $R \equiv \langle v(T_c) \rangle / T_c$ as a function of the parameter ζ for several M_H values [268]. Right: contours of constant $\mu/\mu_{\text{SM}} - 1$ in the Λ vs. M_H plane; the dashed lines delimit the region in which electroweak baryogenesis can take place [111].

Thus, if the electroweak phase transition plays an important role for the generation of the baryon asymmetry of the universe, there is a possibility to test this mechanism in collider experiments and, in particular, at the ILC. A first hint may be obtained in Higgs physics as the nature of the electroweak phase transition is closely related to the structure of the Higgs potential and, as illustrated above, large deviations of the Higgs self–couplings from their SM values are expected in this case. Another important ingredient is the new source of CP violation that triggers the separation of particles and anti-particles during the first–order phase transition. Since the new CP phases are carried by states that are present at the phase transition temperature, that is in the range the electroweak symmetry breaking scale, some of these particles are very likely to be within the kinematical reach of the ILC. Precise determination of particle masses, couplings and CP phases at the ILC will be thus essential to confirm or disprove the electroweak baryogenesis scenario.

7.2.2 Leptogenesis and right–handed neutrinos

If leptogenesis [269] is the origin of the observed baryon asymmetry in the universe, the roots of this phenomenon are located near the GUT or the Planck scale. CP–violating decays of heavy right–handed Majorana neutrinos generate a lepton asymmetry which is transferred to the quark/baryon sector by sphaleron processes. Heavy neutrino mass scales as introduced in the seesaw mechanism [211] for generating light neutrino masses and the size of the light neutrino masses needed for leptogenesis define a self–consistent frame which is compatible with all experimental observations [270].

As discussed in chapter 5, in some supersymmetric models, the size of the heavy seesaw scales can be related to the values of the charged and neutral slepton masses [210]. Of particular interest is the comparison of scalar masses in the tau and the electron sector. If the scalar mass parameters are universal at the GUT scale, as in minimal supergravity for instance, this regularity can be unraveled in the first and second generation of the scalar masses at the electroweak scale. However, slepton masses of the third generation will be different from the first two in theories incorporating the seesaw mechanism. The running of the slepton masses from the GUT to the electroweak scale will be affected by loops involving the heavy right-handed neutrino, with masses in the range 10^{10} – 10^{15} GeV, which have large Yukawa couplings in the third generation. Sum rules for mass differences of sneutrinos and selectrons between the first and third generation can be constructed that project out this contribution.

Being approximately linear in the seesaw scale, the scale can be estimated from the sneutrino and slepton masses with a rather good accuracy. In this way a method has been found by which the large right-handed neutrino mass can, at least indirectly, be measured [210]. The excellent resolution of ILC can be exploited in this way to estimate the mass of the heaviest right-handed neutrino within a factor of two as illustrated in Fig. 7.8.

Thus, by means of extrapolations governed by the renormalization group, the high accuracy that can be achieved at the ILC in the slepton and sneutrino mass measurements, as discussed in chapter 5, can be exploited to determine high-scale parameters that cannot be accessed directly. ILC high-precision measurements in the SUSY sector may shed light on the heavy neutrino sector and on the baryon asymmetry in the universe when realized via leptogenesis, even at scales close to the GUT scale, as it might provide a very valuable input which is the scale of the heavy right-handed neutrinos.

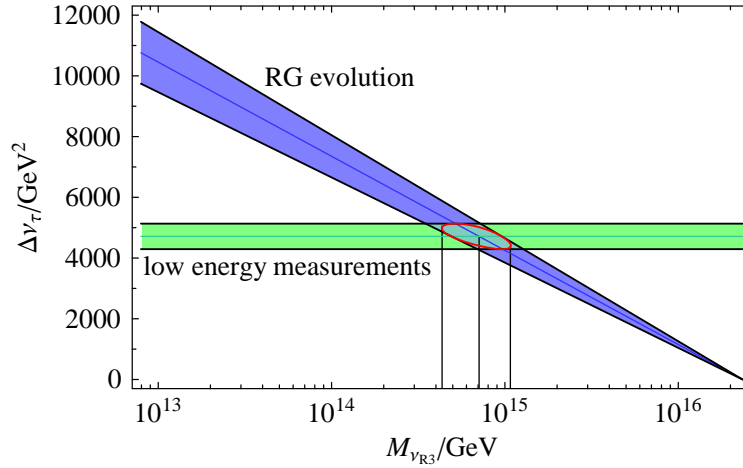


FIGURE 7.8. ILC resolution in the estimate of the mass of the heaviest right-handed neutrino from the RGE evolution of slepton mass [210].

BIBLIOGRAPHY

- [1] A. Albrecht et al., report of the DOE/NSF High Energy Physics Advisory Panel (2004).
- [2] H. Shapiro et al., “Revealing the hidden nature of space and time: charting the course for elementary particle physics”, report of the Committee on Elementary Particle Physics in the 21st Century, Board of Physics and Astronomy, National Research Council, National Academies Press, Washington D.C. (2006).
- [3] “The European Strategy for Particle Physics”, Report of CERN Council Strategy Group (2006).
- [4] GLC project: Linear collider for TeV physics, KEK-REPORT-2003-7.
- [5] I. Corbett et al., Report of the Consultative Group on High-Energy Physics, OECD Global Science Forum (2002).
- [6] S. Yamada et al., Report of the JLC Globalization Committee (2002).
- [7] ECFA/DESY LC Physics WG, J. A. Aguilar-Saavedra et al., hep-ph/0106315.
- [8] ACFA Linear Collider Working Group, K. Abe et al., hep-ph/0109166.
- [9] American Linear Collider Working Group, T. Abe et al., hep-ex/0106057.
- [10] ECFA/DESY LC Physics Working Group, E. Accomando et al., Phys. Rept. **299**, 1 (1998), [hep-ph/9705442].
- [11] J. Bagger et al., “Discovering the Quantum Universe: The role of particle colliders,” report of the DOE/NSF High Energy Physics Advisory Panel (2006).
- [12] ATLAS Collaboration, Physics TDR, CERN-LHCC-99-14 and CERN-LHCC-99-15.
- [13] CMS Collaboration, Physics TDR, CERN/LHCC/2006-021, June 2006.
- [14] R. Cousins, J. Mumford and V. Valuev, CERN-CMS-NOTE-2005-022.
- [15] LHC/LC Study Group, G. Weiglein et al., Phys. Rept. **426**, 47 (2006).
- [16] Parameters for the Linear Collider,
http://www.fnal.gov/directorate/icfa/LC_parameters.pdf.
- [17] G. A. Moortgat-Pick et al., hep-ph/0507011.
- [18] P. D. Grannis, hep-ex/0211002.

BIBLIOGRAPHY

- [19] R. Hawkings and K. Mönig, Eur. Phys. J. direct **C1**, 8 (1999).
- [20] C. A. Heusch, Int. J. Mod. Phys. **A20**, 7289 (2005).
- [21] I. F. Ginzburg, G. L. Kotkin, V. G. Serbo and V. I. Telnov, JETP Lett. **34**, 491 (1981).
- [22] ECFA/DESY Photon Collider Working Group, B. Badelek et al., hep-ex/0108012.
- [23] F. Bechtel et al., Nucl. Instrum. Meth. **A564**, 243 (2006).
- [24] S. Dawson and M. Oreglia, Ann. Rev. Nucl. Part. Sci. **54**, 269 (2004).
- [25] M. Battaglia et al., hep-ex/0603010.
- [26] For a review on ILC physics scenarios: W. Kilian and P. Zerwas, hep-ph/0601217.
- [27] T. Barklow, talk at ILCWS, 2005, Stanford, California.
- [28] S. Hillert, Talk at ILC Software and Physics Meeting, 4-6 April 2006, Cambridge, UK.
- [29] T. Behnke et al., TESLA TDR part 4: A detector for TESLA, DESY-01-011.
- [30] M. A. Thomson, physics/0607261.
- [31] P.W. Higgs, Phys. Rev. Lett. **13**, 508 (1964) and Phys. Rev. **145**, 1156 (1966); F. Englert and R. Brout, Phys. Rev. Lett. **13**, 321 (1964); G.S. Guralnik, C.R. Hagen and T. Kibble, Phys. Rev. Lett. **13**, 585 (1965).
- [32] J. Gunion, H. Haber, G. Kane, and S. Dawson, *The Higgs Hunters Guide*, Addison-Wesley, Reading (USA), 1990. See also, M. Gomez-Bock et al., hep-ph/0509077.
- [33] A. Djouadi, hep-ph/0503172, to appear in Phys. Rept.
- [34] LEP WG for Higgs boson searches, R. Barate et al., Phys. Lett. **B565**, 61 (2003).
- [35] The particle Data Group, J.-W. Yao et al., J. Phys. **G33**, 1 (2006).
- [36] The LEP collaborations and the LEP electroweak working group, hep-ex/0612034.
- [37] T. Hambye and K. Riesselmann, Phys. Rev. **D55**, 7255 (1997).
- [38] B.W. Lee, C. Quigg and H.B. Thacker, Phys. Rev. **D16**, 1519 (1977).
- [39] M. Lüscher and P. Weisz, Phys. Lett. **B212**, 472 (1988); M. Göckeler, H. Kastrup, T. Neuhaus and F. Zimmermann, Nucl. Phys. **B405**, 555 (1993).
- [40] A. Djouadi, hep-ph/0503173, to appear in Phys. Rept.
- [41] S. Heinemeyer, W. Hollik and G. Weiglein, Phys. Rept. **425**, 265 (2006).
- [42] The LEP Collaboration (ALEPH, DELPHI, L3, OPAL), Eur. Phys. J. **C47**, 547 (2006).
- [43] For a recent review, see E. Accomando et al., hep-ph/0608079.
- [44] M. Carena, J. R. Ellis, A. Pilaftsis and C. E. Wagner, Nucl. Phys. B **625**, 345 (2002).

- [45] M. Carena, J. R. Ellis, A. Pilaftsis and C. E. Wagner, Nucl. Phys. B **659**, 145 (2003).
- [46] S.Y. Choi, J. Kalinowski, Y. Liao and P.M. Zerwas, Eur. Phys. J. **C40**, 55 (2005).
- [47] D. J. Miller, R. Nevzorov and P. M. Zerwas, Nucl. Phys. **B681**, 3 (2004).
- [48] See e.g., J. Espinosa and M. Quiros, Phys. Rev. Lett. **81**, 516 (1998).
- [49] See e.g.: U. Ellwanger, C. Hugonie and J. Gunion, JHEP **0502**, 066 (2005).
- [50] For recent analyses, see: U. Ellwanger and C. Hugonie, Eur. Phys. J. **C25**, 297 (2002); U. Ellwanger et al., hep-ph/0111179 and hep-ph/0305109; J. Gunion and R. Dermisek, Phys. Rev. Lett. **95**, 041801 (2005); V. Barger et al., Phys. Rev. **D73**, 115010 (2006).
- [51] See e.g. S. King, S. Moretti and R. Nevzorov, Phys. Rev. **D73**, 035009 (2006).
- [52] See e.g. T. Han, P. Langacker and B. McElrath, Phys. Rev. **D70**, 115006 (2004).
- [53] For a review, see for instance: J. Gunion, hep-ph/0212150.
- [54] M. Hirsch, J. Romao, J. Valle and A. Villanova del Moral, Phys. Rev. **D73**, 055007 (2006); A. Villanova del Moral in Ref. [43].
- [55] L. Randall and R. Sundrum, Phys. Rev. Lett. **83**, 3370 (1999).
- [56] J. L. Hewett and T. G. Rizzo, JHEP **08**, 028 (2003).
- [57] D. Dominici, B. Grzadkowski, J. Gunion and M. Toharia, Nucl. Phys. **B671**, 243 (2003).
- [58] N. Arkani-Hamed, S. Dimopoulos and G. Dvali, Phys. Lett. **B429**, 263 (1998) and Phys. Rev. **D59**, 086004 (1999); A. Antoniadis, N. Arkani-Hamed, S. Dimopoulos and G. Dvali, Phys. Lett. **B436**, 267 (1998).
- [59] G. Giudice, R. Rattazi and J. Wells, Nucl. Phys. **595**, 250 (2001); M. Battaglia, D. Dominici, J. Gunion and J. Wells, hep-ph/0402062.
- [60] J. van der Bij, Phys. Lett. **B636**, 56 (2006); S. Dilcher and J. van der Bij, Phys. Lett. **B638**, 234 (2006); see also, J. Kumar and J.D. Wells, Phys. Rev. **D74**, 115017 (2006).
- [61] N. Arkani-Hamed et al., JHEP **08**, 021 (2002); N. Arkani-Hamed, A. Cohen, E. Katz, and A. Nelson, JHEP **07**, 034 (2002).
- [62] S. Weinberg, Phys. Rev. **D13**, 974 (1979) and Phys. Rev. **D19**, 1277 (1979); L. Susskind, Phys. Rev. **D20**, 2619 (1979).
- [63] For a review on strong EWSB: C. Hill and E. Simmons, Phys. Rept. **381** (2003) 235.
- [64] W. Kilian, D. Rainwater and J. Reuter, Phys. Rev. **D74**, 095003 (2006) [Erratum-ibid. **D74**, 099905 (2006) and Phys. Rev. **D71**, 015008 (2005)].
- [65] G. Giudice, C. Grojean, A. Pomarol and R. Rattazzi, hep-ph/0703164.
- [66] C. Csaki et al., Phys. Rev. **D69**, 055006 (2004); C. Csaki, C. Grojean, L. Pilo and J. Terning, Phys. Rev. Lett. **92**, 101802 (2004).

BIBLIOGRAPHY

- [67] M. Duhrssen et al., Phys. Rev. **D70**, 113009 (2004).
- [68] E. Boos et al., Phys. Rev. **D66**, 055004 (2002); Phys. Lett. **B578**, 384 (2004) and Phys. Lett. **B622**, 311 (2005).
- [69] A. Djouadi, J. Kalinowski and M. Spira, Comput. Phys. Commun. **108**, 56 (1998).
- [70] A. Djouadi, M. Spira and P. M. Zerwas, Z. Phys. **C70**, 427 (1996); A. Djouadi, J. Kalinowski and P. M. Zerwas, Z. Phys. **C70**, 435 (1996); M. Spira et al., Phys. Lett. **B264**, 440 (1991) and Nucl. Phys. **B453**, 17 (1995).
- [71] J. Ellis, M.K. Gaillard and D.V. Nanopoulos, Nucl. Phys. **B106**, 292 (1976); J.D. Bjorken, SLAC Report 198 (1976); B. Ioffe and V.A. Khoze, Sov. J. Part. Nucl. **9**, 50 (1978); D.R.T. Jones and S.T. Petcov, Phys. Lett. **B84**, 440 (1979).
- [72] R.N. Cahn and S. Dawson, Phys. Lett. **B136**, 196 (1984); K. Hikasa, Phys. Lett. **164B**, 385 (1985); G. Altarelli, B. Mele and F. Pitolli, Nucl. Phys. **B287**, 205 (1987); W. Kilian, M. Kramer and P.M. Zerwas, Phys. Lett. **B373**, 135 (1996).
- [73] K. Gaemers and G. Gounaris, Phys. Lett. **B77**, 379 (1978); A. Djouadi, J. Kalinowski and P. M. Zerwas, Z. Phys. **C54**, 255 (1992) and Mod. Phys. Lett. **A7**, 1765 (1992).
- [74] G. Gounaris, D. Schildknecht and F.M. Renard. Phys. Lett. **B83**, 191 (1979); V. Barger et al., Phys. Rev. **D49**, 79 (1994); A. Djouadi, H.E. Haber and P.M. Zerwas, Phys. Lett. **B375**, 203 (1996); V.A. Ilyin et al., Phys. Rev. **D54**, 6717 (1996).
- [75] A. Djouadi, W. Kilian, M. Mühlleitner and P. Zerwas, Eur. Phys. J. **C10**, 27 (1999).
- [76] S. Dittmaier et al., Phys. Lett. **B441**, 383 (1998) and Phys. Lett. **B478**, 247 (2000); A. Denner et al., Nucl. Phys. **B680**, 85 (2004); G. Bélanger et al., Phys. Lett. **B571**, 163 (2003); Y. You et al., Phys. Lett. **B571**, 85 (2003).
- [77] C. Farrell and A. H. Hoang, Phys. Rev. **D74**, 014008 (2006).
- [78] G. Bélanger et al., Phys. Lett. **B576**, 152 (2003); T. Zhang et al., Phys. Lett. **B578**, 349 (2004); Y. Yasue et al., talk at ECFA Workshop, Durham, Sept. 2004.
- [79] P. Niezurawski, A.F. Zarnecki and M. Krawczyk, JHEP **0502**, 041 (2005).
- [80] P. Bambade and F. Richard, hep-ph/0703173.
- [81] K. Desch et al., Report of the Higgs WG for the extended ECFA-DESY study, Amsterdam, 2003, hep-ph/0311092.
- [82] P. Garcia-Abia and W. Lohmann, Eur. Phys. J. direct **C2**, 2 (2000).
- [83] P. Garcia-Abia, W. Lohmann and A. Raspereza, hep-ex/0505096.
- [84] D.J. Miller et al., Phys. Lett. **B505**, 149 (2001).
- [85] V. Barger et al., Phys. Rev. **D49**, 79 (1994).
- [86] M. T. Dova, P. Garcia-Abia and W. Lohmann, hep-ph/0302113.

- [87] M. Schumacher, LC-PHSM-2001-003.
- [88] M. Krämer, J. H. Kühn, M. L. Stong and P. M. Zerwas, Z. Phys. **C64**, 21 (1994).
- [89] B. Grzadkowski, J. Gunion and X. He, Phys. Rev. Lett. **77**, 5172 (1996); P.S. Bhupal Dev et al., arxiv:0707.2878 [hep-ph].
- [90] N. Meyer and K. Desch, Eur. Phys. J. **C35**, 171 (2004).
- [91] M. D. Hildreth, Talk at High-Energy Physics with Colliding Beams, Santa Cruz, 1992.
- [92] M. Schumacher, LC-PHSM-2003-096.
- [93] M. Battaglia, hep-ph/9910271.
- [94] J. C. Brient, LC-PHSM-2002-003.
- [95] G. Borisov and F. Richard, hep-ph/9905413.
- [96] E. Boos et al., Eur. Phys. J. **C19**, 455 (2001).
- [97] T. Kuhl and K. Desch, LC-PHSM-2007-2.
- [98] M. Battaglia, hep-ph/0211461.
- [99] T. Barklow, hep-ph/0312268.
- [100] A. Juste and G. Merino, hep-ph/9910301; K. Desch and M. Schmucher in [15]; S. Dawson, A. Juste, L. Reina and D. Wackerroth in [15].
- [101] A. Gay, Eur. Phys. J. **C49**, 489 (2007).
- [102] A. Juste, hep-ph/0512246.
- [103] K. Hagiwara, H. Murayama and I. Watanabe, Nucl. Phys. **B367**, 257 (1991), S. Bar-Shalom, D. Atwood and A. Soni, Phys. Lett. **B419**, 340 (1998); B. Grzadkowski and J. Pliszka, Phys. Rev. **D60**, 115018 (1999).
- [104] J. Alcaraz and E. Ruiz Morales, Phys. Rev. Lett. **86**, 3726 (2001).
- [105] C. Castanier, P. Gay, P. Lutz and J. Orloff, hep-ex/0101028.
- [106] U. Baur, T. Plehn and D. Rainwater in [15].
- [107] M. Battaglia, E. Boos and W.-M. Yao, hep-ph/0111276.
- [108] Y. Yasui et al., hep-ph/0211047.
- [109] S. Yamashita, talk at LCWS04, Paris. April 2004.
- [110] P. Niezurawski, A. F. Zarnecki and M. Krawczyk, hep-ph/0307183.
- [111] C. Grojean, G. Servant and J. Wells, Phys. Rev. **D71**, 036001 (2005).
- [112] S. Kanemura, Y. Okada and E. Senaha, Phys. Lett. **B606**, 361 (2005).

BIBLIOGRAPHY

- [113] A. Djouadi, Phys. Lett. **B435**, 101 (1998); A. Djouadi and G. Moreau, arXiv:0707.3800 [hep-ph].
- [114] J.F. Gunion et al., Phys. Rev. **D38**, 3444 (1988); A. Brignole et al., Report DESY-92-123B; A. Djouadi, J. Kalinowski and P.M. Zerwas, Z. Phys. **C57**, 569 (1993) and Z. Phys. **C74**, 93 (1997).
- [115] S. Kiyoura et al., hep-ph/0301172.
- [116] J.F. Gunion and H.E. Haber, Phys. Rev. **D48**, 5109 (1993); M.M. Muhlleitner et al., Phys. Lett. **B508**, 311 (2001).
- [117] D. Asner, J. Gronberg and J. Gunion, Phys. Rev. **D67**, 035009 (2003).
- [118] K. Desch, T. Klimkovich, T. Kuhl and A. Raspereza, hep-ph/0406229.
- [119] K. Agashe and G. Servant, Phys. Rev. Lett. **93**, 231805 (2004) and JCAP **0502**, 002 (2005); D. Hooper and G. Servant, Astropart. Phys. **24**, 231 (2005).
- [120] The ALEPH, DELPHI, L3, OPAL, SLD Collaborations, the LEP Electroweak Working Group, the SLD Electroweak and Heavy Flavour Groups, Phys. Rept. **427**, 257 (2006).
- [121] The LEP collaborations and the LEP electroweak working group, CERN-PPE/93-157.
- [122] S. Riemann, LC-TH-2001-007.
- [123] F. Jegerlehner, Nucl. Phys. Proc. Suppl. **162**, 22 (2006), [hep-ph/0608329].
- [124] A. Djouadi, G. Moreau and F. Richard, Nucl. Phys. **B773**, 43 (2007).
- [125] G. Wilson, LC-PHSM-2001-009.
- [126] J.F. Gaemers and G. Gounaris, Zeit. Phys. **C1**, 259 (1979); K. Hagiwara, R. Peccei, D. Zeppenfeld and K. Hikasa, Nucl. Phys. **B282**, 253 (1987).
- [127] W. Menges, LC-PHSM-2001-022.
- [128] K. Mönig and J. Sekaric, Eur. Phys. J. **C38**, 427 (2005), [hep-ex/0410011].
- [129] K. Mönig and J. Sekaric, hep-ex/0507050.
- [130] T. Appelquist and C. Bernard, Phys. Rev. **D22**, 200 (1980); A. Longhitano, Phys. Rev. **D22**, 1166 (1980) and Nucl. Phys. **B188**, 118 (1981); T. Appelquist and G.H. Wu, Phys. Rev. **D48**, 3235 (1993).
- [131] M. Beyer et al., Eur. Phys. J. **C48**, 353 (2006), [hep-ph/0604048].
- [132] O. Biebel, hep-ex/9912051.
- [133] M. Winter, PHSM-2001-016.
- [134] B.C. Allanach et al., hep-ph/0403133 and Nucl. Phys. Proc.Suppl. **135**, 107 (2004).
- [135] E. De Pree and M. Sher, Phys. Rev. **D73**, 095006 (2006).

- [136] R. Chivukula, S. Selipsky and E. Simmons, Phys. Rev. Lett. **69**, 575 (1992); R. Chivukula, E. Simmons and J. Terning, Phys. Lett. **B331**, 383 (1994); K. Hagiwara and N. Kitazawa, Phys. Rev. **D52**, 5374 (1995); U. Mahanta, Phys. Rev. **D55**, 5848 (1996).
- [137] M. Jezabek, T. Nagano and Y. Sumino, Phys. Rev. **D62**, 014034 (2000).
- [138] S. Heinemeyer, S. Kraml, W. Porod and G. Weiglein, JHEP **09**, 075 (2003).
- [139] M. E. Peskin and J. D. Wells, Phys. Rev. **D64**, 093003 (2001).
- [140] K. Fujii, T. Matsui and Y. Sumino, Phys. Rev. **D50**, 4341 (1994).
- [141] M. Martinez and R. Miquel, Eur. Phys. Jour. **C27**, 49 (2003).
- [142] A. H. Hoang and T. Teubner, Phys. Rev. **D60**, 114027 (1999); A. H. Hoang, Z. Ligeti and A. V. Manohar, Phys. Rev. Lett. **82**, 277 (1999).
- [143] A. H. Hoang, Phys. Rev. **D69**, 034009 (2004).
- [144] A. H. Hoang and I. W. Stewart, Phys. Rev. **D67**, 114020 (2003).
- [145] K. G. Chetyrkin and M. Steinhauser, Nucl. Phys. **B573**, 617 (2000); A. Hoang et al., Eur. Phys. J. direct **C2**, 1 (2000).
- [146] S. Boogert and D.J. Miller, hep-ex/0211021; A. Hinze and K. Mönig, physics/0506115.
- [147] K. Mönig, LC-PHSM-2000-060.
- [148] S. T. Boogert in a talk at Snowmass 2005.
- [149] S. Moretti, hep-ph/9911501.
- [150] W. Hollik et al., Nucl. Phys. **B551**, 3 (1999).
- [151] B. Grzadkowski and Z. Hioki, Nucl. Phys. **B585**, 3 (2000).
- [152] S.D. Rindani, Pramana **61**, 33 (2003) and Pramana **54**, 791 (2000).
- [153] B. Grzadkowski and Z. Hioki, Phys. Lett. **B476**, 87 (2000); *ibid.* **557**, 55 (2003).
- [154] W. Bernreuther, talk given at the ECFA/DESY LCWS, Oxford, UK, March 1999.
- [155] M. Beneke et al., hep-ph/0003033.
- [156] P. Batra and T. M. P. Tait, Phys. Rev. **D74**, 054021 (2006).
- [157] J. A. Aguilar-Saavedra and T. Riemann, hep-ph/0102197.
- [158] J.-j. Cao, Z.-h. Xiong and J. M. Yang, Nucl. Phys. **B651**, 87 (2003).
- [159] A. Brandenburg, Eur. Phys. J. **C11**, 127 (1999) and LC-TH-1999-009.
- [160] T. Rizzo, Phys. Rev. **D50**, 4478 (1994); R. Martinez et al., hep-ph/9709478.
- [161] V.A. Khoze, W.J. Stirling and L.H. Orr, Nucl. Phys. **B378**, 413 (1992).

BIBLIOGRAPHY

- [162] V.A. Khoze and T. Sjostrand, Eur. Phys. J. direct **C2**, 1 (2000).
- [163] A. Brandenburg, L. Dixon and Y. Shadmi, Phys. Rev. **D53**, 1264 (1996).
- [164] G.A. Blair, in DESY 97-123E; G.A. Blair et al., in DESY 1997-048.
- [165] J. Wess and B. Zumino, Nucl. Phys. **B70**, 39 (1974); Yu. A. Gol’fand and E. P. Likhtman, JETP Lett. **13**, 323 (1971).
- [166] For a review, see: J. Wess and J. Bagger, “Supersymmetry and Supergravity”, Princeton Series in Physics, New Jersey, 1992.
- [167] E. Witten, Nucl. Phys. **B188**, 513 (1981) and Nucl. Phys. **B202**, 253 (1982).
- [168] L. Ibañez and G. Ross, Phys. Lett. **B110**, 227 (1982); L. Alvarez–Gaumé, J. Polchinski and M. Wise, Nucl. Phys. **B221**, 495 (1983); J. Ellis et al., Phys. Lett. **B125**, 275 (1983); L. Ibanez, C. Lopez and C. Munoz, Nucl. Phys. **B256**, 218 (1985).
- [169] W. J. Marciano and G. Senjanovic, Phys. Rev. **D25**, 3092 (1982); J. Ellis, S. Kelley and D. Nanopoulos, Phys. Lett. **B260**, 131 (1991); U. Amaldi, W. de Boer and H. Fürstenau, Phys. Lett. **B260** 447, (1991); P. Langacker and M. Luo, Phys. Rev. **D44**, 817 (1991); C. Giunti, C. Kim and U. Lee, Mod. Phys. Lett. **A6**, 1745 (1991).
- [170] G.R. Farrar and P. Fayet, Phys. Lett. **B76**, 575 (1978).
- [171] H. Goldberg, Phys. Rev. Lett. **50**, 1419 (1983); J. Ellis et al., Nucl. Phys. **B238**, 453 (1984).
- [172] For reviews, see: G. Jungman, M. Kamionkowski and K. Griest, Phys. Rept. **267**, 195 (1996); G. Bertone, D. Hooper and J. Silk, Phys. Rept. **405**, 279 (2005); M. Drees, hep-ph/0509105; J. Feng, hep-ph/0509309; K. Olive, hep-ph/0412054.
- [173] For reviews, see: H.P. Nilles, Phys. Rept. **110**, 1 (1984); H. Haber and G. Kane, Phys. Rept. **117**, 75 (1985); S. Martin, hep-ph/9709356; M. Drees, R. Godbole and P. Roy, “Theory and Phenomenology of Sparticles”, World Scientific, 2004.
- [174] A.H. Chamseddine, R. Arnowitt and P. Nath, Phys. Rev. Lett. **49**, 970 (1982); R. Barbieri, S. Ferrara and C.A Savoy, Phys. Lett. **B119**, 343 (1982); L. Hall, J. Lykken and S. Weinberg, Phys. Rev. **D27**, 2359 (1983).
- [175] L. Randall and R. Sundrum, Nucl. Phys. **B557**, 79 (1999); G. Giudice, M. Luty, H. Murayama and R. Rattazzi, JHEP **9812**, 027 (1998); J.A. Bagger, T. Moroi and E. Poppitz, JHEP **0004**, 009 (2000).
- [176] For a review, see: G.F. Giudice and R. Rattazzi, Phys. Rept. **322**, 419 (1999).
- [177] J.R. Ellis, J.E. Kim and D.V. Nanopoulos, Phys. Lett. **B145**, 181 (1984); T. Moroi, H. Murayama and M. Yamaguchi, Phys. Lett. **B303**, 289 (1993).
- [178] For reviews, see: H. Dreiner, hep-ph/9707435; G. Barbier et al., hep-ph/9810232.
- [179] J.A. Aguilar–Saavedra et al., Eur. Phys. J. **C46**, 43 (2006).
- [180] J. Kalinowski, hep-ph/0309235.

- [181] H. Baer, ISAJET, F.E. Paige, S.D. Protopopescu and X. Tata, hep-ph/0001086. Other RGE codes are, SuSpect: A. Djouadi, J. L. Kneur and G. Moultaka, Comput. Phys. Commun. **176**, 426 (2007); Softsusy: B. Allanach, Comput. Phys. Commun. **143**, 305 (2002); Sphenox: W. Porod, Comput. Phys. Commun. **153**, 275 (2003).
- [182] B. C. Allanach et al., Eur. Phys. J. direct **C25**, 113 (2002).
- [183] M. Battaglia et al., Eur. Phys. J. **C22**, 535 (2001) and Eur. Phys. J. **C33**, 273 (2004).
- [184] K. Desch et al., in Ref. [15] and JHEP **0402**, 035 (2004) and hep-ph/0410121.
- [185] H.U. Martyn, LC-PHSM-2003-07, hep-ph/0302024 and in Ref. [15].
- [186] C. Hensel, DESY-THESIS-2002-047.
- [187] S.Y. Choi, K. Hagiwara, H. Martyn, K. Mawatari and P. Zerwas, hep-ph/0612301.
- [188] M. Berggren, F. Richard, and Z. Zhang, hep-ph/0510088.
- [189] K. Desch et al., JHEP **0612**, 007 (2006).
- [190] See for instance, A. Bartl, S. Hesselbach, K. Hidaka, T. Kernreiter and W. Porod, Phys. Rev. **D70**, 035003 (2004); S. Hesselbach, Acta. Phys. Pol. **B35**, 2739 (2004).
- [191] A. Freitas, D. J. Miller and P. M. Zerwas, Eur. Phys. J. **C21**, 361 (2001); A. Freitas, A. von Manteuffel, P.M. Zerwas Eur. Phys. J. **C34**, 487 (2004).
- [192] A. Freitas, U. Martyn, U. Nauenberg and P.M. Zerwas, hep-ph/0409129.
- [193] M. Nojiri, Phys. Rev. **D51**, 6281 (1995); M. Nojiri, K. Fujii and T. Tsukamoto, Phys. Rev. **D54**, 6756 (1996).
- [194] E. Boos et al., hep-ph/0211040 and hep-ph/0303110.
- [195] L. Calibbi, Y. Mambrini and S.K. Vempati, arXiv:0704.3518 [hep-ph].
- [196] S.Y. Choi, H.U. Martyn and P.M. Zerwas, Eur. Phys. J. **C44**, 175 (2005).
- [197] S.Y. Choi et al., Phys. Lett. **B606**, 164 (2005).
- [198] J. Hisano, M. M. Nojiri, Y. Shimizu, and M. Tanaka, Phys. Rev. **D60**, 055008 (1999); W. Porod and W. Majerotto, Phys. Rev. **D66**, 015003 (2002).
- [199] F. Deppisch, H. Martyn, H. Päs, A. Redelbach and R. Rückl, hep-ph/0408140.
- [200] A. Finch, H. Nowak and A. Sopczak, hep-ph/0211140, LC-PHSM-2003-075; A. Sopczak et al., talk at SUSY05, Durham.
- [201] H. U. Martyn, Eur. Phys. J. **C48**, 15 (2006).
- [202] See for instance, A. Abada, G. Bhattacharyya and M. Losada, Phys. Rev. **D66**, 071701 (2002); F. Borzumati and J.S. Lee, Phys. Rev. **D66**, 115012 (2002).
- [203] U. Ellwanger and C. Hugonie, Eur. Phys. J. **C5**, 723 (1998) and **C13**, 681 (2000); F. Franke and S. Hesselbach, Phys. Lett. **B526**, 370 (2002) and hep-ph/0210363; G. Moortgat-Pick et al., JHEP **0506**, 048 (2005).

BIBLIOGRAPHY

- [204] S. Y. Choi, J. Kalinowski, G. Moortgat-Pick and P. M. Zerwas, Eur. Phys. J. **C22**, 563 (2001) and *addendum* Eur. Phys. J. **C23**, 769 (2002).
- [205] S. Y. Choi et al., Eur. Phys. J. **C7**, 123 (1999); Eur. Phys. J. **C8**, 669 (1999); Eur. Phys. J. **C14**, 535 (2000); J.L. Kneur and G. Moultaka, Phys. Rev. **D59**, 015005 (1999) and Phys. Rev. **D61**, 095003 (2000).
- [206] R. Lafaye, T. Plehn and D. Zerwas, hep-ph/0404282 and hep-ph/0512028.
- [207] P. Bechtle, K. Desch and P. Wienemann, Comput. Phys. Commun. **174**, 47 (2006).
- [208] G. A. Blair, W. Porod and P. M. Zerwas, Eur. Phys. J. **C27**, 263 (2003).
- [209] P. Binetruy, M. K. Gaillard and B. D. Nelson, Nucl. Phys. B **604**, 32 (2001).
- [210] A. Freitas, W. Porod and P. M. Zerwas, Phys. Rev. **D72**, 115002 (2005).
- [211] P. Minkowski, Phys. Lett. **B67**, 421 (1977); M. Gell-Mann, P. Ramond, and R. Slansky, Proceedings, Workshop Stony Brook 1979; T. Yanagida, Proceedings, Workshop KEK (Tsububa) 1979; R. N. Mohapatra and G. Senjanovic, Phys. Rev. Lett. **44**, 912 (1980).
- [212] T. Appelquist, H.-C. Cheng and B. A. Dobrescu, Phys. Rev. **D64**, 035002 (2001).
- [213] H.C. Cheng and I. Low, JHEP **09**, 051 (2003) and JHEP **08**, 061 (2004); I. Low, JHEP **10**, 067 (2004).
- [214] N. Arkani-Hamed, M. Porrati and L. Randall, JHEP **08**, 017 (2001); R. Rattazzi and A. Zaffaroni, JHEP **04**, 021 (2001).
- [215] R. Contino, Y. Nomura and A. Pomarol, Nucl. Phys. **B671**, 148 (2003); K. Agashe, R. Contino and A. Pomarol, Nucl. Phys. **B719**, 165 (2005).
- [216] L.J. Hall and D. Smith, Phys. Rev. **D60**, 085008 (1999); S. Cullen and M. Perelstein, Phys. Rev. Lett. **83**, 268 (1999); V. Barger, T. Han and R.J. Zhang, Phys. Lett. **B461**, 34 (1999).
- [217] S. Hannestad and J. Raffelt, Phys. Rev. **D67**, 125008 (2003).
- [218] G.W. Wilson, LC-PHSM-2001-010.
- [219] T. G. Rizzo, JHEP **02**, 008 (2003).
- [220] T.G. Rizzo, JHEP **10**, 013 (2002); N. Delerue, K. Fujii and N. Okada, Phys. Rev. **D70**, 091701 (2004).
- [221] H. Davoudiasl, J.L. Hewett and T.G. Rizzo, Phys. Rev. Lett. **84**, 2080 (2000) and Phys. Rev. **D63**, 075004 (2001).
- [222] B. C. Allanach, K. Odagiri, M. A. Parker and B. R. Webber, JHEP **09**, 019 (2000).
- [223] T. Gherghetta and A. Pomarol, Nucl. Phys. **B586**, 141 (2000).
- [224] D. Hooper and S. Profumo, hep-ph/0701197.

- [225] G. Servant and T. Tait, Nucl. Phys. **B650**, 391 (2003); M. Kakizaki, S. Matsumoto, Y. Sato and M. Senami, Phys. Rev. **D71**, 123522 (2005) and Nucl. Phys. **B735**, 84 (2006); F. Burnell and G. Kribs, Phys. Rev. **D73**, 015001 (2006); N. Shah, Nausheen and C. Wagner, Phys. Rev. **D74**, 104008 (2006).
- [226] J. Conley, J. Hewett and M. Le, Phys. Rev. **D72**, 115014 (2005).
- [227] C. Berger, M. Perelstein and F. Petriello, hep-ph/0512053.
- [228] M. Schmaltz, JHEP **08**, 056 (2004).
- [229] T. Barklow, proceedings of the 5th ILCWS, 2000.
- [230] R. Casalbuoni et al., JHEP **9908**, 11 (1999) and Nucl. Phys. **B555**, 3 (1999).
- [231] R. Casalbuoni et al., Nucl. Phys. **282**, 235 (1987) and Phys. Rev. **D53**, 5201 (1996).
- [232] For a review, see: J. Lykken, Czech. J. Phys. **55**, B577 (2005).
- [233] A. Birkedal, K. Matchev and M. Perelstein, Phys. Rev. Lett. **94**, 191803 (2005).
- [234] J. Hewett and T. Rizzo, Phys. Rept. **183** (1989) 193.
- [235] A. Leike, Phys. Rept. **317** (1999) 143; A. Djouadi et al., Z. Phys. **C56** (1992) 289; M. Cvetič and P. Langacker, hep-ph/9707451.
- [236] F. Richard, hep-ph/0303107.
- [237] S. Godfrey, P. Kalyniak and A. Tomkins, hep-ph/0511335.
- [238] S. Godfrey, P. Kalyniak, B. Kamal and A. Leike, Phys. Rev. **D61**, 113009 (2000).
- [239] For a review, see: A. Djouadi, J. Ng and T.G. Rizzo et al., hep-ph/9504210.
- [240] For a detailed simulation, see e.g., A. Djouadi and G. Azuelos, Z. Phys. **C63**, 327 (1994); based on A. Djouadi, Z. Phys. **C63**, 317 (1994).
- [241] W. Buchmüller and C. Greub, Nucl. Phys. **B363**, 345 (1991); M. Spira in Ref. [7].
- [242] J. Hewett and T. Rizzo, Phys. Rev. **D36**, 3367 (1987) and Phys. Rev. **D56**, 5709 (1997); J. Blümlein and R. Rückl, Phys. Lett. **B304** (1993); J. Blümlein, E. Boos and A. Kryukov, Phys. Lett. **B392**, 150 (1997).
- [243] R. Rückl, R. Settles and H. Spiesberger, in DESY 1997-048, chapter 1.8.3.
- [244] T. Rizzo, Int. J. Mod. Phys. **A13**, 2351 (1998); J. Hewett in Ref. [239].
- [245] K. Hagiwara, D. Zeppenfeld and S. Komamiya, Z. Phys. **C29**, 115 (1985); F. Boudjema, A. Djouadi and J. Kneur, Z. Phys. **C57**, 425 (1993) and Phys. Lett. **B240**, 485 (1990).
- [246] J. Bond, G. Efstathiou and Tegmark, Mon. Not. Roy. Astron. Soc. **291**, L33 (1997).
- [247] A. D. Sakharov, Pisma Zh. Eksp. Teor. Fiz. **5**, 32 (1967).
- [248] J. Lubish and P. Meade, Phys. Rev. **D71**, 035016 (2005); A. Birkedal, A. Noble, M. Perelstein and A. Spray, Phys. Rev. **D74**, 035002 (2006).

BIBLIOGRAPHY

- [249] C. Hill and R. Hill, arXiv:0705.0697 [hep-ph].
- [250] For studies at LHC, see e.g., M. Battaglia, I. Hinchliffe and D. Tovey, hep-ph/0406147; M. Nojiri, G. Polesello and D.R. Tovey, JHEP **0603**, 063 (2006).
- [251] J. Ellis, K. Olive, Y. Santos and V.C. Spanos, Phys. Lett. **B565**, 176 (2003).
- [252] E. Baltz, M. Battaglia, M. Peskin and T. Wizansky, Phys. Rev. **D74**, 103521 (2006).
- [253] See e.g.: H. Baer et al., JHEP **0402**, 007 (2004) and JHEP **406**, 061 (2004); A. Djouadi, M. Drees and J.L. Kneur, Phys. Lett. **B624**, 60 (2005) and JHEP **0603**, 033 (2006).
- [254] C. Böhm, A. Djouadi and M. Drees, Phys. Rev. **D62**, 035012 (2000); R. Arnowitt, B. Dutta and Y. Santos, Nucl. Phys. **B606**, 59 (2001); J.R. Ellis, K.A. Olive and Y. Santos, Astropart. Phys. **18**, 395 (2003).
- [255] M. Carena et al., Phys. Rev. **D72**, 115008 (2005); M. Carena, and A. Freitas, Phys. Rev. **D74**, 095004 (2006).
- [256] The figure is originally from J.L. Feng, J. Phys. **G32**, R1 (2006). It has been redrawn by J. Bagger using information from M. Nojiri on LHC measurements [250, 252] and G. Bélanger on ILC measurements [179, 252].
- [257] See e.g.: L. Covi et al., JHEP **0105**, 033 (2001) and JHEP **0406**, 003 (2004).
- [258] For ILC studies, see: H. Baer et al., JHEP **0402**, 007 (2004); B. Allanach et al., JHEP **0412**, 020 (2004); P. Bambade et al., hep-ph/0406010; M. Berggren, F. Richard, Z. Zhang, hep-ph/0510088; V. Khotilovitch et al., hep-ph/0503165.
- [259] G. Bélanger et al., Comp. Phys. Commun. **149**, 103 (2002).
- [260] F.D. Steffen, JCAP **0609**, 001 (2006).
- [261] W. Buchmüller et al., JHEP **0703**, 037 (2007).
- [262] A. de Roeck et al., Eur. Phys. J. **C49**, 1041 (2007).
- [263] K. Kong and K. Matchev, JHEP **01**, 038 (2006).
- [264] M. Battaglia, A. Datta, A. De Roeck, K. Kong and K. Matchev, JHEP **07**, 033 (2005).
- [265] G. Belanger, A. Pukhov and G. Servant, arXiv:0706.0526 [hep-ph].
- [266] A. Cohen, D. Kaplan and A. Nelson, Ann. Rev. N.P. Sci. **43**, 27 (1993); M. Trodden, Rev. Mod. Phys. **71**, 1463 (1999); M. Carena et al., Nucl. Phys. **B503**, 387 (1997).
- [267] H. Murayama and A. Pierce, Phys. Rev. **D67**, 071702 (2003).
- [268] J.R. Espinosa and M. Quiros, hep-ph/0701145.
- [269] M. Fukugita and T. Yanagida, Phys. Lett. **B174**, 45 (1986).
- [270] W. Buchmüller, P. Di Bari and M. Plumacher, Nucl. Phys. **B665**, 445 (2003).

LIST of FIGURES

| | | |
|------|--|----|
| 1.1 | Tracking resolution for a Higgs recoiling against dimuons at a 500 GeV ILC | 7 |
| 1.2 | Simulated purity/efficiency for b,c tagging and purity for WW/ZZ separation | 7 |
| 1.3 | Simulation of a 100 GeV jet using MOKKA for the TESLA TDR detector | 8 |
| 2.1 | Fit to the precision data and theoretical bounds on the Higgs mass in the SM | 10 |
| 2.2 | The masses and couplings to W/Z bosons of the Higgs bosons in the MSSM | 12 |
| 2.3 | The spectrum of neutral Higgs particles in extensions of the MSSM. | 13 |
| 2.4 | The LHC discovery potential for Higgs bosons in the SM and the MSSM. | 16 |
| 2.5 | The decay branching ratios and the total width of the SM Higgs boson | 17 |
| 2.6 | Feynman diagrams for the various Higgs production mechanisms at ILC. | 18 |
| 2.7 | Production cross sections of the SM Higgs boson at 500 GeV and 1 TeV ILC | 19 |
| 2.8 | Distributions of the dimuons recoiling against a SM Higgs boson at the ILC. | 20 |
| 2.9 | The missing mass in $\nu\bar{\nu}b\bar{b}$ final states from WW fusion and Higgs-strahlung | 21 |
| 2.10 | Higgs mass peaks reconstructed in different channels with constrained fits | 22 |
| 2.11 | The determination of the spin and CP-quantum numbers of a SM Higgs | 23 |
| 2.12 | The expected sensitivity on the SM Higgs branching ratios at the ILC | 25 |
| 2.13 | Expected accuracies for the measurement of the top-Higgs Yukawa coupling | 26 |
| 2.14 | Cross sections for double Higgs production and their determination at ILC | 27 |
| 2.15 | Determination of the Higgs two-photon coupling in $\gamma\gamma \rightarrow H \rightarrow b\bar{b}, WW/ZZ$. | 28 |
| 2.16 | ILC determination of the relation between particle couplings and masses | 29 |
| 2.17 | The decay branching ratios of the MSSM Higgs bosons | 30 |
| 2.18 | Production cross sections of the MSSM Higgs bosons at a 500 GeV ILC | 31 |
| 2.19 | Accuracy in the determination of invisible decays of the MSSM Higgs bosons | 32 |
| 2.20 | Cross section contours from various MSSM Higgs production processes | 33 |
| 2.21 | Production cross sections neutral MSSM Higgs bosons in $\gamma\gamma$ collisions | 33 |
| 2.22 | Detection of the heavy neutral and charged MSSM Higgs bosons at the ILC | 34 |
| 2.23 | Determination of the couplings of a SM-like Higgs and MSSM interpretation | 35 |
| 2.24 | Masses, couplings and branching ratios for some NMSSM Higgs bosons | 36 |
| 2.25 | Some decay widths and branching ratios for a Higgs mixing with a radion | 38 |
| 3.1 | Limits on contact interactions from fermion couplings at the ILC | 41 |
| 3.2 | $\sin^2 \theta_{\text{eff}}^l$ vs M_W measurements and compared SM and MSSM predictions | 43 |
| 3.3 | Measurement of anomalous gauge boson couplings at different machines. | 45 |
| 3.4 | Sensitivity on effective weak gauge boson parameters in no Higgs scenarios | 46 |
| 3.5 | Limits on the quartic coupling parameters from the VVV and VV $\ell\ell$ processes | 47 |
| 3.6 | Determination of the evolution of α_s at various e^+e^- energies. | 48 |

LIST OF FIGURES

| | | |
|------|--|-----|
| 3.7 | Extrapolations of the gauge couplings from GigaZ to the unification scale . | 48 |
| 4.1 | Sensitivity of observables to the top mass in a scan around the $t\bar{t}$ threshold | 51 |
| 4.2 | Beam spread, beamstrahlung and ISR effects on the top quark cross section. | 51 |
| 4.3 | Expected bounds on top quark anomalous couplings from the ILC and LHC. | 54 |
| 4.4 | Charged Higgs bosons from top decays: branching ratios and production rates | 56 |
| 5.1 | SUSY spectrum in a benchmark point and production cross sections at ILC | 60 |
| 5.2 | Measurements of cross sections/distributions in chargino production at ILC | 62 |
| 5.3 | Contours for chargino production cross sections with polarized e^\pm beams . . | 63 |
| 5.4 | Slepton mass measurements at the threshold and lepton energy spectra. . . | 64 |
| 5.5 | Lepton energy spectrum for sneutrino production and decay at the ILC . . | 65 |
| 5.6 | Determination of the mass and couplings of the top squark at the ILC . . . | 67 |
| 5.7 | Evolution from low to high scales of SUSY mass parameters in the cMSSM | 72 |
| 5.8 | The evolution of SUSY parameters in effective string and left-right models | 73 |
| 6.1 | Determination of the number of large extra-dimensions at the ILC | 77 |
| 6.2 | Graviton resonance peaks in $e^+e^- \rightarrow \mu^+\mu^-$ in the Randall–Sundrum model | 78 |
| 6.3 | Effects of radions and Kaluza–Klein excitations of gauge bosons at the ILC | 79 |
| 6.4 | Discrimination between SUSY and universal extra dimension models at ILC | 80 |
| 6.5 | The ILC search reach in little Higgs models and comparison with the LHC | 82 |
| 6.6 | Cross sections at ILC for pseudo–axion η production in little Higgs models | 82 |
| 6.7 | ILC sensitivity to new resonances for strong electroweak symmetry breaking | 84 |
| 6.8 | Sensitivity of the ILC on the parameters and particles of the BESS model . | 84 |
| 6.9 | The production of new vector bosons at the ILC in Higgsless scenarios . . . | 85 |
| 6.10 | Mass reach and coupling measurements for a heavy Z' boson at the ILC . . | 87 |
| 6.11 | Cross sections for pair and single production of new leptons at the ILC . . . | 88 |
| 6.12 | Direct production and indirect effects of heavy leptoquarks at the ILC . . . | 89 |
| 7.1 | Favored regions for dark matter in mSUGRA and relic density determination | 94 |
| 7.2 | Determination of the neutralino relic density at the ILC and LHC | 96 |
| 7.3 | Constraints on gravitino and stau masses and ILC stau lifetime measurement | 98 |
| 7.4 | Relic density of the lightest KK particle in universal extra dimensions models | 99 |
| 7.5 | Relic density of the dark matter particle in warped extra dimensional models | 100 |
| 7.6 | Dark matter abundance in an MSSM scenario with electroweak baryogenesis | 102 |
| 7.7 | Constraints and new effects in scenarios with electroweak baryogenesis . . . | 103 |
| 7.8 | ILC resolution on the right–handed neutrino mass in leptogenesis scenarios | 104 |

LIST of TABLES

| | | |
|-----|---|----|
| 2.1 | Expected accuracy on the Higgs branching ratio measurements at the ILC. | 24 |
| 2.2 | Relative precision in the determination of the SM Higgs total decay width. | 25 |
| 2.3 | Summary of the predictions of the SM Higgs couplings at the ILC | 30 |
| 3.1 | Results of parameter fits to the triple gauge boson couplings at the ILC . . | 44 |
| 4.1 | Accuracies in the determination of the top quark couplings to gauge bosons. | 53 |
| 5.1 | Some superparticle masses for two minimal Supergravity benchmark points. | 61 |
| 5.2 | Expected accuracy on some sparticle masses at ILC in a benchmark point . | 69 |
| 5.3 | Determination of the low energy MSSM parameters at the ILC and LHC. . | 71 |
| 5.4 | Determination of the fundamental SUSY parameters at the LHC and ILC. . | 72 |
| 6.1 | ILC sensitivity to the effective gravity scale for large extra dimensions . . . | 77 |
| 6.2 | Accessible scales for new heavy resonances at the ILC in no-Higgs scenarios. | 83 |
| 7.1 | Parameter sets for scenarios with dark matter in the constrained MSSM. . . | 95 |